Surface treated cp-titanium for biomedical applications : a combined corrosion, tribocorrosion and biological approach

Yaqin Yang

ÉCOLE CENTRALE DES ARTS
ET MANUFACTURES
« ÉCOLE CENTRALE PARIS »

THÈSE

présentée par

Yaqin YANG

pour l'obtention du

GRADE DE DOCTEUR

Spécialité : Science des Matériaux

Laboratoire d'accueil : Laboratoire de Génie des Procédés et Matériaux

Surface treated cp-titanium for biomedical applications: a combined corrosion, tribocorrosion and biological approach

soutenue le 16 octobre 2014

devant un jury composé de :

Jean DENAPE , Professeur à ENI-Tarbes	Président du Jury
Véronique MIGONNEY, Professeur à l'Université Paris 13	Rapporteur
Bernard NORMAND, Professeur à INSA-Lyon	Rapporteur
Didier LUTOMSKI, Professeur à l'Université Paris 13	Examinateur
Jean GERINGER , Docteur à ENSM-SE	Examinateur
Stefano MISCHLER, Docteur à EPFL (Suisse)	Examinateur
Bertrand DAVID, Docteur à ECP	Invité
Michel KEDDAM, Docteur à UPMC (Paris 6)	Invité
Vincent VIVIER, Docteur à UPMC (Paris 6)	Invité
Pierre PONTHIAUX, Professeur à ECP	Directeur de thèse

2014-ECAP0050

Acknowledgements

I consider myself to be lucky to have the opportunity to pursue a doctoral degree from Ecole Centrale Paris, one of the most famous Grandes Ecoles in France. At the end of such a long and laborious process, it is a great pleasure for me to express my gratefulness.

Firstly, I would like to thank my supervisor Prof. Pierre Ponthiaux from Ecole Centrale Paris for his constant guidance and endless encouragement in the whole study period. He gave me the opportunity to start this thesis. And it is his enthusiasm and great efforts that make it possible for me to finish my work on schedule. His support and help are so appreciated for me and I cannot forget to recognize that his involvement with other research groups was essential for me to learn more knowledge and skills in this study.

I would also express my sincere thanks to the jury committee members, Prof. Jean Denape from ENI-Tarbes for accepting to be the jury president, Prof. Véronique Migonney from Université Paris 13 and Prof. Bernard Normand from INSA-Lyon for accepting to be the reviewers, Prof. Didier Lutomski from Université Paris 13, Dr. Jean Geringer from ENSM-SE and Dr. Stefano Mischler from EPFL (Switzerland) for accepting to be the examiners of this doctoral research work.

Also, I would like to thank Mr. François Wenger for his guidance and important discussion that motivated me to develop and improve this work in my first year. Even when he retired, he still did me his favor if I had difficulties in the study.

I would like to thank Prof. Elizabeth J. Podlaha from Northeastern University for her kind invitation and guidance in my three-month internship in Boston, USA. In her laboratory, she introduced me a new scientific field in electrochemical deposition of metallic materials. And during this internship period, I finished the preparation of CaP bioactive film on cp Ti, which makes the Chapter 6 and Chapter 7 available in this thesis development.

A special thank you to Dr. Bertrand David and Mr. Eric Perrin in Laboratoire MSSMat for their help and encouragement in the biological culture of NiH/3T3 fibroblast cells on cp Ti. They provided me an opportunity to touch such a brand new area of biology, from which the preliminary experimental results about the biocompatibility of cp Ti have been obtained.

I am grateful to the present and past members of the Laboratoire de Génie des Procédés et Matériaux (LGPM), in particular, to Mathilde Charters and Nathalie Ruscassier for their guidance in SEM manipulation, to Claudiu Ionescu for his efforts in equipment operation, to Sandra Julien-Anchier for her kind help in administrative affair, to Feng Liao for her enthusiastic help in my thesis writing process.

Finally, I would like to dedicate this work to my parents and my sister. It is their unreserved love and support that keeps me moving forward. Without their encouragement, I could not carry out this study.

Contents

List of Symbols and Abbreviations

ΔE	potential drop-down during sliding, V
ΔE_{oc}	open circuit potential fluctuation, V
a	radius of the Hertzian static contact area, mm
A_0	total surface area, cm^2
A'_0	total surface area of surface modified sample, cm^2
A_{act}	area of active material in the wear track, cm^2
ASTM	American Society for Testing and Materials
A_{repass}	area of repassivated material in the wear track, cm^2
A_{tr}	whole wear track area, cm^2
A'_{tr}	whole wear track area of surface modified sample, cm^2
B	constant of 26 mV in this work
CaP	Calcium phosphate
CE	counter electrode
cp Ti	commercially pure titanium (Grade 2 in this study)
CPE	constant phase element
d	density of bare material, $g\ cm^{-3}$
d^*	arithmetic mean of the two diagonals in hardness measurement, mm
D	diameter of the wear track, cm
e	average wear track width, cm
e'	average wear track width of surface modified sample, cm
E	electrical voltage, V
E^*	Elastic modulus, MPa
$E_{applied}$	applied potential, V vs. RE
E_{corr}	corrosion potential, V vs. RE
EDS	energy-dispersive X-ray spectroscopy
EIS	electrochemical impedance spectroscopy
E_{max}	maximum potential value at the start of sliding, V vs. RE
E'_{max}	maximum potential value during intermittent sliding, V vs. RE
E_{min}	minimum potential value during continuous sliding, V vs. RE
E'_{min}	minimum potential value during intermittent sliding, V vs. RE
E_{oc}	open circuit potential, V vs. RE
E_{pp}	primary passive potential, V vs. RE
E_t	potential at time t, V vs. RE
E_{tp}	transpassive potential, V vs. RE

f	frequency, Hz
F	Faraday constant, 96 485 C mol^{-1}
F^*	load in hardness measurement, kg
F_n	normal loading force, N
F_t	tangential force, N
HV	Vickers hardness
i	applied current density, A cm^{-2}
i_0	exchange current density, A cm^{-2}
i_{act}	corrosion current density of the active material, A cm^{-2}
i_{corr}	corrosion current density, A cm^{-2}
i_{crit}	critical current density, A cm^{-2}
i_p	passive current density, A cm^{-2}
I	electrical current, A
ICDD	International Center for Diffraction Data
I_t	current at time t, A
K_c	ratio of the material loss due to corrosion over the material loss due to mechanical wear in the wear track
K_m	ratio of the specific material loss due to mechanical wear of the active material over the specific material loss due to mechanical wear of the repassivated material in the wear track
L	length of the wear track, cm
M	molecular weight, g mol^{-1}
N	total rotation number of cycles
n	number of electrons involved in the oxidation process
OCP	open circuit potential
p	exponent
PBS	phosphate buffered solution
P_{max}	maximum contact pressure, MPa
P_m	average contact pressure, MPa
r_{act}	specific polarization resistance of the active material, Ω cm^2
r_p	specific polarization resistance, Ω cm^2
r'_p	specific polarization resistance of surface modified sample, Ω cm^2
R	electrical resistance, Ω
R^*	radius of the tip of the curved counterbody, mm
R_a	average roughness value, μm
R_{act}	polarization resistance of the active material under continuous sliding condition, Ω
R_{ct}	charge transfer resistance results from the electrochemical reactions at

	the interface of electrode and electrolyte, Ω
RE	reference electrode
R_{film}	resistance of the outer porous $Ca_3(PO_4)_2$ layer for the CaP/TiO_2 bioceramic film coated Ti, Ω
R_{inner}	resistance of the inner compact oxygen-diffused titanium layer for the thermal oxidized Ti, Ω
R_{oxide}	resistance of the inner compact $CaTi_{21}O_{38}$ and TiO_2 layers for the CaP/TiO_2 bioceramic film coated Ti, Ω
R_{outer}	resistance of the outer porous TiO_2 layer for the thermal oxidized Ti, Ω
R_p	polarization resistance of passive and repassivated area under continuous unidirectional sliding conditions, Ω
R'_p	polarization resistance of surface modified sample, Ω
R_{ps}	polarization resistance during continuous sliding of the total area, Ω
R'_{ps}	polarization resistance during continuous sliding of the total area of surface modified sample, Ω
R_s	solution resistance, Ω
S	average cross-sectional area of the wear track, cm^2
S'	average cross-sectional area of the wear track of surface modified sample, cm^2
SEM	scanning electron microscope
SHE	standard hydrogen electrode
t_{lat}	latency time, s
t_{off}	immobile off-time during intermittent unidirectional sliding tests, s
t_{react}	reaction time to form passive surface film, s
t_{rot}	rotation period, s
T	constant, F cm^{-2} $s^{\phi-1}$
TO	thermal oxidation
w^c_{act}	specific material loss due to the corrosion of active material, cm/cycle
w^c_{repass}	specific material loss due to the corrosion of repassivated material, cm/cycle
w^m_{act}	specific material loss due to the mechanical wear of active material, cm/cycle
w^m_{repass}	specific material loss due to the mechanical wear of repassivated material, cm/cycle
W^c	material loss removed by corrosion, cm^3
W^{cm}	modification of the corrosive material loss caused by wear, cm^3
W^c_{act}	material loss due to corrosion of active area in the wear track, cm^3
W^c_{repass}	material loss due to corrosion of repassivated material in the wear track, cm^3

WE	working electrode
W^m	material loss removed by mechanical wear, cm^3
W^{mc}	modification of the mechanical material loss caused by corrosion, cm^3
W^m_{act}	material loss due to mechanical wear of active material in the wear track, cm^3
W^m_{film}	material loss due to the mechanical wear of surface modified film, cm^3
W^m_{repass}	material loss due to mechanical wear of repassivated material in the wear track, cm^3
W^s	material loss due to synergistic effect between wear and corrosion, cm^3
W_{tr}	total material loss in the wear track, cm^3
W'_{tr}	total material loss in the wear track of surface modified sample, cm^3
XRD	X-ray diffraction
Z	impedence, Ω
Z_{im}	imaginary part of the impedance, Ω
Z_{re}	real part of the impedance, Ω
β	Tafel slope
β_a	anodic Tafel slope
β_c	cathodic Tafel slope
ϕ	an exponent between 0 and 1
φ	phase shift angle
ν	Poisson's ratio
ω	angular frequency, rad/s
η	overpotential, V

Chapter 1: Introduction

1.1 Background

The field of biomaterials in orthopedic and dental implants application has attracted more and more attentions, as these materials enhance the quality and longevity of human life. The science and technology associated with this field has led to multi-million dollar business now. According to a research survey [1], the global bio-implants market is estimated to be $94.1 billion in 2012 and is poised to grow at a CAGR (Compound Annual Growth Rate) of 7.3% from 2012 to 2017. As dental implant for example, statistics show that 69% of adults ages 35 to 44 have lost at least one permanent tooth because of an accident, gum disease, a failed root canal or tooth decay. By age 74, 26% of adults have lost all of their permanent teeth. Recently, about 10 millions patients are treated per year with 12 millions implants, but that only covers 1% of missing teeth and the major 99% are untreated due to lack of education of professionals at dental college as well as high out-of-pocket treatment cost [2]. These obtained data indicate that biomedical implants are becoming a personal health issue for most of us with an increase in the number of implantation procedures.

1.2 Titanium based biomedical implants

Titanium and its alloys, as one of the important biomaterials for orthopedic and dental implants, have been tremendously used due to their good mechanical properties, excellent corrosion resistance and adequate biocompatibility [3-5]. The use of titanium in dentistry began in the 1960s with the Branemark system for prosthesis design and surgical procedure [6, 7]. In parallel with this, orthopedic prostheses of titanium for hip-joint fixation or replacement were also developed. However, the bio-inertial property of titanium and its alloys commonly cause a long osseointegration process [8, 9]. The release of ions due to corrosion and wear debris from mechanical friction can result in the infection/inflammation of the surrounding tissues [9, 10]. These disadvantages limit the development of titanium and its alloys as biomedical implant materials. Therefore, to improve the wear resistance and biocompatibility of titanium based implants is not only the focus of most implant industries and manufacturers (see Figure 1-1), but also research interest of scientists and engineers.

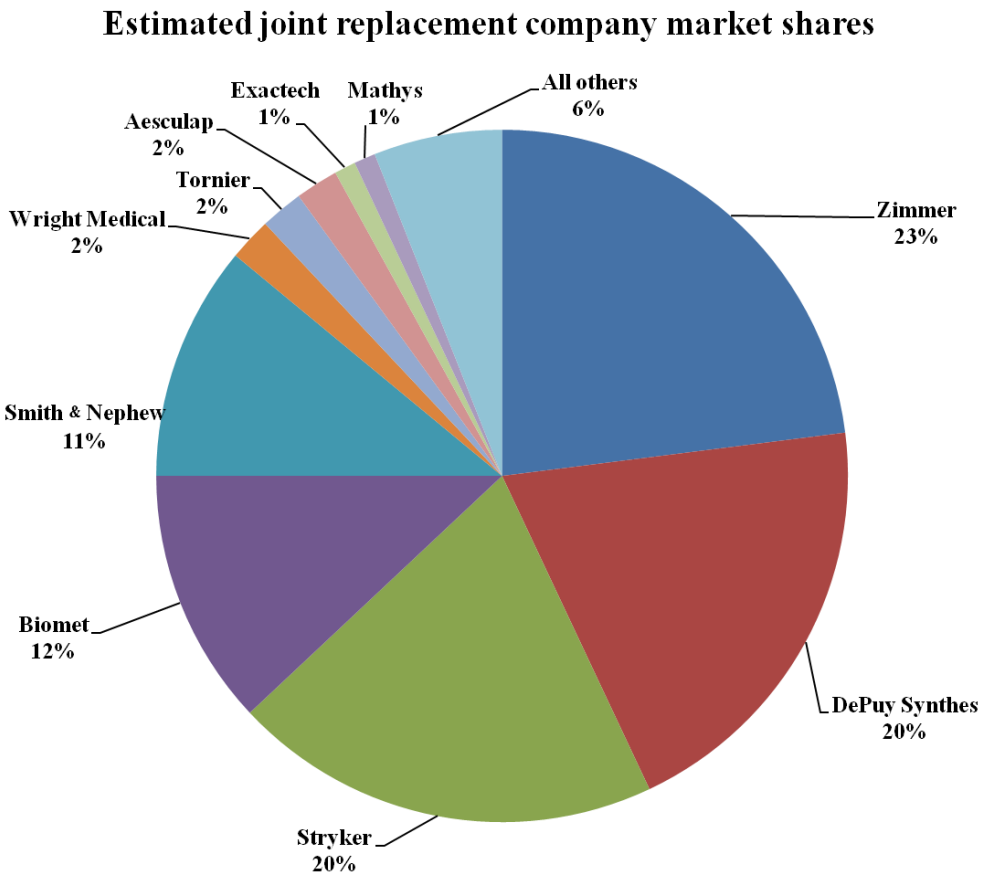

Figure 1-1 International major manufacturers of implant [11].

1.3 Aims and objectives

Wear and corrosion are considered as two important issues for titanium based implants, but few studies have been investigated to understand their combined effect – tribocorrosion for loading implants. Therefore, the aim of this work is to provide a deep insight in the area of tribocorrosion behavior for commercially pure titanium (cp Ti). And then three different surface modification treatments, as (1) one-step thermal oxidation of titania (TiO_2) film, (2) one-step electrochemical deposition of calcium phosphate (CaP) bioactive film, and (3) two-step electrochemical deposition/thermal sintering of CaP/TiO_2 bioceramic film, have been prepared on cp Ti to improve its corrosion/wear resistance, and even to give a promising method in shortening the osseointegration process. Preliminary study in the culture of NiH/3T3 fibroblast cells was done to investigate the cell's proliferation on cp Ti as bioimplant material. The main objectives of this study can be summarized as:

- To analyze the corrosion and tribocorrosion behavior of cp Ti in simulated body fluid by combining tribological and electrochemical tests.
- To characterize the thermal oxidized TiO_2 film and analyze its effect on corrosion and

tribocorrosion behavior of cp Ti.

◆ To characterize the CaP bioactive film and analyze its effect on corrosion and tribocorrosion behavior of cp Ti.

◆ To characterize the CaP/TiO_2 bioceramic film and analyze its effect on corrosion and tribocorrosion behavior of cp Ti.

◆ To study the NiH/3T3 fibroblast cell's proliferation on cp Ti and propose a cell culture procedure on cp Ti.

1.4 Outline of the thesis

This thesis contains nine chapters. General introduction is presented here in Chapter One.

Chapter Two covers the state-of-the-art in the area of biomaterials, basic theories of corrosion and wear, and titanium and its alloys as biomedical implants. Related topics like the development of biomedical implant, the current research status in surface modification of titanium and its alloys, and the understanding of corrosion and tribocorrosion are reviewed.

In Chapter Three, the experimental methodologies, procedures and equipments used in this study are described. Details of a tribocorrosion protocol for cp Ti as a passivating material is also delineated.

Chapter Four, which describes the corrosion behavior of cp Ti in static condition and its tribocorrosion behavior under mechanical loaded condition, represents the contributions of loading force and depassivation/repassivation phenomena in material loss of cp Ti under the guidance of the tribocorrosion protocol.

The influences of thermal oxidized TiO_2 film, CaP bioactive film and CaP/TiO_2 bioceramic film on corrosion and tribocorrosion behavior of cp Ti are discussed in Chapter Five, Chapter Six and Chapter Seven, respectively.

The preliminary study in the culture of NiH/3T3 fibroblast cells on cp Ti without any surface modification was done in Chapter Eight and a feasible cell culture procedure was proposed.

The main conclusions from this study and the possible future work which might be continued are given in Chapter Nine.

Chapter 2: Literature Review

2.1 Biomaterials and biomedical implants

Biomaterials are defined as the materials of natural or manmade origin that are used to direct, supplement, or replace the functions of living tissues [12]. The field of biomaterials is not new and can track back to about 2000 BC, when the Egyptians and Romans had used linen for sutures, gold and iron for dental applications and wood for toe replacement. These were the earliest evidences in the field of biomaterials. Now, this field is of importance for human beings in different area of medical industry [13], especially for the less fortunate people who are suffering from congenital heart disease and also for the aged population who require biomedical implants to increase their lifespan (see Table 2-1).

Table 2-1 Use of Biomaterials [13].

Problem Area	Examples
Replacement of diseased or damaged part	Artificial hip joint, kidney dialysis machine
Assist in healing	Sutures, bone plates, and screws
Improving function	Cardiac pacemaker, intraocular lens
Correct functional abnormality	Cardiac pacemaker
Correct cosmetic problem	Augmentation mammoplasty
Aid to diagnosis	Probes and catheters
Aid to treatment	Catheters, drains

In the case of biomedical implants, thanks to the availability of better diagnostic tools and the advancements in the knowledge on materials and on surgical procedures, implantology has assumed greater. Biomedical implants now can be commonly used in dentistry, orthopedics, reconstructive surgery, ophthalmology, cardiovascular surgery, neurosurgery, immunology, histopathology, experimental surgery and veterinary medicine (see Figure 2-1) [14].

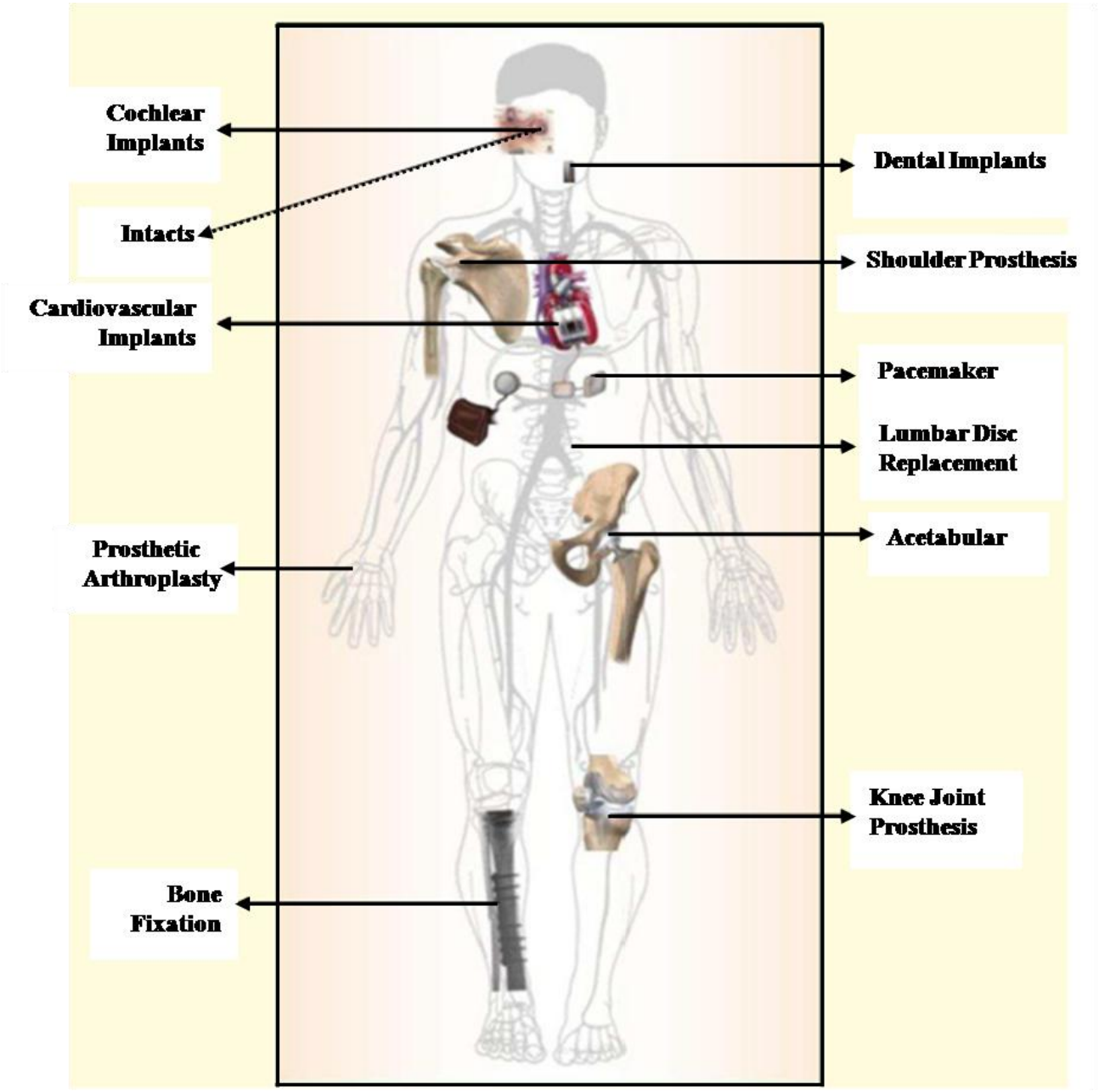

Figure 2-1 Biomaterials for human application [14].

As a very high boom in implant manufacturing is expected in coming years, decreasing the pain during surgery for the patient, cutting down the surgical cost and increasing the success rate are necessary and they require the collaborative effort between material scientists and engineers, biomedical engineers, pathologists and clinicians. In order to serve for longer period without rejection, biomedical implants should meet the special requirements [5, 9]. The first and important requirement is that the material must be biocompatible. That means that the device does not cause any adverse reaction in the body and can be well integrated with the surrounding tissues. The second requirement is that the material must be corrosion resistant in the body aggressive environment. Corrosion resistance ensures that metal ions will not release into the body to take inflammation to human organs and/or

tissues. Furthermore, the implantable device will retain its integrity and not degrade due to corrosion. The third requirement is that the device must have sufficient mechanical strength and fatigue strength. This guarantees the match of modulus between natural tissue, like bones and foreign implants. The fourth requirement is the appropriate design for the intended use. Crevices should be avoided to provide good corrosion resistance. Implant with identified shape of each patient is recommended to increase the success rate of osseointegration. The fifth requirement is the proper surface treatment. Once the device is implanted into the bone, its surface is the part that contacts and interacts directly with body fluids and tissues. Surface treatment controls the nature of surface and is important to act as a method of improving biocompatibility.

Nowadays, implantable devices intended in biomedical application as implants are mainly from bioceramics, biodegradable polymers and metallic material [13, 15-17].

2.1.1 Bioceramics

Bioceramics are generally employed to produce biomedical devices for the functional replacement of hard tissues. In the use of bone tissue engineering, bioceramics can be classified as bioinert (*e.g.*, zirconia and alumina), bioresorbable (*e.g.*, tricalcium phosphate [TCP]) and bioactive (*e.g.* hydroxyapatite [HA] bioactive glasses and HA glassceramics) [18-21]. They can be found in many applications as orthopedic and dental restorations. In the case of orthopedics, bioceramic materials are mainly used in the manufacture of prostheses for joint replacements, and also in osteosynthesis for the reconstruction of a bone. In the case of density, ceramics are used for implants and for the production of artificial teeth, typically in abutment part. In 1969, the first paper about the use of zirconia in biomedical applications was reported [22] and then the first paper to illustrate its use in manufacturing of ball heads for total hip replacement was published in 1988 [23].

When it refers to alumina, a ceramic consists of a polycrystalline monophasic structure and possesses the highest oxidation state (as Al^{3+}), allowing hydrodynamic stability, chemical inertness and corrosion resistance [24]. The hardness of alumina, which is about three times more than that of metallic biomaterials, makes it resistant to scratches and wear. But its flexural strength and fracture toughness are limited under *in vivo* bearing conditions. Comparing with aluminia, zirconia is a white crystalline oxide of zirconium (as Zr^{4+}) and owes a polycrystalline biphasic structure. At high temperatures, pure zirconia has an unstable state of tetragonal phase, but a stable state of monoclinic structure at room temperature. A volume increase of the grain results from the phase transformation from the metastable tetragonal phase into the monoclinic phase, so ageing of zirconia can result in surface roughening. This phenomenon makes the zirconia ceramic with higher tenacity, density and flexural strength, but its hardness, stiffness and grain size are lower than alumina. These properties decrease the risk of breakage in orthopedic application [25].

2.1.2 Biodegradable polymers

Natural and synthetic polymers have shown promise as bone graft materials due to their plastic and viscoelastic properties, degradability, and biocompatibility [26]. Natural polymers like collagen, silk, fibrin, hyaluronic acid, chitosan, and alginate, are often used as bone grafts. The application of synthetic biodegradable polymers started only in 1960s [27], in spite of the fact that the biomedical applications of natural polymers dates back thousands of years. Due to the facility to be shaped with desired pore morphologic features and be designed with chemical functional groups to induce tissue in-growth, synthetic polymers become more and more attractive in recent years. According to the literatures [27-29], the most common biodegradable polymers for bone grafts include poly(glycolic acid) (PGA), poly(lactic acid) (PLA), poly(lactic-co-glycolic acid) (PLGA), poly(caprolactone) (PCL), poly(propylene fumarate) (PPF), polyethylene (PE), polytetrafluoro ethylene (PTFE), poly(ethylene glycol) (PEG) and ultra high molecular weight polyethylene (UHMWPE). As a total hip replacement device for instance, biodegradable polymers like PE, PTFE and UHMWPE are often used as acetabular cup, mating with the metallic femoral.

However, even most of the natural and synthetic polymers are biodegradable and biocompatible, the interior mechanical strength always limits their use in bone repair application. In the use of acetabular cups made of PE, wear creating debris from PE articulating surfaces might accumulate in the interfacial area between tissue and implant, which further leads to loosening of the implant stem [17].

2.1.3 Metallic materials

Metallic materials as metals and alloys are widely employed to produce many types of biomedical devices [30]. They are used for the manufacture of surgical instruments in orthopedic and dental prostheses or as devices for osteosynthesis. In modern history, metals have been used as implants for bone fracture fixation since more than 100 years ago [31]. In the early development, corrosion and insufficient strength were two main problems faced by metal implants [32]. But after the introduction of corrosion resistant 18-8 stainless steel in 1920, it solved the corrosion problem and thereafter promoted the vast clinical use of metal implants.

Up to now, hundreds of type of metals and alloys has been used and commonly been divided into three groups: (1) Stainless steel [33]; (2) cobalt-chromium (Co-Cr) alloys [34]; (3) titanium and its alloys [16, 35]. The corrosion resistance of these metallic biomaterials relies on their passivation by forming a thin surface oxide layer, like Cr_2O_3 and TiO_2 [4, 36-38]. Table 2-2 shows the type of metals which are generally used for different implants division.

Table 2-2 Implants division and type of used metals [39].

Division	Implants	Type of metal
Orthopedic	●Bone fixation	SS316L; Ti; Ti-6Al-4V
	(plate, screw, pin)	SS316L; Ti; Ti-6Al-4V; Ti-6Al-7Nb
	●Spinal fixation	Co-Cr-Mo; Ti-6Al-4V; Ti-6Al-7Nb
	●Artificial joints	
Craniofacial	Plate and screw	SS316L; Co-Cr-Mo; Ti; Ti-6Al-4V
Cardiovascular	●Artificial valve	Ti-6Al-4V
	●Stent	SS316L; Co-Cr-Mo; Ti
	●Pace maker case	Ti; Ti-6Al-4V
	●Stent graft	SS316L
Otorhinology	●Artificial eardrum	SS316L
	●Artificial inner ear	Pt
	(electrode)	
Dentistry	●Filling	Ag-Sn(-Cu) amalgam; Au
	●Inlay, crown, bridge	Au-Cu-Ag; Au-Cu-AG-Pt-Pd; Ti; Co-Cr
	●Orthodontic wire	SS316L; Co-Cr-Mo; Ti-Ni; Ti-Mo
	●Dental implant	Ti; Ti-6Al-4V; Ti-6Al-7Nb; Au

The first stainless steel used for implants contains ~18 wt% Cr and ~8 wt% Ni which make it stronger than the steel and more resistant to corrosion. Further addition of Mo has improved its corrosion resistance, known as SS316. Afterwards, the carbon content has been reduced from 0.08 to 0.03 wt% to improve its corrosion resistance to chloride solution, and named as SS316L. Co-Cr alloys have been utilized for many decades in making artificial joints. They are generally known for their excellent wear resistance. The wrought Co-Ni-Cr-Mo alloy has been used for making heavily loaded joints such as ankle implants. However, elements such as Ni, Cr and Co are found to be released from stainless steel and Co-Cr alloys in the body corrosive environment. The toxic effects of metals are harmful and may cause local adverse tissue reactions. In addition, both stainless steel and Cr-Co alloys possess much higher modulus than bone, leading to insufficient stress transfer to bone, which leads to bone resorption and loosening of implant after some years of implantation. Figure 2-2 shows the elastic modulus of biomedical alloys commonly used in biomedical implants [16].

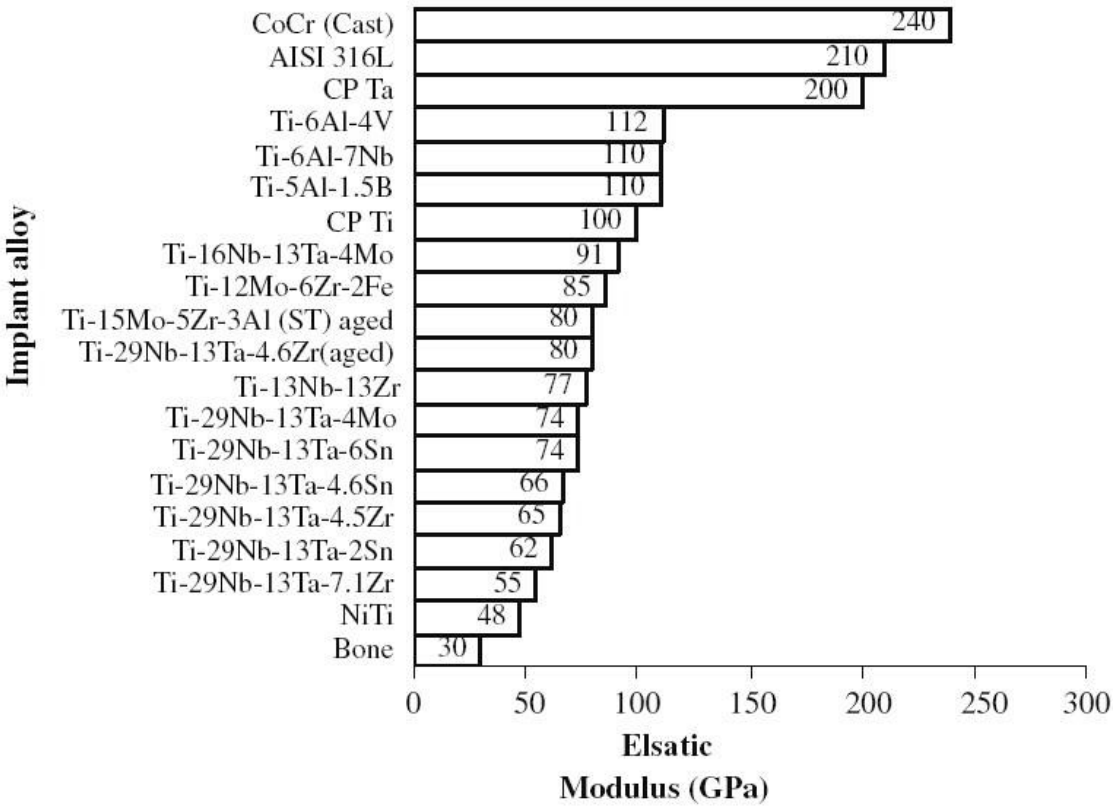

Figure 2-2 Modulus of elasticity medical alloys [16].

Comparing with stainless steel and Co-Cr alloys, titanium has lower modulus vary from 112 GPa to 48 GPa. Furthermore, the light weight of titanium, whose density is only 4.5 g/cm^3 compared to 7.9 g/cm^3 for 316 stainless steel and 8.3 g/cm^3 for cast Co-Cr-Mo alloy, also attracts attentions from patients and manufacturers. The early attempt to use titanium for implant fabrication can date back to the late 1930s, when titanium was found to be well tolerated in cat femur like stainless steel and vitallium (a Co-Cr alloy). Titanium can be alloyed with many elements, like iron (Fe), aluminium (Al), vanadium (V) and molybdenum (Mo), to produce strong, lightweight alloys as desired by the application of medical prostheses, orthopedic implants and dental implants. In order to get a concise understanding about their excellent mechanical properties, cp Ti and some of its important alloys employed in the field of biomedical devices are listed in Table 2-3. With these properties, the use of titanium and its alloys is developed quickly nowadays.

Table 2-3 Mechanical properties of biomedical titanium alloys [16].

Material	Standard	Modulus (GPa)	Tensile strength (MPa)	Alloy type
cp Ti (grade 1-4)	ASTM* 1341	100	240-550	α
Ti-6Al-4V ELI	ASTM F1472	112	895-930	α+β
Ti-6Al-7Nb	ASTM F1295	110	900-1050	α+β
Ti-5Al-2.5Fe	—	110	1020	α+β
Ti-13Nb-13Zr	ASTM F1713	79-84	973-1037	Metastabe β
Ti-12Mo-6Zr-2Fe	ASTM F1813	74-85	1060-1100	β
Ti-35Nb-7Zr-5Ta		55	596	β
Ti-29Nb-13Ta-4.6Zr	—	65	911	β
Ti-35Nb-5Ta-7Zr-0.4O		66	1010	β
Ti-15Mo-5Zr-3Al		82		β
Ti-Mo	ASTM F2066			

*ASTM: American Society for Testing and Materials

2.2 Corrosion and wear of metallic materials

Metallic materials have been used for oral implants and joint replacements due to their high strength, ductility and toughness. There is no doubt that they are good choices for a short-term fixation or substitute of hard tissues. However, the electrochemical reactivity of metal components in a physiological environment (typically as a 37 ℃ aqueous solution at pH of 7.4) restricts their life span as long-term biomedical implants. The applications of metallic material rely on their stability during continuous interactions with biochemical compositions in human body (such as dissolved gases, electrolytes, cells and proteins). The electrochemical potential between metal components and the surrounding corrosive body fluids causes localized anodic reactions. These undesired chemical/electrochemical reaction of metallic implants is also affected by mechanical loading, which is caused during the patient's living activities [40]. The combination effects of chemical/electrochemical and mechanical behavior ultimately incite the degradation of implants and then significantly limit their service life in the human body. This part represents some basic theories of corrosion and wear of metallic materials, and the synergism effect of corrosion and wear defined as tribocorrosion in true application as biomedical implants.

2.2.1 Corrosion

Corrosion is defined as the reaction of a material with its surrounding environment (like seawater, chloride containing body fluid and so forth) with a gradual deterioration in properties of the material. The reaction can be chemical, electrochemical, physical or their combination [41]. Three factors are

essential to study the corrosion phenomenon: the material, the environment and the material/environment interface. Although corrosion can also occur in materials as ceramics and polymers, electrochemical reaction of metallic materials is well referred in the most common sense. It has long been thought to occur by these three means: oxidation, dissolution and electrochemical interaction.

2.2.1.1 Basic processes

Electrochemical corrosion consists of two half-cell reactions: an oxidation reaction at the anode and a reduction reaction at the cathode. The oxidation and reduction reactions which are occurring on the interface of metal/electrolyte during the electrochemical process can be schematically interpreted as:

Oxidation of a metal atom M with transfer of n electrons e^-:

$$\mathbf{M \rightarrow M^{n+} + ne^-} \qquad \text{(2-1a)} \qquad \text{or}$$

$$\mathbf{M + nH_2O \rightarrow MO_{n/2} + nH^+ + ne^-} \qquad \text{(2-1b)}$$

Reduction of the oxidizing agent:

$$\mathbf{H^+ + 2e^- \rightarrow H_2} \qquad \text{(2-2a)} \qquad \text{or}$$

$$\mathbf{O_2 + 2H_2O + 4e^- \rightarrow 4OH^-} \qquad \text{(2-2b)}$$

For the passive metallic materials typically used in biomedical implants (as stainless steel, Co-Cr-based and Ti-based alloys), a self-protected thin oxide film is formed spontaneously, as explained by Eq. 2-1b. This phenomenon of metallic passivity was discovered early in 1790 by Keir, who found that metallic iron violently corroding in the active state in concentrated nitric acid (HNO_3) solution suddenly turned into the passive state where no corrosion was observed. But the presence of an oxide film with several nanometers thick on the surface of passivated metals was not confirmed until 1960s [42, 43]. The passive films formed on stainless steel and Co-Cr-based alloys are stongly enriched in Cr_2O_3 oxide, whereas on Ti-based alloys is mostly composed of TiO_2 [36-38]. Although the thickness of these passive films is only a few nanometers (normally < 10 nm) at room temperature, they act as a high protective barrier between the metal surface and the aggressive environment. The protectiveness of the passive film can be determined by the rate of ion transfer through the film, as well as the stability against oxide film's dissolution.

2.2.1.2 Potential-pH diagram and corrosion potential

Thermodynamics can show that an electrode reaction is reversible at the equilibrium potential, where no net reaction current is observed. It provides a mean to predict the equilibrium state of a system of metallic components. The anodic reaction of metallic corrosion occurs only in the potential range more positive than its equilibrium potential and the cathodic reaction of oxidant reduction occurs only in the potential range more negative than its equilibrium potential. Moreover, it is well known that metallic corrosion in an aqueous solution depends on both the electrode potential and the pH value of solution. In 1974, the thermodynamic prediction of metallic corrosion was firstly illustrated by Pourbaix in the form of a potential-pH diagram, as shown for iron corrosion in Figure 2-3.

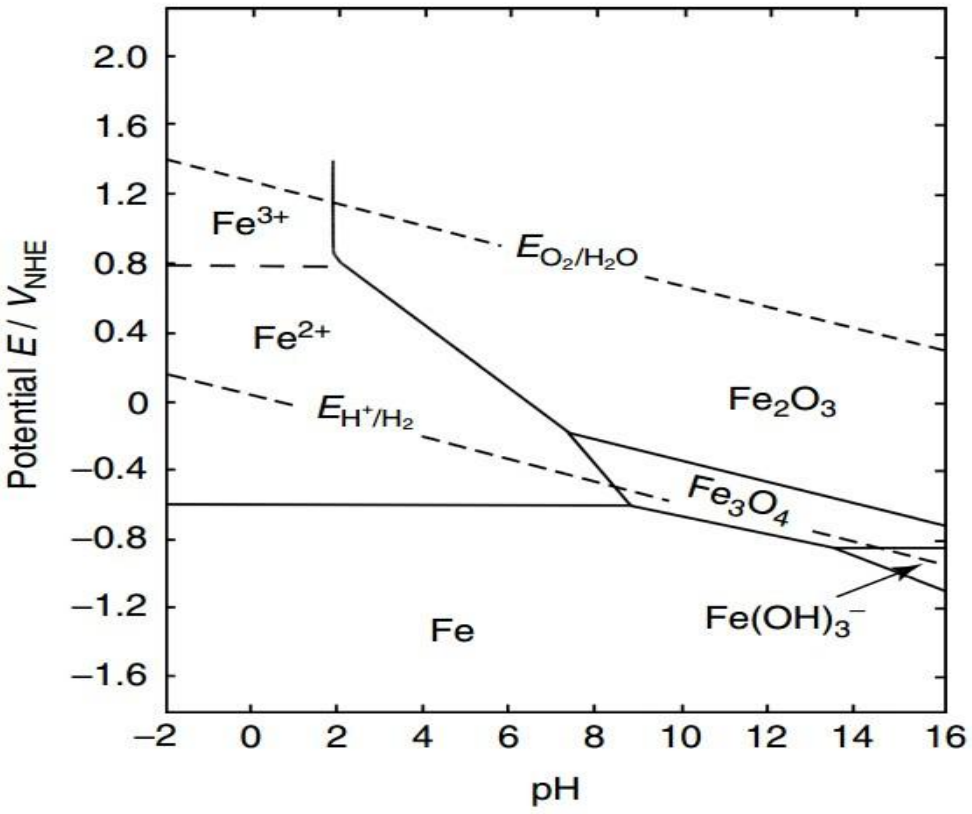

Figure 2-3 Potential-pH diagram for iron corrosion in water at room temperature [44].

($E_{O2/H2O}$ is the equilibrium potential for the oxygen electrode reaction, $E_{H^+/H2}$ is the equilibrium potential for hydrogen electrode reaction, and V_{NHE} is voltage on the normal hydrogen electrode scale.)

The corrosion of metallic iron occurs in the potential-pH regions where ferrous ions Fe^{2+}, ferric ions Fe^{3+} and hydroxo-ferrous ions $Fe(OH)_3^-$ are stable. In contrast, no iron corrosion happens in the region where metallic iron is thermodynamically stable at relatively negative electrode potentials. And in the regions where solid iron oxides Fe_2O_3 and Fe_3O_4 are stable, no iron corrosion into water is expected and the surface of iron substrate is covered with these solid oxide films. From Figure 2-3 we also observe the equilibrium potentials of the hydrogen and oxygen electrode reactions.

Dissolved oxygen from atmosphere may result in ion corrosion in the potential range more negative than the oxygen equilibrium potential, E_{O_2/H_2O}. While protons in aqueous solution can carry iron corrosion in the potential range more negative than the hydrogen equilibrium potential, E_{H^+/H_2}. Here is the potential-pH diagram measured in pure water containing no foreign species. But normally, the presence of foreign ions in aqueous solution like chloride and sulfides [44] affects the corrosion and anticorrosion regions of metallic component in the potential-pH diagram. The diagram in real system is more complicated than in pure water. For metallic biomaterials, it is worth noting that metallic passivity (or passivation) is caused by the formation of an oxide film on the metal in aqueous solution. The passive oxide film with a thickness of several nanometers is sensitive to the environment where it is formed. Its formation and growth processes can be illustrated as: the oxide ions migrate from the solution across the film to the metal-oxide interface forming an inner oxide layer, while the metal ions migrate from the metal to the oxide-solution interface to react with adsorbed water molecules and solute anions forming an outer oxide layer. The passive oxide film on metal is either an insulator (for metallic iron, titanium, nickel, chromium, *etc.*) or a semiconductor (for metallic aluminium, tantalum, *etc.*).

Corrosion potential is the electrode potential where a metallic electrode corrodes in aqueous solution. It stands in the range between the equilibrium potential of the anodic metal dissolution and the equilibrium potential of the cathodic oxidant reduction [42]. At the corrosion potential, the anodic oxidation current of the metal dissolution and the cathodic reduction current of the oxidant are equal. Figure 2-4 shows the schematic corrosion kinetics, which is often called as the polarization curves of corrosion reactions. The corrosion rate of metals is controlled by both the anodic and the cathodic reactions. In acidic solution, the cathodic hydrogen ion reduction controls the rate of metallic corrosion, while the cathodic oxygen reduction controls the corrosion rate of metals in neutral or basic solution.

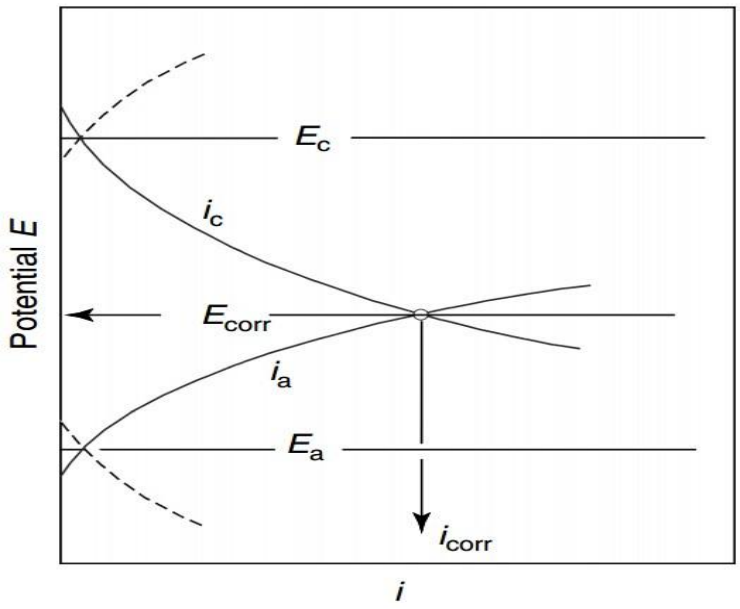

Figure 2-4 Conceptual polarization curves for metallic corrosion [42].

(i_a is the anodic reaction current, i_c is the cathodic reaction current, i_{corr} is the corrosion current, E_a is the equilibrium potential of the anodic reaction, E_c is the equilibrium potential of the cathodic reaction, and E_{corr} is the corrosion potential.)

2.2.1.3 Special modes of corrosion in metallic implants

Due to the corrosive environment of human body and the complicated using conditions after implantation, the metallic implants suffer from the risks of different modes of corrosion [45, 46].

- Pitting corrosion: Pitting corrosion is one common type of localized corrosion, which is caused by local dissolution of the passive film and the formation of cavities surrounded by a passivated surface. In the presence of aggressive ions in body fluid, like chloride ions [47], the passive film on metals breaks down and makes the underlying metals naked and directly exposed to the aggressive environment.

- Crevice corrosion: Crevice corrosion is another type of localized corrosion closely related to pitting corrosion. Preferentially, it occurs in regions on the metal surface where mass transfer is limited, *e.g.* under the deposits or in narrow crevices. In these blocked areas, surface can be activated by the concentration of aggressive chloride ions, the decrease of pH value and the consummation of oxygen [48, 49]. The anodic metal dissolution in a crevice is usually coupled with the cathodic oxidant reduction surrounding the crevice, where a local corrosion cell forms in the view of electrochemistry.

- Galvanic corrosion: Galvanic corrosion occurs between dissimilar metals or alloys in direct electrical contact in a conducting corrosive environment. As a bone screw and a bone plate made of different types of metallic materials for instance, galvanic couple forms in the contact

interface of these two parts. Thereafter, an increase in corrosion is generally observed in the less noble alloy and a decrease or suppression of corrosion in the nobler alloy [50, 51].

- Fretting corrosion and/or wear-corrosion: Fretting corrosion and/or wear-corrosion are in the form of a damage occurring at the interface of two contacting surfaces under continuous oscillating rubbing or cyclic loading[52, 53]. Mechanical damage of the passive oxide film resulting from fretting and/or wear can significantly change the corrosion behavior of metallic materials. Conversely, the corrosion products (acting as the three-body for example) may alter the interface state of the contacting surfaces and then affect the fretting or wear mechanisms. The synergism between mechanical friction and chemical/electrochemical corrosion always leads to an acceleration of material degradation [54-56].

Pitting corrosion was usually found on stainless steel implant materials, resulting in extensive damage and causing release of significant amounts of metal ions. But Ti and Ti-based alloys show very high pitting potentials even in chloride-containing solutions (about 10 V) [46]. Almost no pitting corrosion can be observed for Co-Cr alloys. In simulated physiological solutions, metastable pitting corrosion (taking place in the potential region of stable passivity which is below the pitting corrosion) can be observed in the form of current transients. Even though metastable pitting corrosion does not lead to a serious deterioration of the system, it still indicates that the metal is not completely stable in its environment.

Stainless steel is also the most susceptible to crevice-induced localized corrosion, comparing with other two alloy groups (Co-Cr-based alloys and Ti-based alloys) used as biomedical implants [48]. For Co-Cr-based alloys, due to the very high Cr-content in the passive film, this kind of metallic biomaterial can be expected to be more resistant against activation on local acidification. When referring to Ti-based alloys, the crevice corrosion in chloride ions containing solutions can only occur at elevated temperatures like 70-80 ℃ [57].

Relating to the patients' living activities, fretting corrosion and/or wear corrosion are commonly observed for biomedical implants such as hip, knee and shoulder replacements. Repetitive relative frictional movements are induced at the interface between biomedical implants and natural bones or between different parts of implants in the corrosive body fluids. The generated debris (normally the metal oxide) accumulated at the interface may result in the loosening and failure of implantation surgery. An increase in the hardness of biomedical implant can lead to a reduction of fretting wear, stainless steel and Co-Cr alloys with high value of hardness were found to exhibit better fretting corrosion behavior than titanium and its alloys [58, 59].

2.2.2 Wear

Wear is defined [60-62] as "damage to a solid surface, generally involving progressive loss of material, due to relative motion between that surface and a contacting substance or substances". It is a

critical issue for prostheses, implants and other medical devices. The wear mechanisms in biomedical implants are reported to be a function of type of used materials, contact pressures, surface hardness and roughness, fretting/sliding/rolling velocity, number of applying cycles, environment and lubricant.

2.2.2.1 Classification of wear mechanisms

In biomedical application as implants, wear can occur through five major mechanisms (as seen in Figure 2-5):

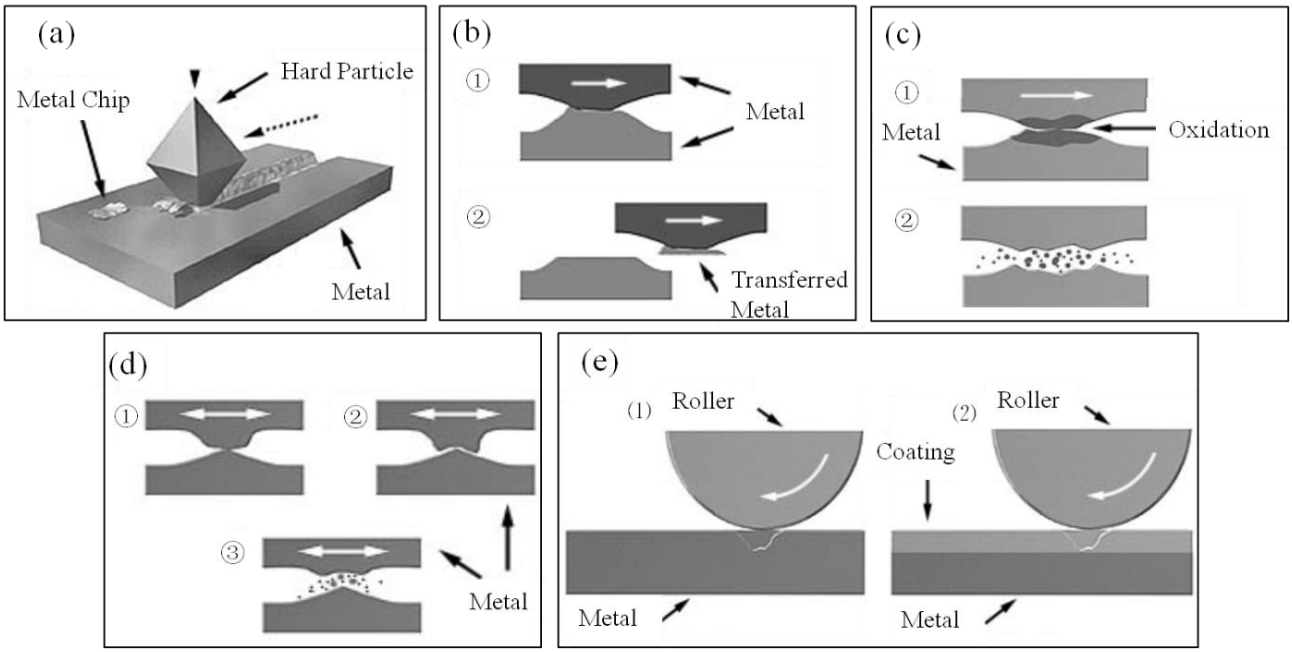

Figure 2-5 Schematic representations of wear mechanisms in biomedical implants: (a) abrasive wear; (b) adhesive wear; (c) oxidative wear; (d) fretting wear; (e) fatigue wear in metal-on-metal mode (1) and metal-on-coating mode (2), respectively.

◆ Abrasive wear: Abrasive wear [61] occurs when a hard and rough surface slides across a softer surface, resulting in the loss of material mainly on the later one. Two-body and three-body abrasive wears are the two typical abrasive wear modes.

◆ Adhesive wear: Adhesive wear [63] (scoring, galling, or seizing) occurs when two solid surfaces in intimate contact with each other, slide under pressure. It can be found between surfaces during frictional contact and generally refers to unwanted displacement and attachment of wear debris and material compounds from one surface to another.

◆ Oxidative (Corrosive) wear: Oxidative wear [64] occurs when chemical reactions corrode a surface by forming an oxide film, which is then removed through wear. Once the oxide film is dissipated, the implant metals are susceptible to the releasing particles and metal ions. The oxide particles mix with metal and form a debris layer in oxidative wear. This type of wear

depends seriously on the environment which determines the growth rate of surface oxide films.

- Fretting wear: Fretting wear [52, 65] is the repeated cyclical rubbing between two surfaces, which is known as fretting, over a period of time which will remove material from one or both surfaces in contact.

- Fatigue wear: Fatigue wear [66] is a process by which the surface of a material is weakened by cyclic loading and surface cyclic shear stresses or strains exceed the fatigue limit for that material. It is produced when the wear particles are detached by cyclic crack growth of microcracks (either superficial cracks or subsurface cracks) on the surface.

In biomedical application as implants, two-body abrasive wear commonly occurs at the interface of ceramic-on-metal total hip replacement, where the harder surface (usually means ceramic part) cuts material away from the opposed metallic part. Three-body abrasive wear occurs when the wear debris (some small hard particles like oxide debris) trapped between the two rubbing surfaces. These particles are not constrained and free to roll and slide down a surface. Due to the average loose abrasive grain spends more time on rolling rather than abrading the sliding surfaces, abrasive wear rates during three-body abrasion are about 10 times less than during two-body abrasion [67].

Adhesive wear is one of the major observations on surface damage and degeneration of ultra-high molecular weight polyethylene (UHMWPE) used in artificial joints [68, 69]. Adhesion is a function of the counterpart material, the relative velocity, the contact pressure and the actual contact area. Because of the strong affinity between metals and carbon or hydrogen, a strong adhesion leads to transfer of polymer to metal surface. The transfer effect can be enhanced when tests are conducted with high loading, but be diminished in exist of lubricant.

Oxidative wear, also called as corrosive wear, is an indirect wear mechanism which occurs commonly in metallic implants. Metallic passivity can form a thin oxide film on the surface of biomedical metals and alloys, like stainless steel, Co-Cr-based alloys, Ti and Ti-based alloys [36-38]. The spall of oxidation acts as wear debris and brings in the third-body effect on the surfaces of contact materials.

Fretting wear is the damage that induced under load and in the presence of repeated relative surface motion, like vibration. It takes place at the contact area of metal-on-metal, ceramic-on-metal, ceramic-on-ceramic, polymer-on-ceramic, and polymer-on-metal prostheses replacements and even the contact area between the natural bone and implants [65, 70]. When fretting wear happens on the surface of metallic implants in a corrosive environment, oxidative wear occurs consequently as the result of passivation/depassivation and repassivation.

Fatigue wear has been identified as one of the major problems associated with implant failure in orthopedic applications like hip joint prostheses [66, 71, 72]. Surface fatigue is observed in metallic,

polymeric and ceramic implant materials. It is influenced by a variety of factors, such as temperature, surface finish, metallurgical microstructure, residual stresses, size and distribution of internal defects, *etc*.

We should recognize that these corrosion modes and wear mechanism don't exist alone but take place consequently or simultaneously in biomedical application as implants. In order to know precisely the degradation of biomaterials, one new research area combining multidisciplinary approaches in tribology and corrosion domains, defined as tribocorrosion, is developed in recent decades [37, 38, 54, 73-83].

2.2.3 Tribocorrosion

Tribocorrosion is a material degradation process due to the combined effect of corrosion and wear [84]. It is defined [73] as the study of the influence of chemical, electrochemical and/or biological environmental factors on the friction and wear behavior of surfaces of materials in mechanical contact with each other, and undergoing a relative motion to each other. Both the separated knowledge of the tribological behavior in the absence of any aggressive media, and the separated knowledge of the electrochemical behavior in the absence of any mechanical impacts are not sufficient to derive the tribocorrosion behavior of a material couple system [85].

In biomedical application as implants, friction between two components or the component and the natural bone may modify the sensitivity of metallic biomaterials to corrosion, and conversely, metallic corrosion may affect the friction between two moving contacts by changing the surface state. Normally, the synergism between mechanical friction and electrochemical corrosion leads to an acceleration of the tribo-chemical degradation of the material [86]. When it concerns to the factors affecting tribocorrosion process and mechanism, three considerations are listed as: (1) the properties of the contacting materials, (2) the mechanics of the tribological contact, and (3) the physiochemical properties of the solution.

In a separated tribological test, some macroscopic quantities are measured conventionally as: the coefficient of friction based on the friction force recorded *in situ*; the wear rate determined *ex situ* from a loss of material on one or both contacting materials (the loss results from the formation and escape of debris by mechanical interactions); the contact temperature measured *in situ* due to the conversion of mechanical energy to heat; the vibrations of the contacting parts and the noise eventually emitted during the test. Referring to the tribocorrosion test, complementary *in situ* measurements [86-89] like the electrochemical potential of the contacting surfaces immersed in a corrosive electrolyte, and/or *in situ* measurement of the corrosion current can be performed during the relative motion of contacting parts. To simulate the patients' living activities, this motion is either a continuous one or an intermittent one, and moving mode is either a unidirectional one (sliding) with different circumferences or a reciprocating one (fretting) with different oscillation amplitudes.

Figure 2-6 presents the influencing factors on tribocorrosion in the case of a sliding contact under electrochemical control conditions.

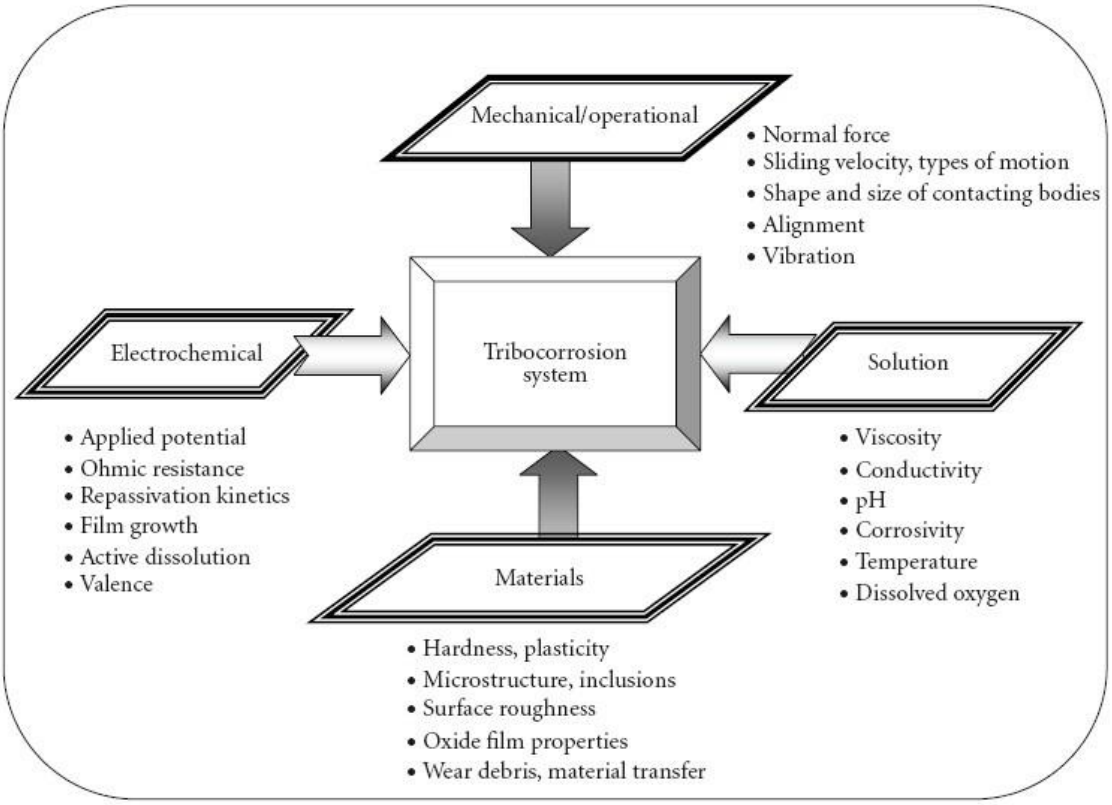

Figure 2-6 Factors influencing the tribocorrosion [84].

Materials' properties like hardness, ductility and yield strength, determine the wear resistance and the existence of a surface oxide film provides good corrosion resistance for passivated metals. The microstructure of materials like phase distribution, grain size and orientation, dislocation density and so forth are critical for the mechanical behavior. The topography and chemical composition of the contacting surfaces like the roughness, the formation of plastically deformed surface layers, the growth and mechanical properties of oxide films, *etc*. also have effects on the tribocorrosion behavior of tested materials.

Mechanical/Operational loading forces, motion velocity and the type of contact (sliding or fretting) determine the rate of trbocorrosion for a given system. The shape and size of contact bodies determine the area of contact zone and the alignment of the rubbing surfaces. While the solution viscosity, conductivity, pH value, temperature and so forth play important roles in tribocorrosion. In the case of aqueous electrolyte, the concentration of dissolved oxygen, aggressive chloride ions and the pH influence the reactivity of metals, which further have effect on tribocorrosion behavior.

Moreover, electrochemical parameters like ohmic resistance, applied potential, passive film growth, active dissolution, and so forth, also have influences on the tribocorrosion. The repassivation kinetics of metal surface activated by the destruction during sliding or fretting attracts more interests from eletrochemists.

The synergistic effect of mechanical friction and electrochemical corrosion (for passivated metals and alloys) is schematically represented in the Figure 2-7. The fact that mechanical removal of a surface passive layer makes the bare material directly exposed to the aggressive electrolyte accelerates corrosion of that bare material; consequently, the corrosion of the bare material can be weakened by the re-growth of a passive film [90], known as repassivation phenomenon. Conversely, the solid corrosion products (like oxide debris) resulting from the mechanical removal of the passive layer lead to a three-body effect in tribocontact [91], and further induce abrasive wear on the bare material. The methodology for tribocorrosion test [92] has evolved recently, the scientists and engineers are trying to build up a standard system to collect and monitor the involving mechanical and corrosion responses. (A protocol for determination of synergism in tribocorrosion of titanium used in this thesis will be illustrated in Chapter 3.)

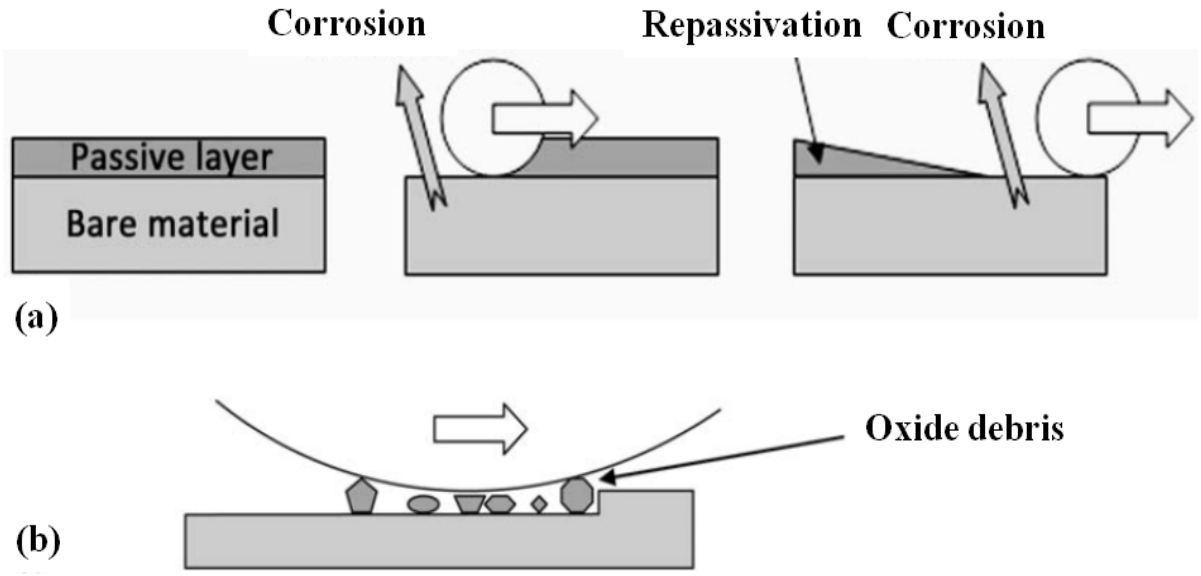

Figure 2-7 Synergistic effect of corrosion on wear and vice versa: (a) Corrosion accelerated by friction; (b) Abrasion accelerated by corrosion products [92].

2.3 Titanium and its alloys as biomedical implants

Titanium is a lustrous transition metal with an incomplete shell in its electromic structure, which enables it to form solid solutions with substitutional elements having a size factor within ±20%. It was discovered in 1798 but until 1910, pure titanium was firstly produced [93]. To get a deep insight into its application as biomedical implants, properties of titanium, titanium oxidation,

corrosion-wear behavior of titanium and its alloys, and current surface modification methods to improve their corrosion-wear resistance are reviewed.

2.3.1 Titanium properties

Titanium and its alloys can be classified into three groups [94]: α type (HCP: hexagonal closed-packed crystalline structure) and near α type, (α + β) type, and β type (BCC: body centered-cubic crystalline structure) and near β type. The transforming temperature of pure titanium from the HCP (α-phase) to the BCC (β-phase) is 882 ℃ as β-transus temperature. In this regard, alloying elements for titanium can be divided into two groups: α-stabilizers, such as Al, Sn, Ga, Zr, O, N and C; and β-stabilizers, such as V, Mo, Nb, Ta, and Cr. When α-stabilizing elements dissolve into the titanium matrix, they increase the phase transformation temperature, while β-stabilizing elements decrease it. It is known that α alloys exhibit superior corrosion resistance, and β alloys exhibit higher strength, good formability and high hardenability. Moreover, β alloys also owns unique possibility of both low elastic modulus and superior corrosion resistance [95, 96]. Table 2-4 shows three groups of titanium materials and the influences of some major alloying elements on titanium.

Commercially pure titanium (cp Ti) and Ti-6Al-4V ELI (representing Extra Low Interstitial) are most commonly used titanium materials for the replacement of hard tissues in biomedical implant applications [3, 77, 97-104]. It is known that Ti-6Al-4V was originally developed for aerospace applications, its high corrosion resistance and excellent biocompatibility led its entry into biomedical industry. However, the long-term performance of Ti-6Al-4V has raised some concerns due to the release of aluminum and vanadium, which are found to be associated with long-term health problems, such as Alzheimer disease, neuropathy and ostemomalacia [105, 106].

Table 2-4 Effects of major alloying elements on titanium [94].

Type/material property	α and near α	$\alpha+\beta$	β and near β
α-stabilizing elements	Al, Sn, Ga, Zr, O, N, C		
β-stabilizing elements			V, Mo, Nb, Ta, Cr
Typical materials	cp Ti	Ti-5Al-2.5Fe	Ti-3Al-8V-6Cr-4Mo-4Zr
	Ti-5Al-2.5Sn	Ti-5Al-2Mo-2Fe	Ti-4.5Al-3V-2Mo-2Fe
	Ti-5Al-6Sn-4Zr-1Mo	Ti-5Al-3Mo-4Zr	Ti-5Al-2Sn-2Zr-4Mo-4Cr
	Ti-6Al-2Sn-4Zr-2Mo	Ti-5Al-2.5Fe	Ti-10V-2Fe-3Al
	Ti-8Al-1Mo-1V	Ti-6Al-7Nb	Ti-13V-11Cr-3Al
		Ti-6Al-4V	Ti-15V-3Cr-3Al-3Sn
		Ti-6Al-6V-2Sn	Ti-35V-15Cr
		Ti-6Al-2Sn-4Zr-6Mo	Ti-8Mo-8V-2Fe-3Sn
			Ti-11.5Mo-6Zr-4.5Sn
			Ti-30Mo, Ti-40Mo
			Ti-13Nb-13Zr
			Ti-25Pd-5Cr
			Ti-20Cr-0.2Sn
			Ti-30Ta
β-transus temperature	Higher ←		→ Lower
Specific density	Lower →		→ Higher
RT[1] strength	→		
RT toughness	→		
Modulus of elasticity	←		
Machinability	←		
Age hardenability	→		
Heat resistance	←		
Weldability	←		
HT[2] strength	←		
Heat-treatability	→		
Plastic formability	→		
Strain-rate sensitivity	→		
Superplastic formability	→		
Creep resistance	←		

1: room temperature; 2: high temperature.

2.3.2 Titanium oxidation

Titanium is a highly reactive metal and a compact oxide layer is easily produced due to its strong chemical affinity to oxygen. It was investigated that an oxide layer with a thickness greater than 10 Å can form rapidly in less than a microsecond in atmosphere [107]. Normally, titanium quickly forms an oxide of 2-7 nm thickness in air or water at room temperature. This oxide layer, which is primarily TiO_2, adheres strongly to the titanium substrate surface. The adhesion and adhesive strength are controlled by the oxidation temperature, the thickness of the oxide layer and the presence of nitrogen in oxidation process [108, 109]. Referring to the primarily formed titanium oxide – TiO_2 on titanium materials, three crystalline structures should be discussed: anatase, brookite and rutile [110]. Anatase-phase TiO_2 is a tetragonal crystalline system with a_0 = 3.78 Å and c_0 = 9.5 Å; brookite-phase TiO_2 has an orthorhombic crystalline structure with a_0 = 9.17 Å, b_0 = 5.43 Å and c_0 = 5.13 Å. The third rutile-phase TiO_2 is also a tetragonal structure and known as the most stable phase.

When titanium materials are used as surgical implants in an aggressive environment, their excellent corrosion resistance is induced due to the formation of a dense, protective and strongly adhered film, which is called a passive film. This passivity appears on certain so-called passivating metals, like Fe, Cr, Zr, and Ti in the category of “transition metals”, characterized by an unfilled group of electrons in an inner electron shell. Therefore, the chemical properties and the interface chemistry are determined by the oxide layer rather than the metal itself. The potential-pH (Pourbaix) diagram for titanium (see Figure 2-8) shows the range where the passive oxide films form, the range where titanium corrodes.

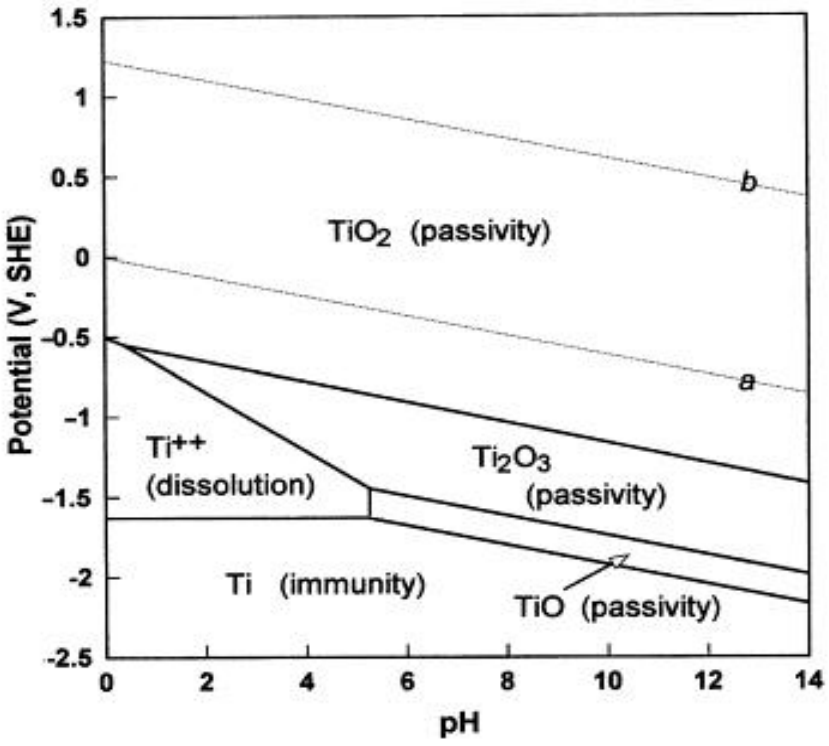

Figure 2-8 Potential-pH (Pourbaix) diagram for the system titanium/water at 37 ℃ [111].

According to the passivity theory, the titanium material system has both the active and passive surfaces simultaneously in contact with electrolytes [112], and undergoes a continuous process of partial dissolution and reprecipitation in the aqueous solution (see Figure 2-9). It was also found that calcium, phosphorous and sulfur are incorporated in the oxide layer on titanium implanted in bones [113]. Calcium phosphates regarded as the main composition of natural bone are precipitated on titanium and its alloys in simulated body fluids. The first stage of calcium phosphate formation is the adsorption of phosphate ions on a hydrated titanium oxide with the release of protons are schematically illustrated as follows [114]:

$$\mathbf{Ti(OH)^{3+}(ox) + H_2PO_4^{-}(aq) \leftrightarrow Ti^{4+}(ox)HPO_4^{2-}(ads) + H_2O} \quad (2\text{-}3)$$

$$\mathbf{Ti^{4+}(ox)HPO_4^{2-}(ads) + OH^{-} \leftrightarrow Ti^{4+}(ox)PO_4^{3-}(ads) + H_2O} \quad (2\text{-}4a) \quad \text{or}$$

$$\mathbf{Ti(OH)^{3+}(ox) + HPO_4^{2-}(aq) \leftrightarrow Ti^{4+}(ox)PO_4^{3-}(ads) + H_2O} \quad (2\text{-}4b)$$

where (ads), (ox) and (aq) represent adsorbed ions, ions in oxide and aqueous solution, respectively. Then calcium ions accumulated on the adsorbed phosphates to form calcium phosphate on titanium implants. The formation of calcium phosphate can promote the osseointegration of biomedical implants and lengthen the life span under *in vivo* condition.

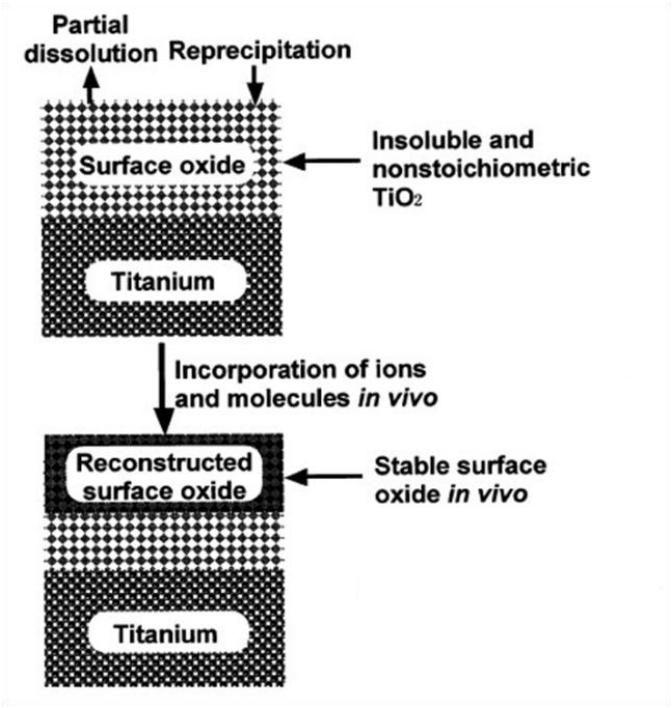

Figure 2-9 Schematics of surface oxide film of titanium and film reconstruction *in vivo* [115].

2.3.3 Corrosion and tribocorrosion of titanium implants

As mentioned above, the excellent corrosion resistance and adequate biocompatibility of titanium materials in biomedical application as implants is due to the simultaneous formation of a thin passive oxide film, mainly as TiO_2. However, when titanium materials are implanted in the body environment, corrosion happens in contact with the aggressive body fluids containing chloride ions and proteins, even other foreign species [116-120] such as fluoride ion (F^-), hydrogen peroxide (H_2O_2) and lactic acid.

The F^- content of commercially fluoridated toothpastes or mouthrinses is known to be corrosive for Ti. It was found that the degradation of titanium in fluoride containing artificial saliva is corresponding to the occurrence of a localized corrosion process, namely pitting corrosion. The fluoride ions are aggressive ions which could cause the breakdown of the protective passivation layer[118], which can be described as resulting from the formation of Ti oxides layer as $Ti(OH)_2F^+$, and the salts as $TiOF_2$, TiH_2, $Na_3Ti_3F_{14}$, TiF_4, $[TiF_6]^{2-}$ in the presence of HF according to the following reactions [116]:

$$\mathbf{TiO_2 + 2HF \rightarrow TiOF_2 + H_2O} \quad (2\text{-}5a) \quad \text{or}$$

$$\mathbf{TiO_2 + 4HF \rightarrow TiF_4 + 2H_2O} \quad (2\text{-}5b) \quad \text{or}$$

$$\mathbf{Ti_2O_3 + 6HF \rightarrow 2TiF_3 + 3H_2O} \quad (2\text{-}5c)$$

Huang *et al.* [121] investigated the effect of fluoride concentration in the additive form of NaF on the corrosion behavior of Ti6Al4V alloy in acid artificial saliva (pH = 5) at 37 ℃. It was found that both the corrosion rate (I_{corr}) and the passive current density (I_{pass}) increased on increasing the NaF concentration from 0% to over 0.15%. When the concentration was increased up to 0.5%, the I_{corr} was around 70 times larger than that in the absence of NaF in the test media, and an anodic active polarization behavior was observed rather than an active-to-passive transition behavior.

In orthopedic implant application, especially the total joint replacements, cyclic loading is inescapable as a consequence of the patients' movements. In this case, fretting corrosion/fretting wear and the induced ions release or corrosion/wear debris *in vivo* are the main reasons of implant failure. It is well known that the accumulation of these wear debris can produce an adverse cellular response leading to inflammation, release of damaging enzymes, bone cell lysis, infection and pain, then implant loosening eventually ensuing [94].

As the original study, Miller *et al.* [122] studied the friction and wear properties of titanium, the results showed the poor wear characteristics for unalloyed Ti. Since the development of electrochemical measurements, *in situ* characterization methods are imposed to investigate the corrosion and tribocorrosion behavior of titanium materials in recent years [70, 123, 124]. Research results indicated that the pH and corrosion inhibitors influenced the tribocorrosion behavior of pure Ti under fretting [125]. The lowering in open circuit potential (OCP) resulted during tribocorrosion test was considered as a mixed potential of unworn and worn surfaces. The higher anodic current measured with sliding than the anodic current measured without sliding was due to more dissolution of titanium in anodic potential range under sliding condition [124]. Comparing with pure titanium, alloying elements like Al and V in the titanium biomaterial reduced the active and passive dissolution, but no effect of the mechanical properties was found on the tribocorrosion response and wear volumes. The presence of bovine serum albumin (BSA) had negligible influence on the corrosion behavior of titanium alloys, and had only a small effect on the mechanical detachment of particles in the continuous sliding tests [123]. The containing of F^- in artificial saliva decreased the OCP under sliding conditions, increased the wear weight loss of cp titanium with the increase of F^- concentration [116].

2.3.4 Surface modifications

From above we know that titanium materials are with poor wear resistant, and their corrosion resistance loose in some cases. Further considered the bio-inert property of titanium materials, which causes a long osseointegration process as implant applications, surface modifications have been widely applied to improve the mechanical, chemical, and biological properties such as wear resistance, corrosion resistance, biocompatibility of titanium and its alloys, aiming to reduce the costs and improve the longevity after implantation inside the bones. Several main methods are reviewed in this section, concerning to the corrosion resistance, wear resistance and biocompatibility

of titanium materials with surface modifications.

2.3.4.1 Ion implantation

Ion implantation is a material engineering process by which ions of a material are accelerated in an electrical field and impacted into a solid. The ions alter the elemental composition of the target, since the ions acting as foreign element stop and stay in the target. The physical, chemical or electrical properties of the target solid are then changed after ion implantation.

Thin-film layer of titanium nitride (TiN) are of great interest in the range of biomedical application, due to its desired mechanical (extreme hardness), thermal (high melting point), chemical (high corrosion resistance) properties [126]. Fernandes et al. investigated the tribocorrosion behavior of plasma nitrided Ti-6Al-4V alloy in a 0.9 wt.% NaCl electrolyte with *in situ* electrochemical measurements like OCP and electrochemical impedance spectroscopy (EIS) [127]. The results clearly showed that nitridation leads to Ti_2N layer on Ti-6Al-4V surface, which resulted in hardness enhancement. The samples after nitridation at 700 ºC (thickness of 0.7 μm) owned higher wear and corrosion resistance than at 600 ºC (thickness of 0.25 μm), indicating that the layer thickness plays a critical role in tribocorrosion. Hanawa *et al.* [128] studied the *in vivo* early bone formation around calcium ion (Ca^{2+})-implanted titanium and found the treated titanium was superior to untreated titanium for bone conduction. In their study, calcium ions were implanted into one side of titanium plates at 10^{17} ions/cm^2. After ion implantation, the Ca^{2+}-treated titanium was surgically implanted into rat tibia for 2, 8, and 18 days. The results showed that even at implantation time of 2 days, a larger amount of new bone was formed on the Ca^{2+}-treated side and part of the bone made contact with this Ca^{2+}-treated surface. But for the untreated side, bone formation was delayed and the bone did not make contact with the surface at 2 days.

2.3.4.2 Chemical treatment

Due to the simplicity, cost effectiveness, bone bonding ability and being applicable to implants with complicated shapes, surface modification of titanium materials by chemical treatment attracted many attentions in recent years. In chemical treatment, the most commonly used reagents for titanium biomaterials are sodium hydroxide (NaOH) and hydrogen peroxide (H_2O_2) solutions [129].

Tamilselvi *et al.* found that chemically treated Ti with NaOH produced sodium-titanate gel layer, which induced the formation of a dense and uniform bone like apatite layer after immersion in simulated body fluid (SBF) and then exhibited excellent corrosion resistance [130]. Pan and co-workers investigated the influence of an H_2O_2 pretreatment on the cell culture process [131]. They found that during the cell culture, the H_2O_2-treated titanium surface favors the ion incorporation and precipitation of the hydroxylcarbonated apatite (HCA)-like compound, which probably is inlaid into the oxide film. Similar phenomenon was observed by Park [132], who found

that a porous coating comprising of mainly hydroxyapatite formed on the H_2O_2-treated titanium substrate, while a uniformed coating comprising of amorphous calcium phosphate (APC) formed on the untreated titanium substrate by electrodeposition in a modified SBF solution. The increased surface area of titanium substrate after H_2O_2-treatment and the OH^- ions released from this modified surface during electrodeposition were considered as the attributions to this great difference. Furthermore, chemical treatment with alkali-hydrogen peroxide and subsequent heat treatment at 600 ℃ for 1 h to improve both the biocompatibility and the corrosion resistance was investigated by Sasikumar [133]. A nanoporous titanate gel layer with anatase phase was obtained on cp Ti and Ti-15Mo alloy after this two-step surface modification. After 7 days of immersion in SBF solution, an apatite layer formed over the gel layer and provided the highest corrosion resistance comparing with the untreated, alkali-hydrogen peroxide treated and alkali-hydrogen peroxide plus heat treated specimens.

2.3.4.3 Thermal oxidation

Thermal oxidation, as a surface modification method, has been successfully developed in recent years. It is a thermochemical process, which is usually carried out in a controlled atmosphere containing oxygen as well as nitrogen. To solve the poor wear resistance and the loss of corrosion resistance by the *in vivo* removal of the simultaneous formed thin passive oxide film of titanium biomedical implants, thermal oxidation is commonly used to form a thick oxide layer with higher hardness, lower electrical and ions conductivity, *etc*.

In 1980s, the growth of titanium oxide overlayers by thermal oxidation of titanium was studied by Padma and co-workers [134]. A layered structure consisting of TiO_2, Ti_2O_3, TiO, titanium, *etc*. from the surface to the metal-oxide interface was observed when the oxide is prepared by a thermal oxidation process. A model for growth of titanium oxide was proposed in their study: when a fresh titanium surface is exposed to an oxygen atmosphere, oxygen is absorbed in the titanium and lower oxides of titanium are expected to form in the first instance; with time progressing, oxygen passes through the initial oxide layer to reach the titanium oxide-titanium interface and forms fresh oxide; as it passes through the lower oxide, some of the oxygen is expected to be absorbed by the oxide which is then converted into a higher oxide form. The oxygen transport and the formation of oxide depend on the temperature and time for thermal oxidation process. With increase in either temperature or time of oxidation, more and more layers from the surface become rich in TiO_2 of the rutile type. The oxide thickness increases with the increase of oxidation temperature [135].

Although it is well known that thermal oxidation can improve the corrosion and wear resistance of titanium materials, there is no one standard modification process until now. Based on the different experimental conditions, the structural features and corrosion resistant properties for thermal oxidized titanium and its alloys differ from each other. Table 2-5 summarizes some of the current literatures results on corrosion and tribological behavior of titanium and its alloys after thermal

oxidation. Recently, TiO_2 nanowires, obtained by thermal oxidation under a limited supply of oxygen, was investigated as a means of improving cell adhesion and proliferation of human osteosarcoma (HOS) cells on Ti-6Al-4V substrates [136, 137]. The nanowire coated samples showed increased cell adhesion and proliferation compared to the non-nanostructured TiO_2 and untreated Ti-6Al-4V samples. This research opened a new sight for thermal oxidation in the fields of material synthesis and biomedical applications.

Table 2-5 Current studies on corrosion and tribological behavior of thermal oxidized titanium.

Ref.	Material	Temperature	Time	Test medium	Remarks
[138]	cp Ti	850 °C	8 h	0.5 M NaCl	Decreased surface roughness improves the corrosion property
[139]	cp Ti	500/650/800 °C	24 h	Ringer's	Corrosion protective ability: cp Ti (800 °C) > cp Ti (650 °C) > cp Ti (500 °C) > untreated cp Ti
[140]	Ti-6Al-4V	500-800 °C	1 h	0.9% NaCl	600 °C is the appropriate temperature for the improvement of corrosion resistance.
[141]	cp Ti	650 °C	8/16/24/48 h	Ringer's	Corrosion protective ability: TO 48 h > TO 16 h > TO 8 h ≈ TO 24 h > untreated
[142]	cp Ti	650 °C	14 h	0.9% NaCl	Faster cooling rate has no deleterious effect on corrosion resistance of TO cp Ti at 650 °C for 14 h but has deleterious effect on corrosion resistance of TO cp Ti at 850 °C
		850 °C	6 h		
[143]	Ti-6Al-4V	600/700/800 °C	4 h	—	Thermal oxidation temperature could effectively influence the microstructural and tribological behavior of Ti-6Al-4V alloy and the optimal temperature was 700 °C.
[144]	cp Ti	600-900 °C	0.25-5 h	—	A thick oxide layer with rutile TiO_2 and oxygen diffused Ti structure exhibited excellent adhesion with the substrate, showing low friction and superior wear resistance during sliding.
[145]	Ti-6Al-4V	900 °C	2 h	—	Thermal oxidation improved the wear resistance of Ti-6Al-4V alloy by reducing the wear volumes in respect of both the untreated and nitrided samples.
[146]	cp Ti	625 °C	36 h	0.89% NaCl	Corrosion-wear resistance of cp Ti and Ti-6Al-4V alloys can be improved by thermal oxidation, but the degradation of exterior TiO_2 (rutile) on both materials is different.
	Ti-6Al-4V				
[147]	cp Ti	650 °C	48 h	Ringer's	Although tribocorrosion performance of TO cp Ti is better than untreated cp Ti, but the greater susceptibility for galvanic corrosion are the major limitations of using it as implant materials.

2.3.4.4 Bioactive coating

The accurate metal analysis of bone and tooth specimens [148] showed that human bone consists of 24.5 wt.% Ca, 11.5 wt.% P, 5.8 wt.% CO_3^-, 0.7 wt.% Na, 0.55 wt.% Mg, 0.03 wt.% K, and a number of trace elements at the ppm level, like Zn, Fe, Sr, Pb, Ba and Cu. Among them, Ca and P as the two main inorganic constituents of bones and teeth, the most abundant mineral in human hard tissues is a basic calcium phosphate idealized as hydroxyapatite (HA, $Ca_{10}(PO_4)_6(OH)_2$). Other calcium phosphates (CaP), such as brushite (DCPD: dicalcium phosphate dihydrate, $CaHPO_4 \cdot 2H_2O$), octacalcium phosphate, $Ca_8H_2(PO_4)_6 \cdot 5H_2O$, whitlockite (β-TCP: β-tricalcium phosphate, $Ca_3(PO_4)_2$), CPPD: calcium pyrophosphate dehydrate, $Ca_2P_2O_7$, and ACP: amorphous calcium phosphates have been identified with or without association with apatite [149].

In the field of biomedical implants, how to enhance the surface biocompatible and osseoconductive properties is then closely related to the surface modification of implants with CaP bioactive coatings. It is well demonstrated that CaP bioactive coatings enhance the cellular adhesion, proliferation and differentiation to promote bone regeneration. The osseoconductive processes occurring at the interface of biomaterials with CaP coating and natural bone after implantation into a living system are schematically represented in Figure 2-10. Partial dissolution of the CaP coating happens when the local pH value decreases. Subsequently, the released Ca^{2+} and PO_4^{3-} ions reprecipitate and incorporate into apatite crystals with the collagen matrix (organic component in bone). The increased concentrations of Ca^{2+} and PO_4^{3-} simulate chemotaxis and promote the osseointegration of biomedical implants and natural bones. Several commonly used CaP phases with Ca/P ratio are summarized in Table 2-6, comparing with that of natural bone.

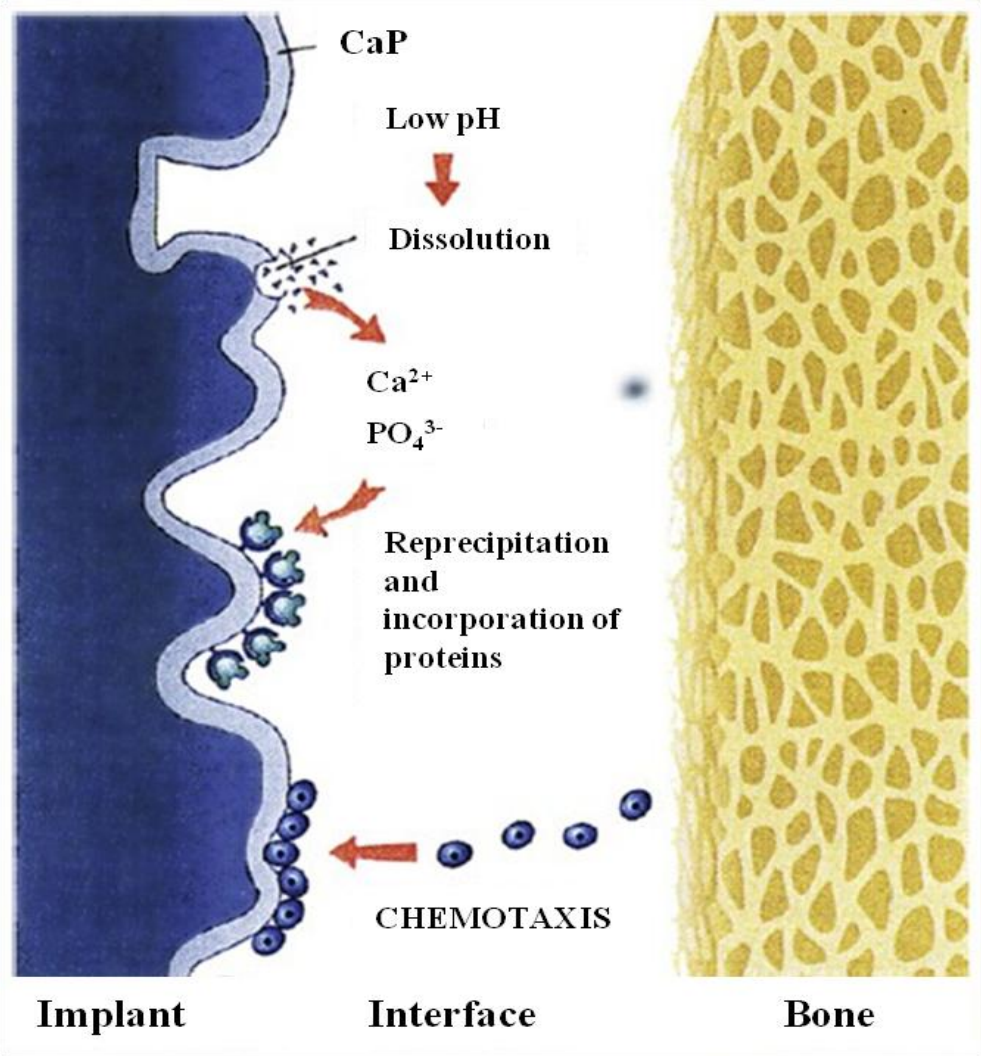

Figure 2-10 Schematic representation of osteoconduction induced CaP coating [150].

Table 2-6 Summary of the CaP phases used as bioactive coatings in orthopedic devices.

Name	Formula	Ca/P ratio
Dicalcium phosphate dihydrate, DCPD (brushite)	$CaHPO_4 \cdot 2H_2O$	1.0
Octacalcium phosphate, OCP	$Ca_8H_2(PO_4)_6 \cdot 5H_2O$	1.33
β-Tricalcium phosphate, β-TCP (whitlockite)	$Ca_3(PO_4)_2$	1.5
Fluorapatite, FA	$Ca_{10}(PO_4)_6F_2$	1.67
Hydroxyapatite, HA	$Ca_{10}(PO_4)_6(OH)_2$	1.67

DCPD, exhibiting greater solubility than most other calcium phosphate phases, has been used in recent investigations as an inexpensive and relatively easy CaP to deposit on to a given metallic substrate. It is stable in the range of pH lower than 5, but with the increase of OH^- ions, DCPD starts to act as a precursor to the more stable phase, like TCP and HA [151, 152]. As an electrochemical deposition process for instance, the formations of DCPD, TCP and HA can be illustrated as followings [153, 154]:

$$H_2O + 2e^- \rightarrow H_2 + 2OH^- \quad (2\text{-}6a) \quad \text{or}$$

$$O_2 + 2H_2O + 4e^- \rightarrow 4OH^- \quad (2\text{-}6b)$$

$$2H_2PO_4^- + 2e^- \rightarrow 2HPO_4^{2-} + H_2 \quad (2\text{-}7a) \quad \text{or}$$

$$H_2PO_4^- + OH^- \rightarrow HPO_4^{2-} + H_2O \quad (2\text{-}7b)$$

$$Ca^{2+} + HPO_4^{2-} + 2H_2O \rightarrow CaHPO_4 \cdot 2H_2O \quad (2\text{-}8)$$

$$2HPO_4^{2-} + 2e^- \rightarrow 2PO_4^{3-} + H_2 \quad (2\text{-}9a) \quad \text{or}$$

$$HPO_4^{2-} + OH^- \rightarrow PO_4^{3-} + H_2O \quad (2\text{-}9b)$$

$$3Ca^{2+} + 2PO_4^{3-} \rightarrow Ca_3(PO_4)_2 \quad (2\text{-}10)$$

$$10Ca^{2+} + 6\,PO_4^{3-} + 2OH^- \rightarrow Ca_{10}(PO_4)_6(OH)_2 \quad (2\text{-}11)$$

Numerous experimental deposition processes such as dip coating [155-157], sol-gel [158], electrophoretic deposition [159], anodization [160, 161], micro-arc oxidation [162-164], plasma spraying [165-167] and electrochemical deposition [168, 169]. In order to get a desired CaP bioactive coating with other properties like good adhesion to the substrate, adequate mechanical stress loading and excellent corrosion and wear resistance, composite coatings like CaP bioceramic/titania [150, 168-172], carbon nanotube reinforced HA, Al_2O_3-TiO_2 nanoparticles/HA bilayer [167, 173] are obtained by the combination of different processes.

The corrosion behavior of some CaP bioactive coating modified titanium biomaterials is summarized in Table 2-7.

Table 2-7 Corrosion resistance of bioactive coating modified titanium**.**

Ref.	Material	Coating composition	Treatment method	Test medium	Remarks
[155]	Ti-6Al-4V	Poly(ε-caprolactone)/ HA	Dip coating	SBF[1]	Addition of polymer to HA improved the adhesion of HA and enhanced corrosion resistance of Ti-6Al-4V alloy comparing with only HA coating.
[167]	cp Ti	Al_2O_3-TiO_2 (AT)/HA	Plasma spraying	SBF	Comparing with a mono layer AT or HA coated surface, bi-layered nanoceramic coating on cp Ti showed the highest corrosion resistance and even acted as a barrier for the metal ion release.
[174]	cp Ti	AgHA/TiO_2	Plasma electrolytic processing	SBF	AgHA/TiO_2 composite coated cp Ti exhibited an improved corrosion resistance and enhanced further formation of apatite in SBF.
[175]	Ti-6Al-4V	HA/SiO_2 (10 wt.%)	Plasma spraying	Ringer's	Results of polarization curve showed that the corrosion current density for surface modified samples were lower than untreated one after 24 h immersion in Ringer's solution.
[161]	Ti-6Al-4V	HA/TiO_2	Electrochemical deposition/ Anodization	Saliva	Impedance results showed that anodized Ti-6Al-4V alloy+HA surface exhibited the higher polarization resistance; moreover, a lower passive current density was found for modified surface.
[173]	cp Ti	CNTs[2]/HA	Electrodeposition (-1.4 V vs SCE[3])	SBF	Lower corrosion current density for CNTs reinforced HA composite coating showed an efficient corrosion protection of modified Ti and 1 wt.% CNTs-HA composite coating was found to be uniform and adherent to Ti.
[176]	cp Ti	HA/TiO_2	Electrophoretic deposition/ Anodization/ Sintering	SBF	Both HA coating and NT[4] TiO_2 structure could provide corrosion protection for Ti; a further sintering process in vacuum had effect on the corrosion protection.

[1]: simulated body fluid; [2]: carbon nanotubes; [3]: saturated calomel electrode; [4]: nanotubular.

Until now, a huge number of studies have concentrated on the corrosion and biocompatibility of CaP bioactive coating modified titanium materials as biomedical implants, but few work [170] was published on their tribocorrosion behavior, which is commonly investigated under mechanical loading conditions in an aggressive environment. It is important to study the tribocorrosion behavior of CaP bioactive film coated titanium as biomedical implants.

Chapter 3: Materials and Experimental Methods

In this chapter, chemical composition/mechanical properties of Ti, thermal oxidation pretreatment, electrochemical deposition of CaP bioactive film, procedures to prepare CaP/TiO_2 bioceramic film and electrolyte used for *in situ* electrochemical characterization will be introduced. Electrochemical and tribological techniques used in the analysis of corrosion and tribocorrosion behavior will be described as well as physical characterization techniques to determine the surface properties. One protocol for the quantitative calculation of material loss of metals and their alloy in tribocorrosion test will be interpreted in the case of untreated cp Ti. For the surface modified Ti by thermal oxidation, electrochemical deposition of CaP bioactive film before and after sintering at high temperature in this work, a simplified assessment criterion in tribocorrosion test will be also proposed.

3.1 Materials and electrolyte

Commercially pure titanium (cp Ti grade 2) (Goodfellow Cambridge Limited, UK) samples were cut into square shape of 20 mm × 20 mm × 2 mm. Chemical composition of this material is shown in Table 3-1. Its mechanical properties are summarized in Table 3-2. All samples were polished with SiC emery papers until to 1200 mesh followed by an ultrasonic cleaning in acetone and then in ethanol for each 5 min before experiment, the final average roughness is about 0.39 μm.

Table 3-1 Chemical composition of cp Ti grade 2.

Element	Wt. %
Nitrogen	≤ 0.03
Carbon	≤ 0.1
Hydrogen	≤ 0.015
Oxygen	≤ 0.25
Iron	≤ 0.3
Titanium	Balance

Table 3-2 Mechanical properties of cp Ti grade 2.

Hardness, Vickers	145
Tensile Strength, Ultimate	344 MPa
Tensile Strength, Yield (0.2% offset)	275 MPa
Elongation at Break	20%
Reduction of Area	35%
Modulus of Elasticity	105 GPa
Compressive Modulus	110 Gpa
Poisson's Ratio	0.37

Thermal oxidation of cp Ti specimen is carried out in a furnace performing at 650 ℃ for 48 h in air atmosphere. After thermal oxidation treatment, samples are gradually cooled to room temperature for about 12 h in the furnace by itself.

Modification of cp Ti with CaP bioactive film is achieved via an electrochemical deposition method in a mixed solution containing 0.042 mol/L $Ca(NO_3)_2 \cdot 4H_2O$ and 0.025 mol/L $NH_4H_2PO_4$ (pH = 4.2). Then sintering step is carried out at 650 ℃ for 6 h to get the CaP/TiO_2 bioceramic film coated Ti samples.

Electrochemical measurements were performed in a phosphate buffered saline (PBS) solution at room temperature (22 ±1 ℃). The composition of the PBS solution with a pH value of 7.4 is displayed in Table 3-3. All chemicals were of analytical grade and used as purchase without any further treatment. De-ionized water was employed for the preparation of the PBS solution.

Table 3-3 Chemical composition of the PBS solution.

Compound	Concentration (g/L)
NaCl	8.19
KCl	0.2235
Na_2HPO_4	1.42
KH_2PO_4	0.272

3.2 Electrochemical techniques

3.2.1 Open circuit potential technique

Open circuit potential (OCP, also referred to as the equilibrium potential, the rest potential, or the corrosion potential) is the potential of the working electrode relative to the reference electrode when no potential or current is being applied to the cell. OCP is a mixed potential determined by oxidation and reduction reactions at the surface of a metal electrode.

The open circuit potential technique or corrosion potential monitoring technique is the simplest and most frequently used technique in corrosion and tribocorrosion measurements. Using a potentiostat or a multimeter and then a reference electrode (RE), the evolution of OCP of a working electrode (WE) can be monitored during immersion in the electrolyte or the corrosive environment. The potential is a basic indicator of the thermodynamic corrosion status. It can be used in conjunction with Pourbaix diagrams. OCP can provide a useful indication of active or passive behavior of investigated metallic material in certain system. For example, the oxide film formation on the surface

of a passive metal or alloy may become more protective with time, resulting of a noble shift in potential. Such a potential shift is thus beneficial to the reduction of corrosion rate if it does not exceed the pitting potential. On the contrary, a potential shift in negative direction may indicate a loss of passivity, see Figure 3-1. Curve (a) is the representative of a passivation process, there is an increase in the more noble direction. Curve (b) is characteristic of an activation process of material that undergoes a uniform corrosion. Curve (c) and curve (d) characterized by a potential drop on immersion indicates the cases where a surface evolution is required to achieve a film growth, like curve (c), or a depassivation phenomenon occurs after the damage of protective film for a short immersion period, like curve (d).

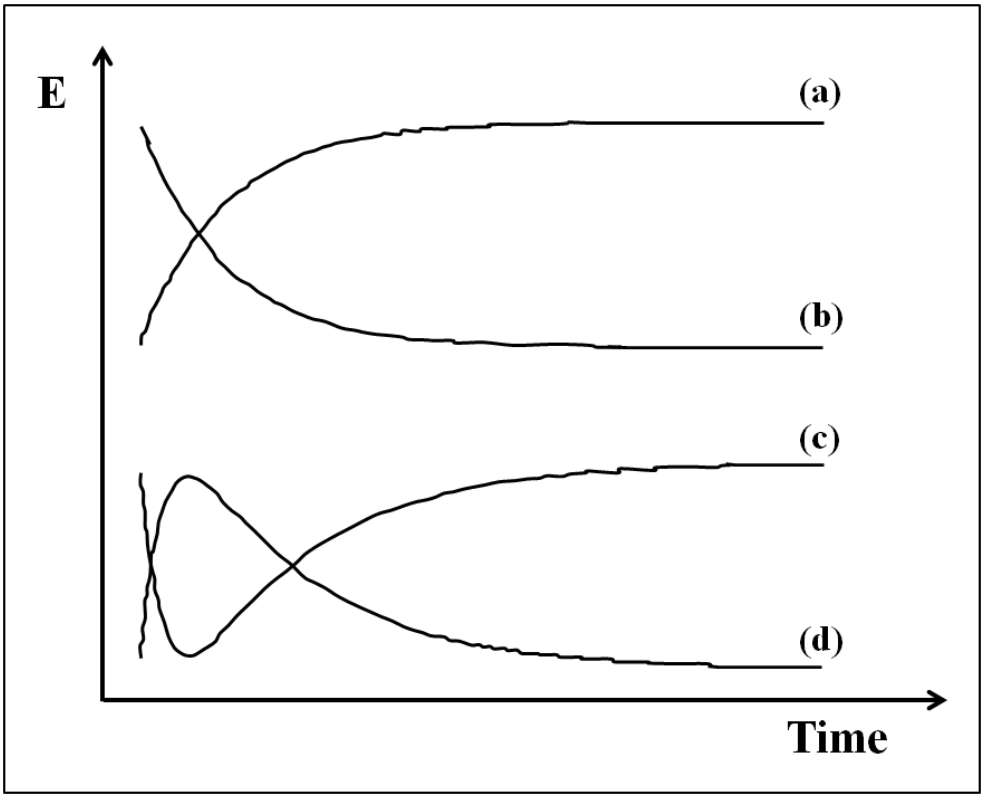

Figure 3-1 OCP evolution classically recorded for passive materials (a, c) and active materials (b, d).

Furthermore, OCP recorded during tribocorrosion tests is a mixed potential reflecting the state of material in the unworn area and the material in the wear track area. We must be aware that a galvanic coupling between worn and unworn parts of the material may take place. Consequently, the OCP value depends on the following parameters: [89]

- The respective intrinsic OCP of the materials in worn and unworn areas. These two OCP are different because that the electrochemical state of the metallic material is disturbed by a wiping of the surface films that may consist of adsorbed species, passive films, or corrosion products in the sliding contact and by a straining of the metal.
- The ratio of worn and unworn areas. In particular, if the extent of the worn area increases,

the OCP of the metallic material will shift depending on the controlling electrochemical processes, being either the anodic reaction (*e.g.*, the dissolution of the metal) or the cathodic reaction (*e.g.*, the reduction of hydrogen or dissolved oxygen).

- The relative position of worn and unworn areas. As a result of the galvanic coupling, a current is flowing between anodic and cathodic areas. The ohmic drop may induce a non-uniform distribution of potential and current density over the disk surface. The measured OCP is thus an average value depending on that distribution.

- The mechanism and kinetics of the anodic and cathodic reactions in worn and unworn areas.

Figure 3-2 shows the typical evolution of OCP before, during, and after loading. A noble shift in potential before loading applied indicates the corrosion behavior of material is becoming passive with time. When load applied, the quick drop-down of OCP displays the disturbance of film removing, and then the placid stage of OCP in cathodic range shows the mixed potential of worn and unworn areas during tribocorrosion. When load stopped, OCP shifts in the noble direction, revealing the repassivation of the worn area.

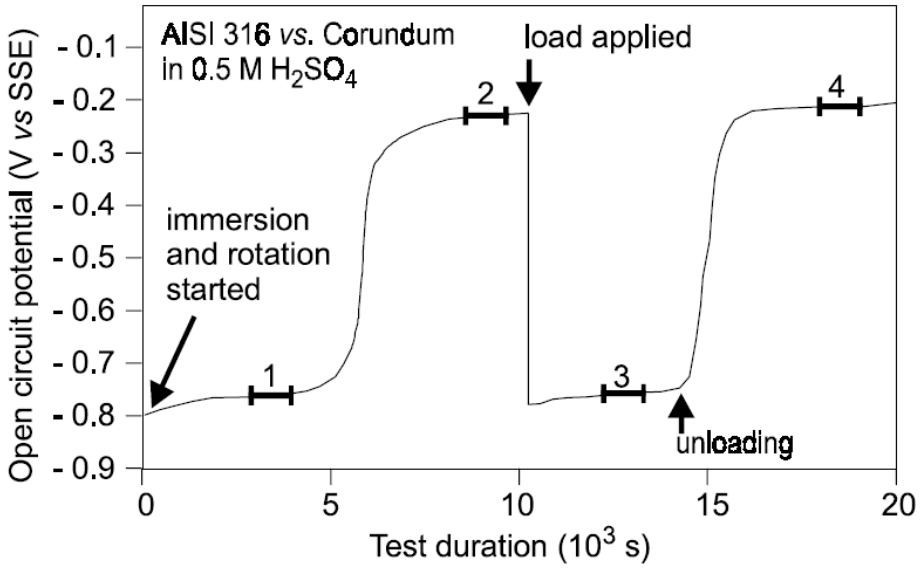

Figure 3-2 Variation of the OCP of a stainless steel disk immersed in 0.5 M H_2SO_4 before (*e.g.*, areas 1 and 2), during (*e.g.*, area 3), and after loading (*e.g.*, area 4) against a corundum ball [89].

3.2.2 Electrochemical impedance spectroscopy

Electrochemical impedance spectroscopy (EIS) is the most sophisticated technique among the electrochemical methods. This technique normally used in a typical three-electrode system controlled by a potentiostat which applies AC voltage amplitude (±10 mV) imposed to the OCP of WE and measures a current response flowing through the electrode. The AC potentials and current responses

are then passed to a frequency response analyzer or a lock-in amplifier to calculate the impedance and phase shift. By varying the frequency of the AC voltage signal, a complete spectrum can be obtained. Explanations of EIS results are usually based on the equivalent circuit models [177].

As known to us, electrical resistance, *R* is the ability of a circuit element to resist the flow of electrical current. Ohm's law (Eq. 3-1) defines resistance in terms of the ratio between voltage, *E*, and current, *I*:

$$\boldsymbol{R = E / I} \qquad (3\text{-}1)$$

while this is a well known relationship, its use is limited to only one circuit element as the ideal resistor. An ideal resistor has several simplifying properties as described below:

- It follows Ohm's law at all current and voltage levels.
- Its resistance value is independent of frequency.
- AC current and voltage signals through a resistor are in phase with each other.

However, the 'real world' contains circuit elements that exhibit much more complex behavior. These elements force us to use impedance in place of the simple concept of resistance. Like resistance, impedance is a measure of the ability of a circuit to resist the flow of electrical current, but it is not limited by the simplifying properties listed above.

Usually, electrochemical impedance is measured by applying an AC potential to an electrochemical cell and then measuring the current through the cell. We apply a sinusoidal potential excitation and the response to this potential is an AC current signal which can be analyzed as a sum of sinusoidal functions (a Fourier series). In order to obtain a pseudo-linear response, electrochemical impedance is normally measured using a small excitation signal. In a linear (or pseudo-linear) system, the current response to a sinusoidal potential will be a sinusoid at the same frequency but shifted in phase (as seen in Figure 3-3).

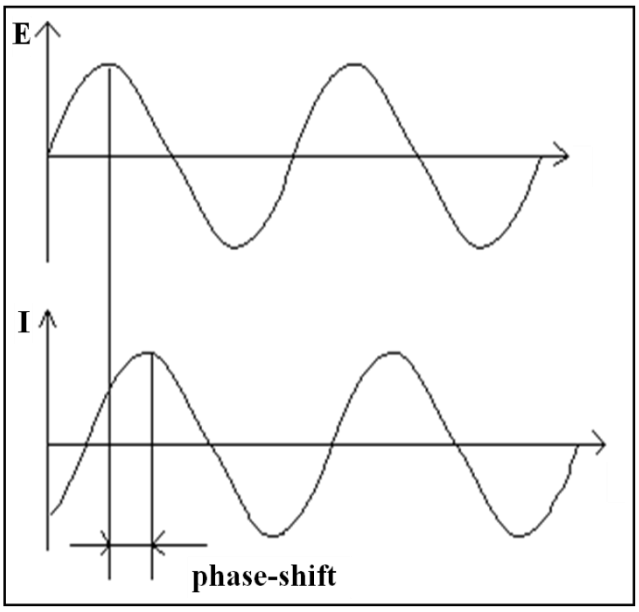

Figure 3-3 Sinusoidal current response in a linear system.

The excitation signal, expressed as a function of time, has the form as:

$$E_t = E_0 \sin(\omega t) \qquad (3\text{-}2)$$

where E_t is the potential at time t, E_0 is the amplitude of the signal, and ω is the radial frequency. The relationship between angular frequency ω (expressed in rad/s) and frequency f (expressed in hertz) is:

$$\omega = 2\,\pi\,f \qquad (3\text{-}3)$$

In a linear system, the response signal, I_t, is shifted in phase (φ) and has a different amplitude than I_0.

$$I_t = I_0 \sin(\omega t + \varphi) \qquad (3\text{-}4)$$

An expression analogous to Ohm's law allows us to calculate the impedance of the system as:

$$Z = E_t / I_t = [E_0 \sin(\omega t)] / [I_0 \sin(\omega t + \varphi)] = Z_0 [\sin(\omega t) / \sin(\omega t + \varphi)] \qquad (3\text{-}5)$$

The impedance is therefore expressed in terms of a magnitude, Z_0, and a phase shift, φ.

With Euler's relationship:

$$\exp(j\varphi) = \cos\varphi + j \sin\varphi \qquad (3\text{-}6)$$

it is possible to express the impedance as a complex function. The potential is then described as:

$$E_t = E_0 \exp(j\omega t) \qquad (3\text{-}7)$$

and the current response as:

$$I_t = I_0 \exp(j\omega t + \varphi) \qquad (3\text{-}8)$$

The impedance is then represented as a complex number:

$$Z(\omega) = E / I = Z_0 \exp(j\varphi) = Z_0 (\cos\varphi + j \sin\varphi) \qquad (3\text{-}9)$$

When the phase angle, φ, between the applied voltage and the induced current is zero, a pure resistance is present. When a phase angle of – 90 °is measured between the voltage and current at the same frequency, a pure capacitance is present. Normally, angles between these values mean that a combination of a capacitor and resistor is present. The expression of $Z(\omega)$ is composed of a real and an imaginary part. Figure 3-4 shows the Nyquist plot and Bode plot with one time constant, which is characterized as a semicircle. The equivalent circuit is also displayed (see the insert).

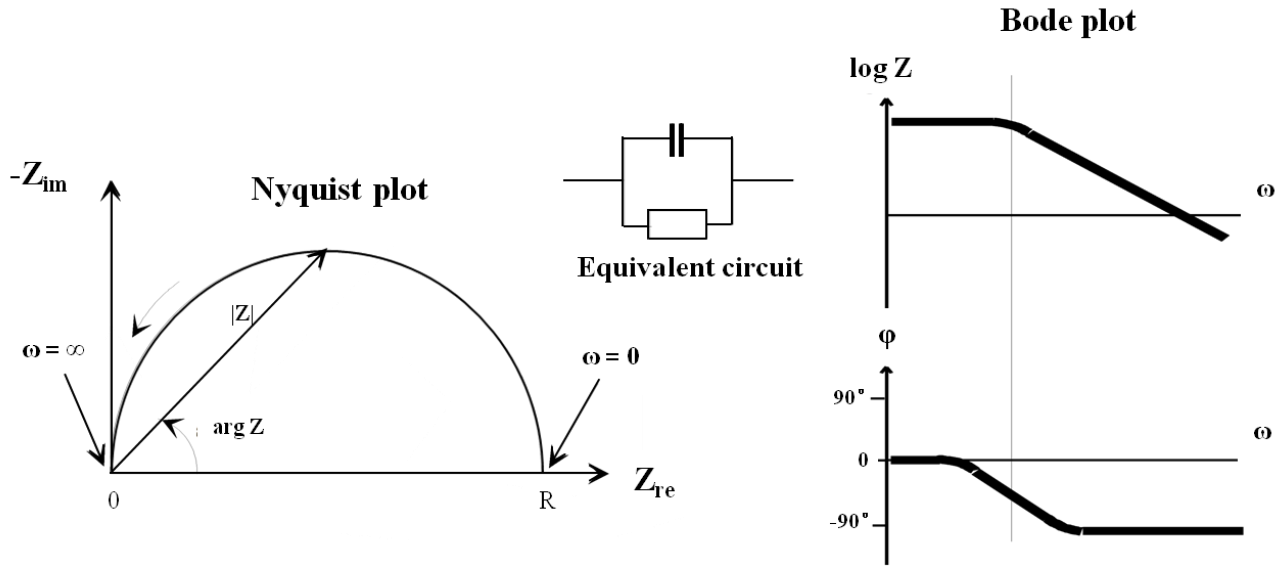

Figure 3-4 Nyquist plot and Bode plot with one time constant (equivalent circuit as the insert).

On the Nyquist plot, the impedance can be represented as a vector (arrow) of length $|Z|$. The angle between this vector and the X-axis, commonly called the "phase angle", is f (= arg Z). It should be noticed that the Y-axis is negative and each point on Nyquist plot is the impedance at one frequency. It is annotated that low frequency data are on the right side of the plot and higher frequencies are on the left. The limitation of Nyquist plot is it cannot show direactly what frequency was used to record each data point on the plot.

Another popular presentation method for impedance test is the Bode plot, which supplements and

shows the frequency information in correspondence with the absolute impedance value, $|Z|$, and the phase angle, φ.

EIS data are commonly analyzed by fitting it to an equivalent electrical circuit model. Most of the circuit elements in the model are common electrical elements such as resistors, capacitors, and inductors. To be useful, the elements in the model should have a basis in the physical electrochemistry of the system. The common circuit elements, the equation for their current versus voltage relationship, and their impedance are listed in Table 3-4.

Table 3-4 Common eletrical elements.

Component	Current vs. Voltage	Impedance
Resistor	E = IR	Z = R
Inductor	E = L di / dt	Z = jωL
Capacitor	I = C dE / dt	Z = 1 / jωC

The mostly used elements in equivalent circuits to analyze the impedance data in this work are shown as following:

- R_s: Solution resistance. It represents the solution resistance between the reference electrode and the working electrode. The ionic concentration, type of ions, temperature, and the geometry of the exposed area are the main effects on the resistance of an ionic solution.
- R_p: Polarization resistance. It is the transition resistance between the electrodes and the electrolyte. Polarization of an electrode causes current to flow due to electrochemical reactions at the electrode surface. High R_p values indicate high corrosion resistance at the electrode surface.
- R_{outer}: Resistance of the outer porous TiO_2 layer for the thermal oxidized Ti samples.
- R_{inner}: Resistance of the inner compact oxygen-diffused titanium layer for the thermal oxidized Ti samples.
- R_{film}: Resistance of the outer porous $Ca_3(PO_4)_2$ layer for the CaP/TiO_2 bioceramic film coated Ti samples.
- R_{oxide}: Resistance of the inner compact $CaTi_{21}O_{38}$ and TiO_2 layers for the CaP/TiO_2 bioceramic film coated Ti samples.
- R_{ct}: Charge transfer resistance results from the electrochemical reactions at the interface of electrode and electrolyte.

◆ CPE: Constant phase element. It describes a non-ideal capacitor when non-uniform current distribution occurs and normally models the behavior of a double layer. The impedance of CPE can be expressed as:

$$Z_{CPE} = 1 / [T (j\omega)^{\phi}] \qquad (3\text{-}10)$$

The corresponding equivalent circuits used in this thesis are presented in the following four Chapters, as presented in Figure 4-3, Figure 5-7, Figure 5-12 and Figure 7-8.

3.2.3 Potentiodynamic polarization technique

The potentiodynamic polarization is a technique where the potential of working electrode is varied at a selected rate by application of a current through the electrolyte. This technique is used as a standard corrosion research method and is mainly applied to measure polarization curve to provide significant useful information regarding the corrosion mechanism, corrosion rate and susceptibility of specific materials to corrosion in designated environment.

Figure 3-5 shows a schematic anodic polarization curve in which it is possible to identify different regions related to the surface behavior. In the active region, as the potential is increased from the corrosion potential, the current increases quickly according to the normal dissolution of metal until a critical value (i_{crit}). This point is defined as the beginning of stability for passive films, which occurs at the potential higher than the primary passive potential (E_{pp}). Beyond this point, the current measured can decrease several orders of magnitude to a residual current, which we call the passive current density (i_p). The correspondence region is defined as the passive region on potentiodynamic polarization curve plot. At higher potential (E_{tp}), breakdown of the passive film might occur with an increase of current in anodic activity region, as metal or alloy enters the transpassive state.

A potentiodynamic anodic polarization plot can give important information such as:

◆ The ability of the material to spontaneously form a passive film on its surface in the particular medium.

◆ The potential region over which the specimen remains passive.

◆ The corrosion rate in the passive region.

Potentiodynamic polarization technique can be also used to measure the corrosion potential (E_{corr}) and its dependent corrosion current density (i_{corr}) if the scan potential starts from more negative range where cathodic current predominates and cannot be ignored. Tafel plot (see Figure 3-6) is the representative method which respects the Tafel equation:

$$\eta = E_{applied} - E_{oc} = \beta \log(i/i_0) \qquad (3\text{-}11)$$

where η is the overpotential, β is the Tafel slope, i the applied current density and i_0 the exchange current density (the reaction rate at the reversible potential for that particular reaction).

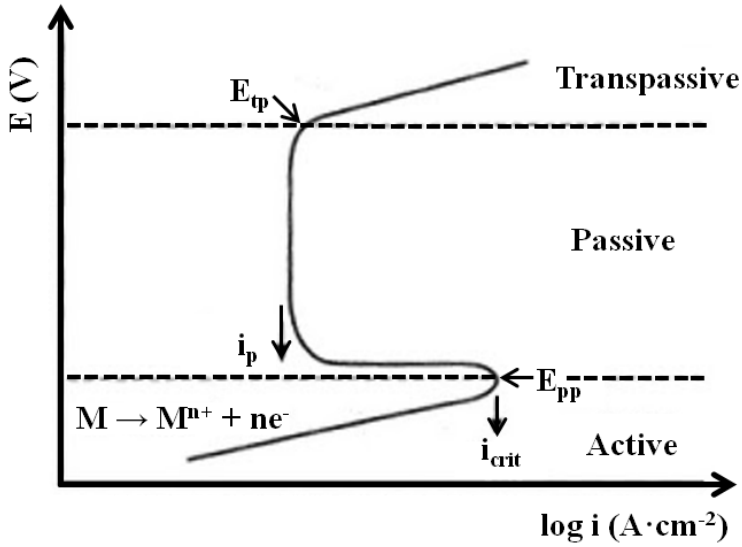

Figure 3-5 Schematic anodic polarization curve.

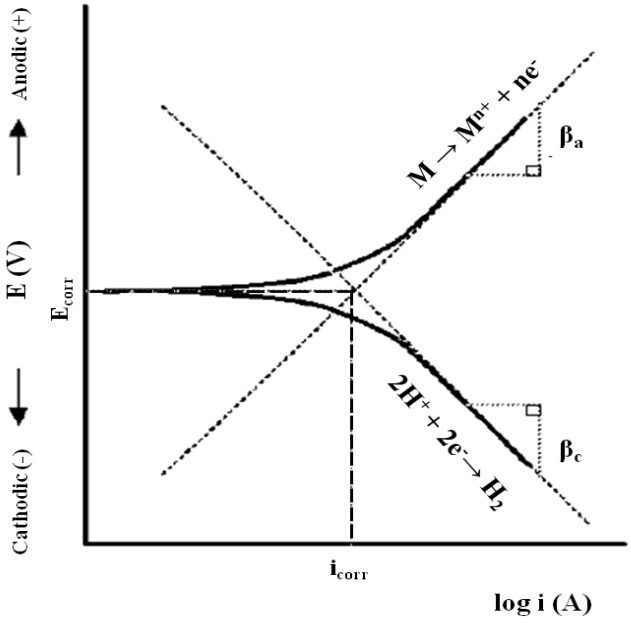

Figure 3-6 Experimentally measured Tafel plot in acidic medium.

The Tafel slope for the anodic and cathodic reactions occurring at open circuit may be obtained from the linear regions of the polarization curve, as illustrated in Figure 3-6. Once these slopes (β_a and β_c) have been established, it is possible to extrapolate back from both the anodic and cathodic regions to the point where the anodic and cathodic currents are equivalent. The current density at that point is the corrosion current density (i_{corr}) and the potential at which it falls is the corrosion potential (E_{corr}).

3.2.4 Potentiostatic technique

Potentiostatic technique needs a typical three-electrode system controlled by a potentiostat, which applies an anodic or cathodic potential to the working electrode and measures the current flowing through working electrode as a function of time. In this mode, the potentiostat will accurately control the potential of the counter electrode (CE) against the WE so that the potential difference between the WE and the RE is well defined, and correspond to the value specified by the user.

This technique can be used to directly observe anodic and cathodic behaviors of a metal surface in electrolytes by applying a constant potential. Furthermore, the investigation of the effect of applied electrochemical potential on the tribocorrosion behavior as well as the wear-corrosion synergism has taken attentions from relative research area in recent years (see in Figure 3-7). More information and further details can be found in [178, 179].

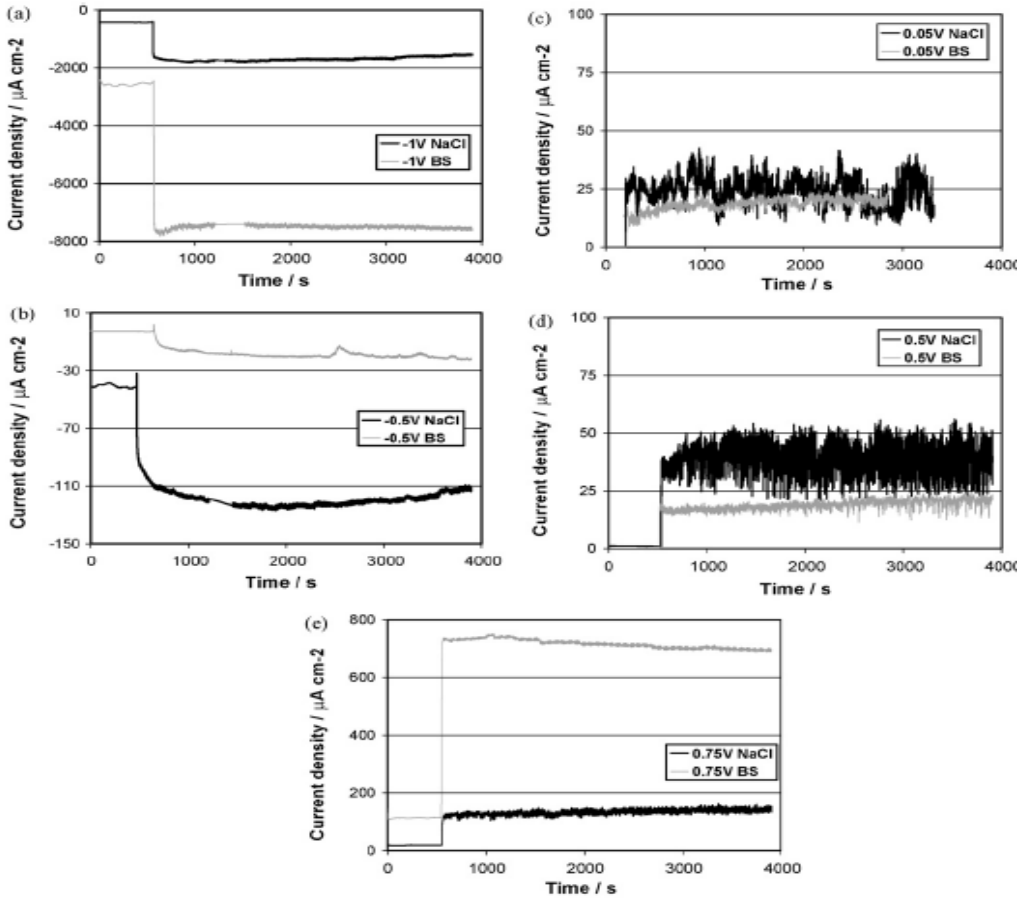

Figure 3-7 Evolution of time with the current density during sliding of a smooth alumina ball against CoCrMo alloy at several imposed potentials (a) -1 V, (b)-0.5 V, (c) 0.05 V, (d) 0.5 V and (e) 0.75 V vs. Ag/AgCl in NaCl and Bovine Serum. Normal loading force of 5 N, pH 7.4 and 37 ℃ [179].

3.3 Characterization techniques

The following paragraphs will summarize the techniques used for the *ex situ* surface characterization in this work.

3.3.1 Vikers hardness test

The Vickers hardness test method consists of indenting the test material with diamond indenter, in the form of a pyramid with a square base and an angle of 136 °between opposite faces subjected to a test force of between 1 g and 100 kg. The full load is normally applied for 10 to 15 seconds. The two diagonals of the indentation left in the surface of the material after removal of the load are measured using a microscope and their average value is calculated. The area of the sloping surfaces of the indentation is then calculated. The Vickers hardness is the quotient obtained by dividing the kg load by the square mm^2 area of indentation, as illustrated in Figure 3-8.

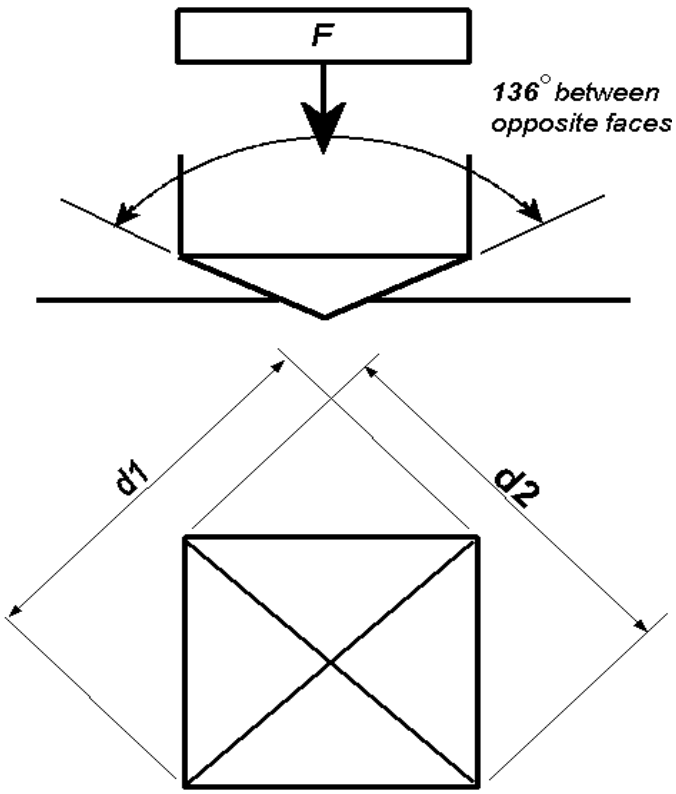

Figure 3-8 Schematic Vickers hardness test.

The formula to calculate is:

$$\mathbf{HV = [2\ F^{*}\ \sin(136\ ^{\circ}/2)]\ /\ d^{*2} = 1.854\ F^{*}\ /\ d^{*2}} \qquad (3\text{-}12)$$

where F^* is the load in kg, d^* is the arithmetic mean of the two diagonals (d^*1 and d^*2 in mm), and HV is the Vickers hardness.

The Vickers hardness should be reported like 800 $HV_{0.1}$, which means a Vickers hardness of 800, was obtained by using a 0.1 kg force.

3.3.2 3D microtopography measurement

Surface microtopography of specimen is measured by a 3D optical profilometry (Micromesure STIL, France) in this work (see Figure 3-9). It is a measuring instrument used to measure surface's profile by a non-contact method. The evaluation of the initial surface roughness for each specimen is obtained by taking the mean value of five squares of 1000 μm × 1000 μm (step of measurement of 1 μm and cadency frequency of 300 Hz) that are displaced in center and ± 4 mm in X-axis and Y-axis from the center of sample, as illustrated in Figure 3-10.

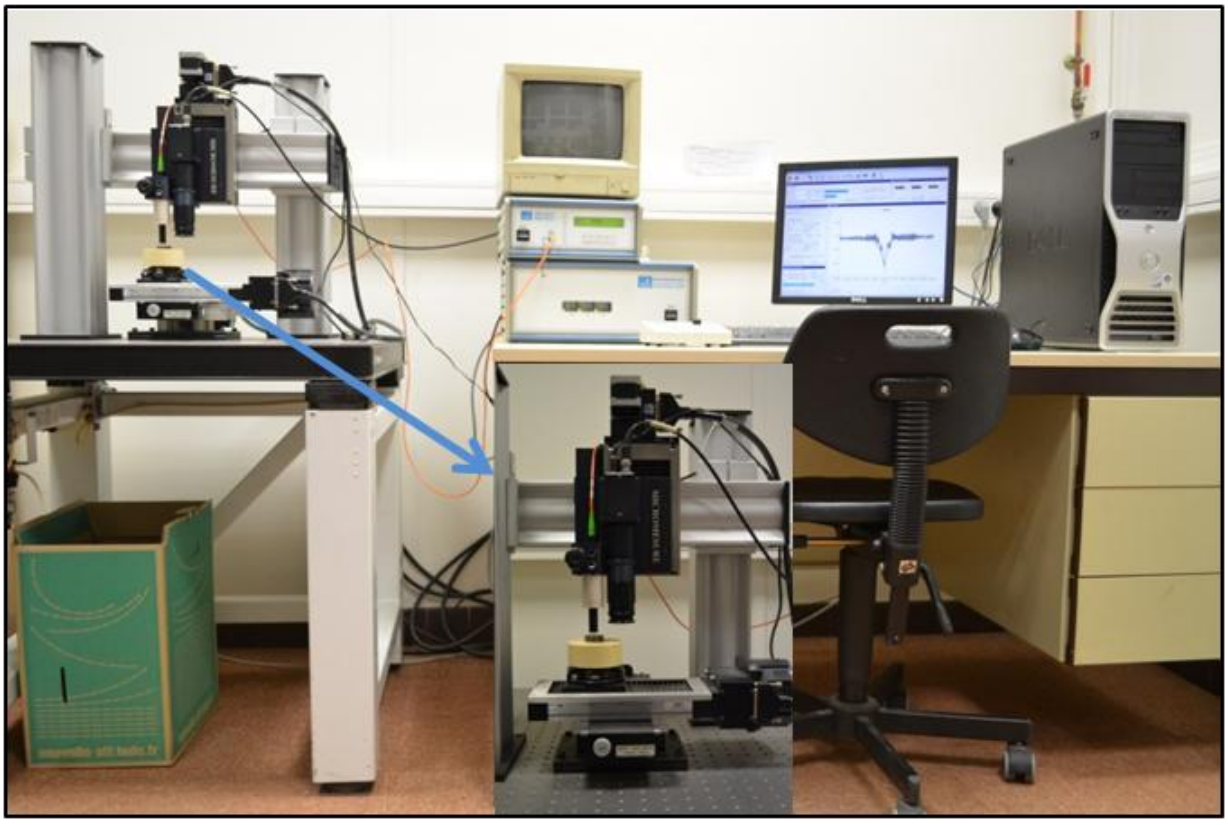

Figure 3-9 3-D optical profilometry used in this work.

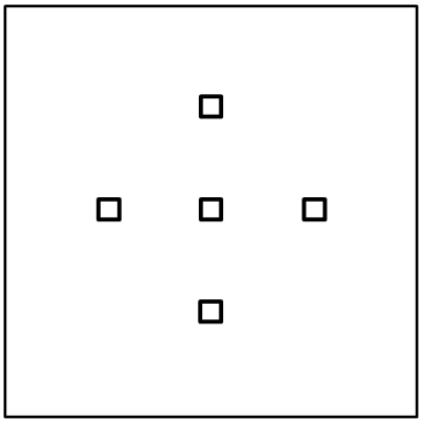

Figure 3-10 Illustration of 5 squares for the measurement of surface roughness.

This profilometry can also be used to measure the total wear track volume of specimen after tribocorrosion test. In order to get a more credible value of the wear track volume, measurement is performed on 4 parts of the wear track (0 °90 °180 °270 °), as illustrated in Figure 3-11. The dimension of the rectangle is keeping the width as 500 µm and the length from 1 mm to 5 mm depending on the track length (step of measurement of 1 µm and cadency frequency of 300 Hz). All data will be analyzed and evaluated by the software (MountainsMap Universal).

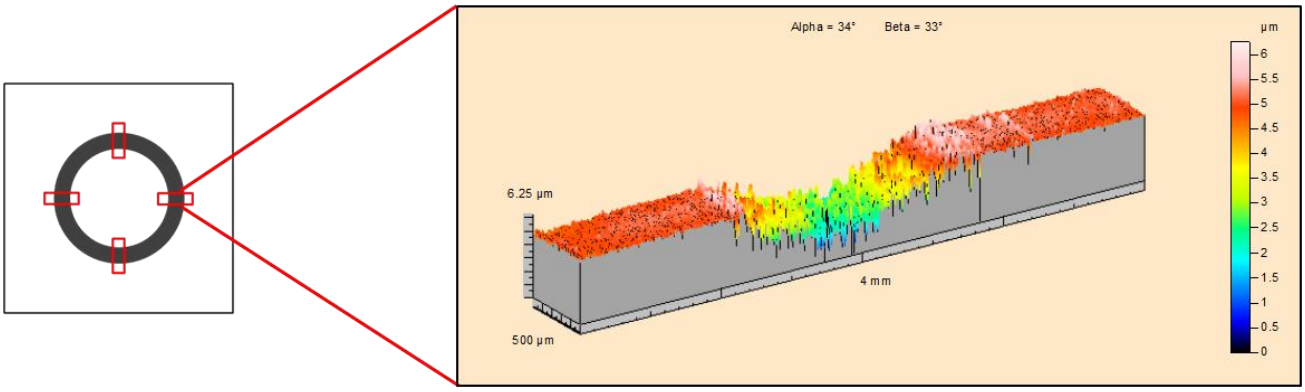

Figure 3-11 Interpretation for the measurement of wear track volume.

3.3.3 Scanning electron microscope

Scanning electron microscope (SEM) is a type of electron microscope that produces images of a sample by scanning it with a high-energy beam of electrons. The electrons interact with atoms in the sample, producing various signals that contain information about the sample's surface topography, composition and other properties such as the electrical conductivity. The electron beam is generally scanned in a raster scan pattern, and the beam's position is combined with the detected signal to produce an image. Specimens can be observed in high vacuum, in low vacuum, and in wet conditions.

The types of signals produced by SEM include secondary electrons (SE), back-scattered electrons (BSE), characteristic X-ray, light (cathodoluminescence, CL) specimen current and transmitted electrons. The signals result from interactions of the electron beam with atoms at or near the surface of the sample. In the most common or standard detection mode, secondary electron imaging, the SEM can produce very high-resolution images of a sample surface, revealing details less than 1 nm in size. Due to the very narrow electron beam, SEM micrographs have a large depth of field yielding a characteristic 3-D appearance useful for understanding the surface structure of a sample. A wide range of magnifications is possible from about 10 times to more than 500 000 times.

3.3.4 Energy-dispersive X-ray spectroscopy

Energy-dispersive X-ray spectroscopy (EDS) is an analytical technique used for the elemental analysis or chemical characterization of some source of a sample. Its characterization capabilities are due in large part to the fundamental principle that each element has a unique atomic structure allowing unique set of peaks on its X-ray spectrum.

To stimulate the emission of characteristic X-rays from a specimen, a high-energy beam of charged particles such as electrons or protons, or a beam of X-ray, is focused into the sample being studied. At rest, an atom within the sample contains ground state (or unexcited) electrons in discrete energy levels or electron shells bound to the nucleus. The incident beam may excite an electron in an inner shell, ejecting it from the shell while creating an electron hole where the electron was. An electron from an outer, higher-energy shell then fills the hole, and the difference in energy between the higher-energy shell and the lower-energy shell may be released in the form of an X-ray. The number and energy of the X-ray emitted from a specimen can be measured by an energy-dispersive spectrometer. As the energies of the X-rays are characteristics of the difference in energy between two shells, and of the atomic structure of the element from which they were emitted, this allows the elemental composition of the specimen to be measured.

SEM coupled with EDS (FEI Quanta 200 FEG) is used to evaluate the morphology and chemical composition of each specimen in this work, shown in Figure 3-12. It is the most versatile high resolution low-vacuum FEG SEM, extending low-vacuum capabilities for the really challenging samples with special properties such as low electrical conductivity.

Figure 3-12 Setup of SEM coupled with EDS.

3.3.5 X-ray diffraction

X-ray diffraction (XRD) is a spectroscopic technique for elucidation of structural information relating to the crystal lattice. Because the physical properties of solid depend on atomic arrangements of materials, determination of the crystal structure is an indispensable part of the structural and chemical characterization of materials. X-ray patterns are used to establish the atomic arrangements of the materials for the fact that the lattice parameter, d (spacing between different planes) is of the order of X-ray wavelength. Further, X-ray diffraction method can be used to distinguish crystalline materials from noncrystalline (amorphous) materials. The structure identification is made from the X-ray diffraction pattern analysis and comparing it with the internationally recognized database containing the reference pattern from the International Center for Diffraction Data (ICDD).

From X-ray pattern we can obtain the information as follows:

- To judge the formation of a particular material system.
- Unit cell structure, lattice parameters, miller indices (hkl).
- Types of phases present in the material.
- Estimation of crystalline/amorphous content in the sample.
- Evaluation of the average crystalline size from the width of the peak in a particular phase

pattern. Large crystal size gives rise to sharp peaks, while the peak width increases with decreasing crystal size.

- An analysis of structural distortion arising as a result of variation in d-spacing caused by the strain, thermal distortion.

In this work, the diffraction patterns are obtained using CuK_{α} ($\lambda = 1.54$ Å) radiation source for a maximum scan range from 10 °to 90 °at a scan rate of 0.02 °/s by a X-ray Diffractometer (D2 PHASER, BRUCKER).

3.4 Tribocorrosion tests

Tribocorrosion experiments were performed in a unidirectional pin-on-disc mode by a tribometer (FALEX TRIBOLOGY or CSM) combined with *in situ* electrochemical measurements, schematic setup is shown in Figure 3-13 (the diameter of rotation cycle is 1 cm in this study). In order to investigate the influence of normal loading force on tribocorrosion behavior of specimen, three different tribometers are used in this work. All equipments and the usage information are shown in Figure 3-14. It should be noticed that the rotation mode for the first tribometer (fabricated by CSM, Switzerland), with the smallest loading force (F_n) range from 10 mN to 1 N, is the disc rotating with a constant speed. The rotation mode for the other two from FALEX TRIBOLOGY (loading force range from 200 mN to 5 N for the second one and from 2 N to 50 N for the last one) is the pin rotating instead.

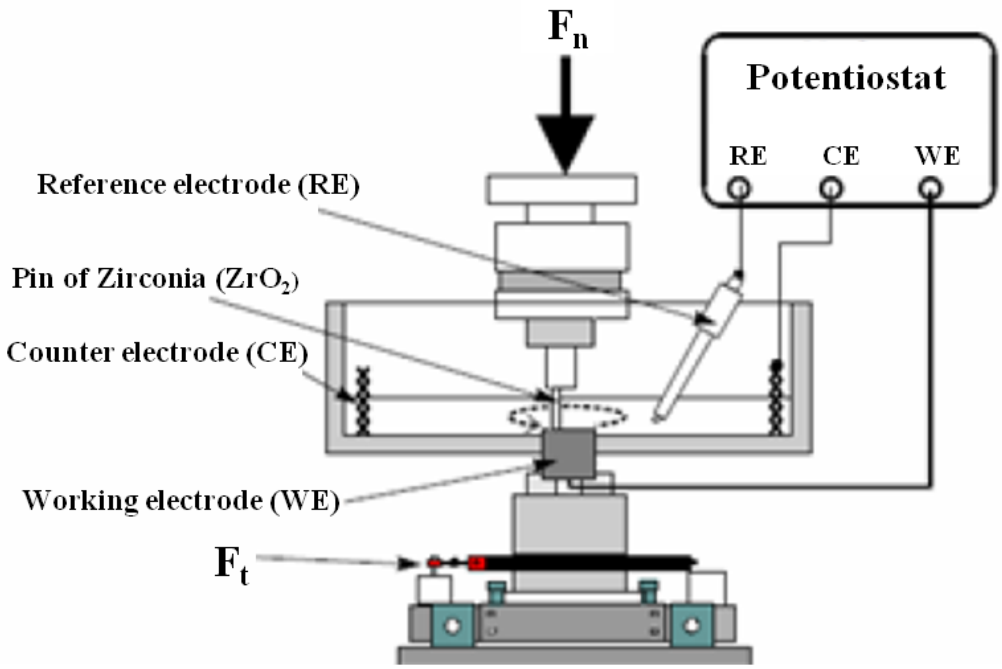

Figure 3-13 Schematic setup for tribocorrosion test.

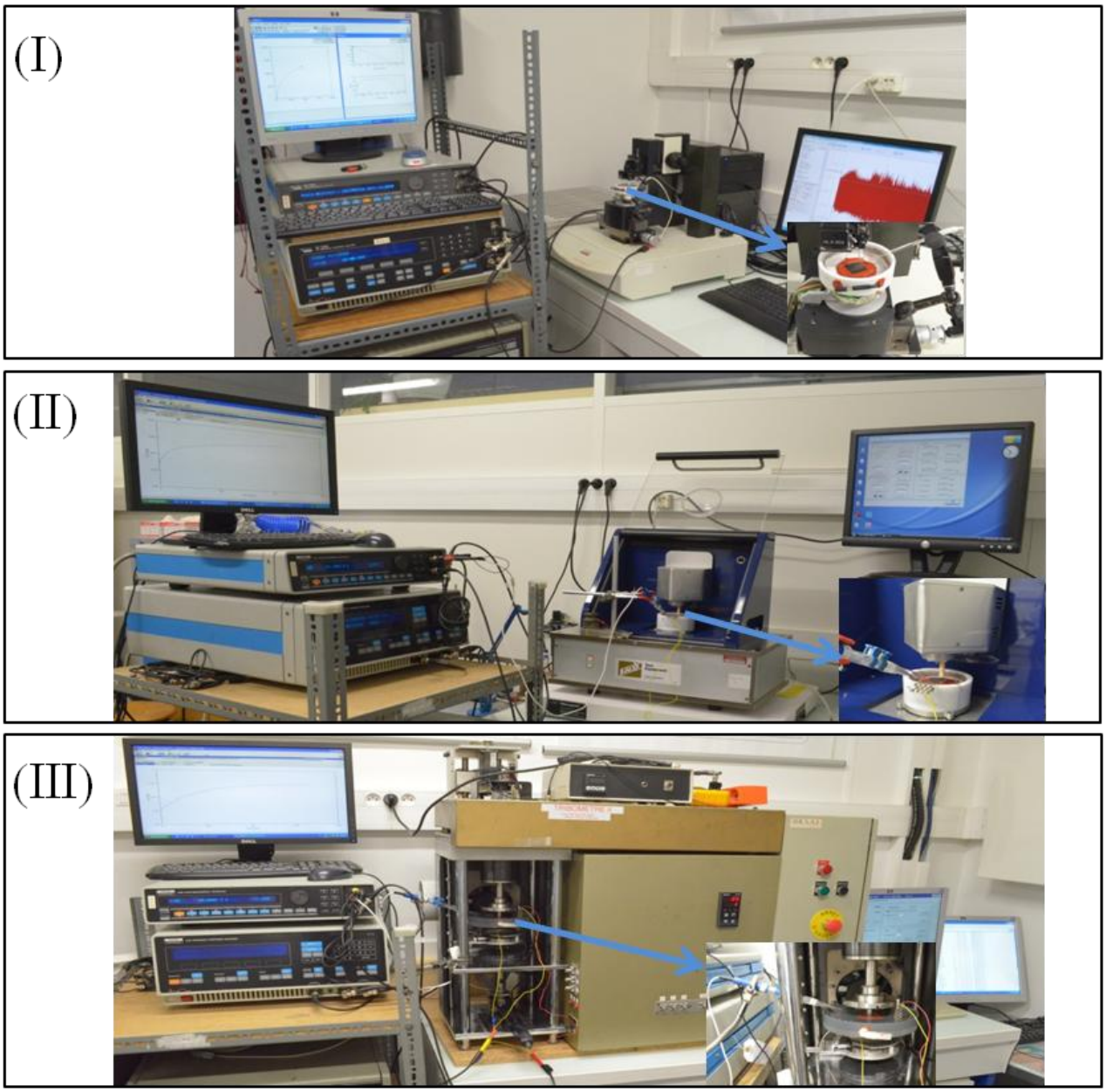

Figure 3-14 Tribocorrosion setup with three different tribometers, loading force range is (I) from 10 mN to 1 N, (II) from 200 mN to 5 N, and (III) from 2 N to 50 N, respectively.

The selection of loading force is based on a principle, which is to generate a maximum Hertzian contact pressure smaller than the yield strength of cp Ti (275 MPa) to avoid plastic deformation. For the cp Ti sample, we consider it as a sphere whose radius is intinity after polishing. According to the Hertzian contact theory where contact happens between two spheres, the calculation of maximum contact pressure (P_{max}) and average contact pressure (P_m) can be illustrated as follows:

$$P_{max} = 3F_n / (2\pi a^2) \quad (3\text{-}13)$$

$$P_m = F_n / (\pi a^2) \quad (3\text{-}14)$$

where a is the radius of the Hertzian static contact area:

$$a^3 = 3F_nR^* / (4E^*) \qquad (3\text{-}15)$$

with F_n the applied normal load, R^* the radius of the tip of the curved counterbody, and E^* the equivalent elastic modulus given by:

$$1 / E^* = (1- \nu_1^2) / E^*_1 + (1- \nu_2^2) / E^*_2 \qquad (3\text{-}16)$$

with ν_1 and ν_2 the Poisson's ratios, and E^*_1 and E^*_2 the elastic moduli of the cp Ti sample and zirconia pin, respectively.

The evolution of maximum and average pressures between ZrO_2 pin with an effective radius of 10 cm and cp Ti are presented in Figure 3-15, from which it can be deduced that loading forces less than 20 N are reasonable in this work.

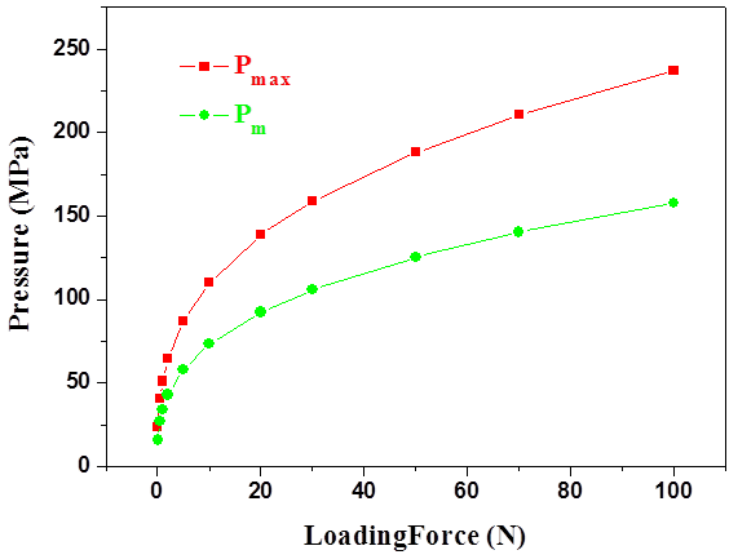

Figure 3-15 Evolution of maximum and average pressures as a function of F_n for cp Ti.

Electrochemical measurements are performed before, during and after unidirectional sliding tests. As working electrode, specimen is fixed in an integrated electrochemical cell (three-electrode setup), a platinized titanium gauze was used as counter electrode and a Ag/AgCl (saturated KCl solution) as reference electrode (+ 197 mV vs. Standard Hydrogen Electrode, SHE). All potentials are given with respect to Ag/AgCl reference electrode. The electrochemical measurements are done using a Solartron 1287 Electrochemical Interface and a Solartron 1255 Frequency Response

Analyzer controlled by a PC running Corrware and Zplot software. Further data analysis was carried out by Cview and ZView softwares from Scribner Associates, Inc.

In the part of tribocorrosion behavior of cp Ti, two types of sliding tests are performed, namely continuous and intermittent unidirectional sliding tests to identify the depassivation/repassivation phenomena during sliding pause periods and their effects on tribocorrosion behavior of cp Ti. During continuous unidirectional sliding tests, the pin rotates permanently with a constant rate as one cycle in t_{rot} during the whole test duration. During intermittent unidirectional sliding tests, the pin rotates for one cycle in t_{rot}, and then remains immobile for a given period of time, t_{off}. The latency time, t_{lat}, is defined as the time between two successive contact events at a given point in the sliding track, so that $t_{lat} = t_{rot} + t_{off}$. In the case of continuous unidirectional sliding tests, the latency time is equal to the rotation period t_{rot} since $t_{off} = 0$. In the case of intermittent unidirectional sliding tests, two different values of t_{off} are selected. The total number of rotation for each test is fixed at 10 000 cycles.

3.5 Tribocorrosion protocol for cp Ti

Over the last years, many studies have been undertaken to investigate the combined corrosion-wear degradation of metallic materials by electrochemical methods in different aqueous media. One common agreement is widespreadly recognized among the tribologists, engineers and scientists in this domain. That is, during tribocorrosion, the synergy between mechanical wear and (electro)chemical corrosion results in a phenomenon that the total loss of removed material, W_{tr}, differs from the sum of material removed seperately by wear and corrosion. The W_{tr} is given as a function of three components:

$$W_{tr} = W^{m} + W^{c} + W^{s} \qquad (3\text{-}17)$$

where W^{m} and W^{c} are the loss of material removed separately by the effects of mechanical wear and (electro)chemical corrosion, respectively. And W^{s} represents the synergistic effect between wear and corrosion. The W^{s} is often expressed as the sum of two terms:

$$W^{s} = W^{mc} + W^{cm} \qquad (3\text{-}18)$$

with W^{mc} the modification of the mechanical material loss caused by the effect of (electro)chemical phenomena, like formation of oxide films, changement of roughness, *etc*. W^{cm} the modification of the corrosive material loss caused by the mechanical sliding effects, like destruction of surface films, straining, *etc*. This approach is used in the current ASTM G119-09 ‘Standard guide for determination synergism between wear and corrosion’[180].

Eq. 3-17 then can be written as follows:

$$W_{tr} = W^{m} + W^{c} + W^{mc} + W^{cm} \qquad (3\text{-}19)$$

In this work, a test protocol refered to "A methodology for the assessment of the tribocorrosion passivating metallic materials" [92] is designed to evaluate the contribution of each component mentioned above on tribocorrosion behavior of untreated cp Ti. It is based on the fact that the surface state of a wear evolves with time for passivating materials. Apart from the general wear for all tribological conditions, another evolution also occurs in the case of tribocorrosion of cp Ti. This evolution results from the repeated removal and subsequent re-growth of a passive surface film when a mechanical loading is applied. The synergism effect in tribocorrosion is thus possible to be investigated by controlling the frequency of the depassivation-repassivation events with respect to the time necessary for film growth. Descriptions for each step are illustrated below

3.5.1 Electrochemical behavior in the absence of unidirectional sliding

The first step of the test protocol [92] is the measurement of electrochemical comportment of cp Ti immersed in PBS without any sliding. Figure 3-16 shows the evolution of OCP, E_{oc}, and from an electrochemical point of view, a stable E_{oc} is obtained at the point where the long-term fluctuations of E_{oc} are below 60 mV/h. The time necessary to reach such a stationary OCP in PBS is an important characteristic of passivating process of cp Ti. In this protocol, it is called the reaction time, t_{react}, and a value of 6000 s is selected for cp Ti in this work. All other time-relative parameters in this tribocorrosion protocol are based on t_{react} = 6000 s.

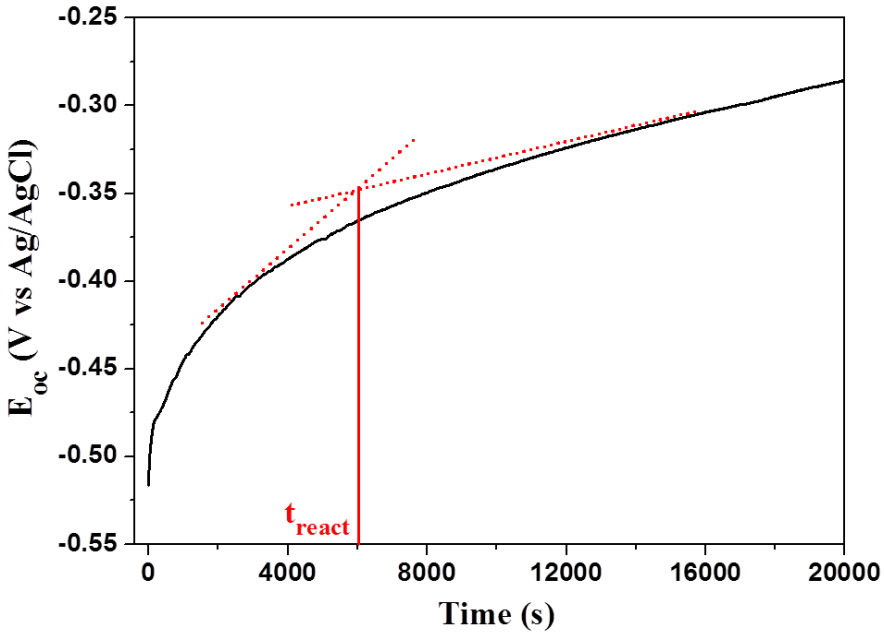

Figure 3-16 OCP evolution versus time of cp Ti in PBS solution.

After achieving a long-term stable OCP which indicates the passivation state of cp Ti in PBS, the polarization resistance value of the passive material, R_p, is measured by EIS. Based on R_p, the specific polarization resistance of passive material, r_p, can be calculated as:

$$\boldsymbol{r_p = R_p A_0} \qquad (3\text{-}20)$$

where A_0 is the total surface area exposed directly to the test electrolyte.

It should be noticed that specific polarization resistance values for metallic materials of 10^3 Ω ċm^2 or lower indicate the presence of an active sample surface, while value around 10^5 Ω ċm^2 or higher indicate a passive sample surface [181]. This criterion is a parallel judgment with the fluctuation of E_{oc} less than 60 mV/h.

The corrosion current density of cp Ti covered by a passive surface film, i_p, is then calculated as:

$$\boldsymbol{i_p = B / r_p} \qquad (3\text{-}21)$$

with B a constant. For metallic materials, B normally varies between 13 mV and 35 mV, depending on the nature of the material and the environment. In this tribocorrosion protocol for cp Ti in PBS, a value of 26 mV is assumed, more details can be referred to Part 4.5 in Ref. [73].

3.5.2 Electrochemical behavior under continuous unidirectional sliding

The second step for this protocol is the determination of the corrosion rate of the depassivated material, which means the corrosion rate of the fully active sliding track of cp Ti in PBS. In order to keep a part of the immersed sample surface in a full and enduring active state, the passive film should be continuously removed by mechanical sliding. It is necessary to select a rotation period, t_{rot}, which is so small compared to t_{react} that the passive film has no time to repassivate in between two successive contact events. Generally, it is assumed that values of t_{rot} less than 1/10 000 of t_{react} reach this requirement. In this work, the rotation period for cp Ti is thus taken as:

$$\boldsymbol{t_{rot} = t_{react} / 10\,000 = 0.6\ s} \qquad (3\text{-}22)$$

During unidirectional continuous sliding test, the whole wear track area, A_{tr}, is in an active state, so that it equals to the active area, A_{act}, as:

$$\boldsymbol{A_{tr} = A_{act}} \qquad (3\text{-}23)$$

After sliding tests, the total area of the sliding track, A_{tr}, and the wear volume, W_{tr}, can be derived from profilometric measurements. Calculations are carried out by the following formula:

$$A_{tr} = eL = e\,\pi d \qquad (3\text{-}24)$$

$$W_{tr} = SL = S\,\pi d \qquad (3\text{-}25)$$

with e the average track width, L the length of the sliding track, d the diameter of the sliding track as 1 cm used in this work, and S the average area of the cross-section of the wear track, see in Figure 3-17.

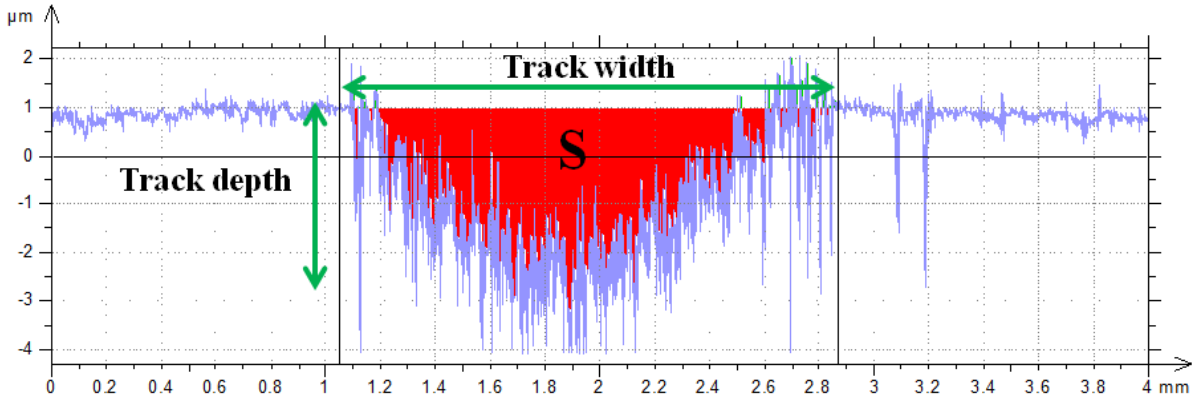

Figure 3-17 A presentation of the intersecting surface of wear track after sliding test.

Despite the fact that the width of the sliding track increases gradually due to wear during sliding, the average track width in this work is still using the track width at the end of sliding test. If we consider the track depth, it is easy to find that the real active track area is larger than the product of track width with the length of sliding track for each contact cycle.

In the second step, the sliding is initiated at the time of a stable E_{oc} is achieved. The E_{oc} value recorded during sliding is a mixed potential resulting from the galvanic coupling of two types of materials existing spontaneously on the surface of sample. One is the material inside the sliding track with an area of A_{tr}, the other is the material outside the sliding track with an area of $(A_0 - A_{tr})$. It is assumed that the kinetics of the redox reactions taking place on each of these two areas, do not vary with the real potential of the sliding track. That means the ohmic drop effect is considered to be negligible in the galvanic coupling between the sliding track and the surrounding area.

EIS can be used to measure the polarization resistance during continuous unidirectional sliding, R_{ps}, of the total surface. As the illustration of E_{oc} during sliding, R_{ps} can be considered as the combination of two polarization resistances, namely R_{act} related to the active area A_{act} (equals to the wear track area, A_{tr} in this case), and R_p which is related to the surrounding unworn and passive area, $(A_0 - A_{tr})$.

$$1/R_{ps} = 1/R_{act} + 1/R_p \qquad (3\text{-}26)$$

where:

$$R_{act} = r_{act} / A_{tr} \qquad (3\text{-}27)$$

and:

$$R_p = r_p / (A_0 - A_{tr}) \qquad (3\text{-}28)$$

Because r_p is known from Eq. 3-20, the specific polarization resistance of the active surface can be derived by substituting Eq. 3-27 and Eq. 3-28 into Eq. 3-26:

$$r_{act} = (A_{tr}\, R_{ps}\, r_p) / [r_p - R_{ps}\, (A_0 - A_{tr})] \qquad (3\text{-}29)$$

It is then possible to calculate the corrosion current density of the active material, i_{act}, by substituting r_p with r_{act} in Eq. 3-21:

$$i_{act} = B / r_{act} \qquad (3\text{-}30)$$

3.5.3 Electrochemical comportment under intermittent unidirectional sliding

In this step, two extreme cases will be characterized for untreated cp Ti in the wear track area, i.e. the repassive material and the active material. When tribocorrosion occurs under intermittent unidirectional sliding, the surface of cp Ti undergoes subsequential events of depassivation and repassivation in-between two successive sliding contacts. It means that a part of the wear track surface at any given time repassivates progressively. Comparing with the continuous unidirectional sliding, where the latency time is defined as $t_{lat1} = t_{rot} = 0.6$ s, the selection of t_{lat} in this part can be carried out with two different values as $t_{lat2} = t_{rot} + t_{off} = 6.6$ s where $t_{off} = t_{react}$ /1000 and $t_{lat3} = t_{rot} + t'_{off} = 12.6$ s where $t'_{off} = t_{react}$ /500. The re-growth of a surface film between two successive contact events with t_{lat2} or t_{lat3} is not negligible anymore, and the wear track area, A_{tr}, is thus separated by two distinct zones as follows:

$$A_{tr} = A_{act} + A_{repass} \qquad (3\text{-}31)$$

where A_{act} is the representative of a fraction of the sliding track from which the initial passive film has been removed during sliding, A_{repass} the remaining sliding track area covered by a repassivated film that is in the same state as the surface before sliding, as illustrated in Figure 3-18.

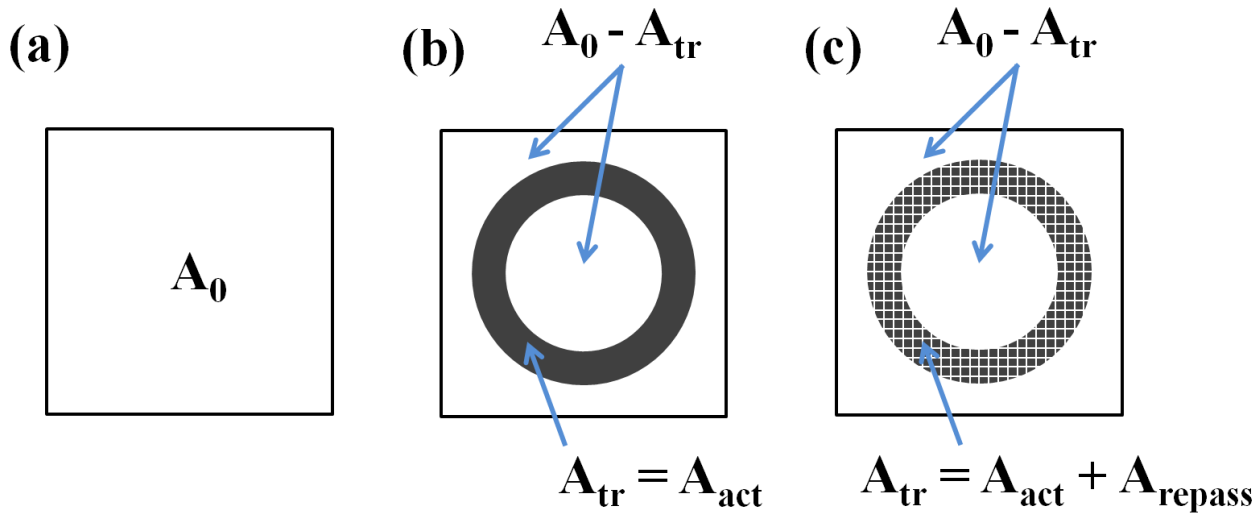

Figure 3-18 Schematic top view of cp Ti: (a) in the absence of sliding, (b) during continuous unidirectional sliding test at t_{lat1} of 0.6 s, and (c) during intermittent unidirectional sliding test at t_{lat2} of 6.6 s or t_{lat3} of 12.6 s.

It should be noticed that under continuous unidirectional sliding, the A_{repass} is assumed as zero because of the stationary electrochemical state condition by constant sliding contacts. Under intermittent unidirectional sliding, the active and repassivated areas in the slidng track evolve with t_{off} since a gradual increase in the coverage of the repassivated area takes place between two successive contact events. It is assumed that the fraction of the sliding track surface covered by the repassive film A_{repass}/A_{tr}, is constant and given by the ratio of t_{lat}/t_{react}:

$$\boldsymbol{A_{repass}/A_{tr} = t_{lat}/t_{react}} \qquad (3\text{-}32)$$

and:

$$\boldsymbol{A_{act}/A_{tr} = 1 - t_{lat}/t_{react}} \qquad (3\text{-}33)$$

As a result, for the two selected values of latency time t_{lat2} = 6.6 s and t_{lat3} = 12.6 s, the corresponding relationships between the repassivated area and the total wear track area are $A_{repass2}$ = 0.0011 A_{tr} and $A_{repass3}$ = 0.0021 A_{tr}, and thus A_{act2} = 0.9989A_{tr} and A_{act3} = 0.9979A_{tr}, respectively.

3.5.4 Analysis and interpretation of sliding test results

The procedure for analyzing the tests results obtained from these three steps above is interpreted in the following paragraphs. For cp Ti without any pretreatment, the total volume of removed material, W_{tr}, is a sum of four components related to both types of zones on the wear track, the zone A_{act} in the active state and A_{repass} in the repassivated state, Eq. 3-19 thus can be expressed as:

$$W_{tr} = W^{m}_{act} + W^{c}_{repass} + W^{m}_{repass} + W^{c}_{act} \qquad (3\text{-}34)$$

with:

- W_{tr} the total material loss in the wear track
- W^{m}_{act} the material loss due to mechanical wear of active material in the wear track
- W^{c}_{repass} the material loss by corrosion of repassivated material in the wear track
- W^{m}_{repass} the material loss due to mechanical wear of repassivated material in the wear track
- W^{c}_{act} the material loss by corrosion of active material in the wear track

Here, the synergism effect is corresponding to the destruction of the passive/repassive film by a mechanical sliding and the material loss due to the dissolution of active metal as:

$$W^{s} = W^{m}_{repass} + W^{c}_{act} \qquad (3\text{-}35)$$

Under continuous unidirectional sliding at low latency time of t_{lat1} = 0.6 s, the calculation of the corrosion current density i_{act1} of the active material was explained in Section 3.5.2 and can be deduced from EIS measurement. The volumetric material loss due to corrosion of the active surface, W^{c}_{act1}, can be calculated by using the appropriate A_{act1} and t_{lat1} values ($A_{act1} = A_{act}$ and $t_{lat1} = t_{lat}$ = 0.6 s) in the following equation:

$$W^{c}_{act1} = [M/(\mathrm{n}F\mathrm{d})]\, i_{act1} A_{act1} N t_{lat1} \qquad (3\text{-}36)$$

where M the molecular weight of cp Ti (47.9 g/mol), n the number of elctrons involved in the oxidation process (for TiO_2, n = 4), d the density of cp Ti (4.508 g/cm^3), F the Faraday constant (96 485 C/mol), and N the total rotation number of cycles (10 000).

In the case of continuous sliding, there is no immobile time between two successive contacts. The components resulted from A_{repass} area can be negligible in Eq. 3-34, from which the volumetric material loss due to mechanical wear of active material in the wear track, W^{m}_{act}, can be calculated by subtracting the material loss by corrosion, W^{c}_{act}, from the total material loss in the wear track, W_{tr}, measured at the end of continuous unidirectional sliding test:

$$W^{m}_{act1} = W_{tr1} - W^{c}_{act1} \qquad (3\text{-}37)$$

For the tests performed under intermittent unidirectional sliding at high latency times (t_{lat2} = 6.6 s and t_{lat3} = 12.6 s), the processing of the test results for calculating W^{c}_{act} is different from that under continuous sliding. Due to the instability of E_{oc} under intermittent sliding, EIS measurement cannot be

performed. The calculation of i_{act} and the volumetric material loss by corrosion of active material in the wear track, W^{c}_{act}, cannot be determined. In this case, an alternative solution is to use the following equation with the appropriate A_{act} and t_{lat} values [73]:

$$W^{c}_{act2/3} = W^{c}_{act1} \, (t_{lat2/3}/t_{lat1})^{(1-p)} (A_{act2/3}/A_{act1}) \qquad (3\text{-}38)$$

where W^{c}_{act1}, t_{lat1}, and A_{act1} are the components related to the continuous unidirectional sliding test at low latency time [see Eq. 3-36]. In this formula, p is an exponent whose value varies from one material-environment system to another, but always $0 < p < 1$. In this tribocorrosion protocol for cp Ti in the PBS solution, a value of $p = 0.7$ is used according to previous studies on the tribocorrosion mechanism of passivating metals and alloys [182].

Under intermittent unidirectional sliding, it is assumed that the mechanical degradation on the active zone of the wear track A_{act} is the same as that under continuous sliding. The duration of latency time does not affect the mechanical wear resistance of the active material. The material loss due to mechanical wear of active material in the wear track, W^{m}_{act}, is calculated by the following equation:

$$W^{m}_{act2/3} = W^{m}_{act1} \, (A_{act2/3}/A_{act1}) \qquad (3\text{-}39)$$

where W^{m}_{act1} and A_{act1} from the previous results under continuous unidirectional sliding test at low latency time of $t_{lat1} = 0.6$ s.

The material loss by corrosion of repassivated material in the wear track, W^{c}_{repass}, is calculated by analogy to Eq. 3-36 but with the corrosion current density of initial material covered by a passive surface film, i_p,

$$W^{c}_{repass2/3} = [M/(\mathrm{n}F\mathrm{d})] \, i_p A_{repass2/3} N \, t_{lat2/3} \qquad (3\text{-}40)$$

for the reason that the repassivated material in A_{repass} is assumed to have the same corrosion behavior as the initial passive material in A_0. The material loss due to mechanical wear of repassivated material in the wear track, W^{m}_{repass}, is then calculated from Eq. 3-34 as follows:

$$W^{m}_{repass2/3} = W_{tr2/3} - (W^{m}_{act2/3} + W^{c}_{repass2/3} + W^{c}_{act2/3}) \qquad (3\text{-}41)$$

For the interpretation of the outcome of tribocorrosion tests, the specific material loss components in the sliding track, w^{j}_{i}, are calculated per unit area and per cycle, based on the material loss and the corresponding surface area and the number of cycles:

$$w^{j}_{i} = W^{j}_{i} / (NA_i) \qquad (3\text{-}42)$$

with $i = act$ or repass and $j = c$ or m. The value w^j_i, expressed in cm/cycle, corresponds to the thickness of the material removed by a corrosive or mechanical action from active or repassivated parts in the wear track area.

A more detailed assessment of the tribocorrosion of a material is possible based on the ratio between corrosive and mechanical material losses, namely:

$$K_c = (W^c_{act} + W^c_{repass}) / (W^m_{act} + W^m_{repass}) \qquad (3\text{-}43)$$

The following three cases can be distinguished based on the value of K_c:

- when $K_c > 1$, corrosion is the predominant contribution to material loss. The total wear will be mainly controlled by the reactivity of the substrate in the test environment.
- when $K_c < 1$, the material loss due to mechanical removal predominates.
- when $K_c << 1$, the contribution due to the acceleration of corrosion induced by the destruction of the passive film, even if it is large ($W^c_{act} >> W^c_{repass}$), will be negligible compared to the total wear.

The effect of the formation of the passive film on the mechanical wear can be evaluated based on the ratio between the specific mechanical wear on the active and on the repassivated part of the sliding track:

$$K_m = w^m_{act} / w^m_{repass} \qquad (3\text{-}44)$$

- when $K_m > 1$, the passive film provides a protection to the material against mechanical removal. The material will be more sensitive to tribocorrosion at low latency time.
- when $K_m < 1$, the formation of the passive film accelerates the mechanical removal of the material. The sensitivity to tribocorrosion will increase with the increase of the latency time, tlat.

3.6 Tribocorrosion protocol for cp Ti after surface modification

After surface modification as thermal oxidation, CaP bioactive film deposit and CaP/TiO_2 bioceramic film modification, the tribocorrosion protocol for cp Ti mentioned above is not suitable to evaluate the tribocorrosion behavior of these modified materials in this work, for the following reasons (more details will be illustrated in the following chapters from Chapter 5 to Chapter 7):

- It is only the oxide film, CaP bioactive film or CaP/TiO_2 bioceramic film who directly contacts with the counter body (ZrO_2) during the whole tribocorrosion test in pin-on-disc mode.

◆ The modifications change the surface properties of cp Ti, such as microhardness, corrosion resistace and wear resistance.

◆ The oxide film, CaP bioactive film or CaP/TiO_2 bioceramic film inhibits the passivation and depassivation/repassivation phenomena of cp Ti, which might be negligible if the removal of material is not sufficient to reach the substrate.

To investigate the tribocorrosion behavior of surface modified cp Ti, tests are just performed in the absence of unidirectional sliding and under continuous unidirectional sliding.

3.6.1 Electrochemical behavior in the absence of unidirectional sliding

Electrochemical measurements such as OCP, EIS and potentiodynamic polarization of surface modified cp Ti are performed in PBS without any sliding. The evolution of OCP is measured at the beginning of immersion time. After a stable E_{oc} achieving, the polarization resistance of surfaced modified cp Ti with the oxide film or CaP bioactive film, R'_p, is measured by EIS. Based on R'_p, the specific polarization resistance of modified material, r'_p, can be calculated as:

$$\boldsymbol{r'_p = R'_p A'_0} \qquad (3\text{-}45)$$

with:

$$\boldsymbol{R'_p = R_{outer} + R_{inner}} \qquad (3\text{-}46a) \text{ for thermal oxidized Ti}$$

$$\boldsymbol{R'_p = R_p} \qquad (3\text{-}46b) \text{ for CaP bioactive film coated Ti}$$

$$\boldsymbol{R'_p = R_{film} + R_{oxide} + R_{ct}} \qquad (3\text{-}46c) \text{ for CaP/}TiO_2\text{ bioceramic film coated Ti}$$

where A'_0 is the total surface area of surface modified cp Ti, R_{outer} and R_{inner} the resistance of the outer rutile film and the inner oxygen-diffused titanium film for thermal oxidized Ti, R_p the polarization resistance for CaP bioactive film coated Ti, R_{film} and R_{oxide} the resistance of CaP bioceramic film and oxide film between CaP bioceramic film and cp Ti substrate.

3.6.2 Electrochemical behavior under continuous unidirectional sliding

The second step for this protocol is to determine the effect of continuous unidirectional sliding on the corrosion behavior of surface modified cp Ti. The rotation period, t'_{rot} = 0.6 s (equals to the value of t_{lat} in Section 3.5.2), is chosen in order to compare the tribocorrosion behavior under sliding with untreated cp Ti. If the oxide film, CaP bioactive film or CaP/TiO_2 bioceramic film remains on the surface of modified cp Ti and not mechanical degradation occurs on cp Ti substrate during the whole sliding period, it can be assumed that the material loss of modified cp Ti in the wear track, W'_{tr}, entirely

corresponds to the material loss due to mechanical wear of oxide film, CaP bioactive film or CaP/TiO_2 bioceramic film in the wear track area, W^m_{film}, as follows:

$$W'_{tr} = W^m_{film} \qquad (3\text{-}47)$$

The calculation of W'_{tr} is carried out by substituting e and S with e' and S' for surface modified cp Ti at the end of sliding test (10 000 cycles in total) if they can be detected with the testing equipments. The calculation is carried out as follows:

$$A'_{tr} = e'L = e'\pi d \qquad (3\text{-}48)$$

$$W'_{tr} = S'L = S'\pi d \qquad (3\text{-}49)$$

In this step, the sliding is initiated at the time of a stable E_{oc} is achieved ($|\Delta E_{oc}| < 60$ mV/h). Due to no cp Ti substrate is destroyed during sliding, the E_{oc} value recorded here reflects the effect of the degradation of oxide film or CaP bioactive film on the oxidation and reduction reactions at the surface of cp Ti substrate. A cathodic shift of E_{oc} during sliding indicates an enhanced anodic reactivity of cp Ti, but an increase in the more noble direction represents a declined anodic reactivity to the contrary.

EIS can be used to measure the polarization resistance of surface modified cp Ti during continuous unidirectional sliding, R'_{p2}. For the same reason as Eq. 3-42, it is assumed that the variation of R'_{ps} is the product mainly due to the mechanical degradation of oxide film, CaP bioactive film or CaP/TiO_2 bioceramic film on the surface of modified cp Ti. And R'_{ps} can be still used to evaluate the corrosion resistance property of surface modified cp Ti during continuous unidirectional sliding test as follows:

$$R'_{ps} = R_{outer2} + R_{inner2} \qquad (3\text{-}50a) \text{ for TO Ti}$$

$$R'_{ps} = R_{p2} \qquad (3\text{-}50b) \text{ for CaP bioactive film coated Ti}$$

$$R'_{ps} = R_{film2} + R_{oxide2} + R_{ct2} \qquad (3\text{-}50c) \text{ for CaP/}TiO_2 \text{ bioceramic film coated Ti}$$

with 2 the symbol of results during sliding.

Chapter 4: Corrosion and tribocorrosion behavior of cp Ti

4.1 Introduction

In this chapter, corrosion and tribocorrosion behavior of cp Ti was monitored and evaluated by electrochemical and friction measurements in the PBS solution at room temperature. Electrochemical measurements such as OCP, EIS, and potentiodynamic polarization were used to characterize the corrosion behavior of cp Ti. SEM coupled with EDS was performed to analyze the surface morphology and chemical compositions inside and outside the track area after sliding tests. Optical profilometry was used to characterize the total wear volume at the end of the sliding tests. The tribocorrosion behavior of cp Ti was investigated under mechanical loaded condition by using a pin-on-disc tribometer. Contributions of normal force and depassivation/repassivation in material loss of cp Ti were determined based on the tribocorrosion protocol [92]. The results showed that cp Ti was a high corrosion resistant metal under static condition. But this capability lost when the surface was destroyed by mechanical friction. The applied normal force affected the corrosion-wear degradation of cp Ti during continuous unidirectional sliding tests. The effect of latency time under intermittent unidirectional sliding had an influence on the depassivation/repassivation behavior of passive films on cp Ti. The high material loss after tribocorrosion tests showed the poor wear resistance property of cp Ti, revealing the necessity of surface modification to improve its anti-corrosion/anti-wear performance in biomedical applications.

4.2 Experimental details

The well polished and cleaned cp Ti specimens were covered with an electrically insulating silicone paste and then kept in air for about 1 h to dry the paste and meanwhile, a stable passive thin film spontaneously forms prior to the start of electrochemical measurements. The exposed geometric surface areas were measured separately for each sample. All tests were performed in the PBS solution at room temperature (22 ±1 ℃). The composition of this electrolyte has been demonstrated in Chapter 3 (see Table 3-3).

Corrosion behavior of cp Ti was characterized under static condition (in the absence of sliding). In order to determine the passivation of cp Ti with immersion time, the evolution of OCP, E_{oc}, within 24 h was performed continuously as well as the EIS measurements with a sinusoidal potential variation of ±10 mV to OCP at frequencies from 10 kHz down to 1.58 mHz, which were measured at different immersion time of 3 h, 6 h, 12 h and 24 h, respectively. Potentiodynamic polarization curve of cp Ti was obtained at the immersion time of 24 h.

Tribocorrosion experiments were performed at OCP in a unidirectional pin-on-disc tribometer, combined with the mentioned three-electrode cell in Chapter 3. Counter bodies (ZrO_2 pins) were degreased and positioned 5 mm eccentric from the rotation axis on top of the test samples. Two types of sliding tests were done, namely continuous and intermittent unidirectional sliding tests. In the case of continuous unidirectional sliding tests, normal loadings, F_n from 1 N to 10 N, corresponding to a

maximum Hertzian contact pressure from 51 MPa to 110 MPa, were used with the latency time as t_{lat1} = t_{rot} = 0.6 s, to investigate the effect of F_n on corrosion-wear degradation of cp Ti. In the case of intermittent unidirectional sliding tests, F_n of 5 N was imposed with the latency time as t_{lat2} = 6.6 s and t_{lat3} = 12.6 s to identify the depassivation/repassivation phenomena during sliding pause periods and their effects on tribocorrosion behavior of of cp Ti.

Under mechanical loaded conditions, OCP evolutions were performed before, during and after unidirectional sliding tests. For EIS, a sinusoidal potential variation of ± 10 mV was superimposed on OCP at frequencies from 10 kHz down to 100 mHz recorded during continuous unidirectional sliding tests or to 1.58 mHz recorded before and after both continuous and intermittent unidirectional sliding tests. The rotation rate was chosen at 100 rpm and the total number of rotation for each test was fixed as 10 000 cycles. The surface morphology and chemical composition inside and outside the track area were characterized by SEM coupled with EDS. The microhardness is detected by Vickers hardness test with a force of 200 gf and full loading period of 15 s. The total wear volume at the end of sliding was observed by optical profilometry.

The experiments were carried out at least twice and the representative mean values were figured out in this work. All calculations were carried out under the guidance of the tribocorrosion protocol for cp Ti, as illustrated in Chapter 3.

4.3 Corrosion behavior of cp Ti under static condition

For the passive metallic material, the potential value during immersion time normally increased in the noble direction with time as the gradual formation of passive film on its surface. This phenomenon is well defined as passivation of metals and alloys, such as Fe, Cr, Ni, Al, Co, Mo and stainless steels [183, 184]. In this study, the electrochemical reactivity of cp Ti was monitored by OCP evolution versus time upon immersion of a fresh sample in the PBS solution under static condition, as seen in Figure 4-1. At the beginning of immersion, E_{oc} is around -0.48 V vs. Ag/AgCl and increases rapidly to -0.25 V vs. Ag/AgCl during the first 5 h. Then the potential increasing rate is slowing down and only a small variation is observed from -0.20 V vs. Ag/AgCl at immersion time of 10 h to -0.16 V vs. Ag/AgCl at immersion time of 24 h. As mentioned in Chapter 3, a stable E_{oc} is obtained where the long-term function of $|\Delta E_{oc}| < 60$ mV/h (see Section 3.5.1). Here, the potential variations indicate the quasi steady-state of sample surface reaching and keeping more and more stable in the PBS solution. This phenomenon can be further proved by the evolution of the polarization resistance, R_p, at the interface between cp Ti and the PBS solution at different immersion time as 3 h, 6 h, 12 h and 24 h. Figure 4-2 shows the EIS plots for cp Ti specimens.

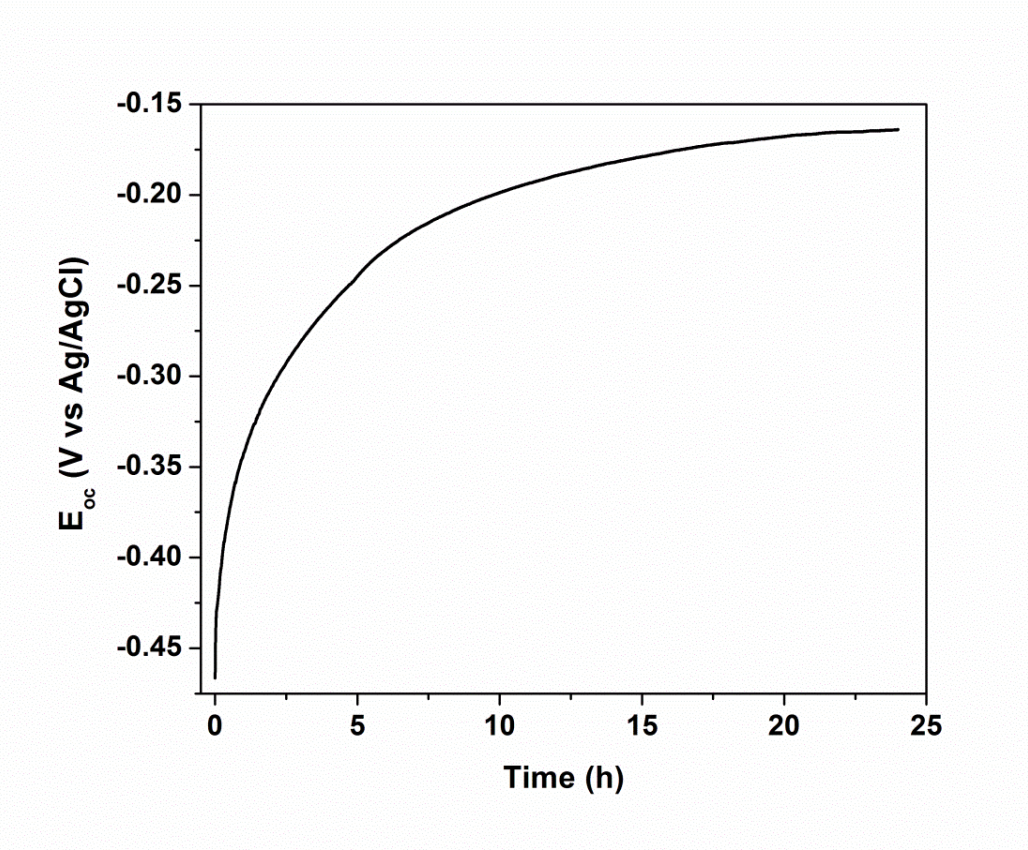

Figure 4-1 OCP evolution of cp Ti within 24 h under static condition in the PBS solution.

The Nyquist plot (Figure 4-2a) shows the imaginary part of the impedance, $-Z_{im}$, versus the real part, Z_{re}, is an arc of a circle. Such an impedance plot corresponds to the equivalent circuit of R_s(CPE||R_p) [183], where R_s is the solution resistance, R_p the polarization resistance of cp Ti due to the barrier property of passive film and CPE a constant phase element (see Figure 4-3). The selection of this circuit was a compromise between a reasonable fitting of the experimental values and a minimum of components in the equivalent circuit. And the impedance of CPE is expressed by Eq. 3-10 in Chapter 3, as follows [185]:

$$\boldsymbol{Z_{CPE} = 1 / [T (j\omega)^{\phi}]} \qquad (3\text{-}10)$$

where j is the imaginary number, $j^2 = -1$, ω is the angular frequency ($\omega = 2\pi f$, f being the frequency), T is a constant in F cm^{-2} $s^{\phi-1}$ and ϕ is related to the angle of rotation purely capacitive line on the complex plane plots. The value of ϕ, between 0 and 1, implies the CPE of the circuit to be pure resistor and pure capacitor, respectively.

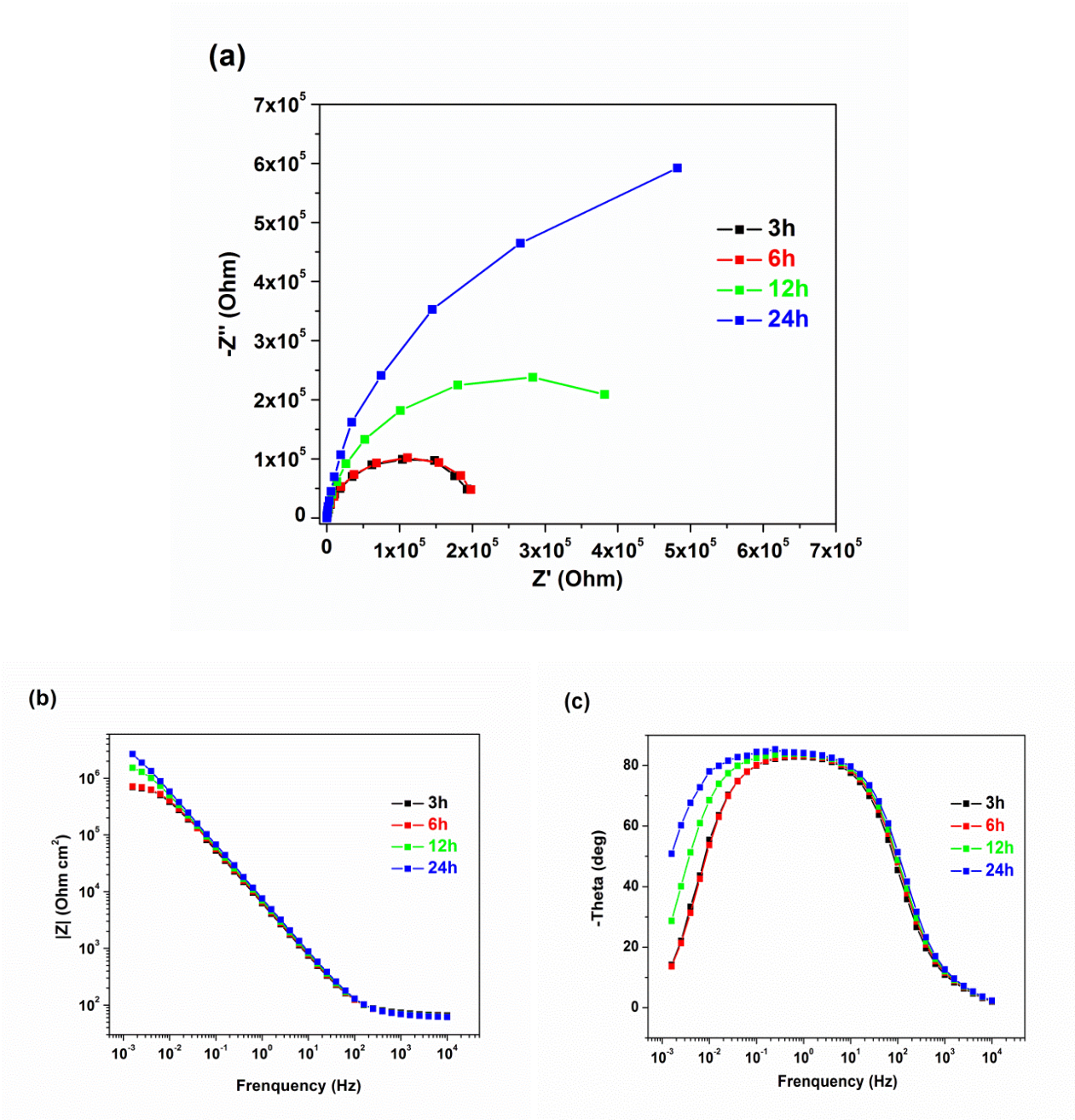

Figure 4-2 Nyquist plots (a), Bode impedance plots (b) and Bode phase angle plots (c) for cp Ti in the PBS solution measured at immersion time of 3 h (black square), 6 h (red square), 12 h (green square) and 24 h (blue square).

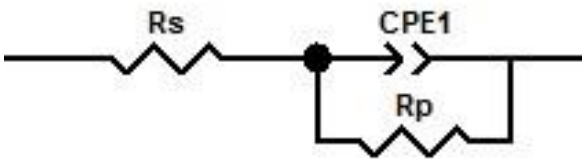

Figure 4-3 Equivalent circuit with one time constant for cp Ti in the PBS solution.

The calculated equivalent circuit elements are shown in Table 4-1. The specific polarization resistance (value per unit of area), r_p, is calculated on the basis of Eq. 3-20. The values of ϕ close to 1 at different immersion time show a near capacitive response for cp Ti in the PBS solution. This phenomenon is indicative of a typical thin passive oxide film on the surface of cp Ti [8]. The r_p value of cp Ti at immersion time of 3 h is $7.69 \times 10^5\ \Omega\ cm^2$, which is higher than $10^5\ \Omega\ cm^2$ confirming the presence of a passive surface [181, 183]. And its increment with immersion time from 3 h to 24 h reveals that the barrier property of thin passive film becomes stronger and stronger. It should be noticed that no obvious r_p value change is found at immersion time from 3 h to 6 h, but it increases quickly after a longer immersion period, such as 12 h ($r_p = 1.86 \times 10^6\ \Omega\ cm^2$) and 24 h ($r_p = 4.70 \times 10^6\ \Omega\ cm^2$) in the PBS solution, where the r_p values are about 2.5 times and 6 times of that measured at immersion time of 3 h.

Table 4-1 Parameters of the equivalent circuit for cp Ti.

A_0 (cm^2)	Time (h)	R_s (Ohm)	T ($\mu F \cdot cm^{-2} \cdot s^{\phi-1}$)	ϕ	R_p (Ohm)	r_p (Ohm·cm^2)
3.51	3	20.1	28.2	0.93	2.19×10^5	7.69×10^5
	6	19.2	27.0	0.93	2.23×10^5	7.83×10^5
	12	19.0	25.2	0.94	5.30×10^5	1.86×10^6
	24	18.7	23.0	0.94	1.34×10^6	4.70×10^6

Potentiodynamic polarization curves of cp Ti in the PBS solution were measured from -1 V to 3V vs. Ag/AgCl at a scan rate of 1 mV/s after immersion for 3 h and 24 h, respectively. The results are plotted in Figure 4-4. For the metals and alloys, which can spontaneously form a passive film on the surface, the obtained potentiodynamic polarization curve is different from that of schematic anodic polarization curve, as shown in Figure 3-5 in Chapter 3. No active region occurs for both measurements, due to the excellent barrier property of cp Ti in the PBS solution. In this case, four domains [161] obtained from potentiodynamic polarization curves for cp Ti are defined as: (I) cathodic domain; (II) prepassive domain; (III) passive domain and (IV) transpassive domain. From Figure 4-4, it is obviously found that immersion time has an important influence on the comportment of prepassive domain. The end potential for prepassive domain of cp Ti extends in the noble direction, approximately from 0.25 V vs. Ag/AgCl after immersion for 3 h to 0.45 V vs. Ag/AgCl after immersion for 24 h in the PBS solution. Meanwhile, the corresponding current density in the anodic branch after immersion for 24 h, as 0.1 V vs. Ag/AgCl for instance, decreases about one order of magnitude when comparing with that of cp Ti after immersion for 3 h. It is consistent with the continuous increment of E_{oc} for cp Ti within 24 h (still in its prepassive domain) in Figure 4-1 and the larger r_p value measured at immersion time of 24 h in Figure 4-2. In the passive domain, the current density keeps the same for both potentiodynamic polarization curves, revealing that the

passive current of cp Ti is not affected by immersion time in the PBS solution. At higher potentials (> 2.8 V vs. Ag/AgCl), current density begins to increase and the transpassivation is induced owing to the dissolution of titanium oxide film in such a high potential range. Under static condition, all experimental results measured by these three mentioned electrochemical methods, demonstrate the excellent corrosion resistant capability of cp Ti in the PBS solution.

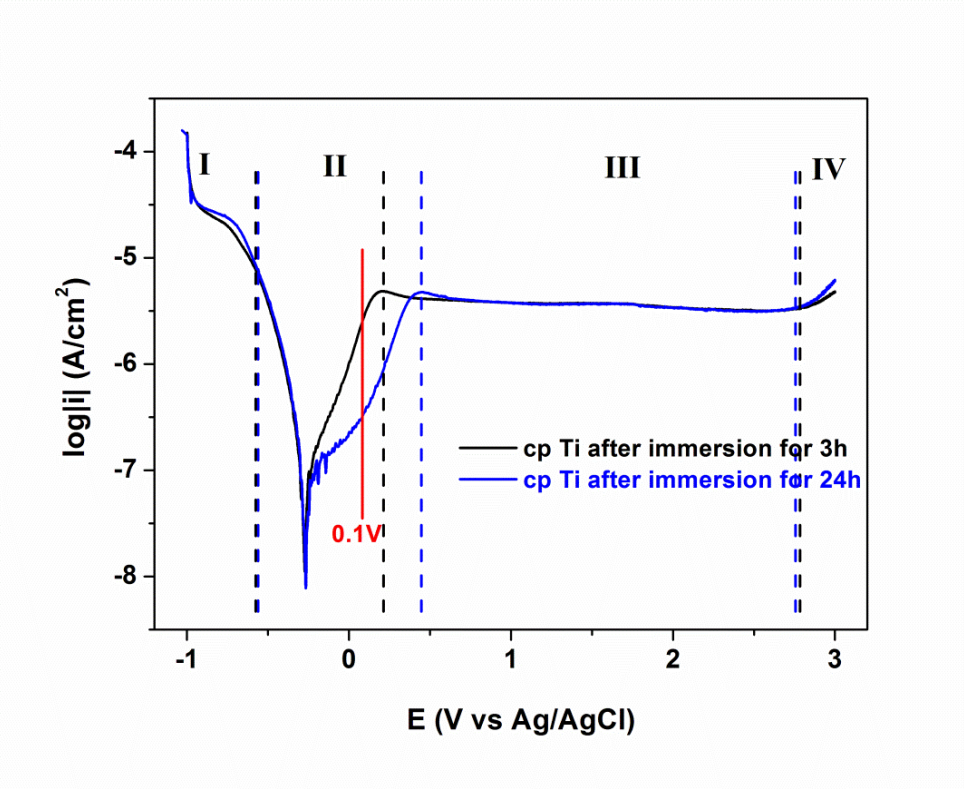

Figure 4-4 Potentiodynamic polarization curves of cp Ti from -1 V to 3 V vs. Ag/AgCl at a scan rate of 1 mV/s after immersion for 3 h and 24 h in the PBS solution.

4.4 Tribocorrosion behavior of cp Ti

As illustrated in Chapter 3, the tribocorrosion behavior of cp Ti is investigated under the guidance of the tribocorrosion protocol for cp Ti. The influences of loading force, $F_{n,}$ and latency time, t_{lat}, are studied under continuous unidirectional sliding tests and intermittent unidirectional sliding tests, respectively. More details can be seen in Section 3.5. Under mechanical unloaded condition, the surface state of cp Ti becomes passive quickly (t_{react} = 6000 s, as illustrated in Figure 3-16, where the surface state of cp Ti is depassivated at -1.6 V vs. Ag/AgCl for 5 min previous to OCP measurement) in the PBS solution. In order to get a well-organized procedure for tribocorrosion test, the whole measurement is divided into three parts: (1) before unidirectional sliding (OCP evolution with immersion time of 3 h and EIS measurement at immersion time of 3 h under mechanical unloaded condition); (2) during continuous unidirectional sliding (OCP evolution in 40 min and after that EIS measurement) or during intermittent unidirectional sliding (OCP evolution in

the whole mechanical loaded period); (3) after unidirectional sliding (OCP evolution in 3 h and after that EIS measurement under mechanical unloaded condition as that before sliding).

4.4.1 Electrochemical behavior of cp Ti before unidirectional sliding test

Figure 4-5 shows the OCP evolution curves of three different cp Ti specimens before unidirectional sliding. The results show that in spite of the different start potentials and end potentials, the evolution tendencies for these three curves are similar to raise in the noble direction. The difference might result from the influence of test conditions, such as the room temperature, the amount of dissolved oxygen and the passive state of cp Ti surface.

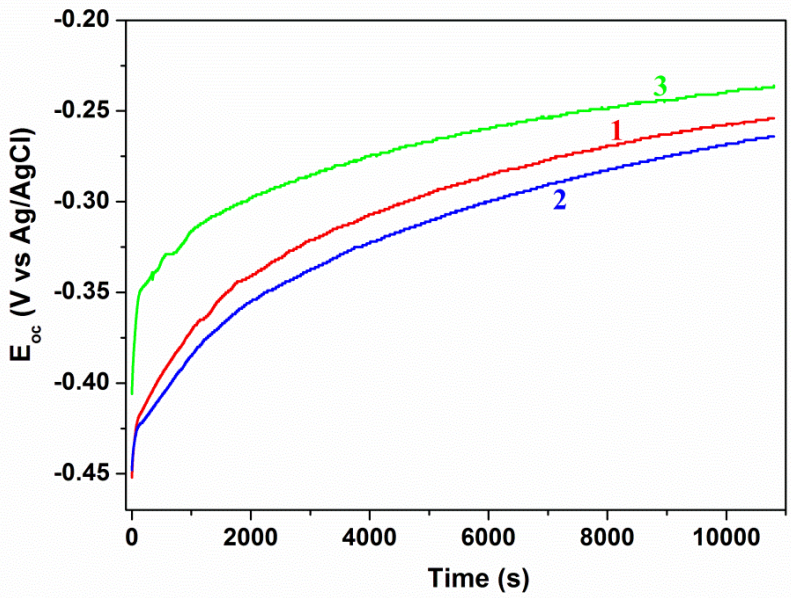

Figure 4-5 Comparison of OCP evolution curves before unidirectional sliding tests, measured with three different cp Ti specimens in the PBS solution.

Here, the red line (curve 1) is chosen as the representative and discussed as following: The electrochemical reactivity of cp Ti under mechanical unloaded condition was monitored by OCP evolution versus time upon immersion of a fresh specimen in the PBS solution for 3 h. At the beginning of immersion, E_{oc} is around -0.45 V vs. Ag/AgCl and increases to -0.26 V vs. Ag/AgCl at the end of OCP measurement (where the variation of potential, $|\Delta E_{oc}|$, is less than 60 mV/h). It indicates a quasi steady-state of sample surface reaching after immersion in the PBS solution for 3 h. The passive state can be further proved by the measurement of the polarization resistance, R_p, at the interface between cp Ti and the PBS solution. EIS spectra of three different cp Ti specimens are plotted in Figure 4-6. The corresponding equivalent circuit is still as presented in Figure 4-3. Under

the guidance of the tribocorrosion protocol for cp Ti in Chapter 3, the calculated equivalent circuit elements on the basis of Eq. 3-20 and Eq. 3-21 are then summarized in Table 4-2.

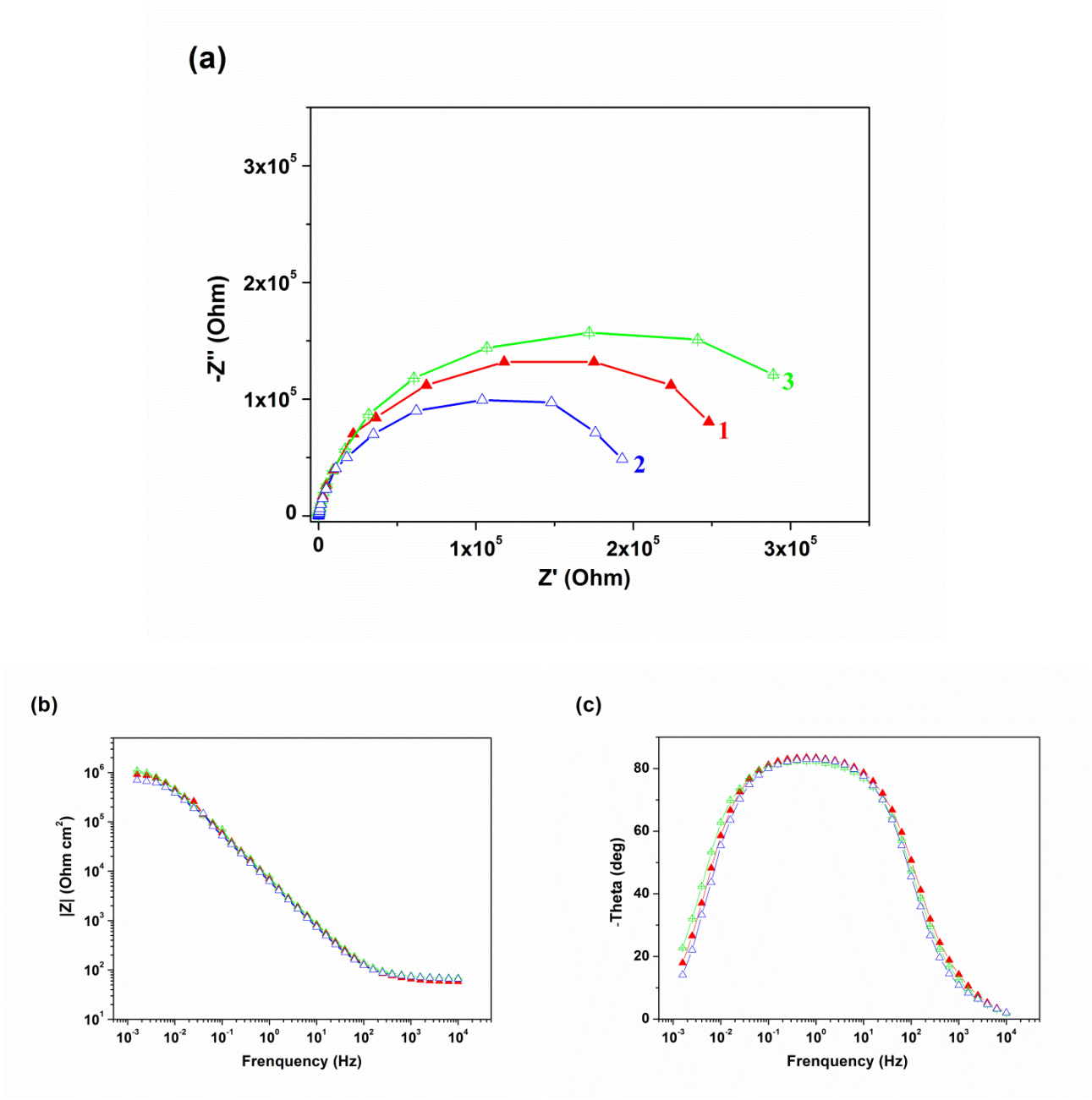

Figure 4-6 Comparison of Nyquist plots (a), Bode impedance plots (b) and Bode phase angle plots (c) for cp Ti before unidirectional sliding tests, measured with three different specimens at immersion time of 3 h before sliding in the PBS solution.

Table 4-2 Specific polarization resistance and corrosion current density of cp Ti immersed in the PBS solution at stable OCP under mechanically unloaded conditions.

Sample	A_0 (cm^2)	R_p (Ohm)	r_p (Ohm·cm^2)	i_p ($A·cm^{-2}$)
1	3.51	2.19×10^5	7.69×10^5	3.38×10^{-8}
2	3.50	2.96×10^5	1.04×10^6	2.51×10^{-8}
3	3.42	3.62×10^5	1.24×10^6	2.10×10^{-8}
Average (Mean ± Sd)	——	——	$1.01 \times 10^6 \pm 2.34 \times 10^5$	$2.67 \times 10^{-8} \pm 6.53 \times 10^{-9}$

The average values of the specific polarization resistance, $r_{p,}$ and the corresponding corrosion current density, $i_{p,}$ in Table 4-2 demonstrate that a stable passive surface state is reached on cp Ti in the absence of mechanical loading. The surface of cp Ti can be considered as covered by a passive TiO_2 film and i_p is linked to the dissolution of Ti through this passive film in the PBS solution.

4.4.2 Tribocorrosion behavior of cp Ti during and after continuous unidirectional sliding test

Tribocorrosion behavior of cp Ti under continuous unidirectional sliding will be discussed in this section. Electrochemical measurements such as OCP and EIS are imposed to characterize the reactivity and polarization resistance of cp Ti during sliding at different normal forces of 1 N, 2 N, 5 N and 10 N. When sliding test stops, OCP evolution and EIS spectra are also measured to investigate the repassivation ability of cp Ti under mechanical unloaded condition.

Figure 4-7 shows the representative OCP evolutions of cp Ti during continuous unidirectional sliding tests. Measurements were performed at different loading forces, F_n of 1 N, 2 N, 5 N and 10 N with a fixed rotation rate of 100 rpm (t_{lat1} = t_{rot} = 0.6 s). The results indicate that although the potential at the start of sliding, E_{max}, is different from each test, the potential drop-down, $\Delta E = |E_{max} - E_{min}|$ (E_{min} represents the minimum potential during each continuous unidirectional sliding test), during continuous unidirectional sliding tests increases versus F_n from 1 N to 5 N and then keeps similar from 5 N to 10 N, as seen in Figure 4-8. At the loading force of 1 N or 2 N, OCP evolution during unidirectional sliding is stable in the test period of 40 min. But at the loading force of 5 N or 10 N, the variation of OCP during sliding becomes larger after ~1500 s at F_n of 5 N and after ~1200 s at F_n of 10 N.

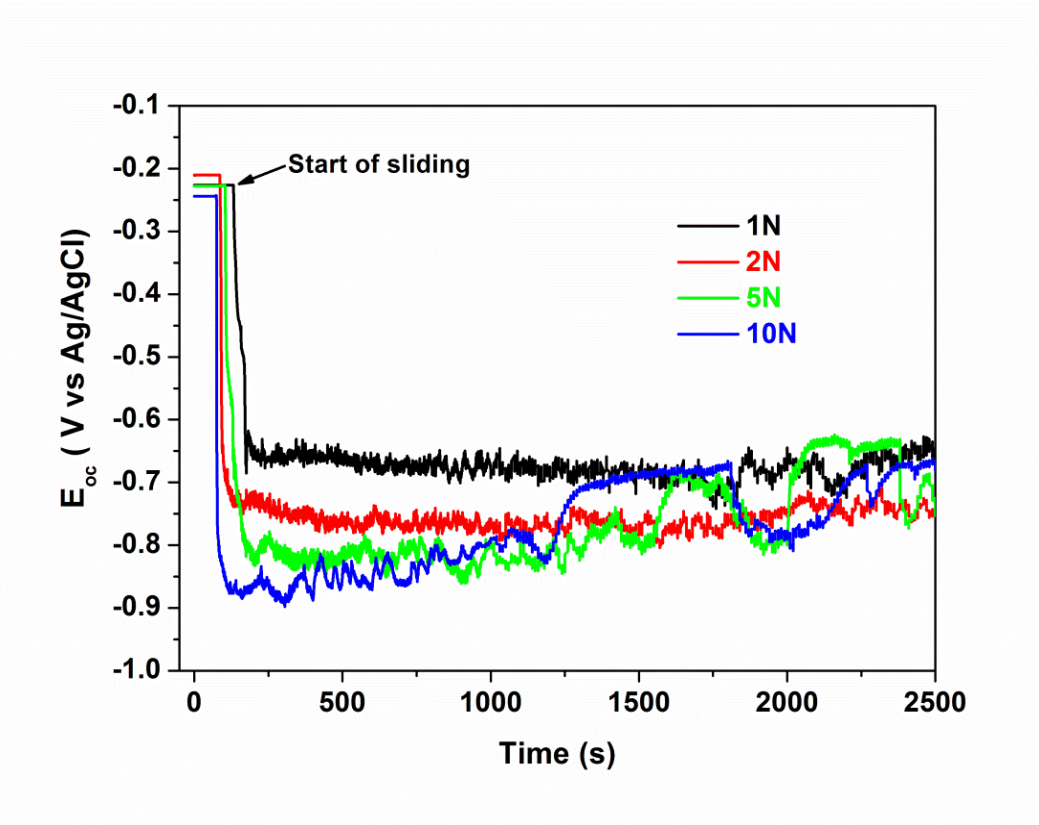

Figure 4-7 OCP evolution of cp Ti during continuous unidirectional sliding tests performed at different F_n of 1 N, 2 N, 5 N and 10 N.

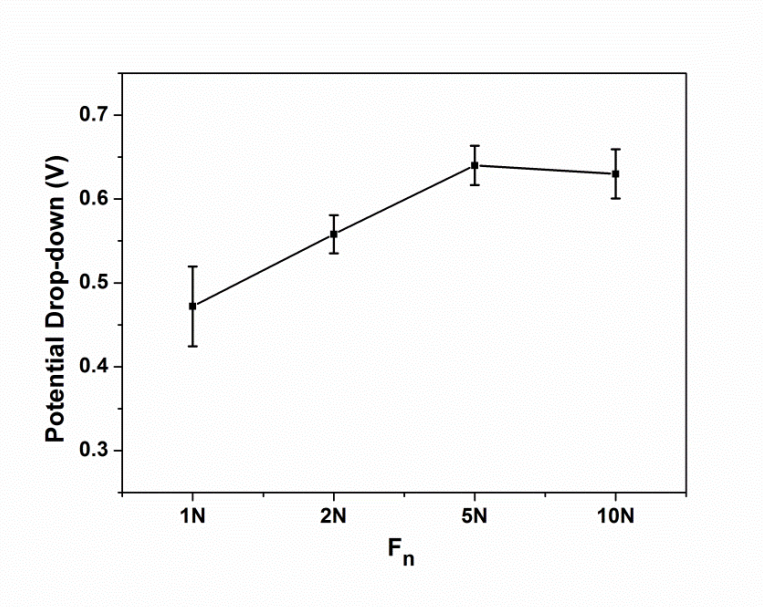

Figure 4-8 Potential drop-down during continuous unidirectional sliding tests versus F_n.

EIS measurements were carried out during continuous unidirectional sliding tests due to the more or less constant E_{oc} value. Figure 4-9 shows the representative EIS spectra of cp Ti during continuous unidirectional sliding test at F_n of 1 N and the fitting results with the corresponding equivalent circuit (inset of Figure 4-9a). In this equivalent, a polarization resistance during sliding, R_{ps}, was obtained instead of the initial polarization resistance, R_p, before sliding. More details have been explained in Section 3.5.2. It should be noticed that R_{ps} can be considered as the combination of two polarization resistances in parallel, namely R_{act} related to the active area A_{act} and R_p related to the surrounding unworn and passive area, $(A_0 - A_{act})$, where A_{act} is equal to A_{tr} [92, 183], as shown in Figure 3-18.

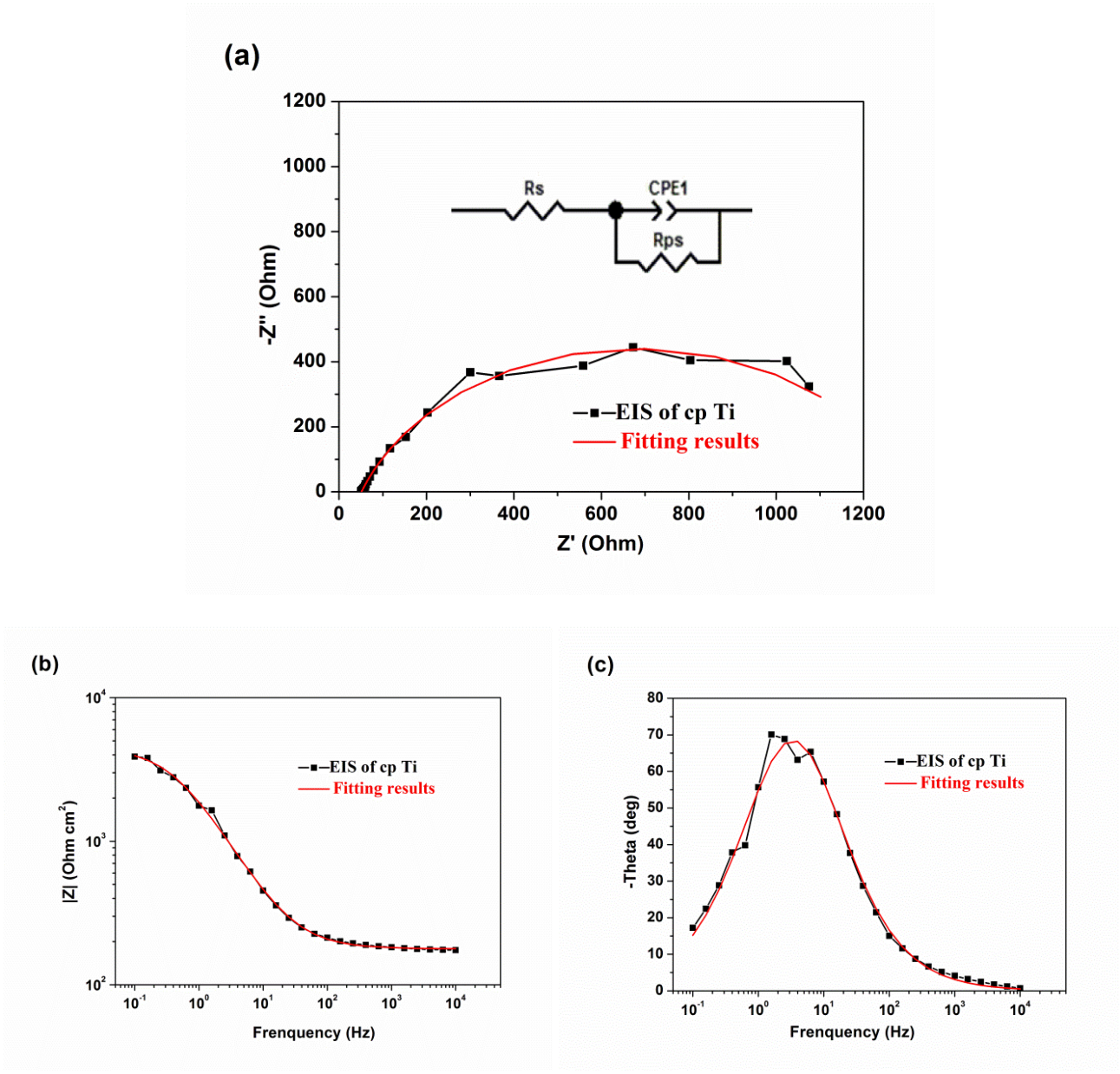

Figure 4-9 Representative Nyquist plot (a), Bode impedance plot (b) and Bode phase angle plot (c) for cp Ti measured during continuous unidirectional sliding test at F_n of 1N in the PBS solution and the fitting results (red line) with the corresponding equivalent circuit as the inset of Nyquist plot.

At F_n of 1 N, three measurements were carried out with different cp Ti specimens. The measured sliding track area, A_{tr}, calculated specific polarization resistance, r_{act}, and corrosion current density, i_{act}, related to the active area of cp Ti on the basis of equations from Eq. 3-26 to Eq. 3-30 are summarized in Table 4-3.

Table 4-3 The sliding track area, specific polarization resistance and corrosion current density of cp Ti under continuous unidirectional sliding test at F_n of 1N.

Sample	A_{tr} (cm^2)	R_{act} (Ohm)	r_{act} (Ohm·cm^2)	i_{act} (A·cm^{-2})
1	0.69	2100	1450	1.79×10^{-5}
2	0.75	1500	1120	2.34×10^{-5}
3	0.64	1400	900	2.88×10^{-5}
Average (Mean ± Sd)	0.69 ± 0.05	1700 ± 400	1160 ± 280	$2.34 \times 10^{-5} \pm 5.46 \times 10^{-6}$

The average values of r_{act} (1160 Ω cm^2) and i_{act} (2.34×10^{-5} A cm^{-2}) in Table 4-3 demonstrate that an active surface state occurs on cp Ti under mechanical loaded condition. The formed passive film is destroyed by the continuously mechanical sliding of ZrO_2 pin on cp Ti surface and meanwhile, i_{act} is linked to the dissolution of Ti substrate through this active area in the PBS solution.

When continuous unidirectional sliding test ends, the E_{oc} of cp Ti increases quickly due to the repassivation of thin oxide barrier film on the sliding track, as seen in Figure 4-10. After continuous unidirectional sliding at F_n of 1 N, the state of cp Ti surface on the sliding track returns back to passive under mechanical unloaded condition, resulting in a potential value of -0.2 V vs. Ag/AgCl at immersion time of 3 h, which is even higher than the value of -0.22 V vs. Ag/AgCl at the beginning of sliding in Figure 4-7.

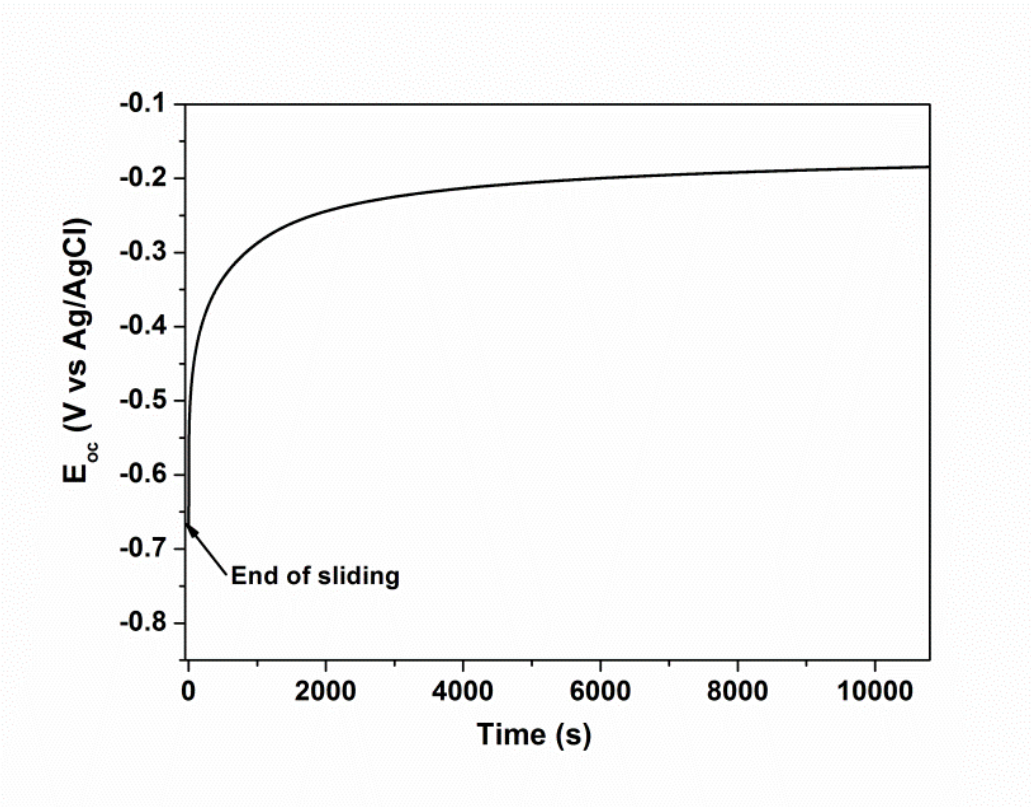

Figure 4-10 OCP evolution of cp Ti after continuous unidirectional sliding test at F_n of 1 N.

Another evidence to support this repassivation phenomenon is the specific polarization resistance, $r_{p'}$, measured when the re-stabilization of E_{oc} reaches after 3 h immersion in the PBS solution from the end of continuous unidirectional sliding at F_n of 1 N (see Figure 4-11). The measured $r_{p'}$ value of near 10^6 Ω cm^2 was obtained. This order of magnitude of $r_{p'}$ ensures the repassivative surface of cp Ti after continuous unidirectional sliding test.

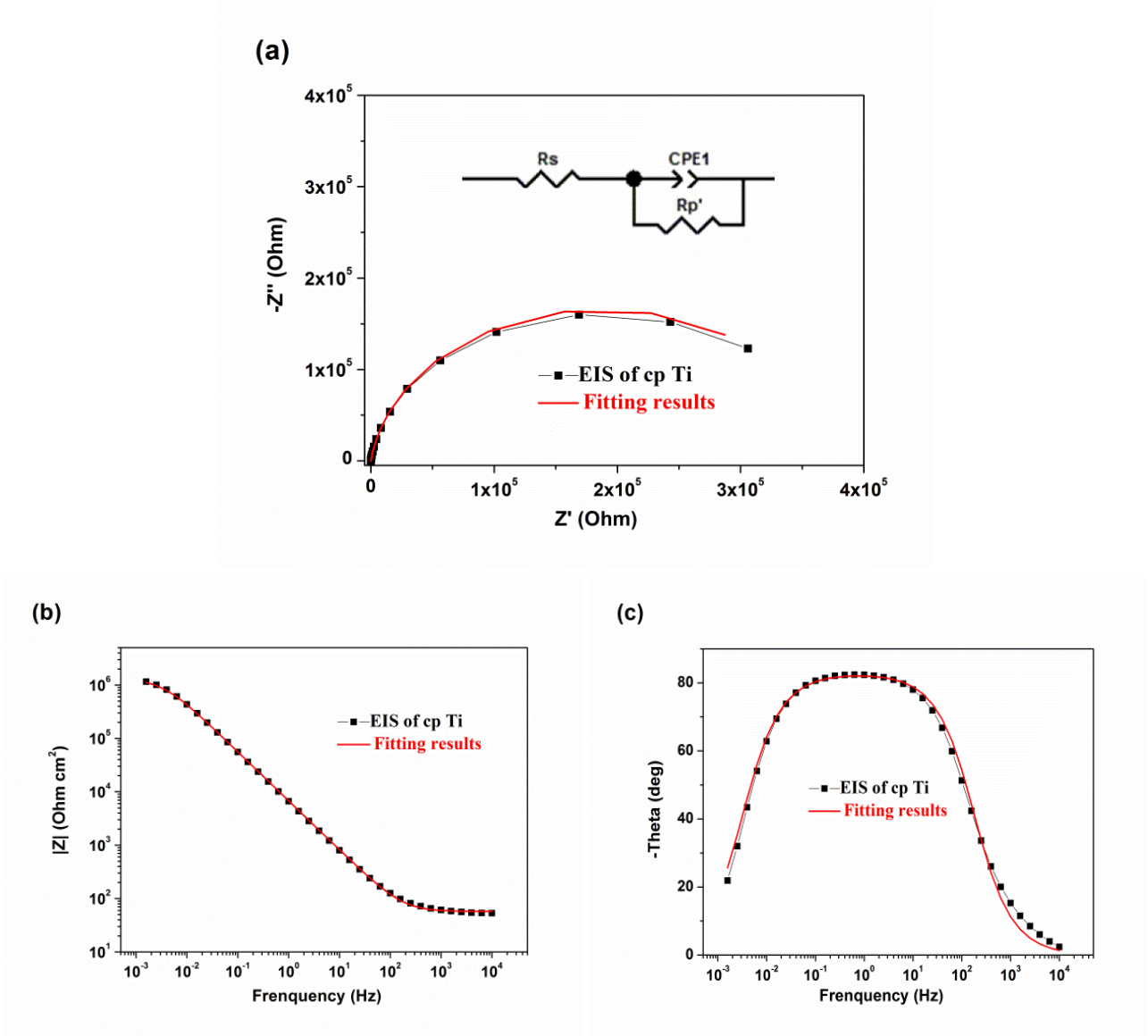

Figure 4-11 Representative Nyquist plot (a), Bode impedance plot (b) and Bode phase angle plot (c) for cp Ti measured after 3 h immersion in the PBS solution from the end of continuous unidirectional sliding at F_n of 1 N and the fitting results (red line) with the corresponding equivalent circuit as the inset of (a).

4.4.3 Characterization and interpretation of the wear track on cp Ti after continuous unidirectional sliding test

Surface morphologies of cp Ti after continuous unidirectional sliding at different F_n from 1 N to 10 N were obtained by SEM, as shown in Figure 4-12. The average track widths, e, are 2.21 mm at F_n of 1 N, 2.67 mm at F_n of 2 N, 2.78 mm at F_n of 5 N and 3.09 mm at F_n of 10 N, respectively. The regular pattern of grooves and a large number of attached debris inside each of the four tracks in Figure 4-12a-d indicate that both abrasive wear and adhesive wear took place interactively during continuous unidirectional sliding tests on cp Ti. The chemical compositions inside (site 1) and outside

(site 2) the track area obtained at F_n of 5 N were analyzed by EDS, and the results are presented in Figure 4-12e and 4-12f.

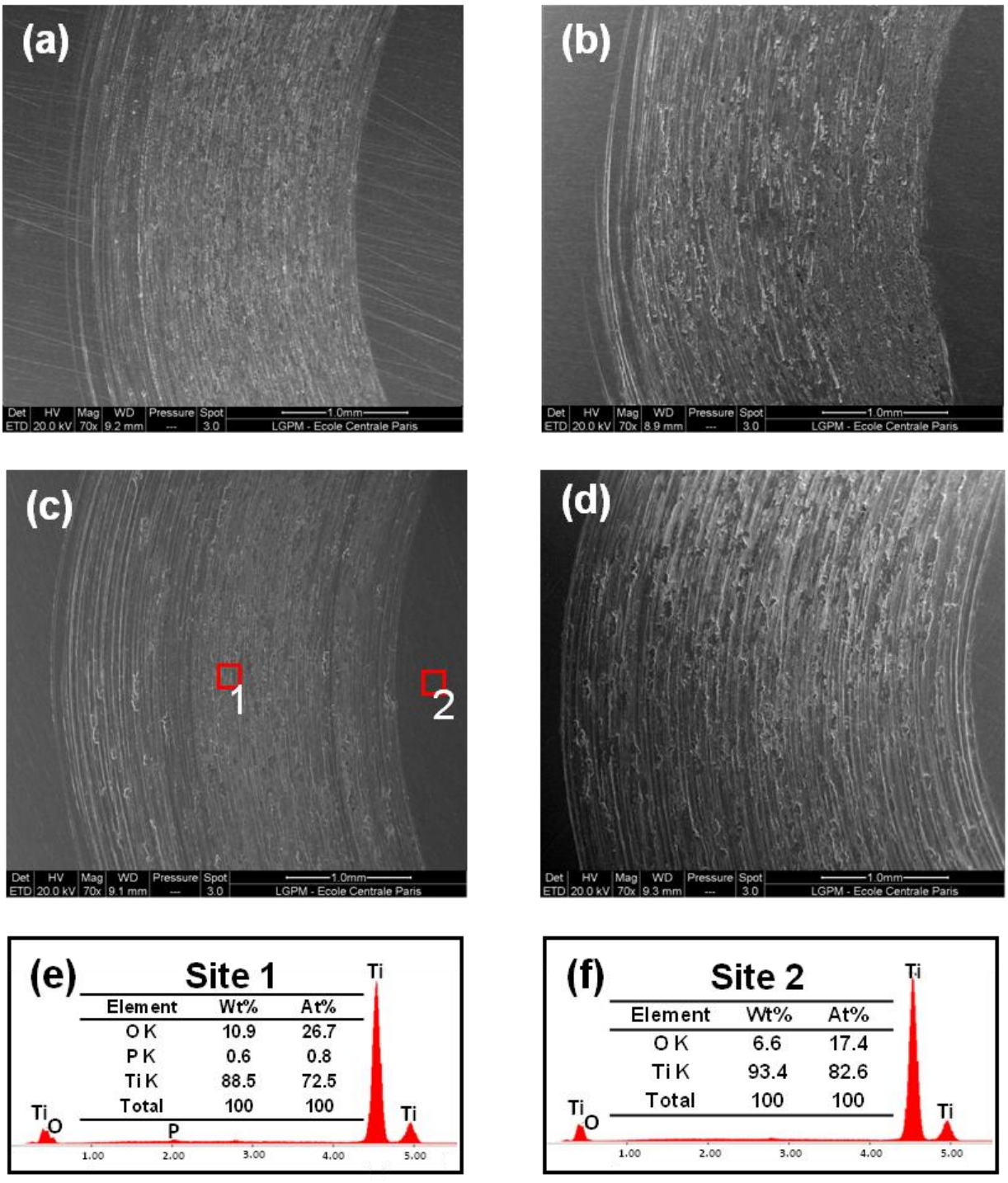

Figure 4-12 SEM of the tracks after continuous unidirectional sliding in the PBS solution at different F_n of 1 N (a), 2 N (b), 5 N (c) and 10 N (d); EDS analysis of the chemical composition inside (site 1, e) and outside (site 2, f) the track area of (c).

Chemical composition analysis of site 1 shows the appearance of small amount of phosphorus (P, 0.6 wt%, originally existing in the PBS solution) inside the track area. Combined with the high content of oxygen (O, 10.9 wt%), corrosion is obviously accelerated in the presence of mechanical wear. Due to the limitations of EDS analysis, it is impossible to identify the forms and valences of Ti, so the corrosion products inside the track are indistinctly considered to consist of titanium oxide, titanium phosphate or trace amount of cladding potassium/sodium phosphate. Chemical composition of site 2 (O, 6.6 wt% and Ti, 93.4 wt%) reveals titanium oxide formed spontaneously when cp Ti was immersed in the PBS solution. This passive film inhibits the corrosive attacks and provides high corrosion resistance under mechanically unloaded conditions.

Figure 4-13 shows the profile of the track and the corresponding microhardness outside/inside the track area after tribocorrosion test at F_n of 1 N. Comparing with the initial microhardness before immersion (176 ± 2 $HV_{0.2}$), there is no change for the value outside the track area (175 ± 7 $HV_{0.2}$). But for the microhardness inside the track area, it increases slightly to 233 $HV_{0.2}$ due to the increase of the roughness in the wear track and the existence of corrosion products like titanium oxide, which is harder than the cp Ti substrate.

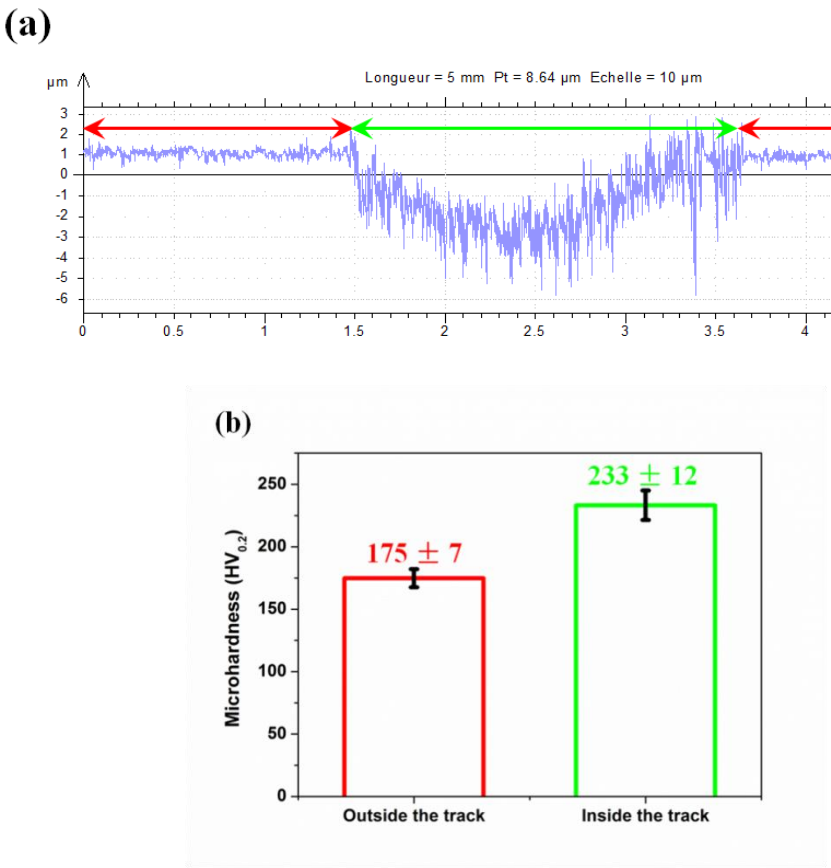

Figure 4-13 Profile of the track (a) and mircohardness (b) of cp Ti outside (red line), inside (green line) the track area after tribocorrosion test at F_n of 1 N.

Under the guidance of tribocorrosion protocol in Chapter 3, the experimental outcomes and calculated two tribocorrosion components, obtained on cp Ti under continuous mechanical loaded condition at different F_n of 1 N, 2 N, 5 N and 10 N, are summarized in Table 4-4. The wear results versus normal force are plotted in Figure 4-14. All wear values are expressed in volumetric material loss.

Table 4-4 Experimental outcomes and calculated two tribocorrosion components obtained on cp Ti under continuous mechanical loding condition at different F_n from 1 N to 10 N in the PBS solution.

F_n (N)	A_{tr} (cm^2)	W_{tr} (cm^3)	W^c_{act} (cm^3)	W^m_{act} (cm^3)
1	0.69	1.72×10^{-4}	2.66×10^{-6}	1.69×10^{-4}
2	0.84	2.45×10^{-4}	4.31×10^{-6}	2.41×10^{-4}
5	0.87	3.82×10^{-4}	4.47×10^{-6}	3.78×10^{-4}
10	0.97	4.14×10^{-4}	5.17×10^{-6}	4.09×10^{-4}

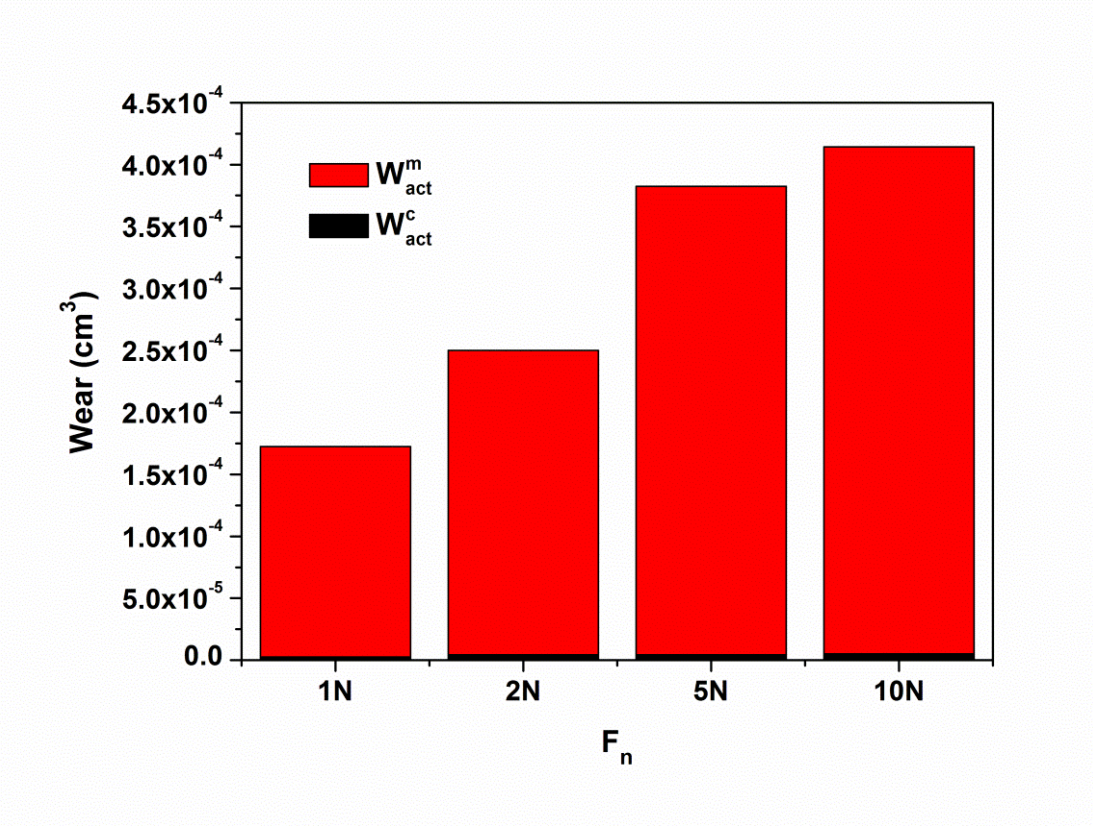

Figure 4-14 Contribution of two different tribocorrosion components to the total volumetric material loss inside the sliding track of cp Ti under continuous mechanical loaded condition at different F_n from 1 N to 10 N in the PBS solution.

In accordance with the track width, the calculated track area enlarges with the increase of F_n from 1 N to 10 N. The increases of both the material loss by corrosion of active material, W^c_{act}, and the material loss due to mechanical wear of active material, W^m_{act}, are also observed when the loading force increase, which can be mainly related to the increase of active area in the sliding track. For all results performed at different F_n, W^m_{act} keeps its dominant contribution to the total volumetric material loss inside the sliding track, revealing the poor wear resistant property of cp Ti.

4.4.4 Tribocorrosion behavior of cp Ti during intermittent unidirectional sliding test

From Figure 4-10, the repassivation ability of cp Ti after continuous unidirectional sliding occurs quickly in the PBS solution. In order to understand the effect of latency time, t_{lat}, on the depassivation/repassivation behavior of passive films on cp Ti, intermittent unidirectional sliding tests are imposed. Such intermittent tests consist of sequences of one sliding cycle (duration of t_{rot} = 0.6 s) followed by a pause for a given time, t_{off}. It can be used to analyze the periodic removal and re-growth of surface films, reflected by a cyclic evolution of E_{oc}. The immobile time, t_{off}, is imposed immediately after each sliding cycle to allow the reaction of bare material in the active area with surrounding electrolyte, resulting in partial or full re-growth of passive film. More details can be seen in Chapter 3 (Section 3.5.3 and Section 3.5.4).

In the case of intermittent unidirectional sliding tests, the re-growth of a surface film in-between two successive contact events cannot be ignored as that in the case of continuous unidirectional sliding tests. The immobile time, t_{off} was selected as t_{react}/1000 and t_{react}/500 in this section. Correspondently, the latency time, $t_{lat} = t_{rot} + t_{off}$ was set as t_{lat2} = 6.6 s and t_{lat3} = 12.6 s.

The experimental outcomes of these two intermittent unidirectional sliding tests are compared to the data from continuous unidirectional sliding test where t_{off} is 0 s (as t_{lat1} = 0.6 s). All three tests were performed on cp Ti at F_n of 5 N in the PBS solution. The evolution of E_{oc} during continuous and intermittent sliding tests is shown in Figure 4-15, demonstrating the effect of latency time, t_{lat}.

During the studied sliding period between 1400 s and 1500 s, in the case of continuous unidirectional sliding tests with t_{lat1} of 0.6 s, the value of E_{oc} is stable around – 0.8 V vs. Ag/AgCl. In the case of intermittent unidirectional sliding tests with t_{lat2} of 6.6 s, E_{oc} drops during the on-period, and then rises during the off-period with a fluctuation between – 0.73 V vs. Ag/AgCl and – 0.53 V vs. Ag/AgCl. A similar trend is noticed at t_{lat3} of 12.6 s with a larger fluctuation between – 0.71 V vs. Ag/AgCl and – 0.46 V vs. Ag/AgCl. These fluctuations of E_{oc} indicate the capacity of cp Ti to reform its surface passive film inside the sliding track in-between successive sliding contacts when immersed in the PBS solution. This self-healing property increases with prolonging t_{lat} from 6.6 s to 12.6 s by observing the higher E'_{min} (the minimum value of E_{oc} during intermittent unidirectional sliding) for the blue line measured at t_{lat3} = 12.6 s.

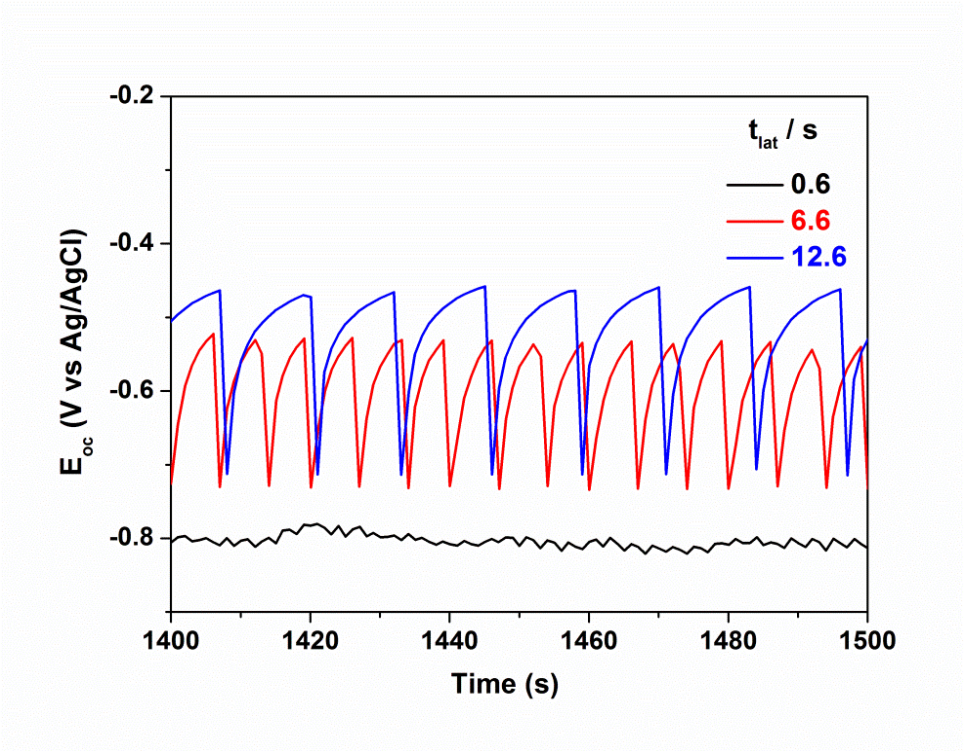

Figure 4-15 Variation of OCP during continuous (t_{lat1} = 0.6 s, black line) and intermittent (t_{lat2} = 6.6 s, red line and t_{lat3} = 12.6 s, blue line) unidirectional sliding tests of cp Ti performed at F_n of 5 N.

The increase of E'_{max} (the maximum value of E_{oc} during intermittent unidirectional sliding) with prolonging t_{lat} from 6.6 s to 12.6 s indicates that the restoration of the passive surface film inside the sliding track during off-time period is just partial, since the E'_{max} (even at t_{lat} = 12.6 s) is still below the stabilized E_{oc} (about – 0.23 V vs. Ag/AgCl) recorded before sliding happened. The full restoration of passive film inside the sliding track needs more time than one hour, as previously investigated E_{oc} evolution after sliding test in Figure 4-10.

The fact that both E'_{min} values for intermittent unidirectional sliding tests are higher than the value of E_{oc} during continuous unidirectional sliding illustrates the significant restoration ability of the passive film inside the sliding track during the off-time period. The repassive film is then partially destroyed during the intermittent unidirectional sliding on-period. The difference between E'_{min} and E'_{max} for t_{lat3} = 12.6 s is 0.25 V and for t_{lat2} = 6.6 s is 0.2 V, respectively. This comparison reveals that surface passive film formation happens faster at the beginning of the sliding off-period. With time going on, this self-healing ability decreases gradually until a full restoration of passive film inside the sliding track. Similar evolutions of E'_{min} and E'_{max} with off-time augmentation were also found in the case of stainless steel [183] and $Al_{71}Cu_{10}Fe_9Cr_{10}$ complex metallic alloy [184].

4.4.5 Results interpretation of corrosion and mechanical wear on cp Ti after intermittent unidirectional sliding test

Under the guidance of tribocorrosion protocol in Chapter 3, the experimental outcomes and calculated tribocorrosion components, obtained on cp Ti for continuous unidirectional sliding and intermittent unidirectional sliding tests at F_n of 5 N in the PBS solution, are summarized in Table 4-5. The wear results versus latency time are plotted in Figure 4-16. As previous results, all wear values are expressed in volumetric material loss.

Table 4-5 Experimental outcomes and calculated tribocorrosion components obtained on cp Ti for continuous unidirectional sliding (t_{lat1} = 0.6 s) and intermittent unidirectional sliding (t_{lat2} = 6.6 s and t_{lat3} = 12.6 s) tests performed at F_n of 5 N in the PBS solution.

t_{lat} (s)	A_{tr} (cm^2)	W_{tr} (cm^3)	W^c_{act} (cm^3)	W^m_{act} (cm^3)	W^c_{repass} (cm^3)	W^m_{repass} (cm^3)
0.6	0.87	3.82×10^{-4}	4.47×10^{-6}	3.78×10^{-4}	--	--
6.6	0.91	4.36×10^{-4}	9.59×10^{-6}	3.95×10^{-4}	4.48×10^{-11}	3.08×10^{-5}
12.6	0.94	5.41×10^{-4}	1.19×10^{-5}	4.04×10^{-4}	1.68×10^{-10}	1.25×10^{-4}

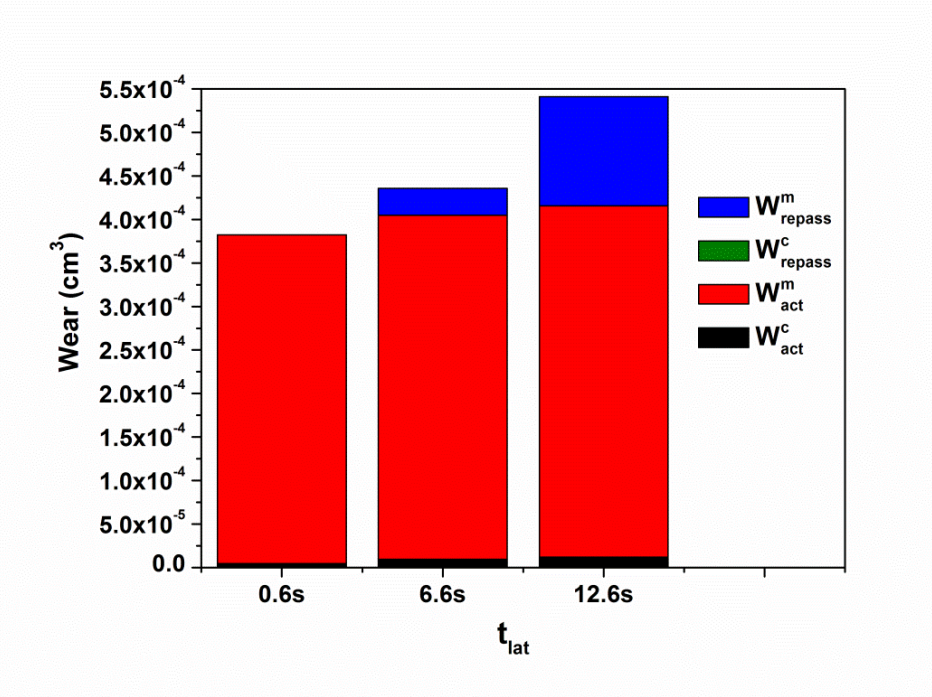

Figure 4-16 Contribution of different tribocorrosion components to the total volumetric material loss inside the sliding track of cp Ti for continuous unidirectional sliding (t_{lat1} = 0.6 s) and intermittent unidirectional sliding (t_{lat2} = 6.6 s and t_{lat3} = 12.6 s) tests performed at F_n of 5 N in the PBS solution.

At F_n of 5 N, the track area and all calculated tribocorrosion components obtained on cp Ti enlarge with the increase of latency time. In order to well identify the interpretation of the outcomes of tribocorrosion tests under intermittent sliding condition, the specific material loss components inside the sliding track, w^j_i, are calculated per unit area and per circle, based on the Eq. 3-42. More detailed assessment of the tribocorrosion of cp Ti is possible based on the ratio K_c and the effect of the formation of the passive film on the mechanical wear can be also evaluated based on the ratio K_m, as explained in Section 3.5.4.

From the data in Table 4-5, the specific material loss components, the ratios K_c and K_m are calculated and summarized in Table 4-6.

Table 4-6 Calculated specific wear components and K_c and K_m ratios from Table 5.

t_{lat} (s)	A_{act} (cm^2)	A_{repass} (cm^2)	w^c_{act} (cm/cyc.)	w^m_{act} (cm/cyc.)	w^c_{repass} (cm/cyc.)	w^m_{repass} (cm/cyc.)	K_c	K_m
0.6	0.873	--	5.12×10^{-10}	4.33×10^{-8}	--	--	0.0118	--
6.6	0.913	0.001	1.05×10^{-9}	4.33×10^{-8}	4.48×10^{-12}	3.08×10^{-6}	0.0225	0.0141
12.6	0.933	0.002	1.28×10^{-9}	4.33×10^{-8}	8.55×10^{-12}	6.27×10^{-6}	0.0225	0.0069

The increase of w^c_{act} with t_{lat} is linked to the increase of the corrosive wear volume on the active area with time. As a result of assumptions in Section 3.5.4, the value of w^m_{act} is constant and shows t_{lat} has no effect on the mechanical wear resistance of the active material. The value of w^c_{repass} is proportional to t_{lat}, revealing that the increase of the latency time increases the corrosion of repassivated material inside the wear track. Finally, the increase in the value of w^m_{repass} with t_{lat} might be related to the decrease in the mechanical wear resistance of the passive film, which can further result in the abrasive wear of debris to remove more material inside the track.

The value of K_c obtained for continuous unidirectional sliding (t_{lat1} = 0.6 s) test indicates that the contribution of mechanical material loss is dominant in total material loss of cp Ti at F_n of 5 N in the PBS solution. Although K_c increases from 0.0118 to 0.0225 with t_{lat2} = 6.6 s and t_{lat2} = 12.6 s, the contribution of corrosive material losses under intermittent mechanical loaded conditions is still smaller than that of mechanical material losses. The small value K_m (< 1) indicates that the formation of the passive film accelerates the mechanical removal of cp Ti. And the sensitivity of the passive film to mechanical material loss is higher than that of the active bare material. Due to the constant of w^m_{act}, the decrease of K_m with t_{lat} can be explained by the increase of w^m_{repass} due to the decrease in the mechanical wear resistance of the passive film.

4.5 Conclusions

The corrosion behavior of cp Ti was investigated under static condition by electrochemical measurements like OCP, EIS and potentiodynamic polarization. The OCP evolution and EIS results obtained at different immersion time in the PBS solution indicate the enhancement of passivation of cp Ti with immersion time. Moreover, immersion time has effect on the reactivity of cp Ti in its prepassive domain where OCP sites, but it doesn't change the current densities in the cathodic and passive domains in this study. These results show that the corrosion resistance of cp Ti is excellent in the absence of mechanical loading.

Continuous unidirectional sliding and intermittent unidirectional sliding tests were imposed to study the tribocorrosion behavior of cp Ti, under the guidance of the tribocorrosion protocol (as illustrated in Chapter 3). Electrochemical techniques like OCP and EIS combined with friction measurements was applied to characterize *in situ* the surface state before, during and after unidirectional sliding. OCP evolution and EIS measurement results during sliding tests show the degradation of passive film when mechanical loading started, resulting in the significant drop-down of potential and huge decrease of the specific polarization resistance.

The quantitative analysis results based on the tribocorrosion protocol indicate that the contribution of mechanical material loss is dominant in the total material loss of cp Ti for both continuous and intermittent unidirectional tests. In the case of continuous unidirectional sliding test, the materials loss increases with the increase of F_n from 1 N to 10 N. In the case of intermittent unidirectional sliding test, the extension of t_{lat} increases the material loss at F_n of 5 N. The formation of the passive film accelerates the mechanical removal of cp Ti and the sensitivity of the passive film to mechanical material loss is higher than that of the active bare material.

Chapter 5: Effect of thermal oxidation on corrosion and tribocorrosion behavior of cp Ti

5.1 Introduction

The use of cp Ti has been limited by its poor resistance to surface degradation processes under mechanical loaded condition. In this chapter, thermal oxidation method is employed to improve the wear resistance and corrosion protective property of cp Ti during continuous unidirectional sliding test. An oxide layer without any spallation is obtained at 650 ℃ for 48 h. The oxide layer consists of rutile (TiO_2) and oxygen-diffused Ti (Ti/TiO_x, x <2) as the predominant phases by the characterization of XRD. Electrochemical and friction measurements in the PBS solution indicate that the oxide layer with an enhanced surface microhardness provides distinguished barrier property to the corrosion and wear degradation of cp Ti. During continuous unidirectional sliding at F_n of 5 N, the variation of OCP is small and the value of polarization resistance obtained by EIS measurement decreases but still keeps in the order of magnitude of passive state. Optical profilometry was used to characterize the initial surface roughness and the total wear volume at the end of the sliding tests. SEM coupled with EDS was performed to analyze the initial surface morphology/chemical composition and the surface morphology/chemical composition inside and outside the track area after sliding tests. Results show that thermal oxidation is an efficient way to modify the surface of cp Ti and further to improve its corrosion and tribocorrosion resistance in biomedical application as implants.

5.2 Experimental details

The well polished and cleaned cp Ti specimens were further oxidized by using a furnace in air atmosphere at 650 ℃ for 48 h, following by a slow cooling rate to the room temperature in the furnace itself. Optical profilometry was used to measure the surface topography of samples and the average roughness value was calculated on square regions with length of 1000 μm × 1000 μm. Vickers microhardness test was performed with a test force of 200 gf and full load period of 15 s. The phase constituents of the untreated Ti and thermal oxidized Ti (TO Ti) samples were determined by XRD using a Cu K_α ($\lambda = 1.54$ Å) radiation source over a scan range from 20 °to 80 °at a scan rate of 0.02 °/s. Surface morphology and chemical composition of the oxide film were observed by SEM coupled with EDS.

Electrochemical and tribocorrosion measurements were performed at OCP in a unidirectional pin-on-disc tribometer, combined with a three-electrode cell in the PBS solution at room temperature (22 ± 1 ℃) as mentioned in Chapter 4. Under static condition, corrosion behavior of TO Ti was characterized. The evolution of OCP, E_{oc}, within 3 h was performed continuously. EIS measurements with a sinusoidal potential variation of ±10 mV to OCP at frequencies from 10 kHz down to 1.58 mHz were measured as well as the potentiodynamic polarization curves from -1 V to 3 V vs. Ag/AgCl at a scan rate of 1 mV/s under static condition at immersion time of 3 h and 24 h, respectively. Tribocorrosion experiments were performed under continuous mechanical loaded condition at F_n of 5 N, with a rotation rate of 100 rpm. The total number of rotation for each test was fixed at 10 000 cycles as the same value in Chapter 4. During continuous unidirectional sliding test, OCP evolution

was recorded following with EIS measurement at frequencies from 10 kHz down to 10 mHz. Friction coefficient was recorded in the whole sliding period. When sliding ended, OCP evolution was performed for 3 h, and EIS measurement was carried out at frequencies from 10 kHz down to 1.58 mHz under static condition as that before sliding. The surface morphology and chemical composition inside the track area were characterized by SEM coupled with EDS. The topography after tribocorrosion test was observed by optical profilometry.

In this chapter, untreated Ti was used as the reference material throughout the experiment. All experiments were repeated at least twice to ensure the reproducibility and the representative mean values were figured out in this work.

5.3 Surface characterization

The surface topographies of TO Ti prepared at 650 ℃ for 48 h and untreated Ti are shown in Figure 5-1. Comparing with the untreated Ti, TO Ti keeps the initial polishing groove on the surface and the average roughness retains and only changes from the initial value of 0.39 μm to 0.40 μm after thermal oxidation at 650 ℃ for 48 h in the furnace, as seen in Figure 5-2. The increase of microhardness value from 176 $HV_{0.2}$ for untreated Ti to 747 $HV_{0.2}$ for TO Ti indicates that thermal oxidation has significant influence on the mechanical property of cp Ti due to the formation of titanium oxides. The higher value of microhardness is one important reason that can improve the wear resistance of titanium and its alloys [145, 186, 187].

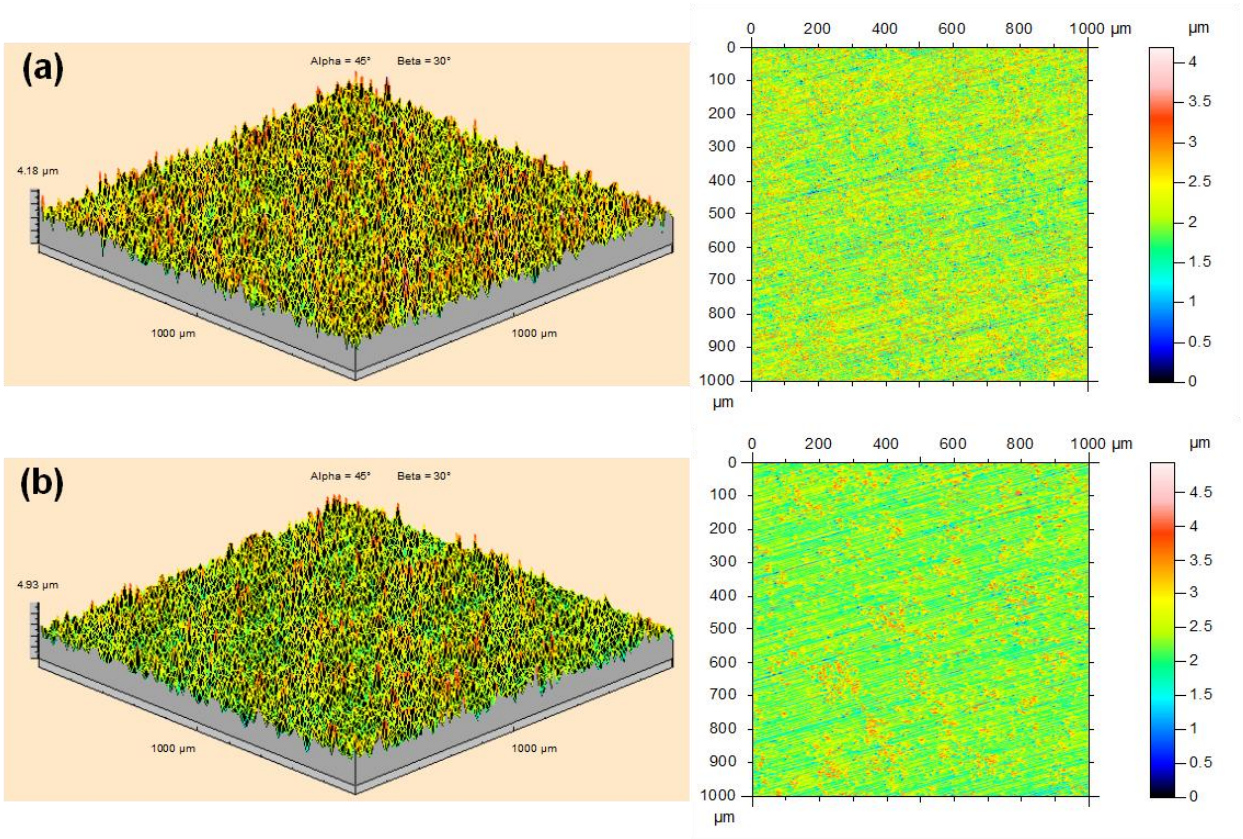

Figure 5-1 Profiles of TO Ti prepared at 650 ℃ for 48 h (a) and untreated Ti (b).

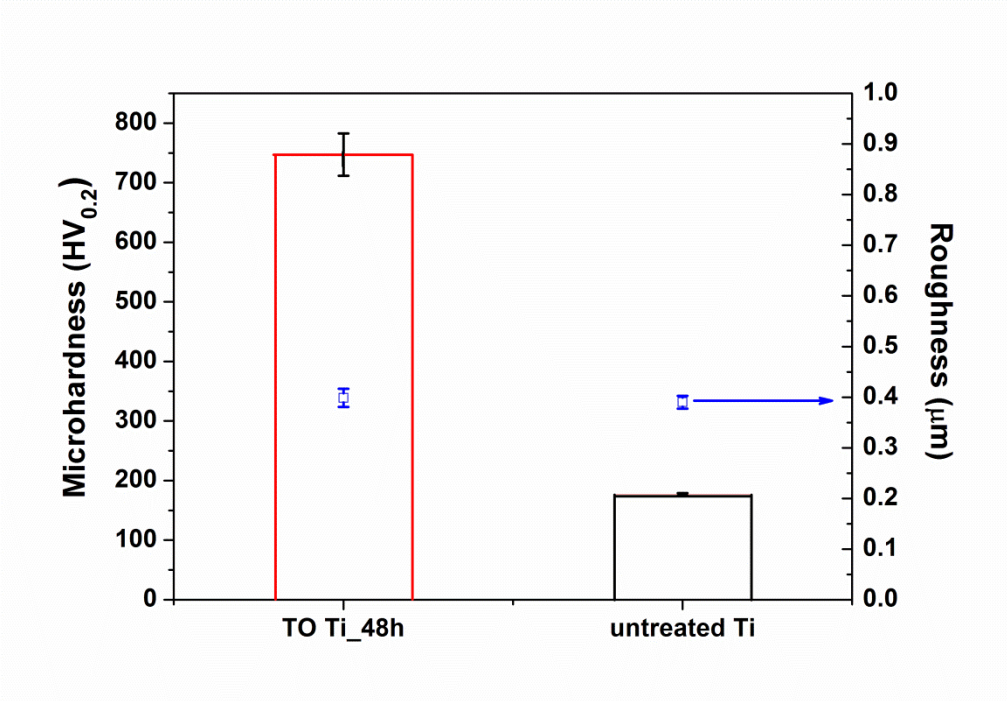

Figure 5-2 Microhardness and surface roughness of TO Ti prepared at 650 ℃ for 48 h and untreated Ti.

As Garcia-Alonso et al. [188] have reported, the surface of Ti-6Al-4V alloy can be fully covered with oxides in just one hour at 700 ℃. But considering the influence of treatment time of thermal oxidation on the corrosion resistance of cp Ti, Kumar et al [141] have found that thermal oxidation at 650 ℃ for 48 h is the best surface treatment among thermally oxidized samples for different treatment time. In this work, thermal oxidation at different temperatures for different time was also investigated, and the experimental results showed that TO Ti at 750 ℃ for 48 h or at 650 ℃ for 96 h results in poor adhesion of the film to cp Ti substrate, revealing the importance of optimized condition in thermal oxidation treatment of cp Ti.

Figure 5-3 shows the XRD patterns of TO Ti and untreated Ti. The untreated Ti is entirely composed of hexagonal α-phase (denoted as "Ti", ICDD card No. 00-005-0682). Compared with untreated Ti, rutile (TiO_2, denoted as "R", ICDD card No. 01-089-4920) peaks were clearly identified in the pattern of TO Ti sample, and the presence of oxygen-diffused Ti (TiO_x) [144] as well as α-Ti indicated that the Cu K_α radiation could penetrate through the thick rutile layer to the cp Ti substrate. Thermal oxidation process in this study contains the nucleation of oxides, the formation of a thin oxide layer and the growth to a thick scale. Hence, the sample weight will gain after thermal oxidation. The weight gain value of cp Ti after TO 650 ℃ for 48h is 0.595 ± 0.032 mg/cm^2, confirming the adsorbance of oxygen on sample surface.

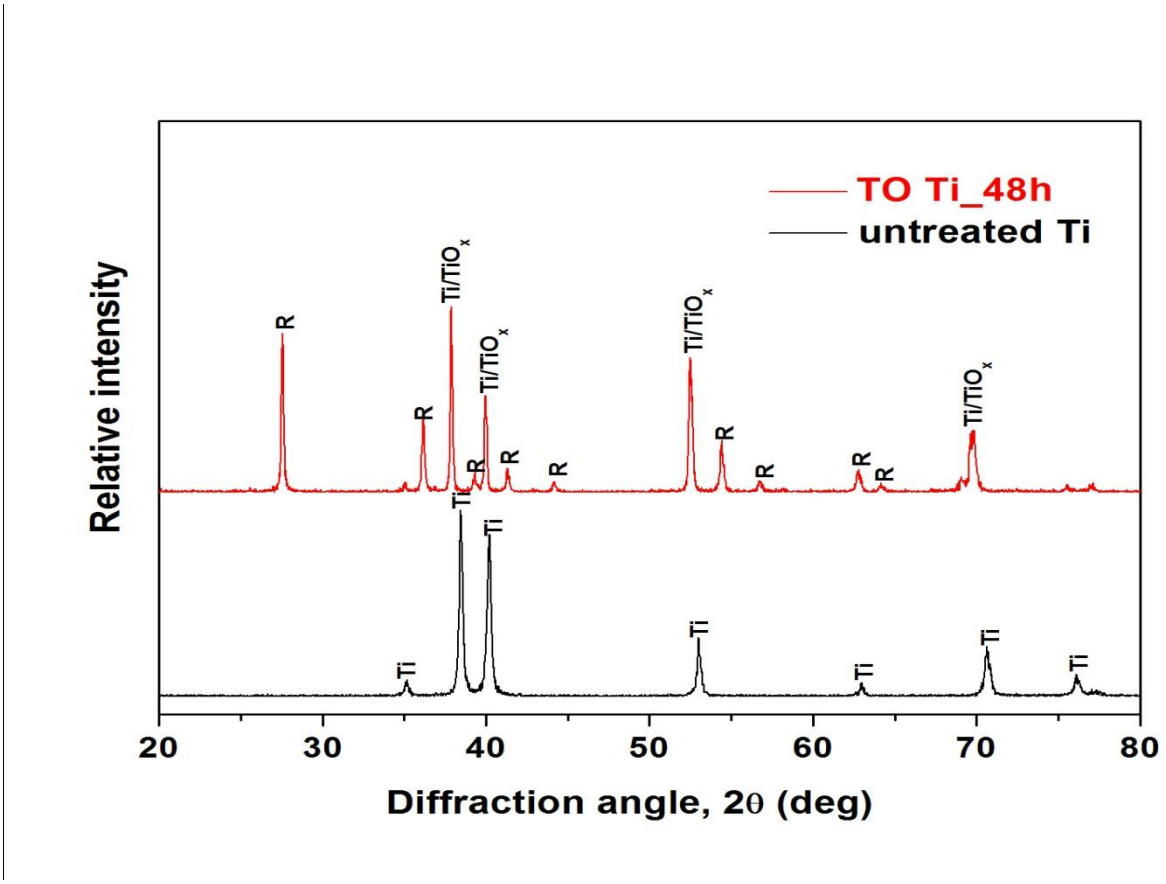

Figure 5-3 XRD patterns of TO Ti prepared at 650 ℃ for 48 h (red line) and untreated Ti (black line).

Surface morphology and chemical composition of TO Ti and untreated Ti were characterized by SEM coupled with EDS analysis, as seen in Figure 5-4. The chemical composition of TO Ti shows a higher oxygen containing status: O = 36.7 wt% and Ti = 63.3 wt%. The atomic ratio of O/Ti is 1.73 (< 2.00, as the standard molar ratio in rutile), revealing the existence of oxygen-diffused Ti as mentioned in Figure 5-3. For untreated Ti, although it is well known that a thin passive oxide film (of several nanometers thick) can spontaneously form on cp Ti surface, but it is so small that cannot be detected in the EDS analysis. So the chemical composition of untreated Ti is only titanium as 100 wt%. It should be also noticed that after thermal oxidation at 650 ℃ for 48 h, some aggregations can be found on sample surface, which might result from the favorite of nucleation of oxides in special sites like the grain boundaries of crystallites.

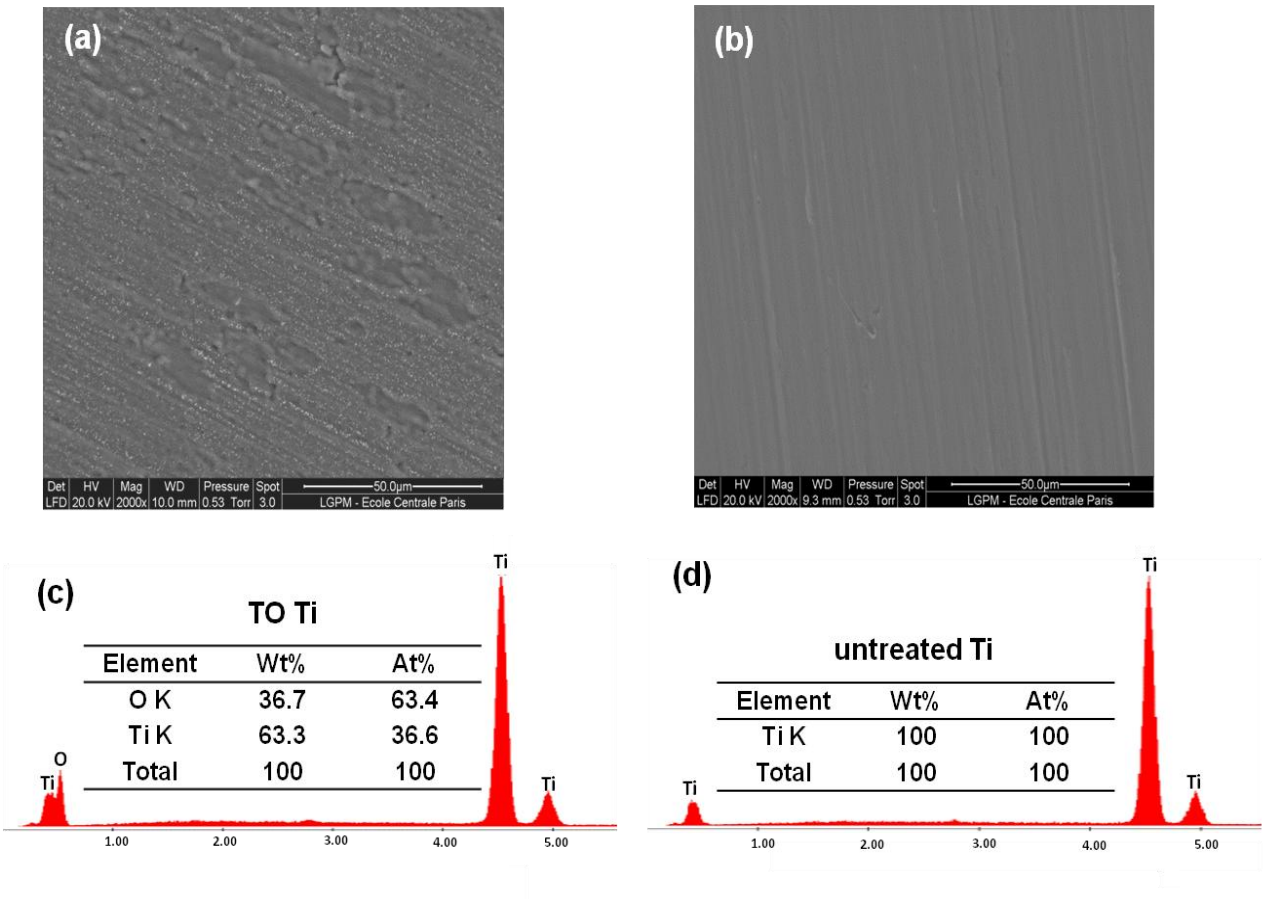

Figure 5-4 SEM and EDS analysis of chemical composition of the surface of TO Ti prepared at 650 ℃ for 48 h (a, c) and untreated Ti (b, d).

5.4 Corrosion behavior of TO Ti under static condition

The OCP evolution curves of TO Ti and untreated Ti in the PBS solution under static condition are shown in Figure 5-5. Like untreated Ti, OCP evolution of TO Ti also shifts in the noble direction but owns a much higher value of -0.08 V vs. Ag/AgCl at the beginning of immersion time. The potential value, E_{oc} raises up quickly during the first 6 minutes from -0.08 V to -0.015 V vs. Ag/AgCl

and then increase smoothly to 0.04 V vs. Ag/AgCl after immersion in the PBS solution for 3 h. For untreated Ti, E_{oc} raises up from -0.45 V to -0.26 V vs. Ag/AgCl after immersion for 3 h, revealing the stronger extent of anodic shift than TO Ti. The OCP of both TO Ti and untreated Ti in the PBS solution are in the TiO_2 stability region of the Ti-H_2O Pourbaix diagram (see Figure 2-8 [111]).

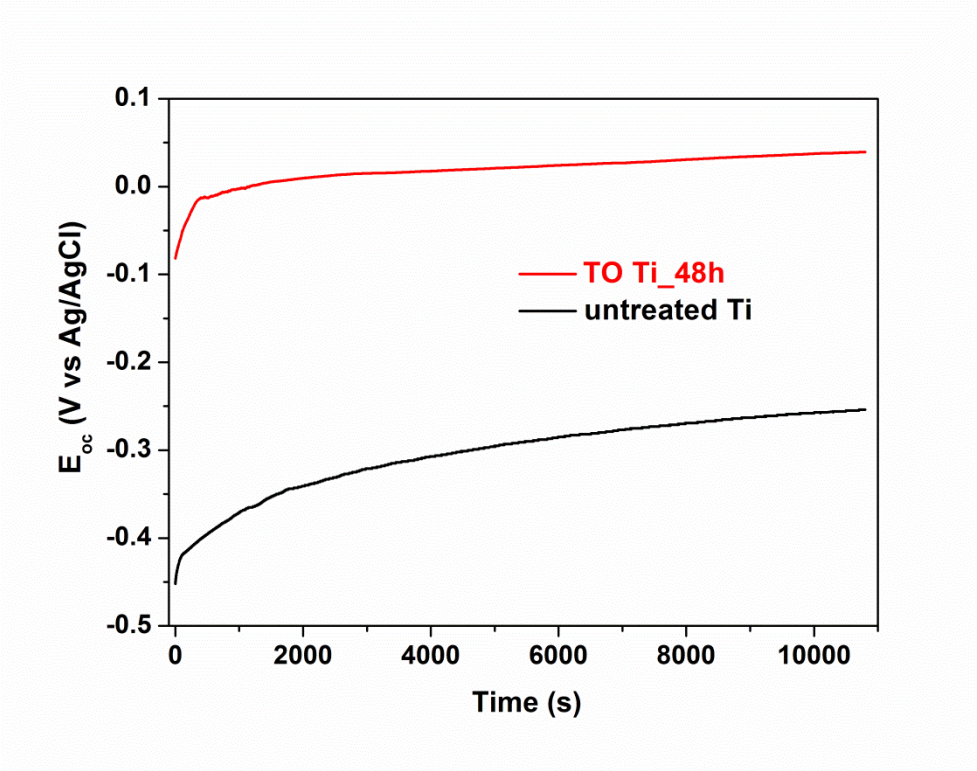

Figure 5-5 OCP evolution of TO Ti prepared at 650 ℃ for 48 h (red line) and untreated Ti (black line) in the PBS solution.

The Nyquist plots for TO Ti and untreated Ti, measured at immersion time of 3 h and 24 h in the PBS solution under static condition, are shown in Figure 5-6a. The untreated Ti exhibits only a single semicircle in the entire frequency range, which corresponds to the equivalent circuit with one time constant as illustrated in Figure 5-7a (the same as Figure 4-3), where R_s is the solution resistance and R_p is the polarization resistance of cp Ti due to the barrier property of passive film. But TO Ti exhibits an irregular arc that can be divided into two semicircles: one in the high frequency range and another in the low frequency range. Such two semicircles can be illustrated by the equivalent circuit in Figure 5-7b, where R_{outer} and R_{inner} correspond to the resistance of the outer porous rutile layer and the resistance of the inner compact oxygen-diffused titanium layer [4, 189], respectively. As illustrated before, the use of CPE rather than a pure capacitance can be expressed by Eq. 3-10 in Chapter 3.

Figure 5-6b and 5-6c show the Bode plots for TO Ti and untreated Ti after immersion for 3 h and 24 h in the PBS solution. From the Bode impedance plots, it is clearly observed that the specific polarization resistance, r_p, of untreated Ti increases from 7.69×10^5 Ω cm^2 at the immersion time of

3 h to 4.70 $\times 10^6$ Ω cm^2 at the immersion time of 24 h, indicating the barrier property of passive film on cp Ti becomes stronger. Correspondingly, the Bode phase angle plot shows a broader frequency range close to -85 º. But for TO Ti, r_p value, the sum of the r_{outer} and r_{inner}, decreases from 6.07 $\times 10^7$ Ω cm^2 measured at immersion time of 3 h to 4.08 $\times 10^7$ Ω cm^2 measured at immersion of 24 h. This phenomenon is due to the solution penetration though the oxide layers, which weakens the barrier property of oxide layers. The phase angle keeps in the entire frequency range for TO Ti, revealing the corrosion mechanism of TO Ti doesn't change within 24 h immersion in the PBS solution.

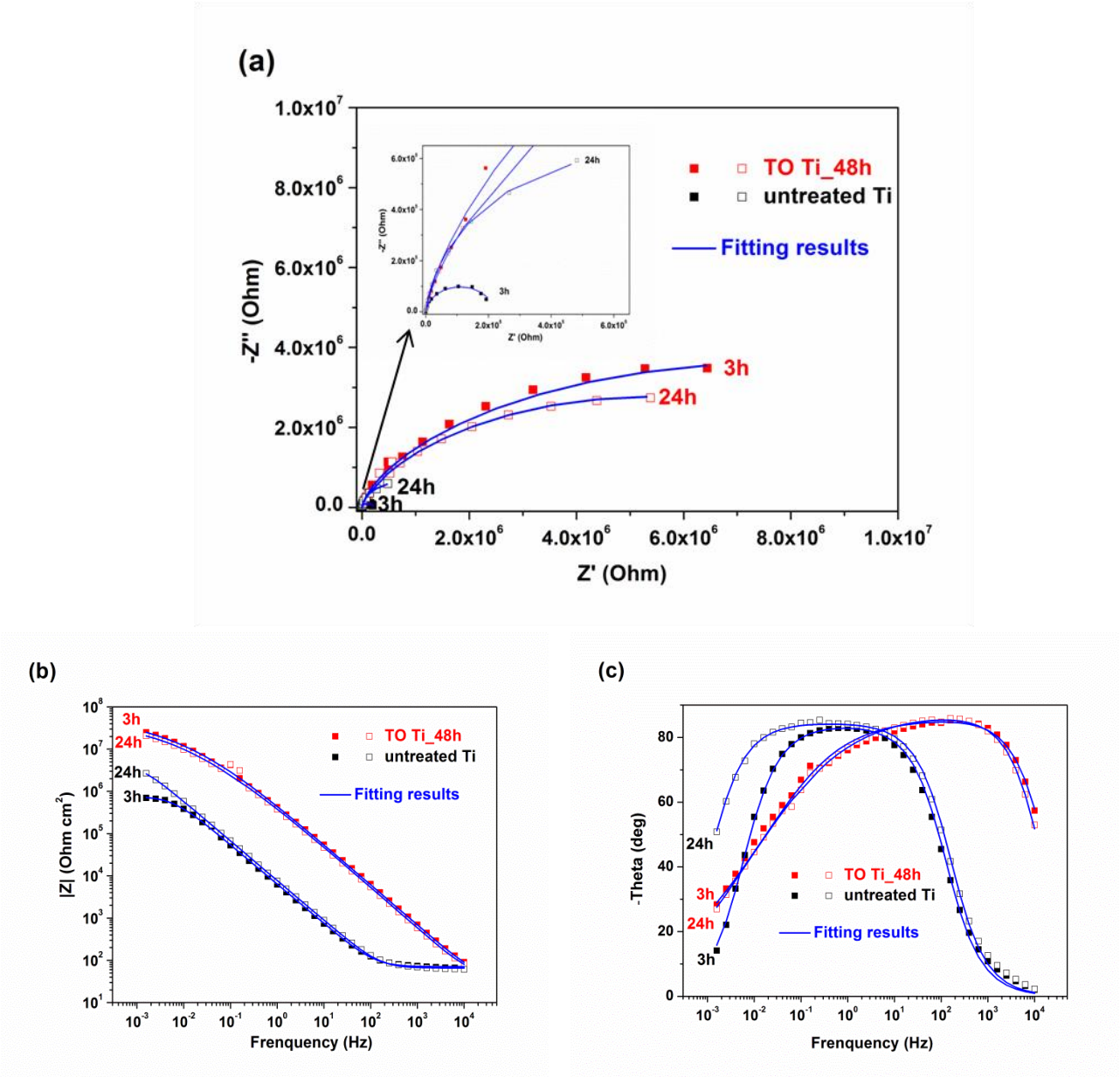

Figure 5-6 Nyquist plots (a), Bode impedance plots (b) and Bode phase angle plots (c) for TO Ti prepared at 650 ℃ for 48 h (red square) and untreated Ti (black square) measured at immersion time of 3 h and 24 h under static condition.

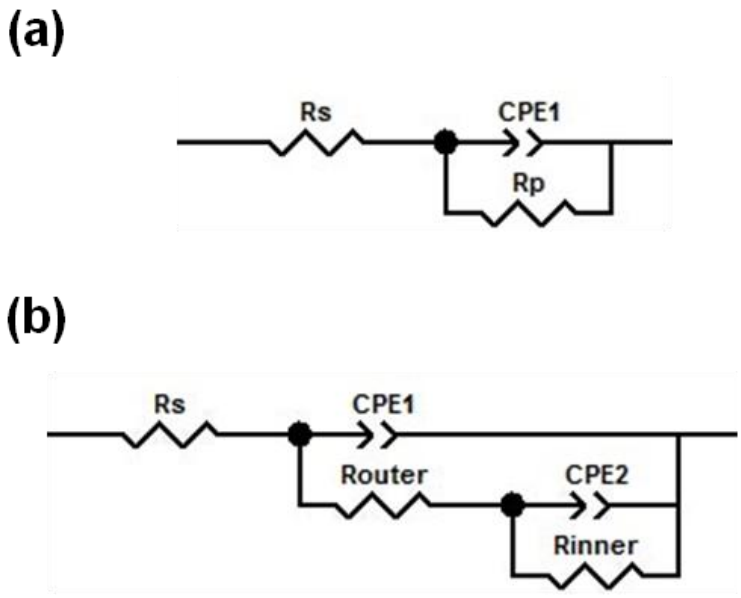

Figure 5-7 Equivalent circuit for untreated Ti with one time constant (a) and TO Ti prepared at 650 ℃ for 48 h with two time constants (b) under static condition.

All the calculated equivalent circuit elements are shown in Table 5-1. The value of ϕ-1 is closed to 1 for both untreated Ti and TO Ti at different immersion time, revealing a near capacitive response for and the outer rutile layer and untreated Ti in the PBS solution. The small value of ϕ-2, 0.44 at the immersion time of 3 h and 0.50 at the immersion time of 24 h for TO Ti shows the near resistive response for the inner oxygen-diffused titanium layer. Both the R_{outer} and R_{inner} values decrease with the increase of immersion time, which might be induced by the deterioration of layers due to the solution penetration.

Figure 5-8 shows the potentiodynamic polarization curves of TO Ti and untreated Ti in the potential range from -1 V to 3 V vs. Ag/AgCl, measured at immersion time of 3 h and 24 h under static condition in the PBS solution. The corrosion potential (E_{corr}) and specific passive current density (i_{pass}) of the TO Ti and untreated Ti are summarized in Table 5-2. Compared with the untreated Ti, TO Ti exhibits a shift in E_{corr} towards the noble direction and both the current density at E_{corr} and i_{pass} show a significant decrease at immersion time of 3 h or 24 h. With immersion time increase, the E_{corr} and i_{pass} of untreated Ti have almost no changes. The same tendency was found for the value of E_{corr} of TO Ti. In spite a slight increase of i_{pass} for TO Ti from 1.88×10^{-8} A cm^{-2} at immersion of 3 h to 3.05×10^{-8} A cm^{-2} at immersion time of 24 h in the PBS solution, it is still two orders of magnitude smaller than that values of untreated Ti.

Table 5-1 Parameters of the equivalent circuit for TO Ti prepared at 650 °C for 48 h and untreated Ti under static condition.

Sample	A_0 (cm^2)	Time (h)	R_s (Ohm)	T-1 ($\mu F \cdot cm^{-2} \cdot s^{\phi-1}$)	ϕ-1	R_{outer} (Ohm)	T-2 ($\mu F \cdot cm^{-2} \cdot s^{\phi-1}$)	ϕ-2	R_{inner} (Ohm)	$^*R_p$ (Ohm)	r_p (Ohm·cm^2)
TO Ti_48h	3.42	3	12.3	0.35	0.95	23500	0.18	0.44	1.77×10^7	1.78×10^7	6.07×10^7
		24	13.5	0.38	0.96	61000	0.26	0.50	1.19×10^7	1.19×10^7	4.08×10^7
untreated Ti	3.51	3	20.1	28.2	0.93	--	--	--	--	2.19×10^5	7.69×10^5
		24	18.7	23.0	0.94	--	--	--	--	1.34×10^6	4.70×10^6

$^*R_p = R_{outer} + R_{inner}$ for TO Ti under static condition.

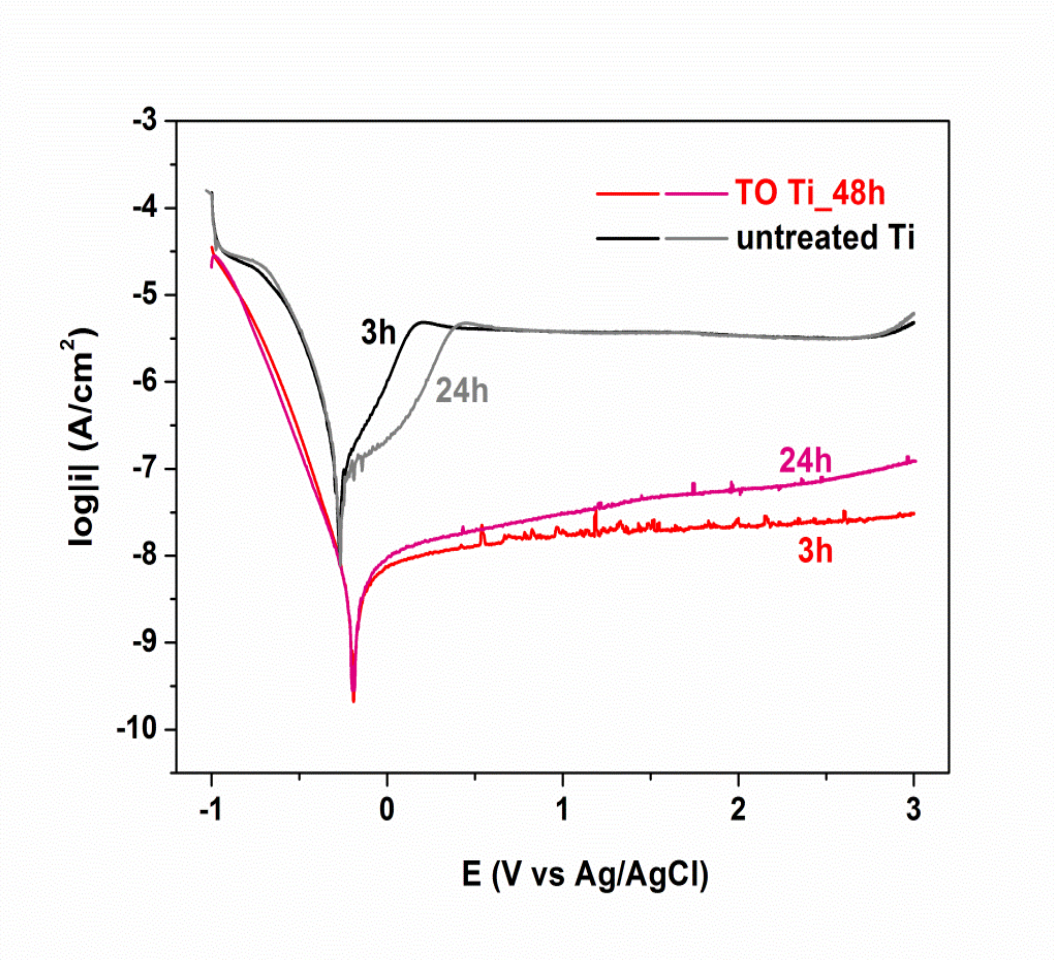

Figure 5-8 Potentiodynamic polarization curves of untreated Ti and TO Ti from -1 V to 3 V vs. Ag/AgCl at a scan rate of 1 mV/s measured at immersion time of 3 h and 24 h under static condition.

Table 5-2 Electrochemical data obtained from potentiodynamic polarization tests.

Sample	Time (h)	E_{corr} (V)	$*i_{pass}$ (A·cm^{-2})
TO Ti_48h	3	-0.19	1.88×10^{-8}
	24	-0.19	3.05×10^{-8}
untreated Ti	3	-0.27	3.78×10^{-6}
	24	-0.27	3.77×10^{-6}

*i_{pass}: specific passive current density at 1 V vs. Ag/AgCl.

5.5 Tribocorrosion behavior of TO Ti during and after continuous unidirectional sliding test

Tribocorrosion tests were performed when E_{oc} got stabilized after immersion for 3 h in the PBS solution. A loading force, F_n of 5 N is imposed to evaluate the wear-corrosion behavior of TO Ti and untreated Ti during continuous unidirectional sliding at a rotation rate of 100 rpm and the total rotation number of 10 000 cycles. The OCP evolution curves and friction coefficient curves of both the TO Ti and untreated Ti during sliding are shown in Figure 5-9. For untreated Ti, with the onset of sliding, a sudden drop from -0.22 V to -0.87 V vs. Ag/AgCl (cathodic shift of potential in the negative direction with respect to E_{oc} before sliding) is observed, revealing the change of surface state from passive to active inside the sliding track area of untreated Ti. During sliding test period, although the E_{oc} variation of untreated Ti is large, the E_{oc} value is still below -0.7 V vs. Ag/AgCl. The variation might result from the periodic removal and growth of corrosion debris of cp Ti. Similar observations were made earlier by Kumar et al. [147] for cp Ti in Ringer's solution and by Barill et al. [58] for Ti-6Al-4V alloy in 0.9% NaCl.

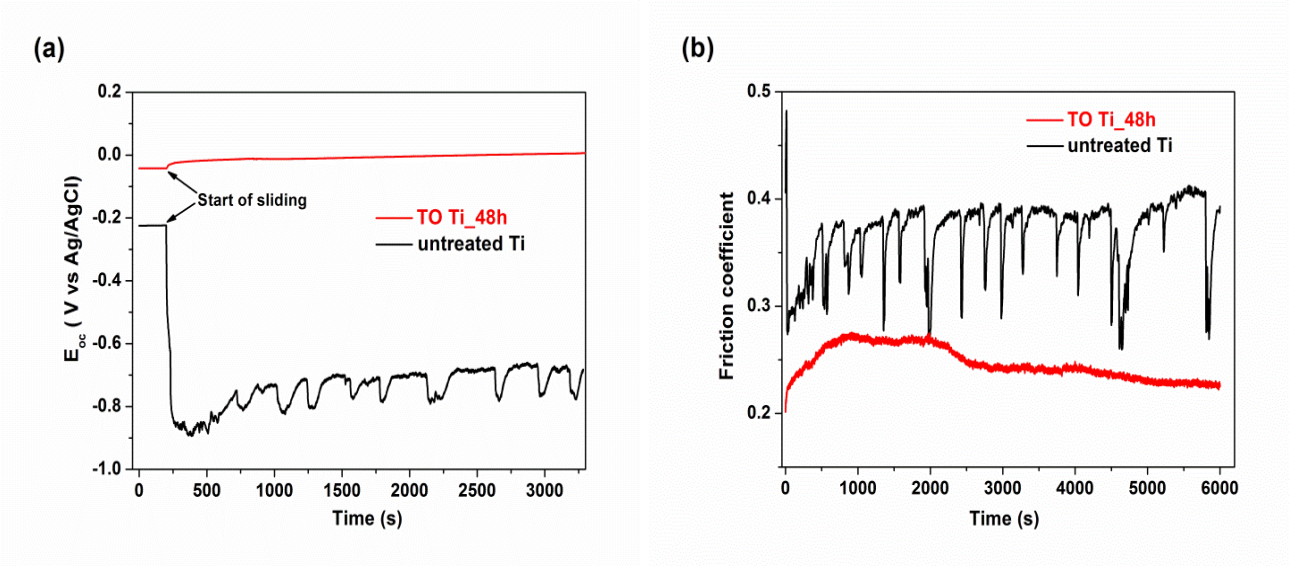

Figure 5-9 OCP evolution (a) and friction coefficient curves (b) of TO Ti prepared at 650 ℃ for 48 h (red line) and untreated Ti (black line) during continuous unidirectional sliding tests performed at F_n of 5 N.

Unlike untreated Ti, TO Ti did not exhibit many fluctuations in E_{oc} value during sliding. Since the surface is still covered with a thick oxide film, and no fluctuation in OCP is reflected if the oxide film haven't been destroyed in the sliding period at F_n of 5 N and a rotation rate of 100 rpm. For TO Ti, the slight increase of E_{oc} when sliding starts and continuous increase during the whole sliding period might result either from the growth of a passive film on the electrode with a consequent decrease in anodic current or from the promotion of oxygen reduction with a consequent increase in

cathodic current from an electrochemical reaction point of view. With the protection of thermal oxidized thick film, the passive film on the surface of cp Ti substrate cannot be destroyed by the counter body (ZrO_2) under mechanical loaded condition. In contrast, it grows continuously even during sliding test. The corresponding high friction coefficient fluctuation in this study provides supplemental evidence for this phenomenon (see Figure 5-9b). Comparing with untreated Ti, the friction coefficient curve for TO Ti keeps below that value of untreated Ti and its fluctuation is smoother than untreated Ti. These two aspects indicate that thermal oxidation of cp Ti has significantly improved the friction characteristics.

When continuous unidirectional sliding motion stops, the OCP evolution curve for untreated Ti exhibits an anodic shift, suggesting the occurrence of repassivation of the active surface inside the sliding track area, and the continuous increase of E_{oc} for TO Ti after sliding indicates the growth of passive film on the cp Ti substrate, as seen in Figure 5-10. After continuous unidirectional sliding test for about 3 h, untreated Ti returns back to the E_{oc} value of -0.25 V vs. Ag/AgCl close to the initial potential value before sliding test (see in Figure 5-9a). Similar observation has been illustrated in the previous Chapter 4 after continuous unidirectional sliding test at F_n of 1 N, as seen in Figure 4-10. Comparing with the final potential values of these two tests, it can be found that after the same immersion time when sliding motion stops, E_{oc} in Figure 4-10 is higher than that in Figure 5-10, indicating that the total wear area (corresponding values can be seen in Table 4-4) has an effect on the recovery potential (a mixed potential of the worn and unworn areas).

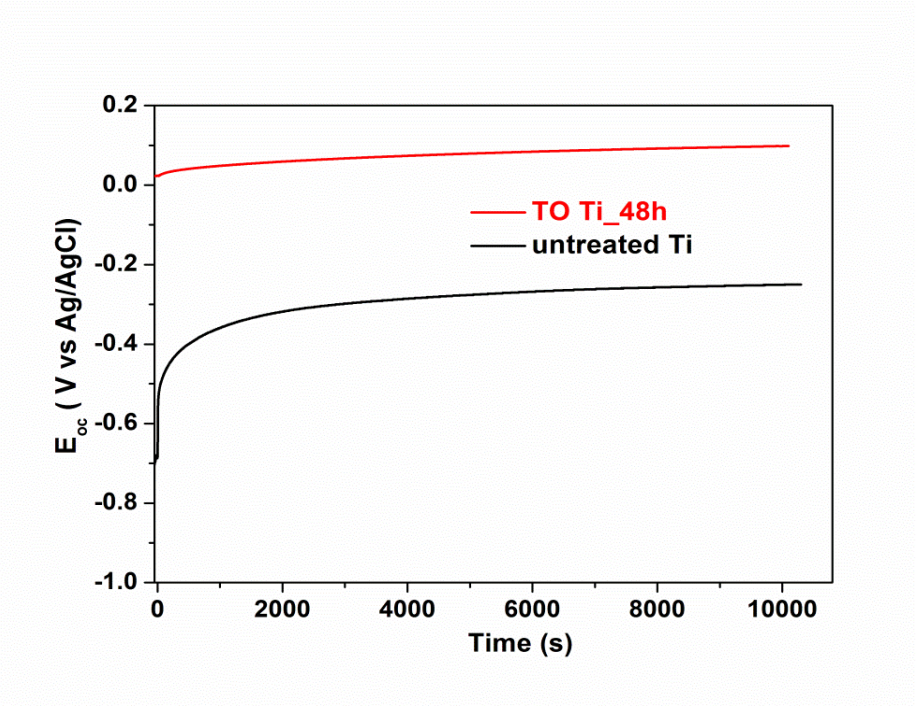

Figure 5-10 OCP evolution of TO Ti prepared at 650 ℃ for 48 h (red line) and untreated Ti (black line) after continuous unidirectional sliding tests.

The Nyquist plots for TO Ti and untreated Ti, measured before, during and after unidirectional sliding at F_n of 5 N in the PBS solution, are shown in Figure 5-11a1 and 5-11a2. For TO Ti, the impedance comportment during and after sliding test exhibits an irregular arc in the high frequency region that can be divided into two semicircles like those before sliding (Figure 5-7b), but an added arc appears in the low frequency region shows another time constant, corresponding to the charge transfer resistance (R_{ct}) and double layer capacitance (CPE3) at the interface of cp Ti substrate and the penetrated electrolyte. As explained in Chapter 4, the selection of equivalent circuit was a compromise between a reasonable fitting of the experimental values and a minimum of components in the equivalent circuit. So, such a complex Nyquist plot for TO Ti during and after sliding test can be illustrated by the equivalent circuit in Figure 5-12. The fitted parameters of the equivalent circuits for TO Ti before and during/after sliding test are summarized in Table 5-3. The R_{ct} values obtained by the fitting results for TO Ti during and after sliding test are 1×10^{20} Ω toward infinity (ω), due to the lack of experimental results in the low frequency region towards 0 Hz (the actual lowest frequency is 1.58 mHz in this study). In this case, we also use the R_p value as the sum of R_{outer} and R_{inner} as illustrated in Figure 5-7b and Table 5-1. The real r_p value is no doubt much higher than the calculated one as shown in Table 5-3. From the inset of Figure 5-11a2, it is obviously to see that even during sliding test, the Nyquist plot for untreated Ti still exhibits only one single semicircle in the entire frequency range. The equivalent circuit for untreated Ti in the whole test period (before, during and after sliding) is the same as illustrated in Figure 5-7a with one time constant, R_s(CPE||R_p). The fitted parameters of the equivalent circuit for untreated Ti are summarized in Table 5-4.

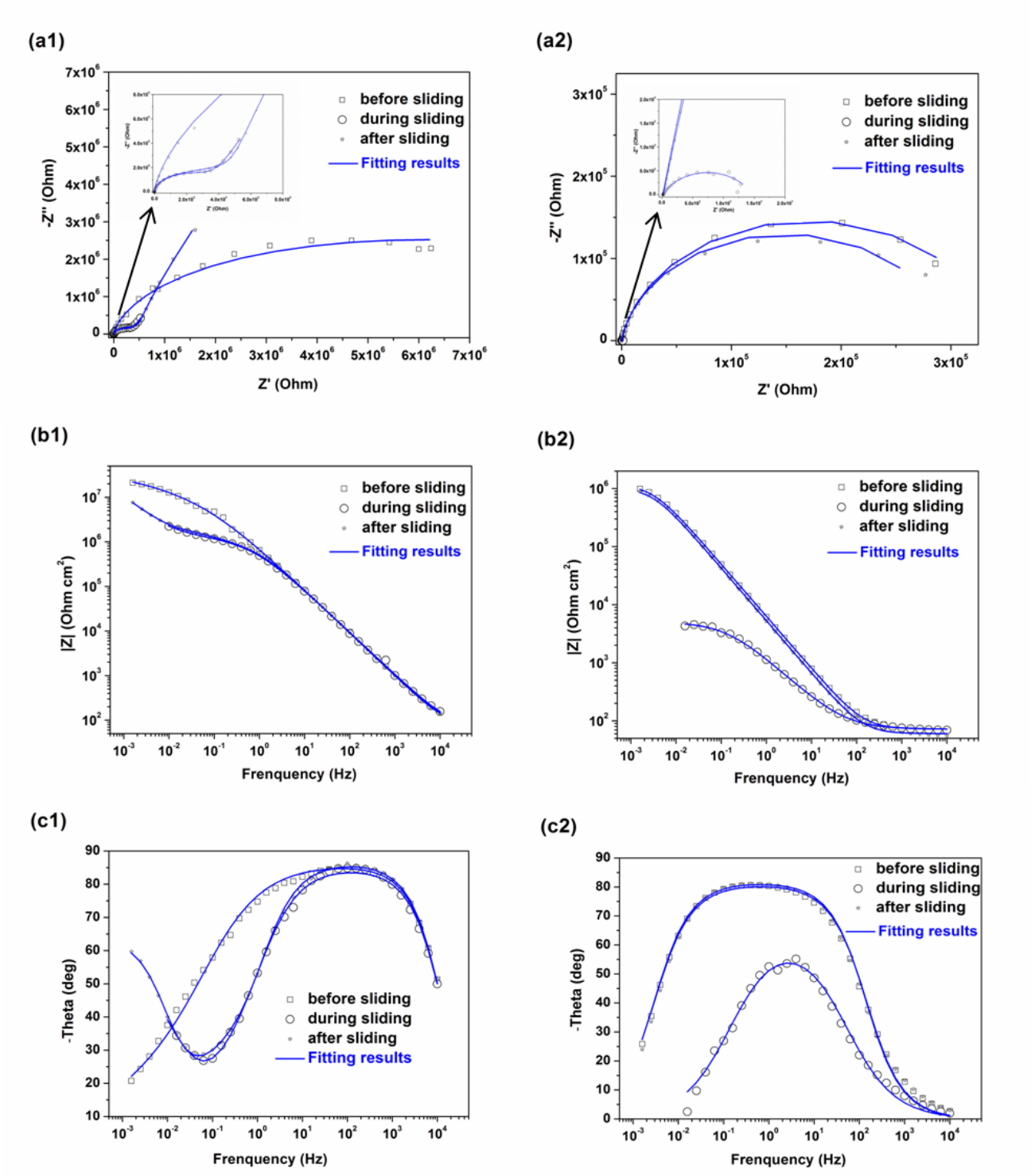

Figure 5-11 Nyquist plots (a), Bode impedance plots (b) and Bode phase angle plots (c) for TO Ti prepared at 650 ℃ for 48 h (1) and untreated Ti (2) measured before (square), during (ring) and after (star) continuous unidirectional sliding tests at F_n of 5 N in the PBS solution.

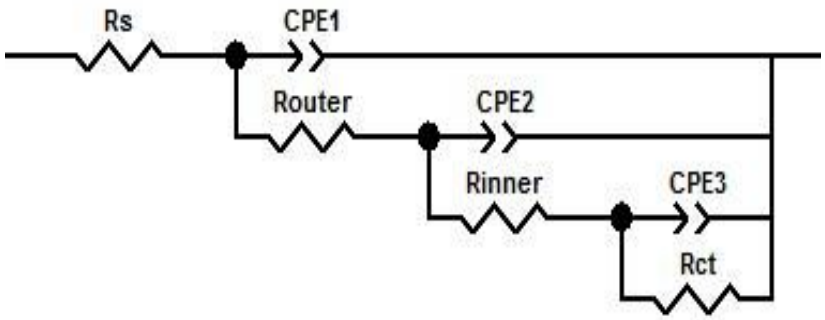

Figure 5-12 Equivalent circuit with three time constants for TO Ti prepared at 650 ℃ for 48 h during and after sliding tests.

Table 5-3 Parameters of the equivalent circuit for TO Ti prepared at 650 ℃ for 48 h, measured before, during and after continuous unidirectional sliding test at F_n of 5 N in the PBS solution.

A_0 (cm^2)	test	R_s (Ohm)	ϕ-1	R_{outer} (Ohm)	ϕ-2	R_{inner} (Ohm)	ϕ-3	R_{ct} (Ohm)	$*R_p$ (Ohm)	r_p (Ohm·m^2)
	before	26.6	0.95	191000	0.39	1.44×10^7	--	--	1.46×10^7	4.80×10^7
3.29	during	27.4	0.94	190200	0.57	338100	0.77	ω_1 × 10^{20}	5.28×10^5	1.74×10^6
	after	25.4	0.96	211800	0.60	596700	0.91	ω_1 × 10^{20}	8.09×10^5	2.66×10^6

*$R_p = R_{outer} + R_{inner}$ for TO Ti before, during and after sliding test.

Table 5-4 Parameters of the equivalent circuit for cp Ti measured before, during and after continuous unidirectional sliding test at F_n of 5 N in the PBS solution.

A_0 (cm^2)	test	R_s (Ohm)	ϕ-1	R_p (Ohm)	r_p (Ohm·cm^2)
	before	20.7	0.90	3.42×10^5	1.19×10^6
3.49	during	20.6	0.73	1400	5000
	after	17.2	0.91	3.00×10^5	1.05×10^6

Comparing the r_p values for TO Ti and untreated Ti measured with different samples in Table 5-1, 5-3 and 5-4, it should be noticed that for both TO Ti and untreated Ti, the reproducibility of electrochemical measurement results is not well but the values for each type are in the same order of magnitude. The intrinsic property of sample surface and the actual experimental environment have significant influence on the electrochemical measurement results. So, for the explication of resistance change before, during and after siding test, all values presented here should be considered as the qualitative changes rather than the quantitative changes. To get more accurate information, the strict control of experimental operation in the thermal oxidation process for TO Ti and in the electrochemical measurement process and more parallel repetitions with different samples are necessary in the future work.

For untreated Ti, the r_p value decreases from 1.19×10^6 Ω·cm^2 measured before sliding to 5000 Ω·cm^2 measured during continuous unidirectional sliding test at F_n of 5 N. Not like a further calculated specific polarization resistance in the active area, r_{act}, under the guidance of a tribocorrosion protocol for surface modified Ti in Chapter 3, a general specific polarization resistance is used in this chapter to give a qualitative comparison with that value of TO Ti during sliding test. The tremendous decrease in r_p value indicates the destruction of passive film on untreated Ti surface, which makes the active area contact directly with the aggressive electrolyte (the PBS solution). Since the continuous sliding motion of ZrO_2 counter body, repassivation inside the track area cannot occur during sliding test. But once sliding stops, the r_p value returns back to 1.05×10^6 Ω·cm^2, revealing the strong repassivation ability of untreated Ti to form again a passive film inside the track area in the PBS solution.

For TO Ti, the R_{outer} value keeps stable before, during and after sliding test but the R_{inner} value decreases significantly from 1.44×10^7 Ω measured before sliding to 3.38×10^5 Ω measured during continuous unidirectional sliding test at F_n of 5 N. The later results in the decrease of r_p value decreases from 4.80×10^7 Ω·cm^2 measured before sliding to 1.74×10^6 Ω·cm^2 measured during sliding. This value change indicates that the thermal oxidized film at 650 ℃ on cp Ti was destroyed when sliding motion occurs at F_n of 5 N. This film deterioration couldn't be detected by the OCP evolution in Figure 5-9. When sliding motion stops, the destroyed thermal oxidized film doesn't show a self-healing process like repassivation of untreated Ti in the PBS solution. The increase of r_p to 2.66×10^6 Ω·cm^2 measured after sliding might result from the continuous growth of passive film on cp Ti substrate under the thermal oxidized film. Although the destruction of TO Ti is an irrecoverable process, the corrosion resistance after sliding is still much higher than untreated Ti by considering the great R_{ct} value for TO Ti.

5.6 Characterization of the wear track on TO Ti after continuous unidirectional sliding test

Surface morphologies of TO Ti and untreated Ti after continuous unidirectional sliding at F_n of 5 N were obtained by SEM, as shown in Figure 5-13. The track width of untreated Ti is about 2.78 mm after sliding test at F_n of 5 N. The regular pattern of grooves and a large number of attached corrosion debris inside the track area reveals that the untreated Ti was worn severely by both the abrasive and adhesive wear mechanisms, so that the wear track is wide and deep with a very rough surface appearance, as seen the track profile of untreated Ti in Figure 5-14b. The track depth of ~ 9 μm indicates the serious material loss of untreated Ti, which has been quantitatively analyzed in Chapter 4 under continuous unidirectional sliding tests. On the contrary, TO Ti experiences only mild wear caused by the abrasion of the counter body. The resultant wear track on TO Ti surface is narrow with a width of 0.35 mm and shallow with a smooth and polished appearance, as seen in Figure 5-14a. No spallation and flake of the oxide layer has been observed in the track of TO Ti after sliding test at F_n of 5 N. The superior wear resistance of TO Ti is derived from its good adhesion with the substrate, high hardness and much improved frictional behavior during sliding.

The chemical compositions inside the track areas of TO Ti (square in Figure 5-13a) and untreated Ti (square in Figure 5-13b) obtained at F_n of 5 N were analyzed by EDS, and the results are presented in Figure 5-13c and 5-13d. For untreated Ti, the appearance of high amount of oxygen (O, 10.9 wt%) indicates the repassivation of cp Ti to form the titanium oxide film. The small amount of phosphorus (P, 0.6 wt%, existing originally in the PBS solution) shows that species in the solution takes part in the corrosion of substrate or is packed into the corrosion product. Chemical composition of the track on TO Ti after sliding test is listed as O 39.9 wt%, Ti 58.9 wt%, P 0.9 wt% and Ca 0.3 wt%. Comparing with the initial chemical composition in Figure 5-4 (O, 63.4 at% and Ti 36.6 at%), the Ti/O atomic ratio inside the track area (O, 66.3 at% and Ti 32.7 at%) increases slightly, revealing the oxygen containing species in the solution like HPO_4^{2-} and $H_2PO_4^-$ penetrate through the thermal oxidized film to augment the percentage of O after sliding test.

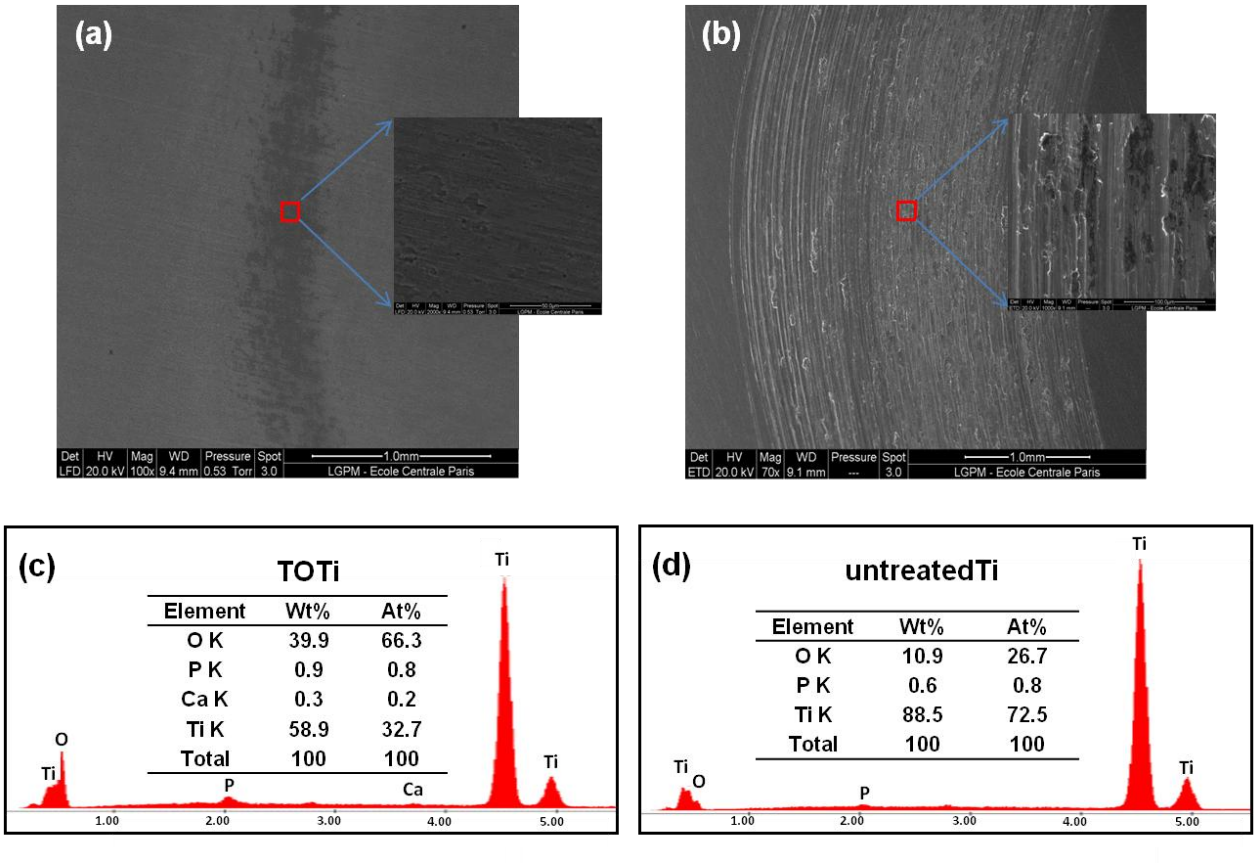

Figure 5-13 SEM images (a, b) and EDS analysis inside the tracks (c, d) of TO Ti prepared at 650 ℃ for 48 h (left) and untreated Ti (right) after continuous unidirectional sliding tests at F_n of 5 N in the PBS solution.

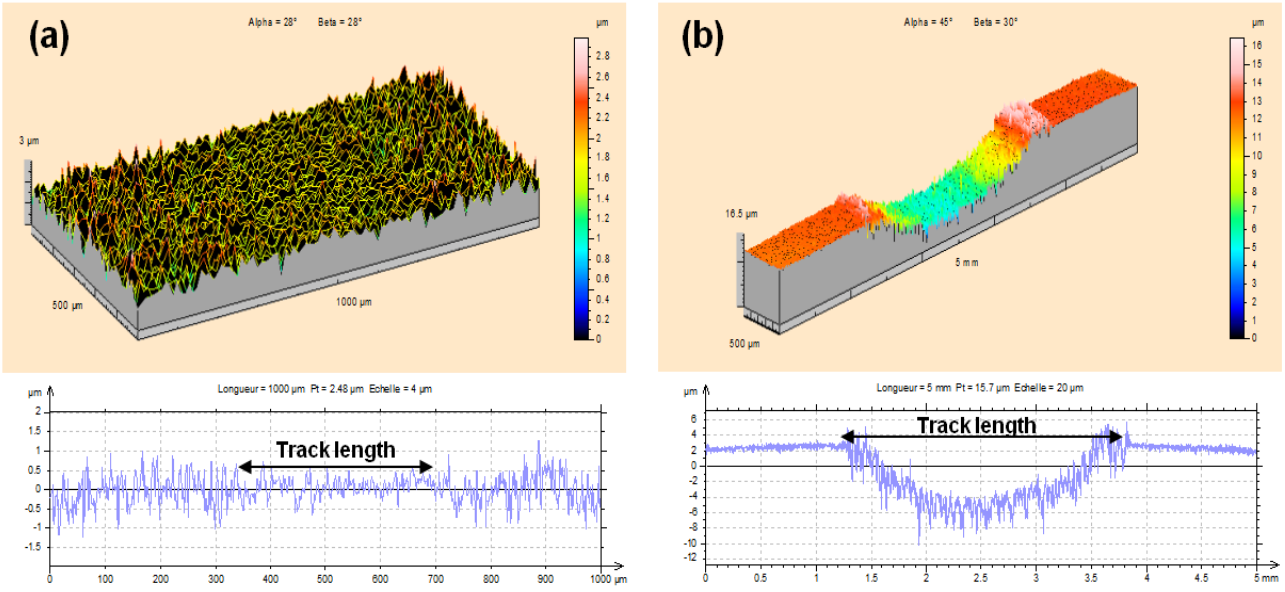

Figure 5-14 Profiles of TO Ti prepared at 650 ℃ for 48 h (a) and untreated Ti (b) after continuous unidirectional sliding tests at F_n of 5 N in the PBS solution.

5.7 Conclusions

Thermal oxidation of cp Ti in air atmosphere at 650 ℃ for 48 h leads to the formation of an oxide film throughout the surface without any spallation. The oxide film consists of rutile and oxygen diffused titanium as the predominant phases characterized by XRD. Comparing with untreated Ti, the oxide film has no effect on the average roughness of the surface but significantly increases the microhardness from 176 $HV_{0.2}$ to 747 $HV_{0.2}$.

The OCP evolution before sliding under static condition, during sliding under mechanical loaded condition at F_n of 5 N and after sliding under static condition, for untreated Ti clearly changes when sliding motion starts or stops. While for TO Ti, a mild continuous increase of E_{oc} in the whole test period reveals the growth of passive film on the substrate under the thermal oxidized film. Results of EIS and potentiodynamic polarization measurements at immersion time of 3 h and 24 h showed that the corrosion resistance of untreated Ti enhances with immersion time incrase. The i_{pass} value for untreated Ti decreases and the r_p value incrases at immersion time of 24 h. In contrast, the i_{pass} value increases and the r_p value decreases at immersion time of 24 h for TO Ti. Deterioration of thermal oxidized film occurs during the long-term immersion in the PBS solution.

Under mechanical loaded condition, the impedance values r_p of both TO Ti and untreated Ti decrease due to the removal of passive film for untreated Ti and the destruction of thermal oxidized film for TO Ti. After sliding test, unlike the repassivation ability of cp Ti inside the track area on untreated Ti, the destruction of the thermal oxidized film on TO Ti is an irrecoverable process. Although the r_p value of TO Ti after sliding is smaller than the value measured before sliding, its corrosion resistance is still much higher than untreated Ti. Combined with the improved frictional behavior during sliding, thermal oxidation is sure to be considered as an excellent method to ameliorate the corrosion and tribocorrosion behavior of cp Ti, especially under a high mechanical loaded condition

.

Chapter 6: Effect of CaP bioactive film on corrosion and tribocorrosion behavior of cp Ti

6.1 Introduction

As a biomedical material, cp Ti is expected to own bioactivity to promote the growth of bone on its surface. In this chapter, CaP bioactive film in the form of brushite ($CaHPO_4 \cdot 2H_2O$) was obtained directly on cp Ti by electrochemical deposition method. The influences of cathodic potential and deposition time were investigated in a calcium and phosphate containing solution. An optimized deposition condition was chosen as -1.8 V vs. Ag/AgCl for 30 min from the potential range from -1.4 V to -2.1 V vs. Ag/AgCl, basing on a relative compact and uniform film measured by X-ray fluorescence (XRF) spectrometry. Surface morphology/chemical composition, crystalline phase and topography were characterized by SEM coupled with EDS, XRD and optical profilometry. The effect of CaP bioactive film on the corrosion behavior of cp Ti was studies by electrochemical measurements like OCP, EIS and potentiodynamic polarization in the PBS solution. Considering the fragile property of CaP bioactive film and preventing the strong destruction of cp Ti substrate, a relative small loading force, F_n of 500 mN was imposed to investigate the tribocorrosion behavior of CaP bioactive film coated Ti under continuous mechanical loaded condition by using a pin-on-disc tribometer. Results show that surface modification of cp Ti with CaP bioactive film can provide not only higher corrosion and tribocorrosion resistance but also becomes the *in situ* source of Ca and P ions by the dissolution of its own as the precursor for the hydroxyapatite (HA) deposition.

6.2 Experimental details

The well polished and cleaned cp Ti specimens were used as working electrodes and the electrochemical deposition of CaP bioactive film was carried out potentiostatically at -1.8 V vs. Ag/AgCl for 30 min in a calcium and phosphate containing solution [0.042 mol/L $Ca(NO_3)_2 \cdot 4H_2O$ + 0.025 mol/L $NH_4H_2PO_4$] with a pH value of 4.2. The deposition conditions were based on the experimental results of a relative compact and uniform film measured by XRF spectrometry, choosing from the analysis results of films obtained at different potentials from -1.4 V to -2.1 V vs. Ag/AgCl. Optical profilometry was used to measure the surface topography of samples before and after surface modification and the average roughness value was calculated on square regions with length of 1000 μm × 1000 μm. Vickers microhardness test was performed with a test force of 200 gf and full load period of 15 s. The phase constituents of the untreated Ti and CaP bioactive film coated Ti samples were determined by XRD using a Cu K_α ($\lambda = 1.54$ Å) radiation source over a scan range from 10 °to 80 ° at a scan rate of 0.02 °/s. Surface morphology and chemical composition of the film were observed by SEM coupled with EDS.

Electrochemical and tribocorrosion measurements were performed at OCP in a unidirectional pin-on-disc tribometer, combined with a three-electrode cell in a PBS solution at room temperature (22 ± 1 ℃). Under static condition, corrosion behavior of CaP bioactive film coated Ti was characterized. The evolution of OCP, E_{oc}, within 3 h was performed continuously. EIS measurements with a sinusoidal potential variation of ±10 mV to OCP at frequencies from 10 kHz down to 3.98 mHz

were measured as well as the potentiodynamic polarization curves from -1 V to 1 V vs. Ag/AgCl at a scan rate of 1 mV/s of CaP bioactive film coated Ti at immersion time of 3 h and 24 h, respectively. Tribocorrosion experiments were performed under continuous mechanical loaded condition at F_n of 500 mN, with a rotation rate of 100 rpm and a total rotation number of 10 000 cycles. During continuous unidirectional sliding test, OCP evolution was recorded following with EIS measurement at frequencies from 10 kHz down to 39.8 mHz. Friction coefficient was recorded in the whole sliding period. When sliding ended, OCP evolution was performed for 3 h, and EIS measurement was carried out at frequencies from 10 kHz down to 3.98 mHz as that before sliding. Untreated Ti was used as control throughout the experiment. The surface morphology and chemical composition inside the track area were characterized by SEM coupled with EDS. The topography after tribocorrosion test was observed by optical profilometry.

In this chapter, untreated Ti was used as the reference material throughout the experiment. All experiments were repeated at least twice to ensure the reproducibility and the representative mean values were figured out in this work.

6.3 Electrochemical deposition of CaP bioactive film

In a mixing solution of $Ca(NO_3)_2 \cdot 4H_2O$ and $NH_4H_2PO_4$, three cathodic reactions [190] can be identified as:

The reduction of oxygen in the region from -0.15 V to -0.9 V vs. Ag/AgCl:

$$\mathbf{O_2 + 2H_2O + 4e^- \rightarrow 4OH^-} \qquad (6\text{-}1)$$

The cathodic reaction of hydrogen ions from $H_2PO_4^-$ from -0.9 V to -2 V vs. Ag/AgCl:

$$\mathbf{2H_2PO_4^- + 2e^- \rightarrow 2HPO_4^{2-} + H_2} \qquad (6\text{-}2)$$

The reduction of water at more cathodic potentials (< -2 V vs. Ag/AgCl):

$$\mathbf{2H_2O + 2e^- \rightarrow H_2 + 2OH^-} \qquad (6\text{-}3)$$

The HPO_4^{2-} ions produced by cathodic reaction completely react with Ca^{2+} ions and form a CaP bioactive film in the mixing solution on the electrode surface according to the following reaction:

$$\mathbf{Ca^{2+} + HPO_4^{2-} + 2H_2O \rightarrow CaHPO_4 \cdot 2H_2O} \text{ (brushite)} \qquad (6\text{-}4)$$

The current-time curves for CaP bioactive film deposition on cp Ti at different potentials from -1.4 V to -2.1 V vs. Ag/AgCl for 30 min were shown in Figure 6-1. The current density decreases

quickly at the very beginning, revealing the formation of CaP bioactive film which covers the surface of cp Ti substrate and inhibits the ions transfer at the interface between the solution and the substrate. Then a relative stable current density occurs after several minutes and no big difference in the ending current density is found when deposition potential is higher than -2 V vs. Ag/AgCl. But at the deposition potential of -2.1 V vs. Ag/AgCl, current density is enhanced possibly due to the reduction of water.

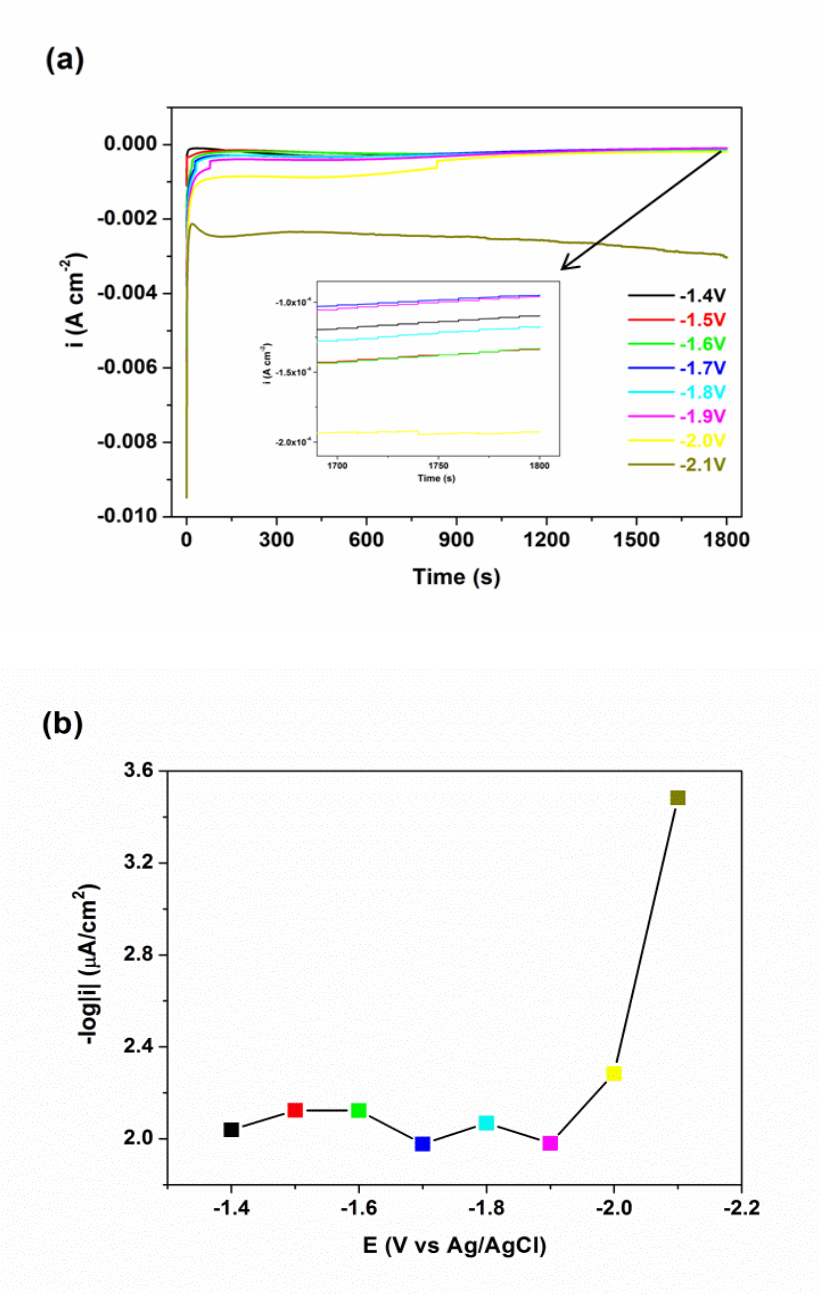

Figure 6-1 Current-time curve during deposition (a) and the ending current density of deposition (b) of CaP bioactive film on cp Ti at different potentials (vs. Ag/AgCl) for 30 min.

The thickness and Ca/P molar ratio of CaP bioactive film on cp Ti obtained at different deposition potentials for 30 min are measured by XRF spectrometry, as seen in Figure 6-2. The film thickness is around 3 μm when the deposition potential is in the range from -1.4 V to -1.9 V vs. Ag/AgCl. And then film thickness increases with the decrease of deposition potential from -1.9 V to -2.1 V vs. Ag/AgCl. The corresponding Ca/P molar ratio values obtained at potential range from -1.4 V to -2.0 V vs. Ag/AgCl are about 1.2 as referred to hydroxyapatite (HA, Ca/P ratio of 1.67), confirming the main cathodic reaction in this region is Eq. 6-2. It should be noticed that the Ca/P molar ratio vale is not 1.0 as that value of $CaHPO_4 \cdot 2H_2O$, indicating either the existence of other CaP components or the inaccuracy of XRF test results. Photos of CaP bioactive film coated Ti at different deposition potential for 30 min in Figure 6-3 shows the effect of deposition potential on the macrostructure of films. Combined with the results of film thickness and Ca/P molar ratio, an optimized deposition potential at -1.8 V is chosen to prepare a relative compact and uniform CaP bioactive film on cp Ti from an energy-saving point of view. All the following sections in this study are based on samples obtained under this electrochemical deposition condition.

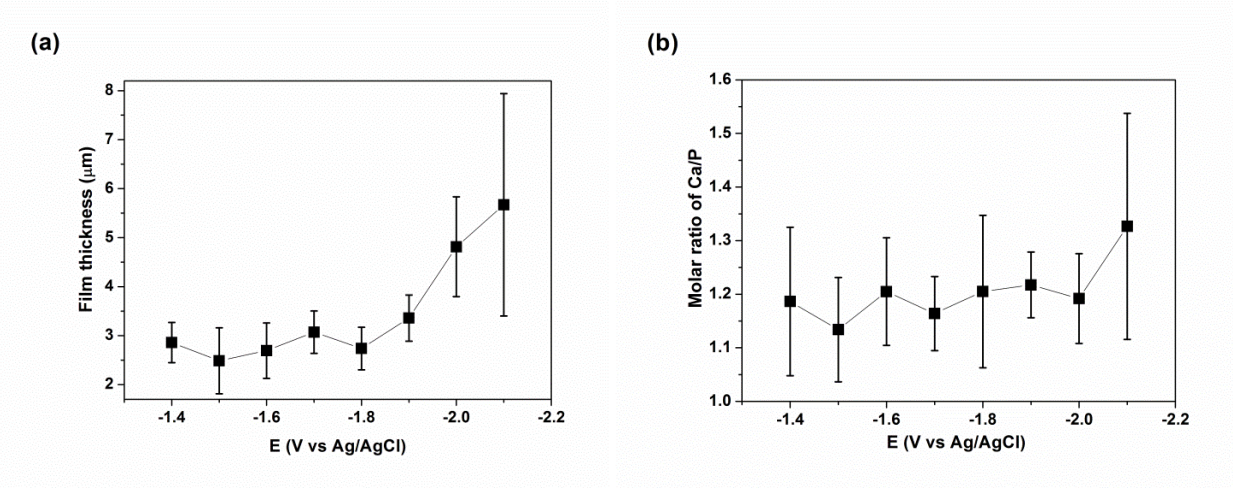

Figure 6-2 Film thickness (a) and Ca/P molar ratio (b) of CaP bioactive film on cp Ti obtained at different deposition potentials (vs. Ag/AgCl) for 30 min.

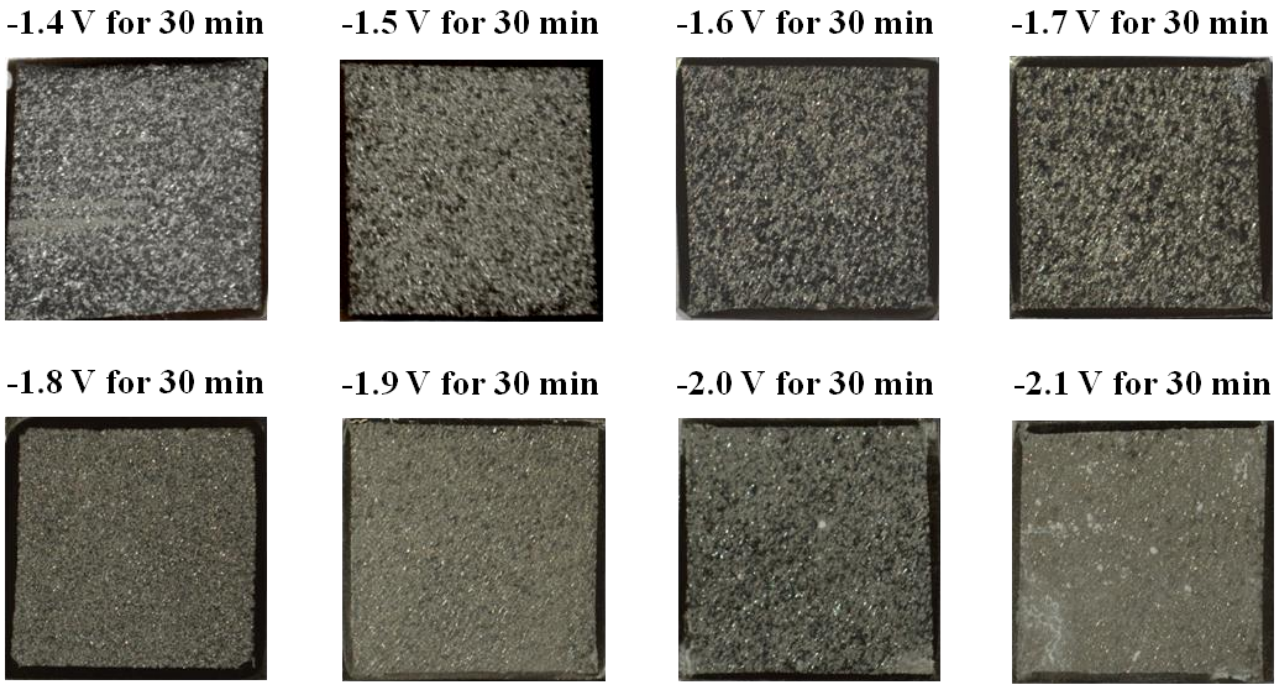

Figure 6-3 Photos of CaP bioactive film coated Ti obtained at different potentials (vs. Ag/AgCl).

6.4 Surface characterization

The surface topographies of CaP bioactive film coated Ti obtained at -1.8 V vs. Ag/AgCl for 30 min and untreated Ti are shown in Figure 6-4. And from this part on, all CaP bioactive film coated Ti samples were obtained at this cathodic potential for 30 min. Comparing with the untreated Ti, volcano-like topography on the surface CaP bioactive film coated Ti reveals that the film formation was faster at some sites, which might result from the preferred evolution of hydrogen and then get suitable local pH value for the formation of brushite during cathodic charging process at -1.8 V vs. Ag/AgCl. The average roughness value (R_a) of the CaP bioactive coated Ti increases from 0.39 μm to 2.01 μm and the microhardness value decreases from 176 $HV_{0.2}$ to 122 $HV_{0.2}$ (see Figure 6-5), indicating that the CaP bioactive film totally changes the surface topography and mechanical property of cp Ti.

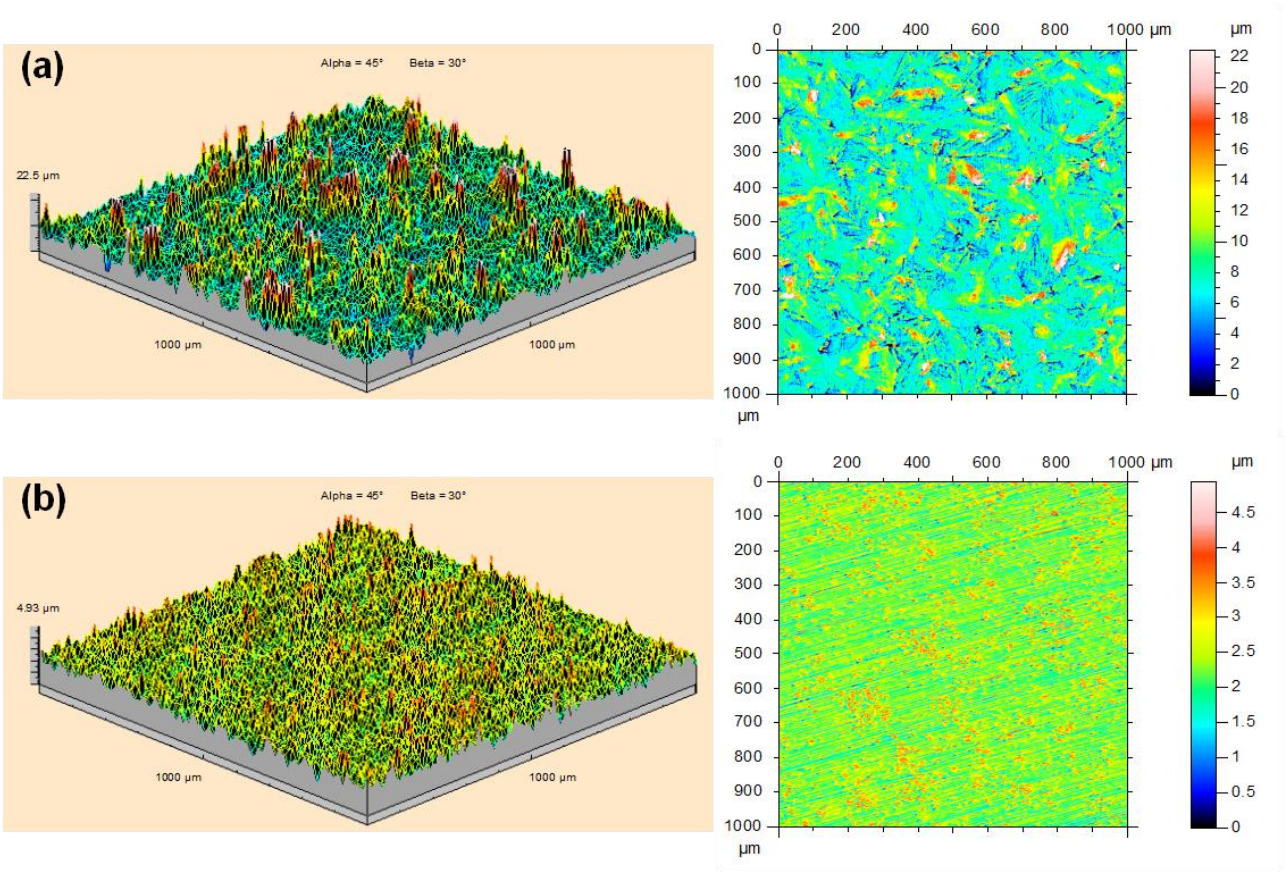

Figure 6-4 Profiles of CaP bioactive film coated Ti (a) and untreated Ti (b).

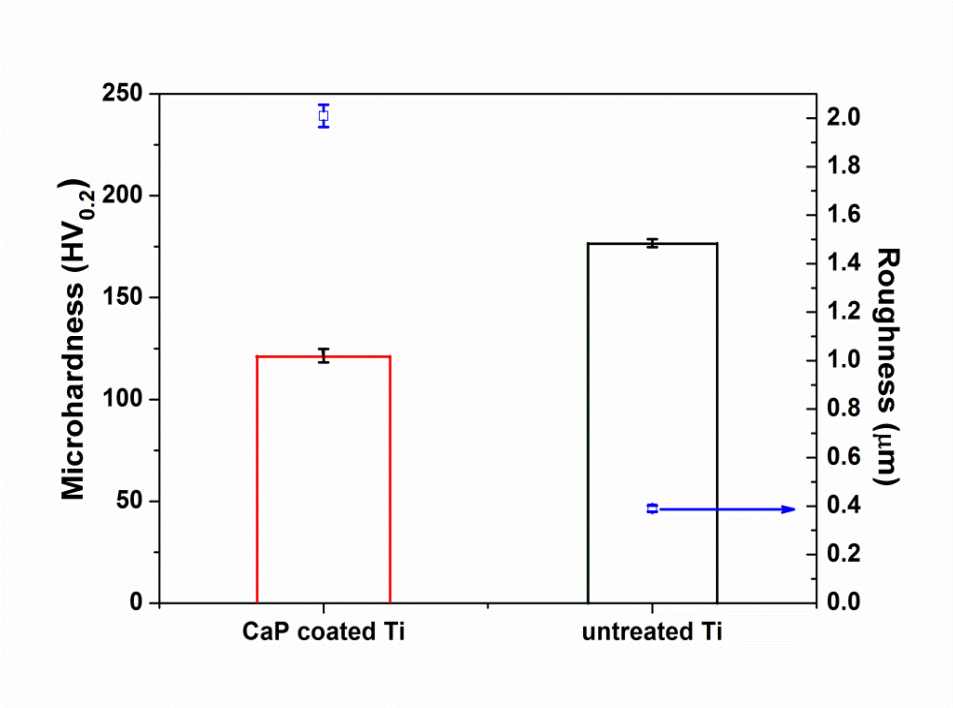

Figure 6-5 Microhardness and surface roughness of CaP bioactive film coated Ti and untreated Ti.

XRD patterns of CaP bioactive film coated Ti and untreated Ti samples are shown in Figure 6-6. Comparing with untreated Ti, typical brushite ($CaHPO_4 \cdot 2H_2O$, ICDD card No. 00-011-0293) peaks were clearly identified in the pattern of CaP bioactive film coated Ti. The diffraction peak (2θ) values of 11.8 °, 21.1 °, 23.5 °and 29.4 °were assigned to (020), (-121), (040) and (-112) planes of brushite. The remaining small peaks at 38.5 °and 40.2 °were attributed to (002) and (101) planes of cp Ti (ICDD card No. 00-005-0682). From this XRD patterns, it is concluded that cp Ti samples was covered with CaP bioactive film in the form of brushite, which is in accordance with Eq. 6-4.

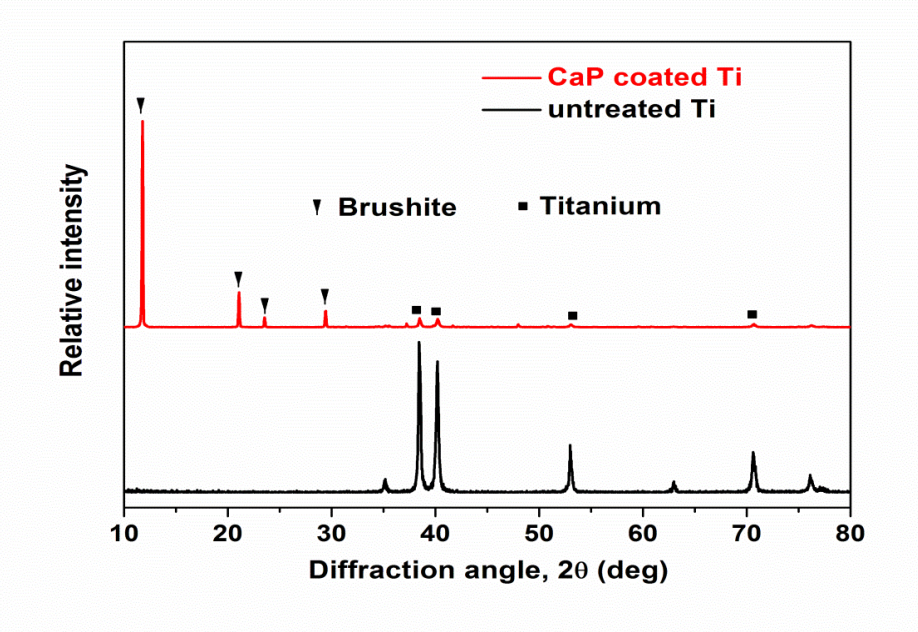

Figure 6-6 XRD patterns of CaP bioactive film coated Ti (red line) and untreated Ti (black line).

Surface morphology and chemical composition of CaP bioactive film coated Ti and untreated Ti were characterized by SEM coupled with EDS analysis, as seen in Figure 6-7. A complanate surface with regular grooves and small dot-like defaults was observed on untreated Ti after polishing with SiC emery papers. However, after electrochemical deposition process at -1.8 V vs. Ag/AgCl for 30 min, a flower-like CaP bioactive film entirely covered the surface of cp Ti. The similar morphologies were obtained in other groups [152, 154, 190, 191]. Comparing with the EDS analysis result of untreated Ti (see Figure 6-7d), the CaP bioactive film has a following composition: O = 52.1 wt%, P = 17.0 wt%, Ca = 20.3 wt% and Ti = 10.6 wt% (see Figure 6-7c). The atomic ratio value of Ca/P is 0.92, which is very close to 1.00 as the standard molar ratio value of Ca/P in $CaHPO_4 \cdot 2H_2O$. Different Ca/P molar ratio values, as ~ 1.2 obtained by XRF analysis and 0.92 obtained from EDS analysis, are shown in this study, revealing the fact that further accurate atomic analysis methods are needed in characterization of CaP bioactive film.

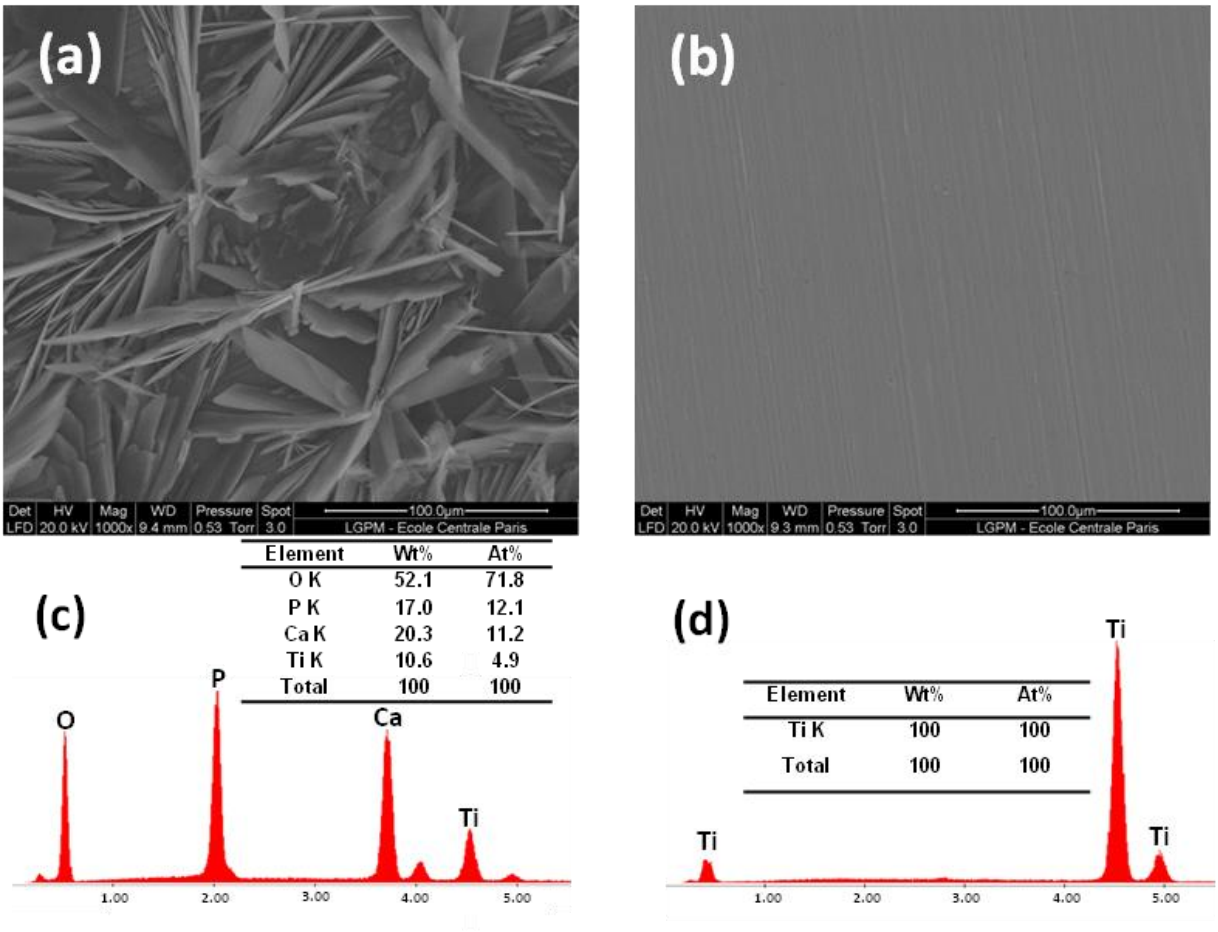

Figure 6-7 SEM images and EDS analysis of chemical composition of CaP bioactive film coated Ti (a, c) and untreated Ti (b, d).

6.5 Corrosion behavior of CaP bioactive film coated Ti under static condition

The OCP evolution curves of CaP bioactive film coated Ti and untreated Ti under static condition in the PBS solution are shown in Figure 6-8. It was observed that the OCP evolution of both samples shifted significantly in the noble direction. For untreated Ti, the E_{oc} value raises up from -0.45 V to -0.25 V vs. Ag/AgCl after immersion in the PBS solution for 3h due to the continuous growth of the passive oxide film on the surface of untreated Ti. For CaP bioactive film coated Ti, the E_{oc} value of -0.28 V vs. Ag/AgCl at the beginning of immersion is higher than that of untreated Ti and shifted to -0.14 V vs. Ag/AgCl after immersion in the PBS solution for 3 h. The OCP of both untreated Ti and CaP bioactive film coated Ti are in the TiO_2 stability region of the Ti-H_2O Pourbaix diagram (as seen in Figure 2-8 [111]). And the more noble OCP exhibits by CaP bioactive film reveals the improved corrosion resistance of film coated Ti surface. That can be attributed to the inhibition property of CaP bioactive film to the ions penetration combined with the continuous growing TiO_2 passive layer at the interface between cp Ti substrate and CaP bioactive film.

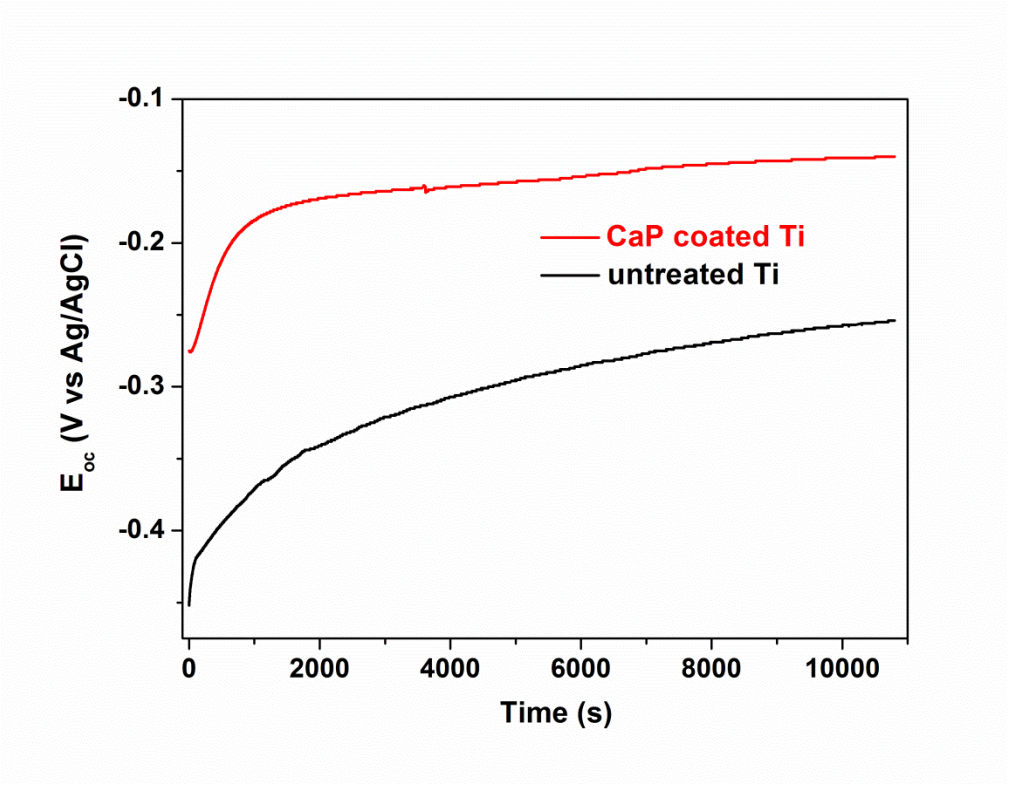

Figure 6-8 OCP evolution of CaP bioactive film coated Ti (red line) and untreated Ti (black line) in the PBS solution.

The Nyquist plots for CaP bioactive film coated Ti and untreated Ti, measured at immersion time of 3 h and 24 h under static condition in the PBS solution, are shown in Figure 6-9a. Both CaP bioactive film coated Ti and untreated Ti exhibit only a single semicircle in the entire frequency range, which corresponds to the equivalent circuit of R_s(CPE||R_p) with one time constant as presented as the inset in Figure 6-9a (the same as Figure 4-3), where R_s is the solution resistance and R_p is the polarization resistance of CaP bioactive film coated Ti or untreated Ti due to the barrier property of passive film. No existence of an added constant phase element (CPE2) for the CaP bioactive film reveals that this film has no effect on the corrosion mechanism of the cp Ti substrate. The selection of this equivalent circuit was a compromise between a reasonable fitting of the experimental values and a minimum of components in the equivalent circuit. The fitting procedure revealed that better agreement between theoretical and experimental data was obtained for both CaP bioactive film coated Ti and untreated Ti as seen the fitting curves in Figure 6-9. The parameters of the equivalent circuit are shown in Table 6-1.

The Bode impedance plots and Bode phase angle plots for CaP bioactive film coated Ti and untreated Ti after immersion for 3 h and 24 h in the PBS solution are shown in Figure 6-9b and 6-9c, respectively. From the Bode impedance plots, it is clearly observed that the specific polarization resistance, r_p, of CaP bioactive film coated Ti increases from 1.02×10^7 Ω cm^2 at the immersion time of 3 h to 1.56×10^7 Ω cm^2 at the immersion time of 24 h. For untreated Ti, r_p value increases from

7.69 × 10^5 Ω cm^2 at the immersion time of 3 h to 4.70 × 10^6 Ω cm^2 at the immersion time of 24 h, indicating that the corrosion resistance becomes stronger due to the growth of the passive film on the surface of untreated Ti. Correspondingly, the Bode phase angle plot shows a broader frequency range close to -85 º.

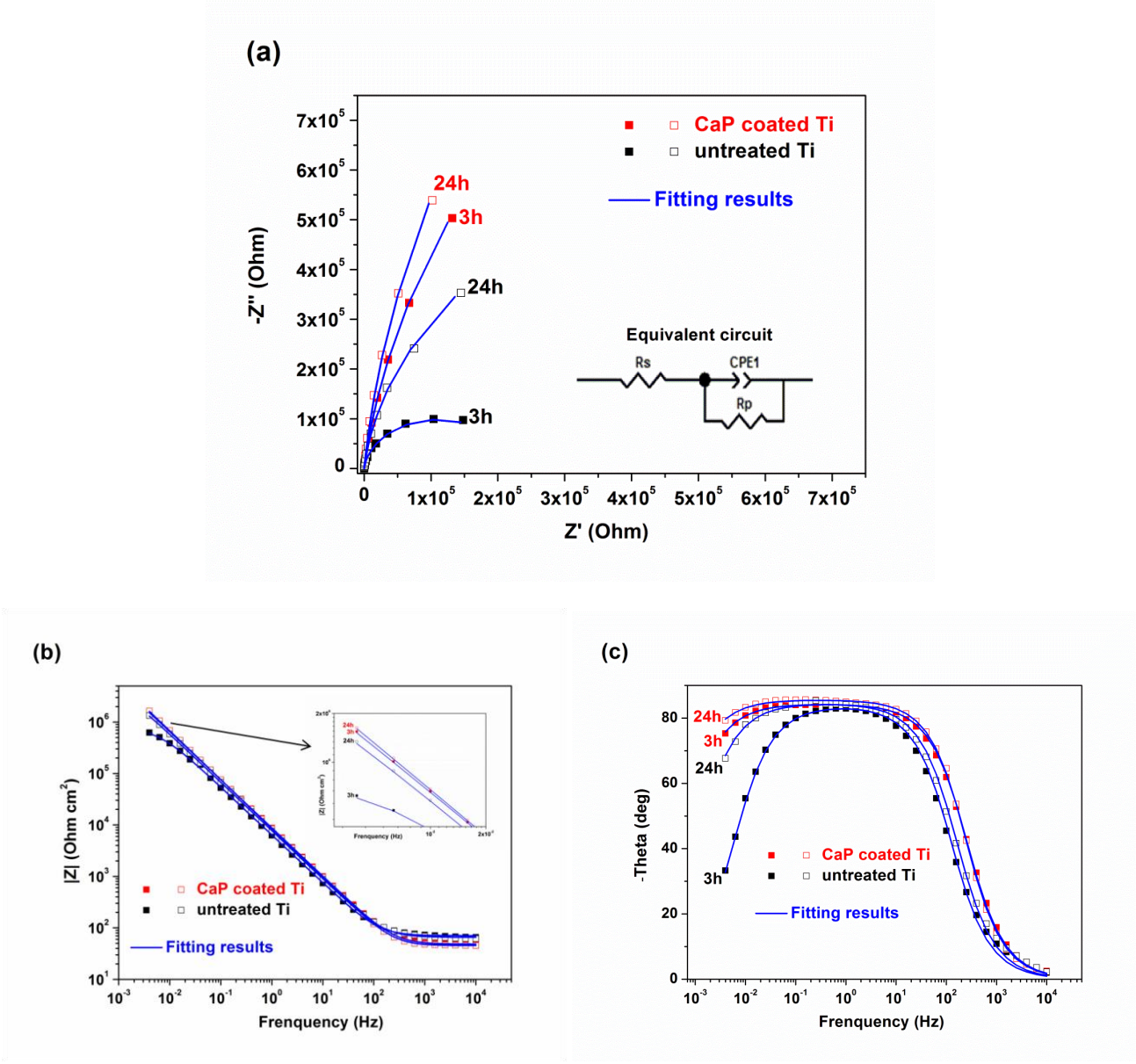

Figure 6-9 Nyquist plots (a), Bode impedance plots (b) and Bode phase angle plots (c) for CaP bioactive film coated Ti (red square) and untreated Ti (black square) measured at immersion time of 3 h and 24 h under static condition in the PBS solution.

Table 6-1 Parameters of the equivalent circuit for CaP bioactive film coated Ti and untreated Ti under static condition.

Sample	A_0 (cm^2)	Time (h)	R_s (Ohm)	T-1 ($\mu F \cdot cm^{-2} \cdot s^{\phi-1}$)	ϕ-1	R_p (Ohm)	r_p (Ohm·cm^2)
CaP coated Ti	2.98	3	16.2	20.3	0.94	3.41×10^6	1.02×10^7
		24	15.2	20.4	0.95	5.24×10^6	1.56×10^7
untreated Ti	3.51	3	20.1	28.2	0.93	2.19×10^5	7.69×10^5
		24	18.7	23.0	0.94	1.34×10^6	4.70×10^6

*A_0 is the total surface area exposed to the electrolyte.

As demonstrated in previous chapters, the specific polarization resistance values for metallic materials in the range of 10^3 Ω cm^2 (or lower) indicate the presence of an active surface, while values around 10^5 Ω cm^2 (or higher) indicate a passive surface [181, 183]. All the r_p values in Table 6-1 reveal that a passive surface state reached on either CaP bioactive film coated Ti or untreated Ti under static condition in the PBS solution. And the increase of r_p value in this study confirms the enhanced anti-corrosive property of cp Ti due to the growth of passive oxide layer on the surface. It should be noticed that during the studied period, even the increase extent of r_p for untreated Ti is larger, the r_p value measured at immersion time of 24 h is still smaller than r_p of CaP bioactive film coated Ti at immersion time of 3 h. The results indicate that surface modification of cp Ti with CaP bioactive film strongly improves the corrosion resistance of cp Ti but still keeps the growth of passive oxide layer on its surface.

Figure 6-10 shows the potentiodynamic polarization curves of CaP bioactive film coated Ti and untreated Ti in the potential range from -1 V to 1 V vs. Ag/AgCl, measured at immersion time of 3 h and 24 h under static condition in the PBS solution. As illustrated in Chapter 4, the potentiodynamic polarization curves for untreated Ti can be divided into four domains: (I) cathodic domain; (II) prepassive domain; (III) passive domain and (IV) transpassive domain (see Section 4.3). Under static condition in this study, all OCP evolution values of CaP bioactive film coated Ti and untreated Ti are in the prepassive domain. And as dental and orthopedic implant materials, the current densities in the body potential range of 400-500 mV vs. Ag/AgCl (defined by Velten et al. [192]) are more interested. Here, the polarization parameters like corrosion potential (E_{corr}), the specific current density at the prepassive potential of 0.1 V vs. Ag/AgCl, $i_{prepass}$ and the specific current density at the body potential of 0.4 V vs. Ag/AgCl, i_{bp} of CaP bioactive film coated Ti and untreated Ti are summarized in Table 6-2. Compared with the untreated Ti, CaP bioactive film coated Ti shows a shift of E_{corr} (about -0.08 V) in the cathodic direction, but the decrease in current density at E_{corr} indicates the improved corrosion resistance of CaP bioactive film coated Ti. The shift of E_{corr} in cathodic direction might due to the influence of the easy hydrogen evolution in the presence of $CaHPO_4$, as illustrated as follows:

$$2HPO_4^{2-} + 2e^- \rightarrow 2PO_4^{3-} + H_2 \qquad (6\text{-}5)$$

With local pH value changes during potential scanning, the corrosion mechanism on cp Ti substrate under CaP bioactive film is altered. With immersion time increase, the $i_{prepass}$ for untreated Ti significantly decreases, revealing the improved corrosion resistance of untreated Ti due to the growth of passive oxide film on cp Ti substrate in the PBS solution. Almost no change occurs in the value of i_{bp} for untreated Ti. But for CaP bioactive film coated Ti, both the values of $i_{prepass}$ and i_{bp} increase slightly, might resulting from the dissolution of CaP bioactive film when local pH value changes, see Figure 6-11. It is clearly observed the film prints, where preferential growth of calcium phosphate took place. But the major CaP bioactive film has disappeared and only very small amount of film remains (P, 5.3 wt% and Ca, 5.9 wt% can be detected by EDS) on the surface of cp Ti substrate after immersion time of 24 h under static condition in the PBS solution.

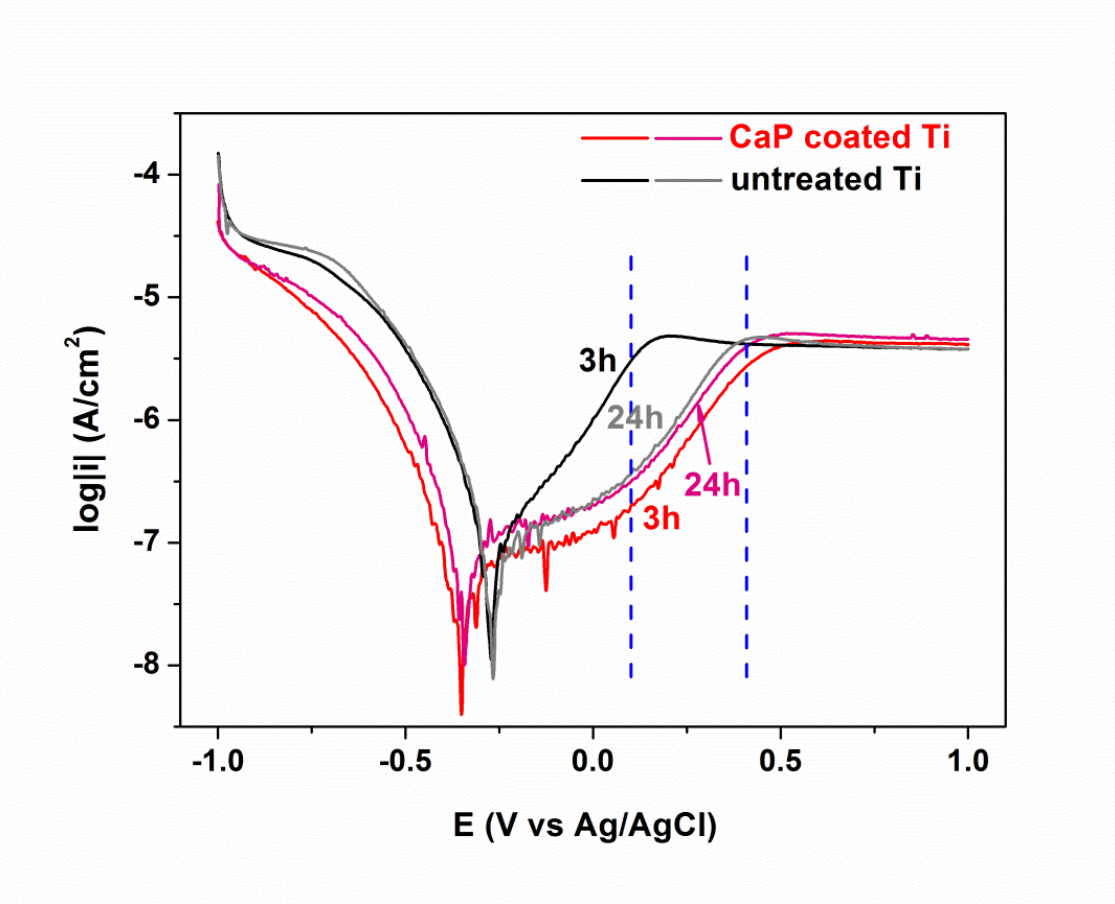

Figure 6-10 Potentiodynamic polarization curves of CaP bioactive film coated Ti and untreated Ti from -1 V to 1 V vs. Ag/AgCl at a scan rate of 1 mV/s measured at immersion time of 3 h and 24 h under static condition in the PBS solution.

Table 6-2 Electrochemical data obtained from potentiodynamic polarization tests.

Sample	Time (h)	E_{corr} (V)	$*i_{prepass}$ ($A \cdot cm^{-2}$)	$*i_{bp}$ ($A \cdot cm^{-2}$)
CaP coated Ti	3	-0.35	1.98×10^{-7}	2.55×10^{-6}
	24	-0.35	3.08×10^{-7}	3.80×10^{-6}
untreated Ti	3	-0.27	3.01×10^{-6}	4.19×10^{-6}
	24	-0.27	3.50×10^{-7}	4.43×10^{-6}

$*i_{prepass}$: specific current density at prepassive potential of 0.1 V vs. Ag/AgCl

$*i_{bp}$: specific current density at body potential of 0.4 V vs. Ag/AgCl

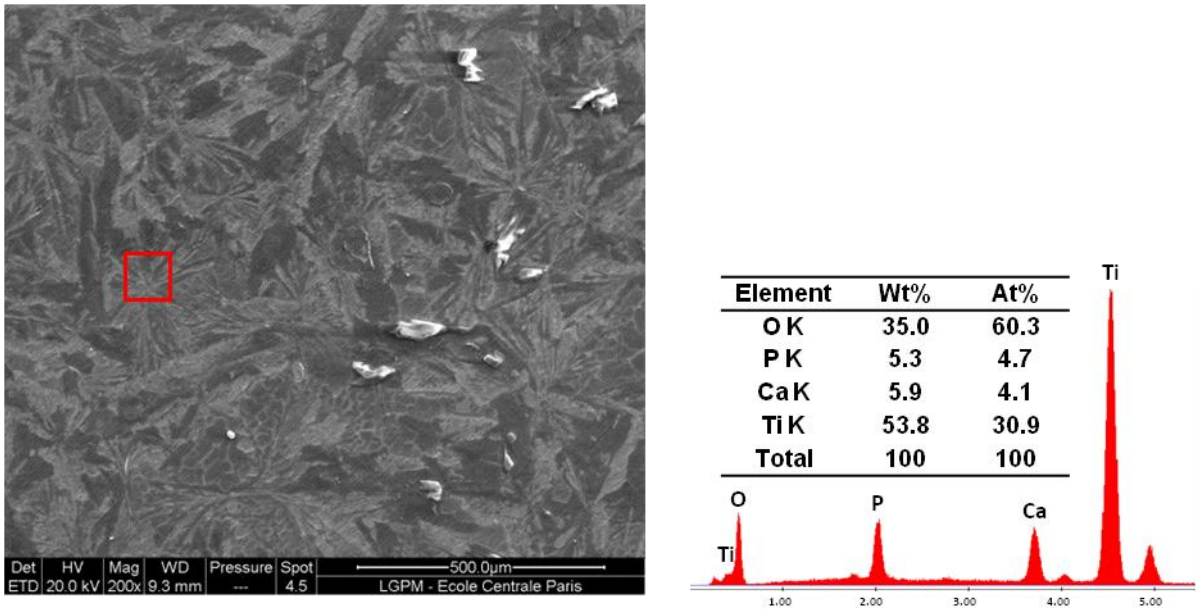

Figure 6-11 SEM image and EDS analysis (the marked square) of CaP bioactive film coated Ti after potentiodynamic polarization test at immersion time of 24 h in the PBS solution.

6.6 Tribocorrosion behavior of CaP bioactive film coated Ti during and after continuous unidirectional sliding test

Tribocorrosion tests were performed when E_{oc} got stabilized after immersion for 3 h in the PBS solution. In order to evaluate the wear-corrosion behavior of CaP bioactive film coated Ti and untreated Ti during continuous unidirectional sliding, a relative small loading force, F_n of 500 mN is imposed at a rotation rate of 100 rpm and the total rotation number of 10 000 cycles. The OCP evolution curves and friction coefficient curves of both CaP bioactive film coated Ti and untreated Ti samples during sliding are shown in Figure 6-12.

The results in Figure 6-12a shows that E_{oc} dropped sharply down to a more negative potential value at the moment when sliding motion starts. It reveals the change of surface state from passive to active on the sliding track of both samples. In the case of untreated Ti, the potential drop-down, $\Delta E = |E_{max} - E_{min}|$ during sliding test was 0.26 V, where E_{max} presents the potential at the start of sliding and E_{min} the minimum potential during continuous unidirectional sliding at F_n of 500 mN. And for CaP bioactive film modified Ti, a larger ΔE value of 0.51 V was obtained. Furthermore, the E_{oc} variation of CaP bioactive film coated Ti during sliding test period is higher than that of untreated Ti. These phenomena demonstrate the influence of the destruction and dissolution of CaP bioactive film on OCP evolution of cp Ti.

The friction coefficient curves were measured during sliding, as shown in Fig. 5-15b. Unlike the higher E_{oc} fluctuation, the coefficient evolution of CaP bioactive film coated Ti is a bit smaller and smoother than that of untreated Ti in the time range from 1500 s to 3000 s, corresponding to the rotation number range from 2500 cycles to 5000 cycles. This may be due to the lubricant effect of CaP bioactive film in the wear track. After that, the coefficient values for both samples are almost the same (about 0.62) until the end of sliding tests, revealing that a similar contact mode as untreated Ti was inducted for CaP bioactive film coated Ti when the major $CaHPO_4 \cdot 2H_2O$ was dissolved after rotation of 5000 cycles under mechanical loaded condition.

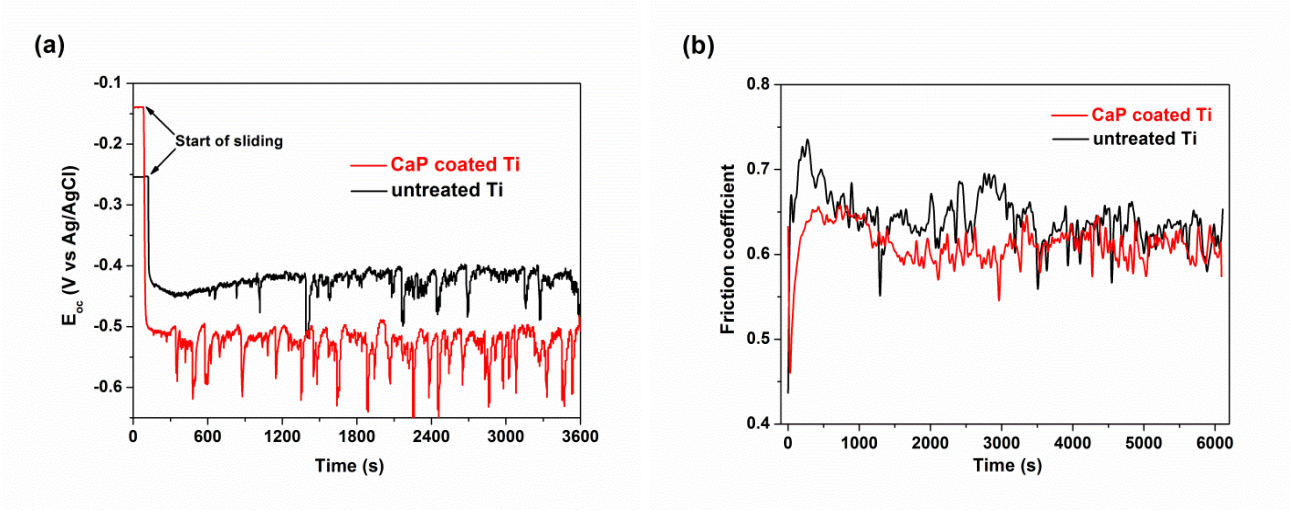

Figure 6-12 OCP evolution (a) and friction coefficient (b) of CaP bioactive film coated Ti (red line) and untreated Ti (black line) during continuous unidirectional sliding tests performed at F_n of 500 mN.

When continuous unidirectional sliding motion stops, the OCP evolution curves for both the untreated Ti and CaP bioactive film coated Ti exhibit an anodic shift (see Figure 6-13), indicating the occurrence of repassivation of the active surface inside the sliding wear track area. Although it takes shorter time to return back to the initial E_{oc} value of -0.25 V vs. Ag/AgCl for untreated Ti, the final potential of CaP bioactive film coated Ti is still higher than untreated Ti after sliding for ~3 h immersion under static condition in the PBS solution.

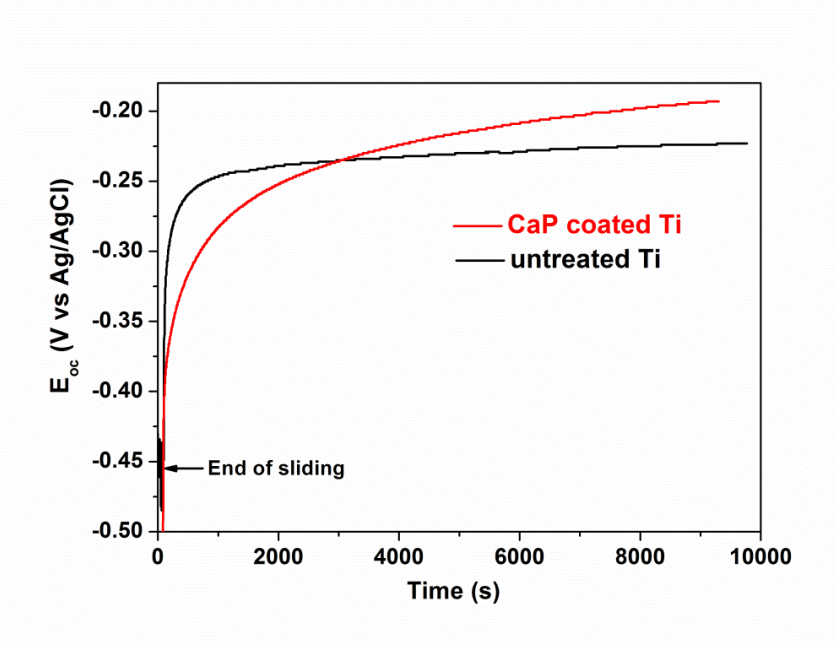

Figure 6-13 OCP evolution of CaP bioactive film coated Ti (red line) and untreated Ti (black line) after continuous unidirectional sliding tests.

The Nyquist plots for CaP bioactive film coated Ti and untreated Ti, measured before, during and after unidirectional sliding at F_n of 500 mN in the PBS solution, are shown in Figure 6-14a1 and 6-14a2. It is clearly to see that only one single semicircle in the entire frequency range was plotted for both samples measured before, during and after sliding tests. The same equivalent circuit as the inset of Figure 6-9a with one time constant, R_s(CPE||R_p) can be used to fit the experimental data obtained by EIS measurement. The fitted parameters of the equivalent circuit for CaP bioactive film coated Ti and untreated Ti are summarized in Table 6-3.

Table 6-3 Parameters of the equivalent circuit for for CaP bioactive film coated Ti and untreated Ti measured before, during and after continuous unidirectional sliding test at F_n of 500 mN.

Sample	A_0 (cm^2)	test	R_s (Ohm)	T-1 ($\mu F \cdot cm^{-2} \cdot s^{\phi-1}$)	ϕ-1	R_p (Ohm)	r_p (Ohm·cm^2)
CaP coated Ti	3.30	before	16.1	20.2	0.94	5.01×10^6	1.65×10^7
		during	15.3	31.4	0.91	9600	3.17×10^4
		after	14.7	22.3	0.95	1.75×10^6	5.79×10^6
untreated Ti	3.40	before	13.7	25.2	0.96	1.36×10^5	4.63×10^5
		during	13.4	29.3	0.94	3100	1.05×10^4
		after	12.8	22.9	0.95	2.51×10^5	8.54×10^5

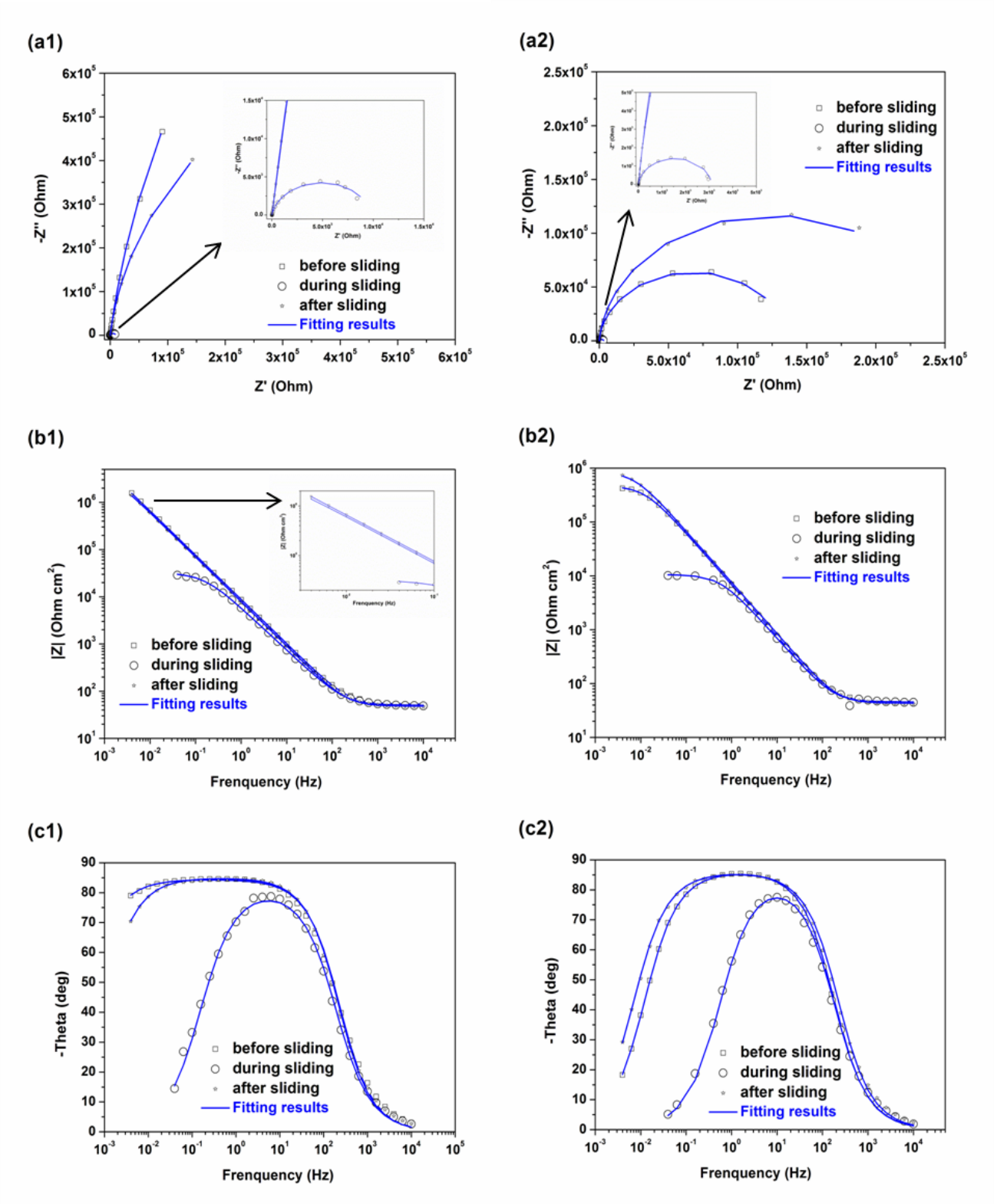

Figure 6-14 Nyquist plots (a), Bode impedance plots (b) and Bode phase angle plots (c) for CaP bioactive film coated Ti (1) and untreated Ti (2) measured before (square), during (ring) and after (star) continuous unidirectional sliding test at F_n of 500 mN.

Comparing the r_p values for CaP bioactive film coated Ti and untreated Ti measured with different samples in Table 6-1 and 6-3, it should be noticed that the reproducibilities of electrochemical measurement results are not well but the values for each type of material are in the same order of magnitude. As explained in the previous chapters, the intrinsic property of sample surface and the actual experimental environment have significant influence on the electrochemical measurement results. So, all values presented here should be considered as the qualitative changes rather than the quantitative changes for the explication of resistance change before, during and after sliding test. To get more accurate information, the strict control of experimental operation in the electrochemical measurement and more parallel repetitions with different samples are necessary in the future work.

During continuous unidirectional sliding tests at F_n of 500 mN, the r_p value decreased from 1.65 $\times 10^7$ Ω·cm^2 measured before sliding to 3.17 $\times 10^4$ Ω·cm^2 for CaP bioactive film coated Ti and from 4.63 $\times 10^5$ Ω·cm^2 measured before sliding to 1.05 $\times 10^4$ Ω·cm^2 for untreated Ti. Under the guidance of the tribocorossion protocol for surface modified Ti in Chapter 3, a general specific polarization resistance is used in this chapter to give a qualitative comparison between CaP bioactive film coated Ti and untreated Ti. The significant decrease in r_p value can be explained by the destruction of passive film on the surface of cp Ti under mechanical loading condition. In the absence of protective oxide layers in the sliding track, bared substrate directly exposes to the corrosive electrolyte, which permitted the entrance of corrosive species and then corrosion reactions occur at the interface between cp Ti and the PBS solution. The higher r_p value of CaP bioactive film coated Ti during sliding test confirms the better barrier performance of CaP bioactive film on cp Ti. It might prolong the path of entrance for corrosive species and inhibit the corrosion reactions on the surface of Ti substrate.

When sliding motion stops, both the r_p values of CaP bioactive film coated Ti and untreated Ti increase quite a lot, suggesting a self-healing process as repassivation of cp Ti in the PBS solution. But it should be noticed that a significant decrease of specific polarization resistance from 1.65 $\times 10^7$ Ω·cm^2 measured before sliding down to 5.79 $\times 10^6$ Ω·cm^2 measured after sliding is observed for CaP bioactive film coated Ti. This reveals that the destruction of CaP bioactive film affects the recovery of sample's barrier property. In contrast, an increase of the r_p value from 4.63 $\times 10^5$ Ω·cm^2 measured before sliding up to 8.54 $\times 10^5$ Ω·cm^2 measured after sliding for untreated Ti indicates the efficient repassivation inside the track area of cp Ti without any modification. Combined with the sustained TiO_2 film growth outside the track area, corrosion resistance of untreated Ti enlarges with immersion time after mechanical loading perturbation at F_n of 500 mN. This excellent property attracts the attentions in biomedical application as dental and orthopedic implants. And the higher corrosion resistance property of CaP bioactive film coated Ti makes it become an attractive material instead of the untreated Ti.

6.7 Characterization of the wear track on CaP bioactive film coated Ti after continuous unidirectional sliding test

Figure 6-15 shows the SEM images and EDS analysis inside the track areas of CaP bioactive film coated Ti (a, c) and untreated Ti (b, d) after 10 000 cycles of continuous unidirectional sliding at F_n of 500 mN. For CaP bioactive film modified Ti, a track width of 0.62 mm is obtained. The track area covers the removal of CaP bioactive film and the further destruction of cp Ti substrate under CaP bioactive film. Chemical composition analysis result inside the track area is presented in Figure 6-15c. Although major amount of CaP bioactive film has been dissolved, the remaining contents of phosphorus (P, 0.8 wt%) and calcium (Ca, 0.4 wt%) indicate that a small amount of CaP bioactive film still stays on the surface of cp Ti even after rotation of 10 000 cycles. The higher wear resistance of CaP bioactive film coated Ti is derived from the good adhesion of the initial not the further growing CaP bioactive film with the substrate. Once this film is extremely thin or partially total destroyed by sliding motion of ZrO_2 counter body, the friction coefficient value becomes similar as that of untreated Ti, as seen in Figure 6-12b. For untreated Ti, a track width of about 0.5 mm is obtained. The regular pattern of grooves and attached corrosion debris inside the track area of untreated Ti shows the substrate was worn by sliding motion of ZrO_2 counter body in this study. Chemical composition analysis result in Figure 6-15d shows the appearance of high oxygen content (O, 12.0 wt%) indicates the repassivation of cp Ti to form the titanium oxide film on its surface.

The track profiles of CaP bioactive film coated Ti and untreated Ti after continuous unidirectional sliding tests at F_n of 500 mN are shown in Figure 6-16. The track depth and track width of both samples are difficult to well identified, due to the higher roughness of CaP bioactive film coated Ti and the tiny material loss of untreated Ti. At F_n of 500 mN, the low material loss in this study reveals that both CaP bioactive coated Ti and untreated Ti are good choice for biomedical implant application in the mild loading applied parts. But CaP bioactive film coated Ti is the better one as it can be regard as the source of Ca and P ions for the formation of HA.

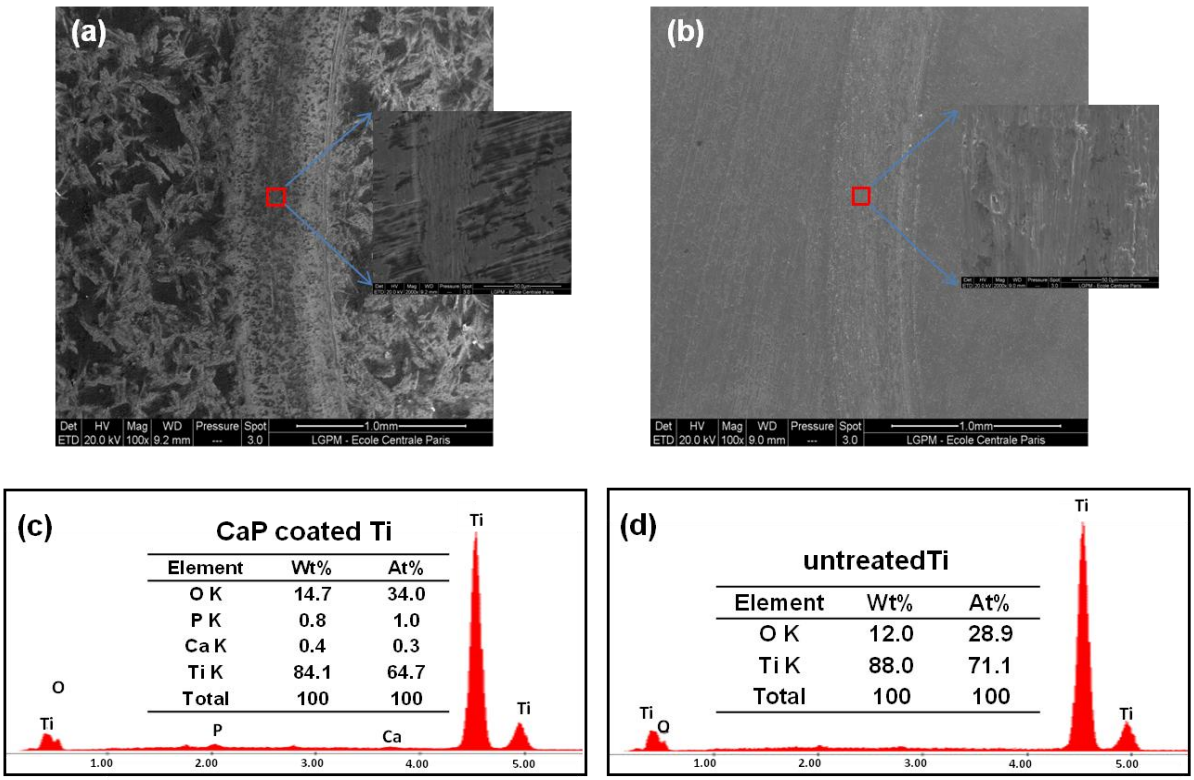

Figure 6-15 SEM images (a, b) and EDS analysis inside the tracks (c, d) of CaP bioactive film coated Ti (a, c) and untreated Ti (b, d) after continuous unidirectional sliding tests at F_n of 500 mN.

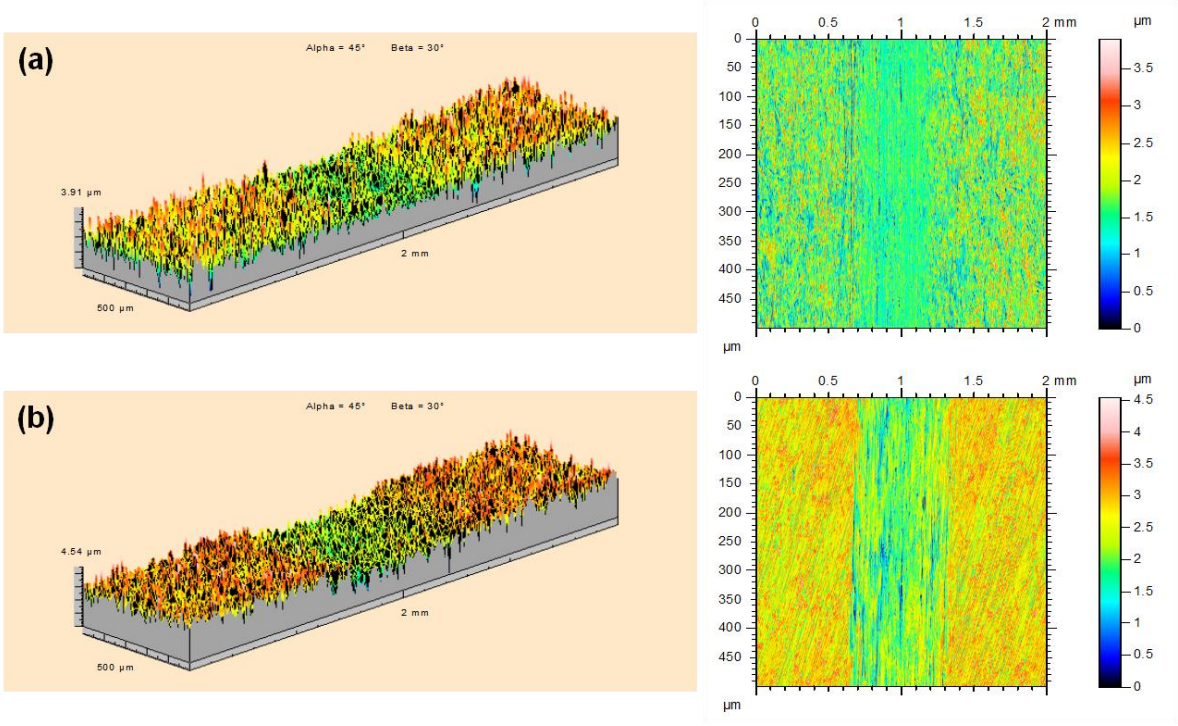

Figure 6-16 Profiles of CaP bioactive film coated Ti (a) and untreated Ti (b) after continuous unidirectional sliding tests at F_n of 500 mN.

6.8 Conclusions

Surface modification of cp Ti with electrochemical deposition of CaP bioactive film is a good method to improve its bioactivity. An optimized deposition condition was selected as -1.8 V vs. Ag/AgCl for 30 min in this study. This film is mainly in the form of brushite ($CaHPO_4\ 2H_2O$) characterized by XRD. The surface roughness and microhardness of CaP bioactive film are different from the values of cp Ti substrate.

The OCP evolution curves before sliding under static condition, during sliding under mechanical loaded condition at F_n of 500 mN and after sliding under static condition, for both CaP bioactive film coated Ti and untreated Ti, change significantly in the whole test period. The decrease of E_{oc} at the moment when sliding motion starts is due to the destruction of passive film on the surface of cp Ti substrate. While the increase of E_{oc} at the moment when sliding motion stops is due to the repassivation of passive film. Results of EIS and potentiodynamic polarization measurements show that the corrosion resistance of untreated Ti enhances with immersion time increase. The $i_{prepass}$ value for untreated Ti decreases and its r_p value incrases at immersion time of 24 h, comparing with the values measured at immersion time of 3 h. For CaP bioactive film coated Ti, the same tendency occurs to its r_p value, but the $i_{prepass}$ value just slightly increases at immersion time of 24 h. The dissolution of CaP bioactive film is thought to change the local pH value and further induce the increase of $i_{prepass}$.

Under mechanical loaded condition, the impedance values r_p of both CaP bioactive film coated Ti and untreated Ti decrease significantly due to the dissolution and removal of CaP bioactive film/passive film on CaP bioactive film coated Ti and the removal of passive film on cp Ti. Although the value of E_{oc} during sliding decreases more for the former sample, its higher r_p value combined with the relative lower friction coefficient in the rotation number range from 2500 cycles to 5000 cycles indicates the improved corrosion-wear performance of cp Ti with surface modification of CaP bioactive film.

When mechanical solicitation stops, the higher impedance value r_p of CaP bioactive film coated Ti than that of untreated Ti indicates that surface modification with CaP bioactive film can become an attractive method to promote the application of cp Ti as biomedical implants.

Chapter 7: Effect of CaP/TiO_2 bioceramic film on corrosion and tribocorrosion behavior of cp Ti

7.1 Introduction

From Chapter 6, the dissolution of CaP bioactive film (in the form of brushite, $CaHPO_4 \cdot 2H_2O$) and high friction coefficient limits this material as an excellent surface modification of cp Ti. In order to improve the wear resistance and keep a long term bioactive effect on cp Ti, CaP bioactive film coated Ti was further sintered at 650 ℃ for 6 h. Longer sintering time as 48 h as mentioned in Chapter 5 is not suggested, since the aim of this step is mainly to change the property of CaP film rather than cp Ti substrate. A composite of CaP/TiO_2 bioceramic film was then obtained in the forms of whitlockite ($Ca_3(PO_4)_2$), rutile (TiO_2) as well as a few $CaTi_{21}O_{38}$ at the interface of CaP bioactive film and cp Ti substrate by the characterization of XRD. Surface morphology/chemical composition and topography were characterized by SEM coupled with EDS and optical profilometry. The effect of CaP/TiO_2 bioceramic film on the corrosion behavior of cp Ti was studies by electrochemical measurements like OCP, EIS and potentiodynamic polarization under static condition in the PBS solution. The tribocorrosion behavior of CaP bioactive film coated Ti before and after sintering was investigated under mechanical loaded condition by using a pin-on-disc tribometer at F_n of 500 mN to prevent the strong destruction of cp Ti substrate. Results show that a significant improvement in corrosion and tribocorrosion resistance was detected for the CaP/TiO_2 bioceramic film coated Ti than CaP bioactive film coated Ti. Moreover, material loss of the CaP/TiO_2 bioceramic film coated Ti was significantly decreased due to the low dissolution rate and the high hardness of the bioceramic film. Moreover, thermal oxidized Ti prepared at 650 ℃ for 6 h without any CaP bioactive film (TO Ti_6h) was also studied as a supplementary reference in this study. Although TO Ti_6h owns better corrosion and tribocorrosion resistance (similar to that value in Chapter 5) than CaP/TiO_2 bioceramic film coated Ti, it is still inferior to CaP/TiO_2 bioceramic film coated Ti due to its mismatch in mechanical property with natural bone and its poor bioactivity.

7.2 Experimental details

The CaP bioactive film coated Ti samples, prepared by an electrodeposition method at -1.8 V vs. Ag/AgCl for 30 min as mentioned in Chapter 6, were further sintered in a furnace at 650 ℃ for 6 h, following by a slow cooling rate to the room temperature in the furnace itself to obtain the CaP/TiO_2 bioceramic film coated Ti samples. Optical profilometry was used to measure the surface topography and the average roughness value was calculated on square regions with length of 1000 μm × 1000 μm. Vickers microhardness test was performed with a test force of 200 gf and full load period of 15 s. The phase constituents CaP/TiO_2 bioceramic film coated Ti was determined by XRD using a Cu K_α (λ = 1.54 Å) radiation source over a scan range from 20 ° to 80 ° at a scan rate of 0.02 °/s. Surface morphology and chemical composition of the film were observed by SEM coupled with EDS.

Electrochemical and tribocorrosion measurements were performed at OCP in a unidirectional pin-on-disc tribometer, combined with a three-electrode cell in a PBS solution at room temperature (22 ± 1 ℃). Before sliding, corrosion behavior of CaP/TiO_2 bioceramic film coated Ti was

characterized by electrochemical measurements, such as OCP evolution within 3 h, the potentiodynamic polarization curves from -1 V to 3 V vs. Ag/AgCl at a scan rate of 1 mV/s as well as EIS measurements with a sinusoidal potential variation of ± 10 mV to OCP at frequencies from 10 kHz down to 3.98 mHz at immersion time of 3 h. Tribocorrosion experiments were performed under continuous mechanical loaded condition at F_n of 500 mN, with a rotation rate of 100 rpm and a total rotation number of 10 000 cycles. During continuous unidirectional sliding test, OCP evolution was recorded following with EIS measurement at frequencies from 10 kHz down to 39.8 mHz. Friction coefficient was recorded in the whole sliding period. After sliding, OCP evolution was performed for 3 h, and EIS measurement was carried out at frequencies from 10 kHz down to 3.98 mHz as that before sliding. The surface morphology and chemical composition inside the track area were characterized by SEM coupled with EDS. The topography after tribocorrosion test was observed by optical profilometry.

In this chapter, both CaP bioactive film coated Ti before sintering and TO Ti_6h (prepared at 650 ℃ for 6 h without any CaP bioactive film) were used as the reference materials throughout the experiment. All experiments were repeated at least twice to ensure the reproducibility and the representative mean values were figured out in this work.

7.3 Surface characterization

The surface topographies of CaP/TiO_2 bioceramic film coated Ti, CaP bioactive film coated Ti and TO Ti_6h are shown in Figure 7-1. Comparing with CaP bioactive film coated Ti, the volcano-like topography keeps on the surface of CaP/TiO_2 bioceramic film coated Ti, indicating that the sintering condition at 650 ℃ for 6 h takes no collapse of CaP bioactive film. The average roughness value of CaP/TiO_2 bioceramic film coated Ti increases from 2.01 μm to 2.37 μm and the microhardness value increases from 122 $HV_{0.2}$ to 177 $HV_{0.2}$ (see Figure 7-2), revealing that the sintering process slightly changes the surface topography of CaP bioactive film coated Ti and the higher wear resistance of CaP/TiO_2 bioceramic film coated Ti occurs due to the formation of harder titanium oxides. As supplementary reference, TO Ti_6h exhibits a rather smooth surface with an average roughness value of 0.39 μm (the same as that of untreated Ti, seen in Figure 5-1), and it owns a harder surface with the microhardness value of 395 $HV_{0.2}$.

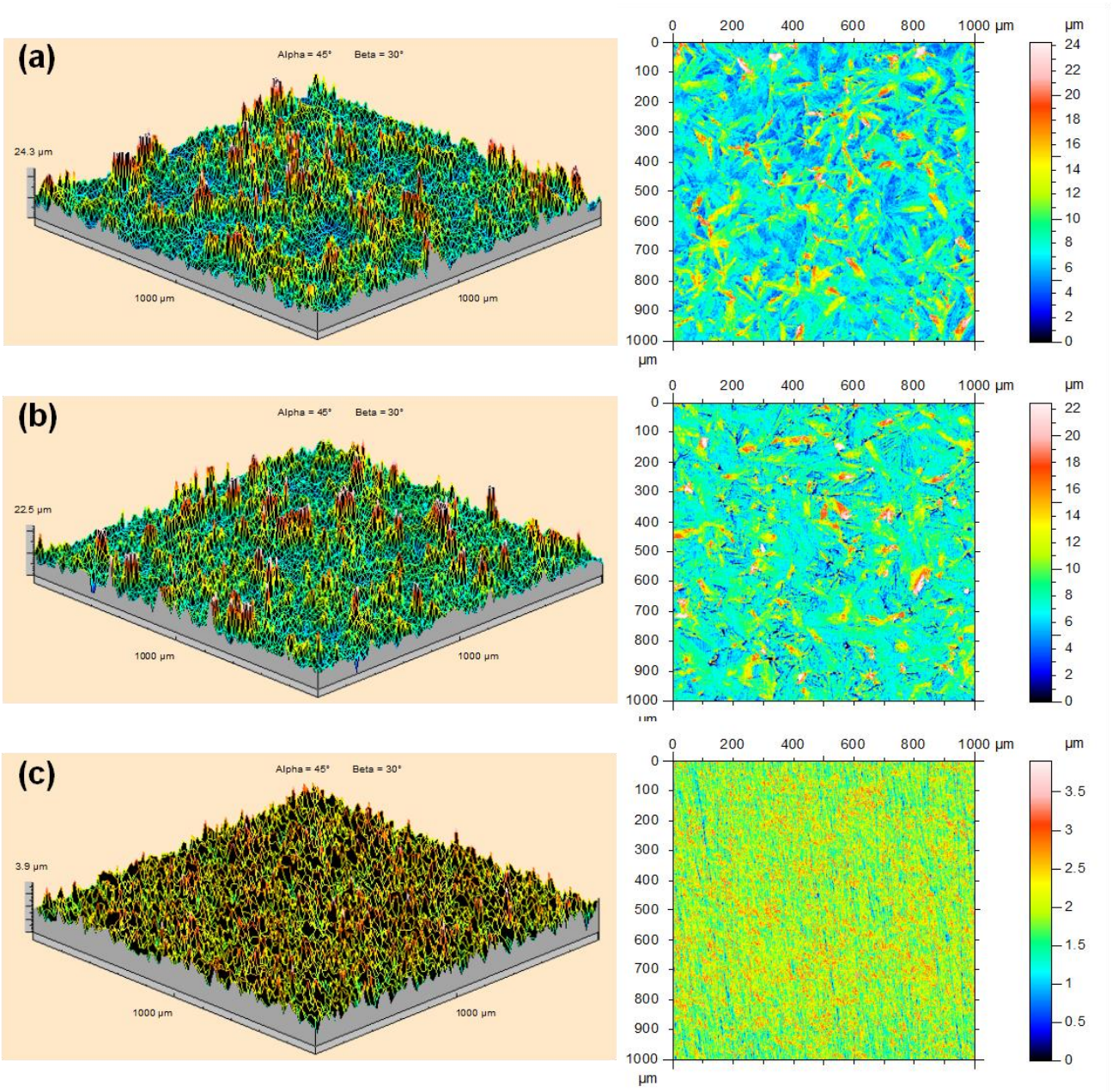

Figure 7-1 Profiles of CaP/TiO_2 bioceramic film coated Ti (a), CaP bioactive film coated Ti (b) and TO Ti_6h (c).

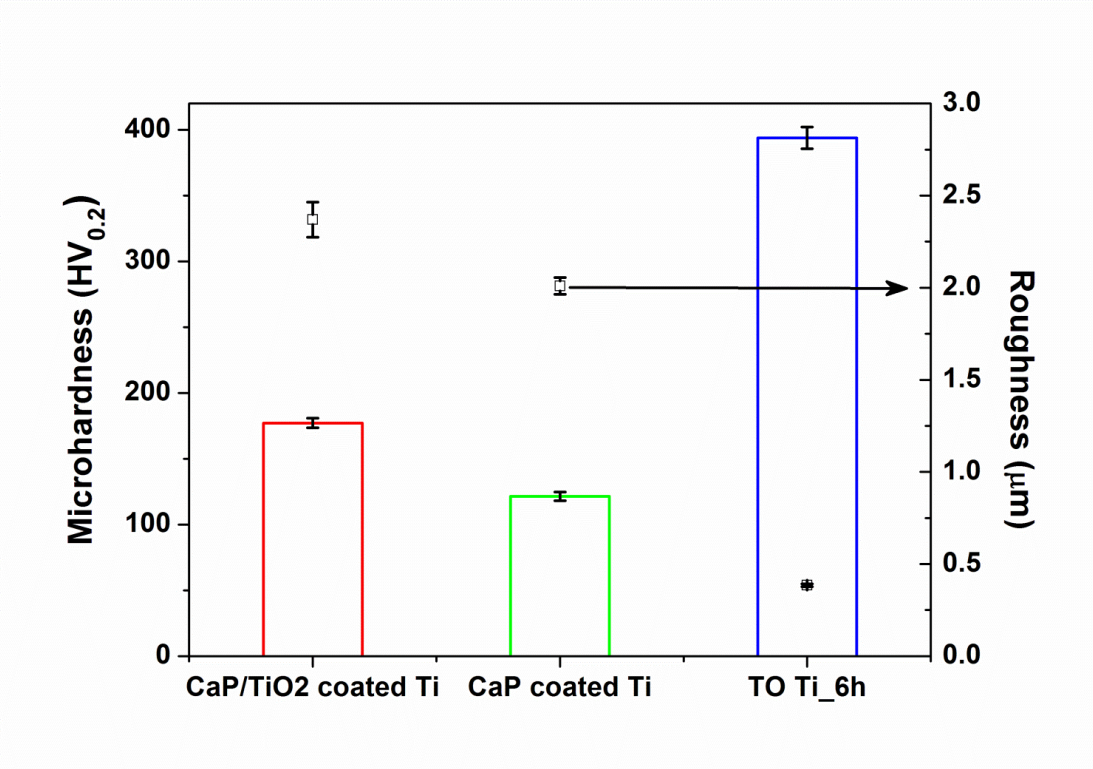

Figure 7-2 Microhardness and surface roughness of CaP/TiO_2 bioceramic film coated Ti, CaP bioactive film coated Ti and TO Ti_6h.

Figure 7-3 shows the XRD patterns of CaP/TiO_2 bioceramic film coated Ti, CaP bioactive film coated Ti and TO Ti_6h samples. To avoid the influence of the strongest peak (11.8 °) of brushite and get more details around diffraction peak value of 40 °, a scan range from 20 ° to 80 ° was used in this study. As illustrated in Chapter 6, typical brushite ($CaHPO_4 \cdot 2H_2O$, ICDD card No. 00-011-0293) peaks were clearly identified in the pattern of CaP bioactive film coated Ti. The remaining small peaks of cp Ti (ICDD card No. 00-005-0682) indicate that the Cu K_α radiation could penetrate through CaP bioactive film to the cp Ti substrate. Typical rutile (TiO_2, ICDD card No. 01-089-4920) peaks were identified in the pattern of TO Ti_6h sample, and the presense of oxygen-diffused Ti (TiO) [144] as well as Ti indicated that the penetration of Cu K_α radiation to the cp Ti substrate. Comparing with CaP bioactive film coated Ti and TO Ti_6h, all peaks of brushite disappear and typical $Ca_3(PO_4)_2$ (ICDD card No. 00-009-0169), rutile (exhibiting lower intensity than TO Ti_6h) and $CaTi_{21}O_{38}$ (ICDD card No. 00-042-1368) peaks are identified in the pattern of CaP/TiO_2 bioceramic film coated Ti. From XRD patterns, it is concluded that sintering process at 650 ℃ for 6 h makes the major phase transfer from $CaHPO_4 \cdot 2H_2O$ to $Ca_3(PO_4)_2$. Meanwhile, thermal oxidation of cp Ti results in the product of rutile of the substrate with different composition from that of TO Ti_6h prepared at 650 ℃ for 6 h without any CaP bioactive film. And at the interface of CaP bioactive film and cp Ti, the appearance of $CaTi_{21}O_{38}$ shows the element shift or replacement at high temperature. The same observation was found by Wei et al. [193] in the preparation of calcium titanate/titania bioceramic composite coatings on titanium alloy. Another calcium titanate ($CaTiO_3$) was commonly produced [194] by the interaction between titanium and hydroxyapatite (HA, $Ca_{10}(PO_4)_6(OH)_2$). But in this

study, no peak from $CaTiO_3$ was observed.

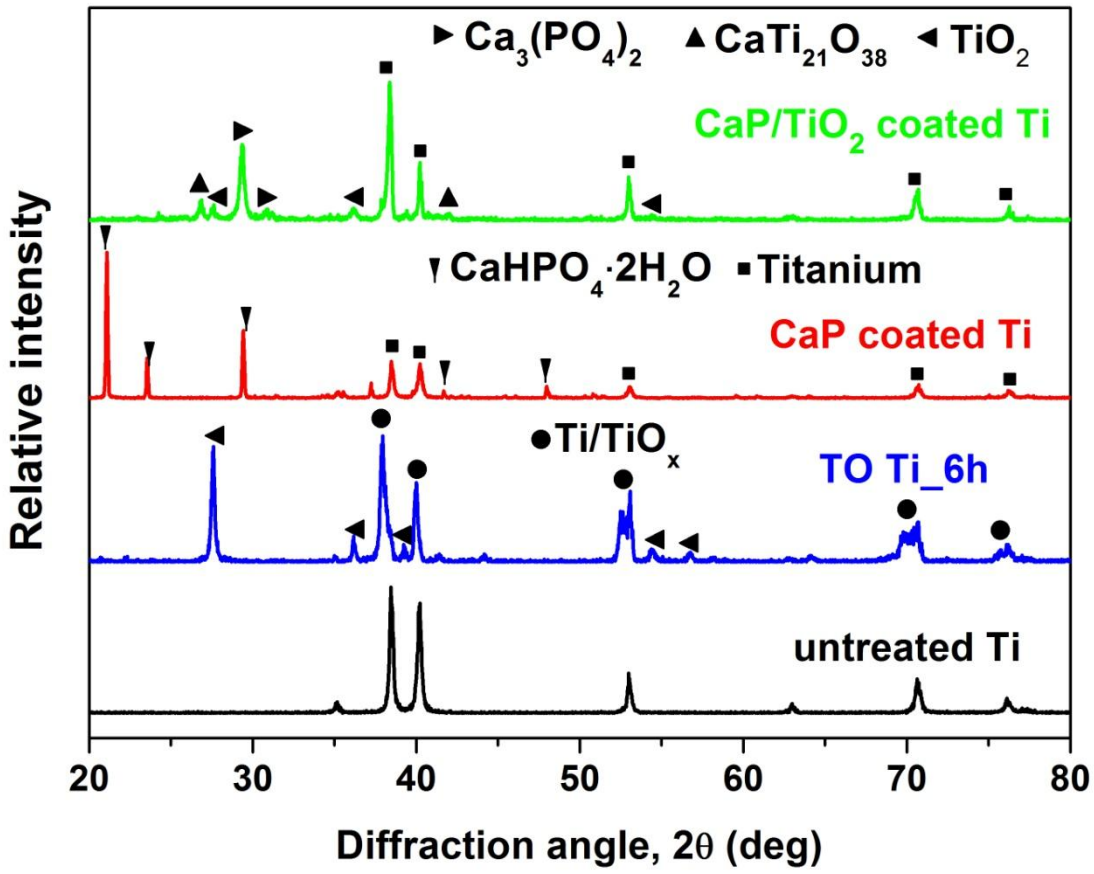

Figure 7-3 XRD patterns of CaP/TiO_2 bioceramic film coated Ti (green line), CaP bioactive film coated Ti (red line), TO Ti_6h (blue line) and untreated Ti (black line).

Surface morphology and chemical composition of CaP/TiO_2 bioceramic film coated Ti, CaP bioactive film coated Ti and TO Ti_6h were characterized by SEM coupled with EDS analysis, as seen in Figure 7-4. The flower-like morphology of CaP bioactive film on cp Ti keeps after sintering at 650 ℃ for 6 h. Chemical compositions of CaP/TiO_2 bioceramic film coated Ti, CaP bioactive film coated Ti and TO Ti_6h are noted as follows: (i) O = 40.8 wt%, P = 20.2 wt%, Ca = 25.1 wt% and Ti = 13.9 wt% for CaP/TiO_2 bioceramic film coated Ti (see Figure 7-4d); (ii) O = 52.1 wt%, P = 17.0 wt%, Ca = 20.3 wt% and Ti = 10.6 wt% for CaP bioactive film coated Ti (see Figure 7-4e); (iii) O = 33.6 wt% and Ti = 66.4 wt% for TO Ti_6h (see Figure 7-4f). Comparing with CaP bioactive film coated Ti, the decrease of oxygen content in CaP/TiO_2 bioceramic film indicates that the elimination of crystal water of $CaHPO_4 \cdot 2H_2O$ at high temperature, even the formation of TiO_2 offsets somewhat of oxygen decrease. The atomic ratio value of Ca/P for CaP/TiO_2 bioceramic film coated film is 0.96, which is similar as that value (0.92) for CaP bioactive film coated Ti. As identified by XRD pattern, the

existence of $CaTi_{21}O_{38}$ can enhance the content of Ca in CaP/TiO_2 bioceramic film, but the atomic ratio value of Ca/P is still lower than 1.5 the standard molar ratio value of $Ca_3(PO_4)_2$. This might be explained by the existence of amorphous phosphates that cannot be characterized by XRD.

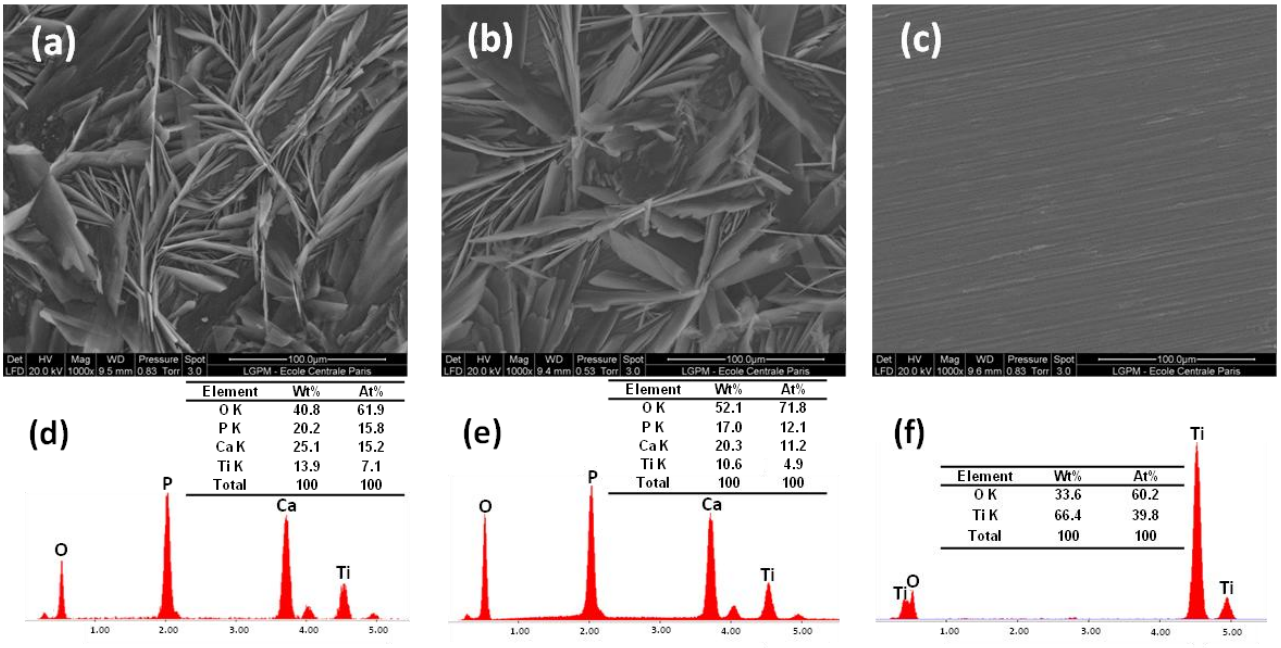

Figure 7-4 SEM images and EDS analysis of CaP/TiO_2 bioceramic film coated Ti (a, d), CaP bioactive film coated Ti (b, e) and TO Ti_6h (c, f).

7.4 Corrosion behavior of CaP/TiO_2 bioceramic film coated Ti under static condition before sliding

Figure 7-5 shows the OCP evolution curves of CaP/TiO_2 bioceramic film coated Ti, CaP bioactive film coated Ti and TO Ti_6h in the PBS solution. For CaP bioactive film coated Ti, the E_{oc} value raises up quickly from -0.28 V to -0.18 V vs. Ag/AgCl after immersion for 1200 s in the PBS solution, following with a smooth potential increase to -0.14 V vs. Ag/AgCl at the end of immersion time. For TO Ti_6h, E_{oc} value also raises up from a higher initial starting value of -0.08 V to -0.03 V vs. Ag/AgCl at the end of immersion time (3 h under static condition). On the contrary, the E_{oc} value of CaP/TiO_2 bioceramic film coated Ti goes down from 0.03 V to -0.04 V vs. Ag/AgCl after immersion for 20 min in the PBS solution. Then an insignificant potential difference of 10 mV was found until the end of immersion time of 3 h in this study. The decrease of E_{oc} during the first 20 min might be resulted from the penetration of electrolyte through $Ca_3(PO_4)_2/CaTi_{21}O_{38}$ bioceramic film, which are more hydrophilic than TiO_2 passive film or cp Ti substrate. When electrolyte reaches the interface between the substrate and the film, passivation occurs on cp Ti substrate, which leads to a slight increase of E_{oc}. The more noble OCP value of CaP/TiO_2 bioceramic film coated Ti reveals its improved corrosion resistance than CaP bioactive film coated Ti before sintering.

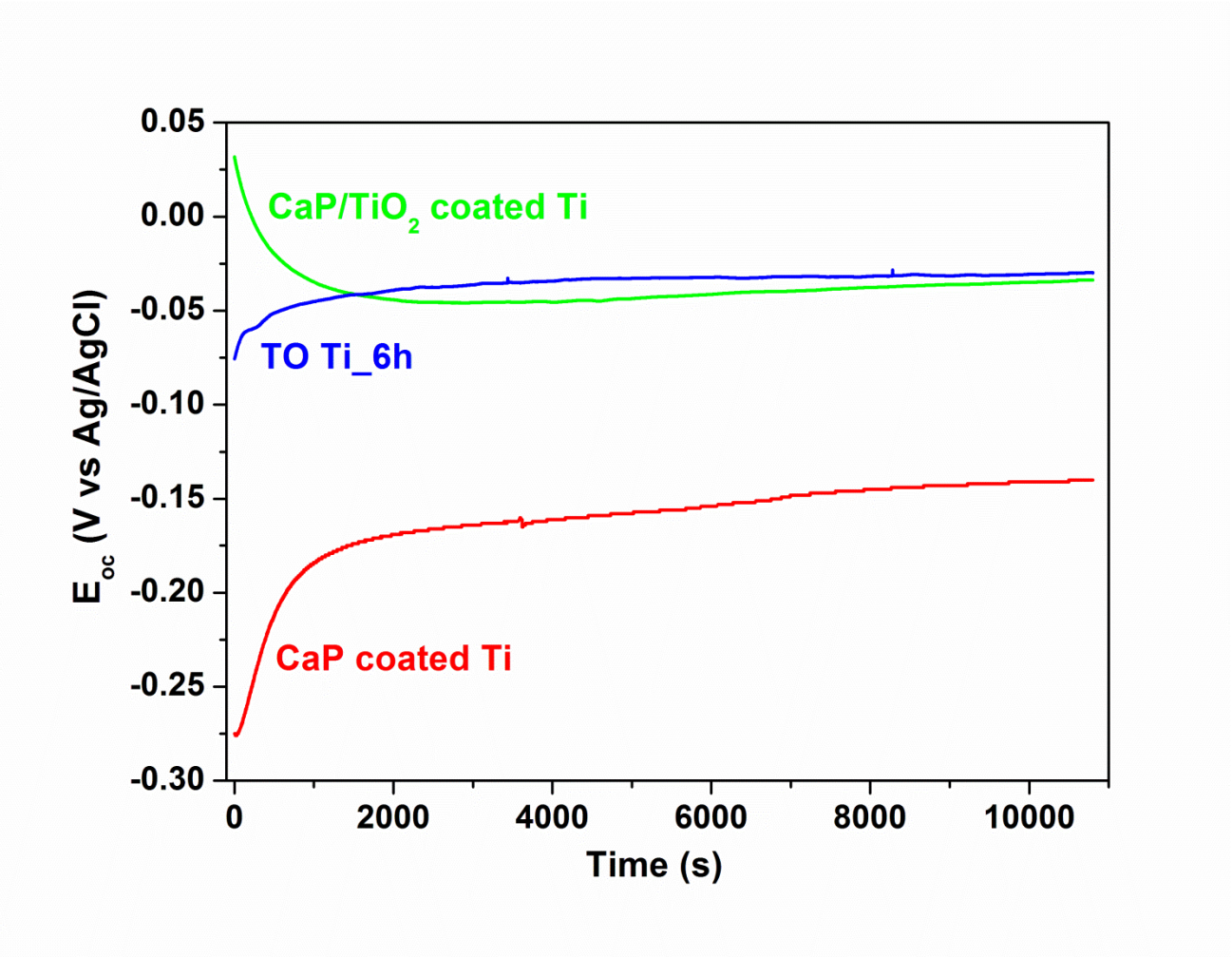

Figure 7-5 OCP evolution of CaP/TiO_2 bioceramic film coated Ti (green line), CaP bioactive film coated Ti (red line), TO Ti_6h (blue line) in the PBS solution.

The potentiodynamic polarization curves of CaP/TiO_2 bioceramic film coated Ti, CaP bioactive film coated Ti and TO Ti_6h measured in the potential range from -1 V to 3 V vs. Ag/AgCl after immersion for 3 h in the PBS solution are shown in Figure 7-6. The values of corrosion potential (E_{corr}), specific current density at body potential of 0.4 V vs. Ag/AgCl (i_{bp}) and specific current density at passive potential of 1 V vs. Ag/AgCl (i_{pass}) are summarized in Table 7-1. The E_{corr} of CaP/TiO_2 bioceramic film coated Ti is more noble than that of CaP bioactive film coated Ti but much less than that of TO Ti_6h, its corresponding current density at E_{corr} and even up to 0 V is the highest among these three samples. From Figure 7-6, no prepassive domain could be identified for the CaP/TiO_2 bioceramic film coated Ti and TO Ti_6h, due to the formation of more resistant $CaTi_{21}O_{38}$ and TiO_2 layers on cp Ti substrate after sintering at 650 ℃ for 6 h for the former and the formation of TiO_2 and Oxygen-diffused TiO_x layers on cp Ti substrate after thermal oxidation at 650 ℃ for 6 h for the later.

Not like the quick current density increase for CaP bioactive film coated Ti in the prepassive

domain, the current density keeps stable in the whole passive domain from -0.32 V to ~ 1 V vs. Ag/AgCl for CaP/TiO_2 bioceramic film coated Ti and from 0.2 V to 1.7 V vs. Ag/AgCl for TO Ti_6h. It should be noticed that for TO Ti_6h, current density increases significantly at 1.7 V vs. Ag/AgCl and then keeps more or less stable after 2V vs. Ag/AgCl, revealing the dissolution and repassivation of titanium oxides in such a high potential range. Comparing with CaP bioactive film coated Ti, the difference of one order of magnitude in current densities of i_{bp} and i_{pass} for CaP/TiO_2 bioceramic film coated Ti shows its better corrosion resistance in this potential range. But after 1 V vs. Ag/AgCl, the current density increases significantly and even exceeds the value of CaP bioactive film coated Ti in the potential range from 2.5 V to 3 V vs. Ag/AgCl. This might be resulted from the local concentration increase of the ions, due to the chemical transformation of $Ca_3(PO_4)_2$ to $CaHPO_4$ or $Ca(H_2PO_4)_2$ as the following reactions:

The anodic reaction at high potential (referred to the Pourbaix diagram of titanium/water system in Figure 2-8 [111]):

$$\mathbf{2H_2O \rightarrow O_2 + 4H^+ + 4e^-} \qquad (7\text{-}1)$$

The chemical transformations between calcium phosphate salts:

$$\mathbf{Ca_3(PO_4)_2 + 2H^+ \rightarrow 2CaHPO_4 + Ca^{2+}} \qquad (7\text{-}2a) \quad \text{or}$$

$$\mathbf{Ca_3(PO_4)_2 + 4H^+ \rightarrow Ca(H_2PO_4)_2 + 2Ca^{2+}} \qquad (7\text{-}2b)$$

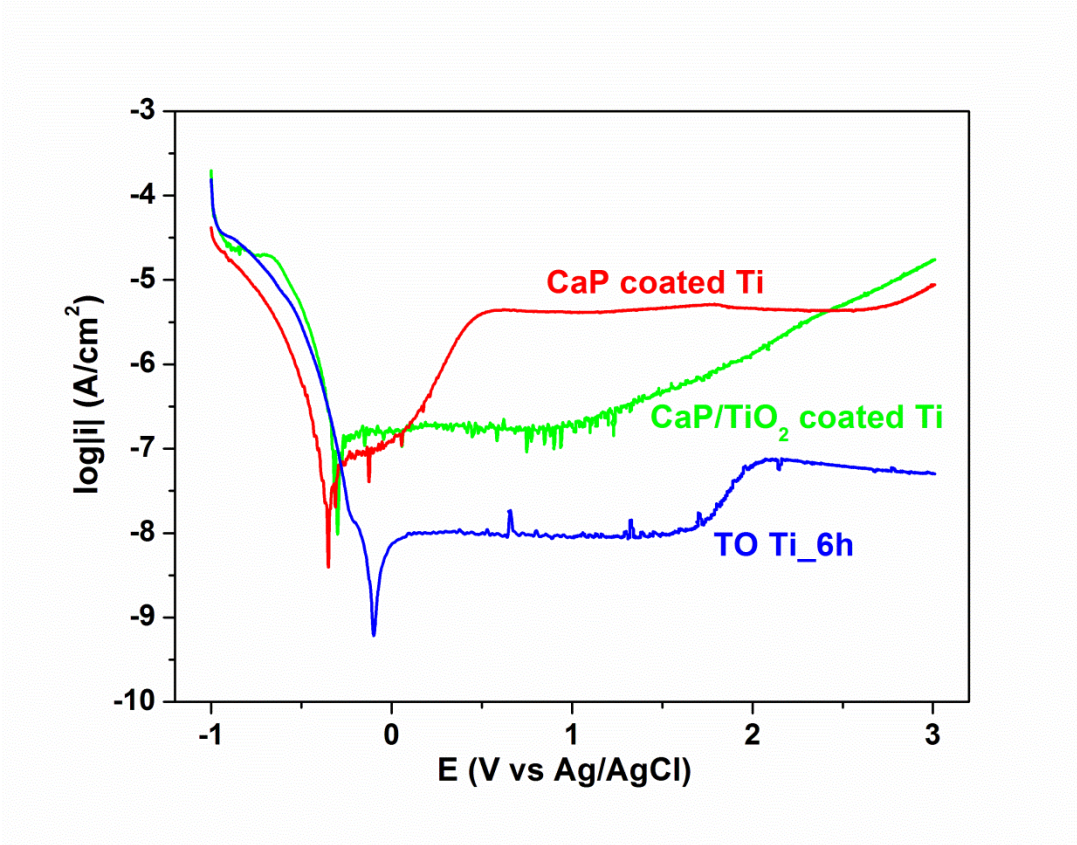

Figure 7-6 Potentiodynamic polarization curve of CaP/TiO_2 bioceramic film coated Ti (green line), CaP bioactive film coated Ti (red line) and TO Ti_6h (blue line) from -1 V to 3 V vs. Ag/AgCl at a scan rate of 1 mV/s measured at immersion time of 3 h under static condition in the PBS solution.

Table 7-1 Electrochemical data obtained from potentiodynamic polarization tests measured at immersion time of 3 h.

Sample	E_{corr} (V)	$*i_{bp}$ (A·cm^{-2})	$*i_{pass}$ (A·cm^{-2})
CaP/TiO_2 coated Ti	-0.32	1.83×10^{-7}	1.87×10^{-7}
CaP coated Ti	-0.35	2.55×10^{-6}	4.13×10^{-6}
TO Ti_6h	-0.10	1.02×10^{-8}	9.01×10^{-9}

*i_{bp}: specific current density at body potential of 0.4 V vs. Ag/AgCl.
*i_{pass}: specific current density at passive potential of 1 V vs. Ag/AgCl.

The Nyquist plots for CaP/TiO_2 bioceramic film coated Ti, CaP bioactive film coated Ti and TO Ti_6h, measured at immersion time of 3 h in the PBS solution under static condition before sliding, are shown in Figure 7-7a. The CaP bioactive film coated Ti exhibits only a single semicircle in the entire frequency range, which corresponds to the equivalent circuit of R_s(CPE||R_p) with one time constant as illustrated in Figure 7-8a (the same as Figure 4-3), where R_s is the solution resistance and R_p is the polarization resistance of CaP bioactive film coated Ti due to the barrier property of passive film. TO Ti_6h exhibits an irregular arc that can be divided into two semicircles. This can be illustrated by the equivalent circuit in Figure 7-8b with two time constants (the same as Figure 5-7b), where R_{outer} and R_{inner} correspond to the resistance of the outer porous rutile layer and the resistance of the inner compact oxygen-diffused layer [4, 189], respectively. But CaP/TiO_2 bioceramic film coated Ti exhibits a more complicated irregular arc that can be divided into three semicircles: one in the high frequency range, one in the medium frequency range and a third in the low frequency range. Such three semicircles can be illustrated by the equivalent circuit in Figure 7-8c, where R_{film} corresponds to the resistance of the outer porous $Ca_3(PO_4)_2$ layer, R_{oxide} is the resistance of the inner compact $CaTi_{21}O_{38}$ and TiO_2 layers and R_{ct} is the charge transfer resistance due to the chemical/electrochemical reaction on cp Ti substrate, respectively.

As illustrated before, the use of CPE rather than a pure capacitance can be expressed by Eq. 3-10 in Chapter 3. The well agreement between the theoretical and the experimental data can be seen by the fitting results plotted in Figure 7-7 for all these three samples. The parameters of the equivalent circuits are shown in Table 7-2. Comparing with R_{ct}, the sum of R_{film} (930 Ω) and R_{oxide} (1530 Ω) is negligible that the total polarization resistance R_p for CaP/TiO_2 bioceramic film coated Ti is equal to the value of R_{ct} as 2.43×10^7 Ω. And for TO Ti_6h, the total polarization resistance R_p is the sum of R_{outer} and R_{inner}.

Figure 7-7b and 7-7c show the Bode plots for CaP/TiO_2 bioceramic film coated Ti, CaP bioactive film coated Ti and TO Ti_6h after immersion for 3 h in the PBS solution. From the Bode impedance plots, it is clearly observed that at the lowest frequency of 3.98 mHz in this study, the resistance value of TO Ti_6h is the highest in the study, and the resistance value of CaP bioactive film coated Ti is also higher than that of CaP/TiO_2 bioceramic film coated Ti. But combined with the Bode phase angle plots, a phase decrease occurs for both TO Ti_6h and CaP bioactive film coated Ti. In contrast, a continuous increased tendency of Bode phase angle for CaP/TiO_2 bioceramic film coated Ti indicates that higher resistance value will reach if the test frequency could get close to 0 Hz. The fitting results in Table 7-2 give the simulated values of both samples. And the r_p value of 6.32×10^7 Ω cm^2 for CaP/TiO_2 bioceramic film coated Ti is about 4 times of the r_p value of 1.65×10^7 Ω cm^2 for CaP bioactive film coated Ti and more than 4 times of the r_p value of 1.46×10^7 Ω cm^2 for TO Ti_6h. This phenomenon shows the barrier property of CaP bioactive film is further enhanced after sintering at 650 ℃ for 6 h by forming a CaP/TiO_2 bioceramic film on cp Ti, which is also higher than the TO Ti_6h prepared at 650 ℃ for 6 h without any CaP bioactive film.

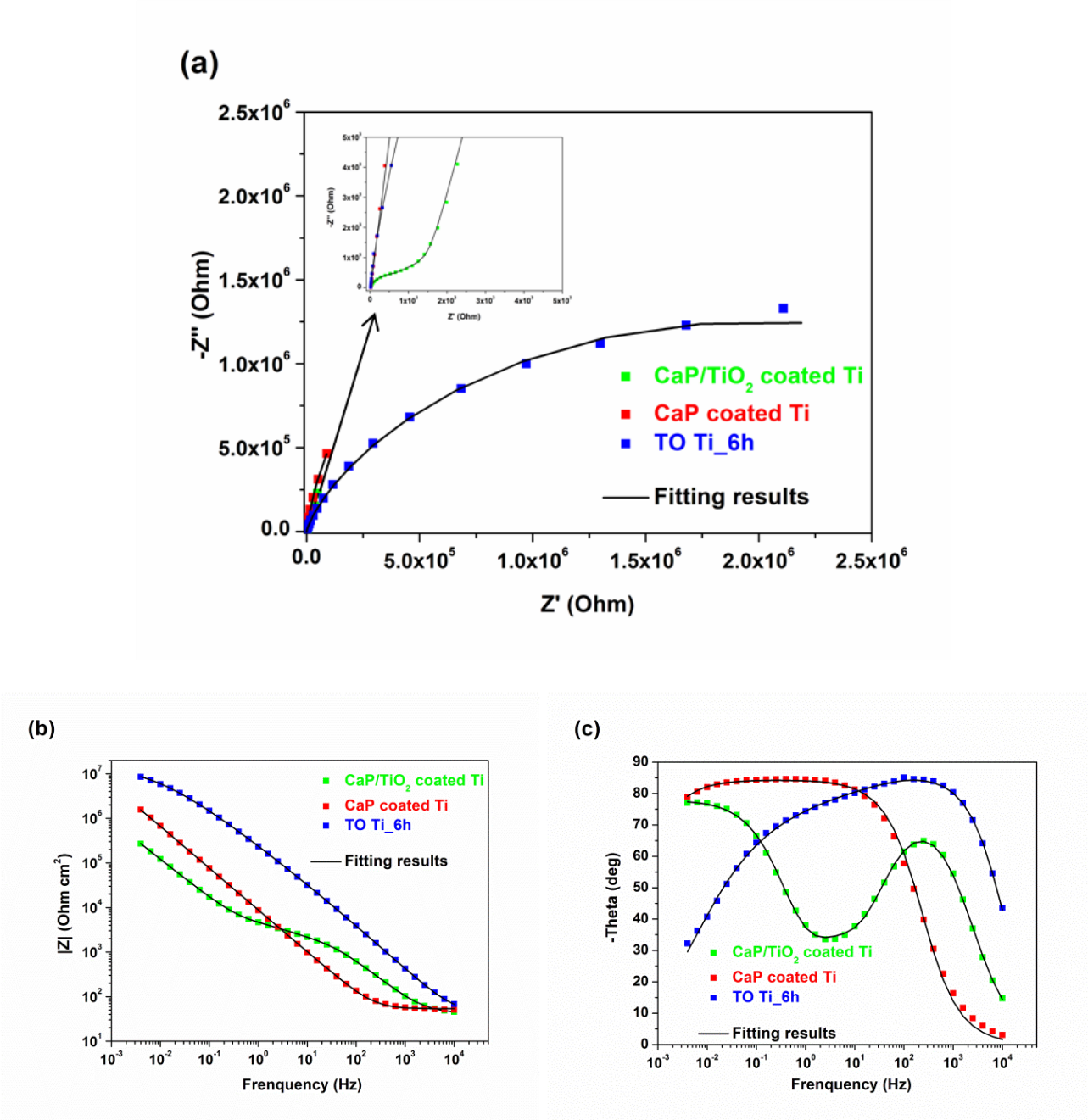

Figure 7-7 Nyquist plot (a), Bode plots (b and c) for CaP/TiO_2 bioceramic film coated Ti (green square), CaP bioactive film coated Ti (red square), TO Ti_6h (blue square) measured at immersion time of 3 h before sliding tests in the PBS solution.

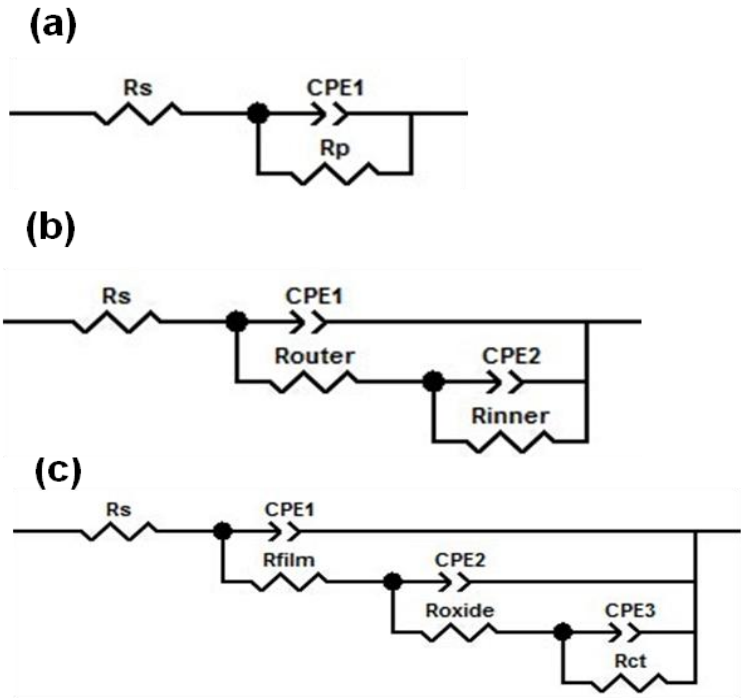

Figure 7-8 Equivalent circuit for CaP bioactive film coated Ti (a) with one time constant, TO Ti_6h (b) with two time constants sand CaP/TiO_2 bioceramic film coated Ti (c) with three time constants in the PBS solution.

Table 7-2 Parameters of the equivalent circuit for CaP/TiO_2 bioceramic film coated Ti, CaP bioactive film coated Ti and TO Ti_6h before sliding tests.

Sample	A_0 (cm^2)	R_s (Ohm)	ϕ-1	$R_{film\ /\ outer}$ (Ohm)	ϕ-2	$R_{oxide\ /\ inner}$ (Ohm)	ϕ-3	R_{ct} (Ohm)	$*R_p$ (Ohm)	r_p (Ohm·cm^2)
CaP /TiO_2 coated Ti	2.60	16.1	0.88	930	0.85	1530	0.881	2.43×10^7	2.43×10^7	6.32×10^7
CaP coated Ti	3.30	16.1	0.94	--	--	--	--	--	5.01×10^6	1.65×10^7
TO Ti_6h	3.51	13.7	0.96	21700	0.60	4.13×10^6	--	--	4.15×10^6	1.46×10^7

*$R_p = R_{film} + R_{oxide} + R_{ct}$ [= R_{ct} if ($R_{film} + R_{oxide}$) << R_{ct}] for CaP/TiO_2 bioceramic film coated Ti under static condition.
*$R_p = R_{outer} + R_{inner}$ for TO Ti_6h under static condition.

7.5 Tribocorrosion behavior of CaP/TiO_2 bioceramic film coated Ti during and after continuous unidirectional sliding test

After immersion for 3 h in the PBS solution, tribocorrosion test of CaP/TiO_2 bioceramic film coated Ti was performed by imposing the continuous unidirectional sliding at F_n of 500 mN with a rotation rate of 100 rpm. The tribocorrosion behavior of CaP bioactive film coated Ti without sintering treatment and tribocorrosion behavior of TO Ti_6h were also evaluated as the references.

The OCP evolution curves and friction coefficient curves of all three samples during sliding are shown in Figure 7-9.

For CaP bioactive film coated Ti, with the onset of sliding, a sudden drop occurs from -0.14 V to -0.51 V vs. Ag/AgCl, the cathodic shift of E_{oc} in the negative direction reveals the change of surface state from passive to active inside the sliding track area of CaP bioactive film coated Ti. Meanwhile, the friction coefficient of CaP bioactive film coated Ti during sliding keeps a high value as 0.6 due to the continuous destruction of CaP bioactive film and/or the thin passive oxide film on cp Ti substrate. For CaP/TiO_2 bioceramic film coated Ti, only a slight E_{oc} decrease of about 0.03 V occurs when sliding motion starts within the first 5 min. The corresponding friction coefficient during this period decreases quickly from 0.55 to 0.35, revealing the destruction of the outer $Ca_3(PO_4)_2$ layer by the sliding of the harder counter body (ZrO_2). After that, a stable E_{oc} with a continuous slight increase in the noble direction was observed with almost the same E_{oc} value as that of TO Ti_6h. Even lower friction coefficient of about 0.3 for CaP/TiO_2 bioceramic film coated Ti can be detected until the end of sliding motion, it is still higher than that of TO Ti_6h (about 0.2). This reveals the effects of initial roughness and hardness on friction coefficient evolution during continuous sliding test. These results show the CaP/TiO_2 bioceramic film coated Ti after sintering at 650 ℃ for 6 h in the furnace has significantly improved corrosion and friction characteristics under mechanical loaded condition at F_n of 500 mN.

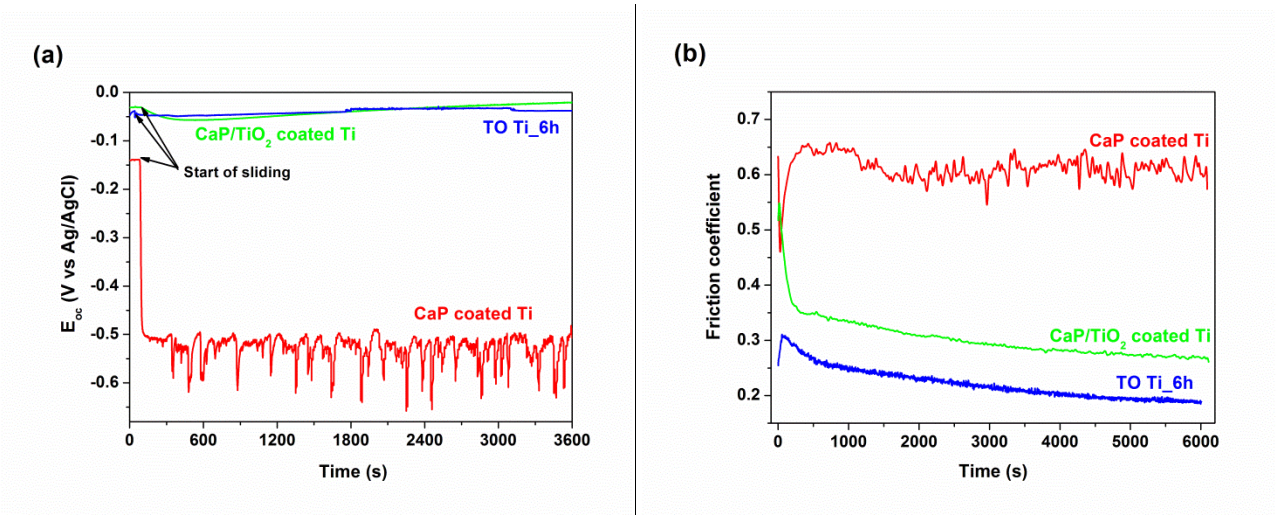

Figure 7-9 OCP evolution (a) and friction coefficient (b) of CaP/TiO_2 bioceramic film coated Ti (green line), CaP bioactive film coated Ti (red line) and TO Ti_6h (blue line) during continuous unidirectional sliding tests performed at F_n of 500 mN.

The Nyquist plots for CaP/TiO_2 bioceramic film coated Ti, CaP bioactive film coated Ti and TO Ti_6h during continuous unidirectional sliding at F_n of 500 mN in the PBS solution are shown in Figure 7-10a. There is no doubt that the Nyquist plot for CaP bioactive film coated Ti during sliding test still exhibits only one single semicircle in the entire frequency range and its equivalent circuit is the same as illustrated in Figure 7-8a. The Nyquist plots for TO Ti_6h and CaP/TiO_2 bioceramic film

coated Ti still have the similar comportments as those before sliding and the corresponding equivalent circuits are the same as illustrated in Figure 7-8b and 7-8c. It should be noticed that in the Bode impedance plots, the resistances during sliding tests at lowest frequency of 39.8 mHz for all three samples are smaller than those values measured at the same frequencies before sliding. This decrease phenomenon can be further proved by the fitting results (also plotted in Figure 7-10) with the equivalent in Figure 7-8, as seen in Table 7-3.

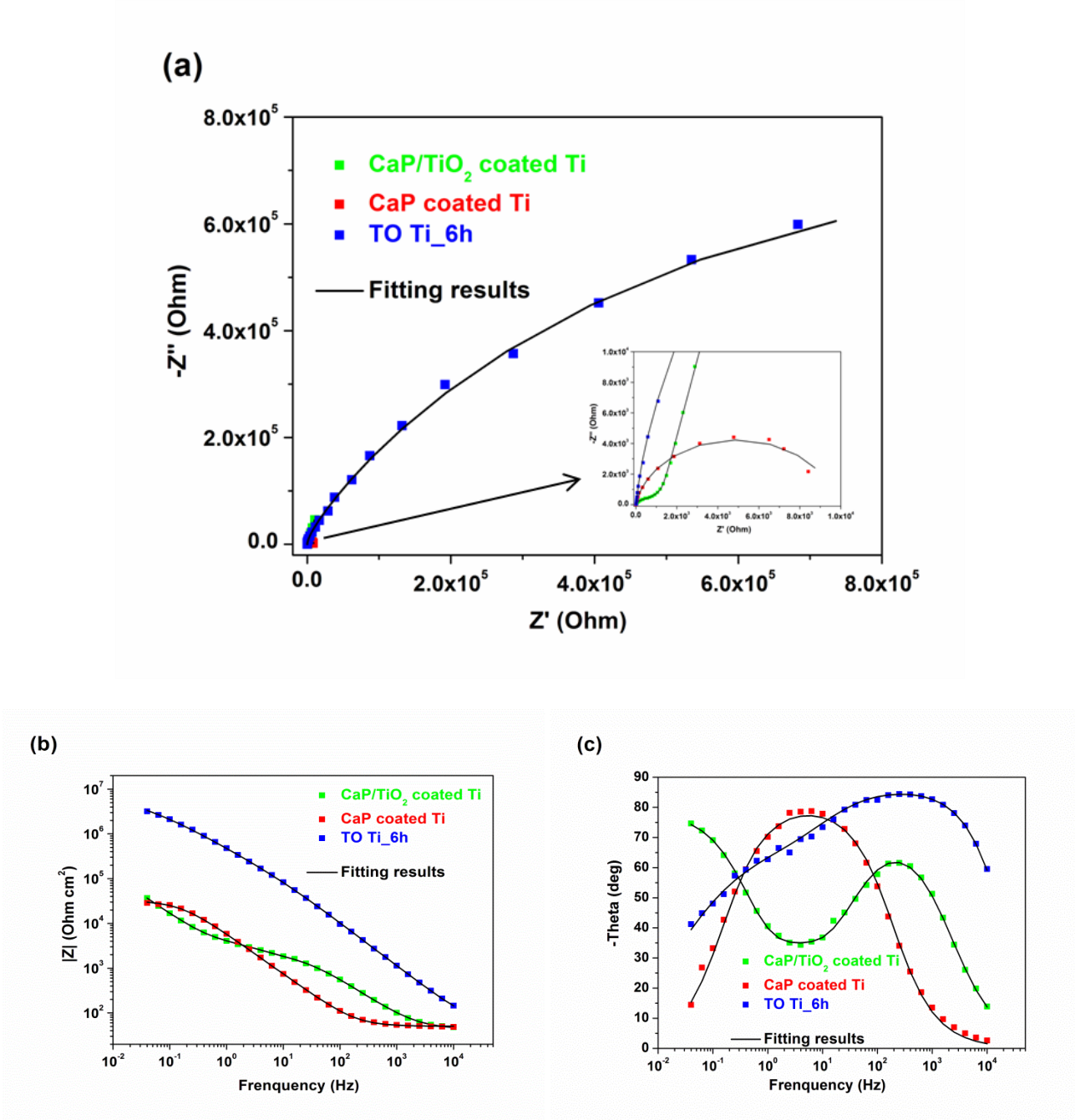

Figure 7-10 Nyquist plots (a), Bode impedance plots (b) and Bode phase angle plots (c) for CaP/TiO_2 bioceramic film coated Ti (green square), CaP bioactive film coated Ti (red square), TO Ti_6h (blue square) during continuous unidirectional sliding tests performed at F_n of 500 mN.

Table 7-3 Parameters of the equivalent circuit for CaP/TiO_2 bioceramic film coated Ti, CaP bioactive film coated Ti and TO Ti_6h during sliding tests at F_n of 500 mN.

Sample	A_0 (cm^2)	R_s (Ohm)	ϕ-1	$R_{film\ /\ outer}$ (Ohm)	ϕ-2	$R_{oxide\ /\ inner}$ (Ohm)	ϕ-3	R_{ct} (Ohm)	$*R_p$ (Ohm)	r_p (Ohm·cm^2)
CaP /TiO_2 coated Ti	2.60	16.6	0.85	830	0.86	1480	0.90	9.60×10^6	9.60×10^6	2.50×10^7
CaP coated Ti	3.30	15.3	0.91	--	--	--	--	--	9600	3.17×10^4
TO Ti_6h	3.51	18.8	0.96	26400	0.60	2.29×10^6	--	--	2.87×10^6	1.01×10^7

$*R_p = R_{film} + R_{oxide} + R_{ct}$ for CaP/TiO_2 bioceramic film coated Ti under mechanical loaded condition.
$*R_p = R_{outer} + R_{inner}$ for TO Ti_6h under mechanical loaded condition.

It is clearly observed that the R_p value decreased tremendously from 5.01×10^6 Ω measured before sliding to 9600 Ω measured during continuous unidirectional sliding test at F_n of 500 mN for CaP bioactive film coated Ti. And only small R_p decrease was observed from 4.15×10^6 Ω to 2.87×10^6 Ω for TO Ti_6h. For CaP/TiO_2 bioceramic film coated Ti, the R_{film} value decreases from 930 Ω to 830 Ω, and R_{oxide} value decreases from 1530 Ω to 1480 Ω. These tiny changes can be ignored when comparing with the difference of R_{ct} measured before and during sliding. From Table 7-3, the R_p value of 9.60×10^6 Ω for CaP/TiO_2 bioceramic film coated Ti was obtained by the sum of R_{film}, R_{oxide} and R_{ct}. It is smaller than the R_p value of 2.43×10^7 Ω measured under static condition before sliding test. As illustrated in Chapter 3, with the guidance of tribocorrosion protocol for surface modified Ti, the specific polarization resistance, r_p is obtained directly by the multiplication of R_p with the total exposed area, A_0 in this study (see Eq. 3-40).

The decrease of r_p from 1.65×10^7 Ω cm^2 to 3.17×10^4 Ω cm^2 for CaP bioactive film coated Ti, from 1.46×10^7 Ω cm^2 to 1.01×10^7 Ω cm^2 for TO Ti_6h and from 6.32×10^7 Ω cm^2 to 2.50×10^7 Ω cm^2 for CaP/TiO_2 bioceramic film coated Ti indicate that during sliding tests, the destruction of film and disturbance of measured electrolyte by sliding motion of counter body (ZrO_2) weaken the barrier properties of the previous films on cp Ti and then promote the entrance of chemical ions to the surface of cp Ti substrate.

Figure 7-11 shows the OCP evolution curves of CaP/TiO_2 bioceramic film coated Ti, CaP bioactive film coated Ti and TO Ti_6h after sliding tests. Once the continuous unidirectional sliding motion stops, the E_{oc} value of CaP bioactive film coated Ti exhibits a strong anodic shift from -0.6 V to -0.2 V vs. Ag/AgCl, indicating the occurrence of repassivation of the active surface inside the sliding track. For TO Ti_6h, the E_{oc} increases continuously in the noble direction from -0.04 V to 0.1 V vs. Ag/AgCl, indicating its high corrosion resistant property in the PBS solution. And for CaP/TiO_2 bioceramic film coated Ti, the E_{oc} value with a continuous tiny increase in the noble direction from -0.02 V to 0.02 V vs. Ag/AgCl is presented as the similar evolution before and even during sliding test. This might be attributed to the continuous growth of the thin passive oxide film

on cp Ti substrate.

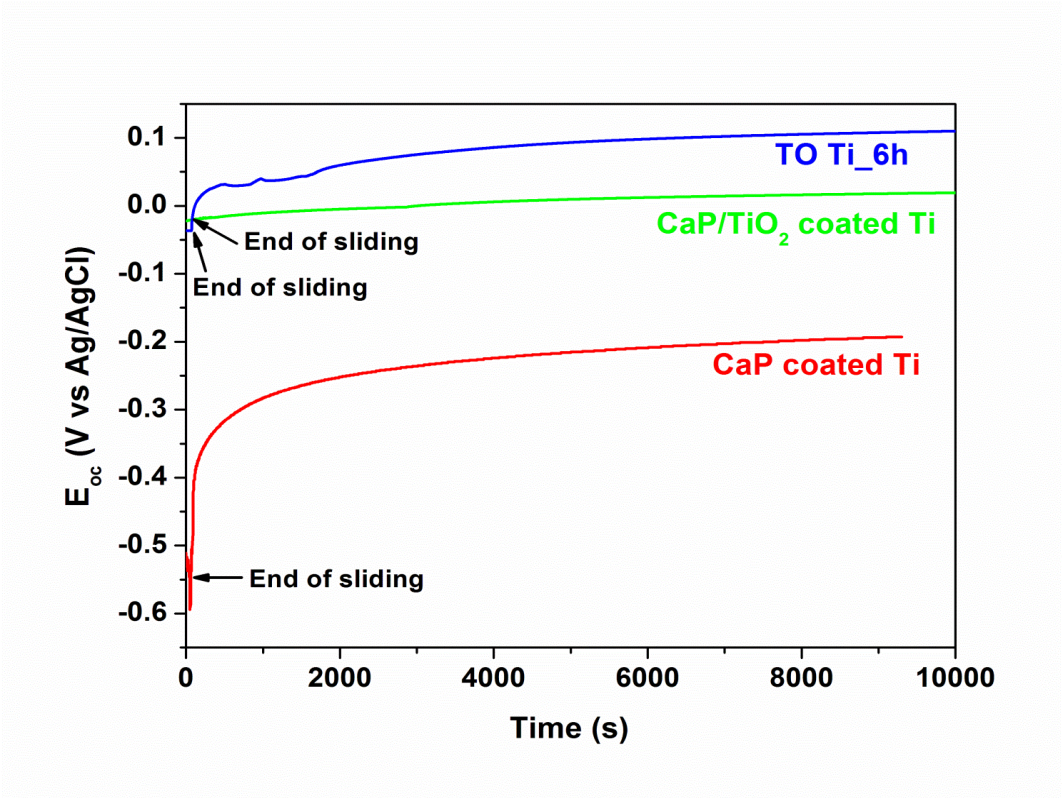

Figure 7-11 OCP evolution of CaP/TiO_2 bioceramic film coated Ti (green line), CaP bioactive film coated Ti (red line) and TO Ti_6h (blue line) after continuous unidirectional sliding tests.

The EIS plots for CaP/TiO_2 bioceramic film coated Ti, CaP bioactive film coated Ti and TO Ti_6h after sliding tests for about 3 h immersion in the PBS solution are shown in Figure 7-12. The Nyquist plot for CaP bioactive film coated Ti still has only one single semicircle. An irregular arc that can be divided into two semicircles for TO Ti_6h and a more complicated irregular arc that can be divided into three semicircles for CaP/TiO_2 bioceramic film coated Ti are still observed. The same equivalent circuits in Figure 7-8 are used to fit the experimental data after continuous unidirectional sliding tests. The fitting results are also plotted in Figure 7-12 and the parameters of the equivalent circuits are shown in Table 7-4.

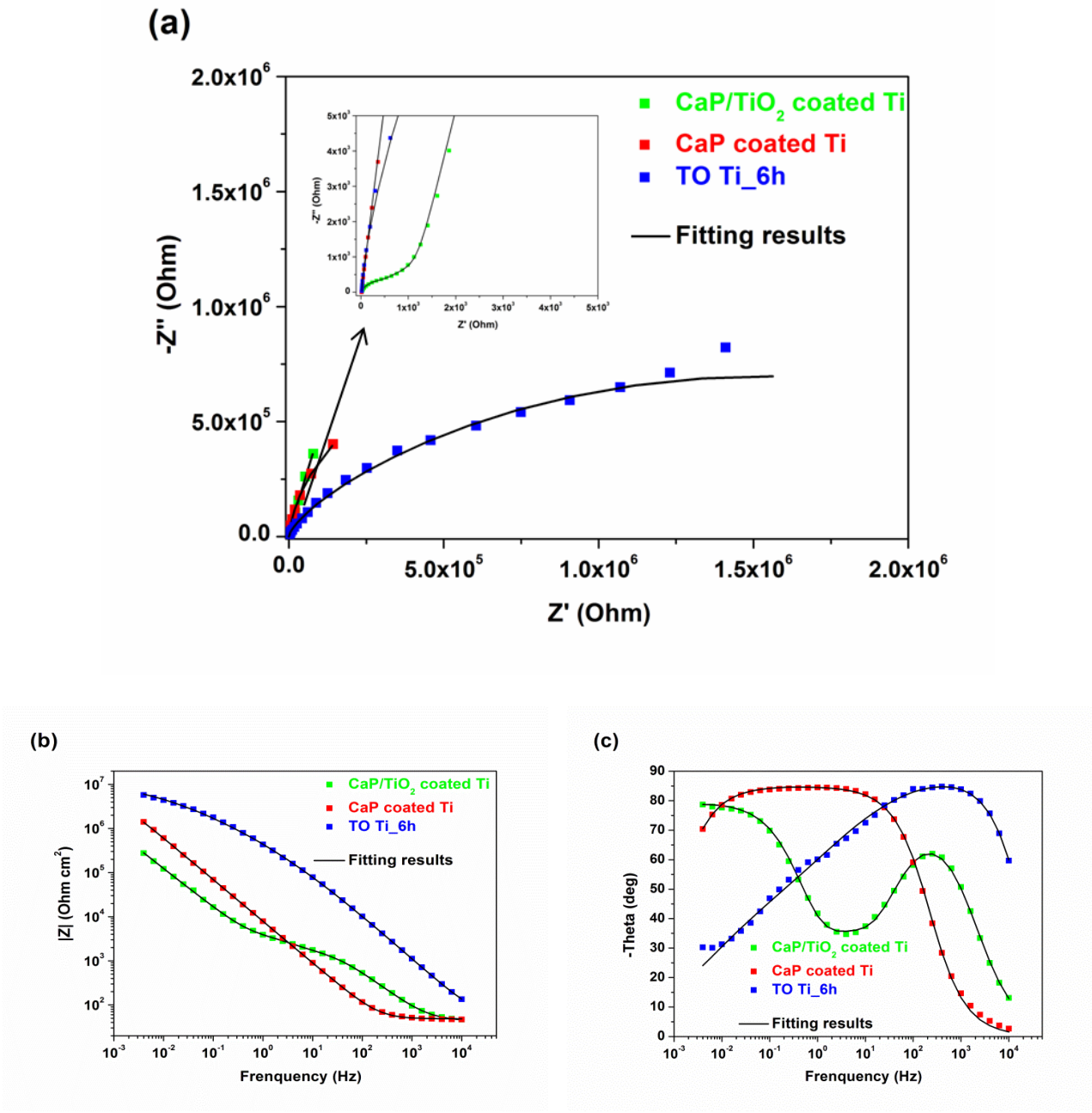

Figure 7-12 Nyquist plots (a), Bode impedance plots (b) and Bode phase angle plots (c) for CaP/TiO_2 bioceramic film coated Ti (green square), CaP bioactive film coated Ti (red square), TO Ti_6h (blue square) after continuous unidirectional sliding tests.

Table 7-4 Parameters of the equivalent circuit for CaP/TiO_2 bioceramic film coated Ti, CaP bioactive film coated Ti and TO Ti_6h after sliding tests.

Sample	A_0 (cm^2)	R_s (Ohm)	ϕ-1	$R_{film\ /\ outer}$ (Ohm)	ϕ-2	$R_{oxide\ /\ inner}$ (Ohm)	ϕ-3	R_{ct} (Ohm)	$*R_p$ (Ohm)	r_p (Ohm·cm^2)
CaP/TiO_2 coated Ti	2.60	16.4	0.87	740	0.89	1200	0.89	1.19×10^7	1.19×10^7	3.10×10^7
CaP coated Ti	3.30	14.7	0.95	--	--	--	--	--	1.75×10^6	5.79×10^6
TO Ti_6h	3.51	18.1	0.98	13200	0.50	3.19×10^6	--	--	3.21×10^6	1.13×10^7

$*R_p = R_{film} + R_{oxide} + R_{ct}$ [$= R_{ct}$ if $(R_{film} + R_{oxide}) << R_{ct}$] for CaP/TiO_2 bioceramic film coated Ti under static condition.
$*R_p = R_{outer} + R_{inner}$ for TO Ti_6h under static condition.

When sliding stops, repassivation occurs in the track area on CaP bioactive film coated Ti and it makes the r_p value increases from $3.17 \times 10^4\ \Omega\ cm^2$ to $5.79 \times 10^6\ \Omega\ cm^2$. But for TO Ti_6h and CaP/TiO_2 bioceramic film coated Ti, both the TiO_2 film and the CaP/TiO_2 bioceramic film exhibit excellent wear resistant properties that can protect cp Ti substrate from the severe destruction by the sliding motion of counter body (ZrO_2). So the r_p value for TO Ti_6h has no significant difference as $1.13 \times 10^7\ \Omega\ cm^2$ under re-static condition or as $1.01 \times 10^7\ \Omega\ cm^2$ under mechanical loaded condition. The same evolution also occurs for CaP/TiO_2 bioceramic film coated Ti with a r_p value change as $3.10 \times 10^7\ \Omega\ cm^2$ under re-static condition and $2.50 \times 10^7\ \Omega\ cm^2$ under mechanical loaded condition.

7.6 Characterization of the wear track on CaP/TiO_2 bioceramic film coated Ti after continuous unidirectional sliding test

Surface morphologies of CaP/TiO_2 bioceramic film coated Ti, CaP bioactive film coated Ti and TO Ti_6h after continuous unidirectional sliding at F_n of 500 mN were obtained by SEM, as shown in Figure 7-13a-c. The EDS analysis results inside the tracks for all three samples (as the local magnifications in the SEM images) are presented in Figure 7-13d-f, respectively.

For CaP bioactive film modified Ti, the major $CaHPO_4 \cdot 2H_2O$ film has disappeared and only the film prints, where preferential growth of calcium phosphate took place in electrochemical deposition process, are clearly observed outside the track area. A track width of 0.62 mm is obtained after 10 000 cycles of sliding. The track area consists of the removal of CaP bioactive film and the destruction of the thin passive film on cp Ti substrate. Chemical composition analysis results as phosphorus (P, 0.8 wt%) and calcium (Ca, 0.4 wt%) indicate that a small amount of CaP bioactive film still stays on the surface of cp Ti even after the continuous removal of 10 000 cycles.

For CaP/TiO_2 bioceramic film coated Ti, except for the film removal inside the track area, the

major film still stays on the surface of cp Ti substrate. Even inside the track area, the remaining contents of P (4.1 wt%) and Ca (2.8 wt%) are still higher than those of the CaP bioactive film coated Ti. This confirms that the film destruction for CaP/TiO_2 bioceramic film coated Ti is less after 10 000 cycles of sliding. All remaining films inside and outside the track provide excellent corrosion and wear resistance during sliding test, resulting of a higher specific polarization, r_p value and a lower friction coefficient value as illustrated in Section 7-5.

For TO Ti_6h, the wear track is so small that only a tiny track width of 0.15 mm is observed after 10 000 cycles of sliding. But no surface destruction can be detected in the wear track. Chemical composition inside the wear track measured by EDS analysis is listed as O 33.9 wt% and Ti 66.1 wt%, which is almost the same as the initial chemical composition as shown in Figure 7-4f. These results indicate that under mechanical loaded condition at F_n of 500 mN, TO Ti_6h exhibits the highest wear resistant property among these three samples.

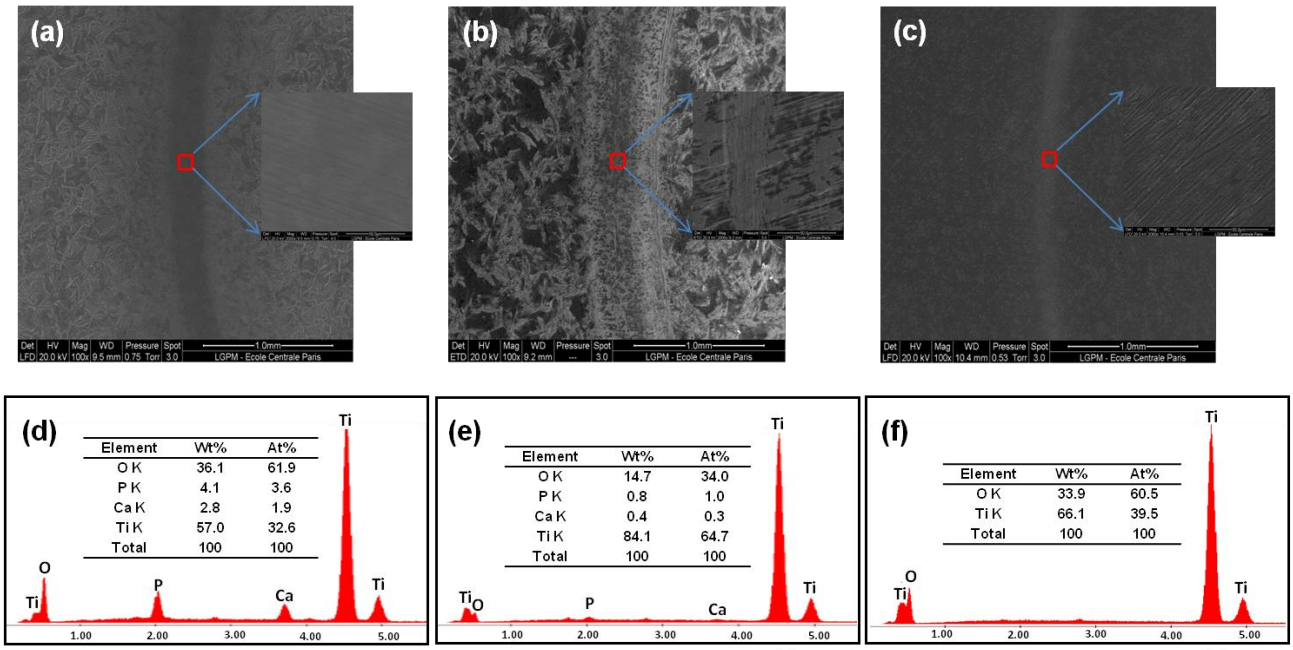

Figure 7-13 SEM images and EDS analysis inside the tracks of CaP/TiO_2 bioceramic film coated Ti (a, d), CaP bioactive film coated Ti (b, e) and TO Ti_6h (c, f) after continuous unidirectional sliding tests at F_n of 500 mN in the PBS solution.

The track profiles of CaP/TiO_2 bioceramic film coated Ti, CaP bioactive film coated Ti and TO Ti_6h after continuous unidirectional sliding tests at F_n of 500 mN are shown in Figure 7-14. Due to the dissolution of $CaHPO_4$ $2H_2O$ film on CaP bioactive film coated Ti, the undetected material loss on TO Ti_6h and the high roughness of $Ca_3(PO_4)_2$ layer on CaP/TiO_2 bioceramic film coated Ti, the track depth and track width of all three samples are difficult to identified. It seems that the track width of CaP/TiO_2 bioceramic film coated Ti is the largest one, but it should be noticed that all material loss on CaP/TiO_2 film coated Ti doesn't not contain the loss of cp Ti substrate. In this case,

it is very hard to compare the material loss for these three samples.

Besides the film dissolution of CaP bioactive film during immersion in the PBS solution, there is no doubt that the material loss for these three samples is relatively low under mechanical loaded condition at F_n of 500 mN in this study, revealing that CaP/TiO_2 bioceramic film coated Ti, CaP bioactive coated Ti and TO Ti_6h are all good choices for biomedical implant applications in the mild loading applied parts. However, considering the long-term bioactivity, CaP/TiO_2 bioceramic film coated Ti is regarded as the best one among these three samples.

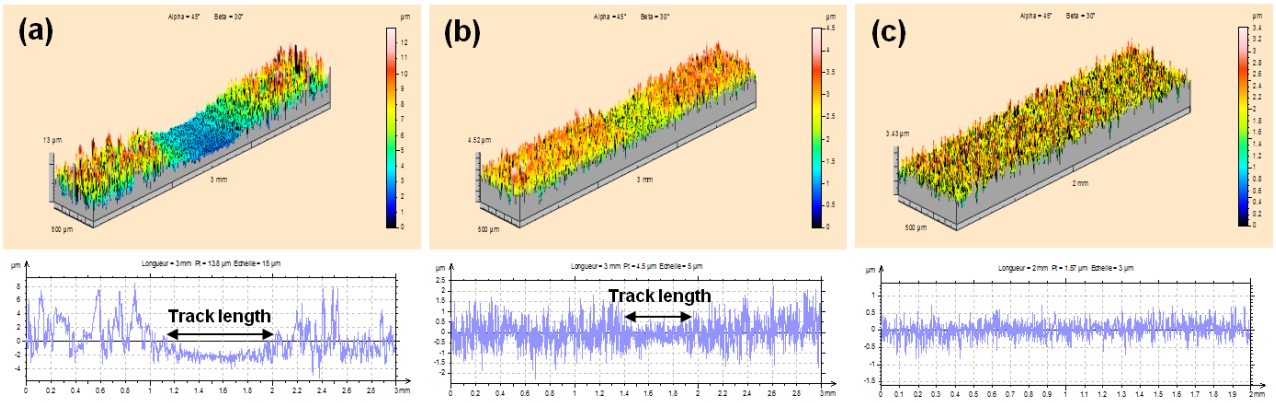

Figure 7-14 Profiles of CaP/TiO_2 bioceramic film coated Ti (a), CaP bioactive film coated Ti (b) and TO Ti_6h (c) after continuous unidirectional sliding tests at F_n of 500 mN in the PBS solution.

7.7 Conclusions

Surface modification of cp Ti with electrochemical deposition of CaP bioactive film and then sintering at 650 ℃ for 6 h to get a composite of CaP/TiO_2 bioceramic film is a good method to improve its wear resistance and provide a long-term bioactivity. The CaP/TiO_2 bioceramic film is mainly in the forms of $Ca_3(PO_4)_2$, TiO_2 and $CaTi_{21}O_{38}$ characterized by XRD. The surface roughness of CaP/TiO_2 bioceramic film coated Ti increases slightly from increases to 2.37 μm when comparing with that of CaP bioactive film coated Ti as 2.01 μm. The microhardness is enhanced to 177 $HV_{0.2}$ by the formation of harder $CaTi_{21}O_{38}$/TiO_2 layers after the sintering treatment, but still less than the microhardness value of TO Ti_6h (about 395 $HV_{0.2}$) prepared at 650 ℃ for 6 h without any CaP bioactive film. Surface morphology/chemical composition of CaP/TiO_2 bioceramic film coated Ti remains like the CaP bioactive film coated Ti with the same flower-like structure and the similar atomic ratio value of Ca/P.

Potentiodynamic polarization measurement results show that, the E_{corr} of CaP/TiO_2 bioceramic film coated Ti is more noble than that of CaP bioactive film coated Ti but still less noble than that of TO Ti_6h. From the potential polarization curves, it seems like TO Ti_6h exhibits the most excellent corrosion resistant property in the whole test potential range from -1 V to 3 V vs. Ag/AgCl. However,

the effect of CaP film change on current density cannot be ignored during the test potential range. The lower current densities of i_{bp} and i_{pass} (about one order of magnitude less than those of CaP bioactive film coated Ti) indicate the better corrosion resistance of CaP/TiO_2 bioceramic film coated Ti in this study.

The OCP evolution curves before sliding under static condition, during sliding under mechanical loaded condition at F_n of 500 mN and after sliding under re-static condition for CaP bioactive film coated Ti significantly change in the whole test period, especially at the moment when sliding starts or sliding stops. But those curves for CaP/TiO_2 bioceramic film coated Ti and TO Ti_6h have relative slight change in the noble direction in the whole test period, revealing that no destruction occurs on cp Ti substrate under the protection of CaP/TiO_2 bioceramic film and TiO_2 film. The excellent corrosion resistance can be further confirmed by the specific polarization resistance, r_p value measured during sliding test at F_n of 500 mN. Unlike the big changes in r_p value of CaP bioactive film coated Ti before, during and after sliding test, no depassivation/repassivation occurs on CaP/TiO_2 bioceramic film coated Ti and TO Ti_6h. Their r_p values keep relative stable (always in the same order of magnitude as 10^7 $\Omega \cdot cm^2$) in the whole test period.

Under mechanical loaded condition, the lower friction coefficients for CaP/TiO_2 bioceramic film coated Ti and TO Ti_6h in this study indicate the improved wear resistance of cp Ti with surface modification of CaP/TiO_2 bioceramic film and TiO_2 film. The remaining film inside and outside the track area of CaP/TiO_2 bioceramic film coated Ti after sliding test also proofs its excellent wear resistant property. Combining with its long-term bioactivity, CaP/TiO_2 bioceramic film coated Ti is considered to be the best choice for biomedical implant application in the mild loading applied parts.

Chapter 8: Culture of NiH/3T3 fibroblast cells on cp Ti

8.1 Introduction

Titanium and its alloys have been widely used in biomedical applications such as dental and orthopedic implants, due to their good mechanical properties, excellent corrosion resistance and adequate biocompatibility. To investigate the biocompatible property of commercially pure titanium (cp Ti), NiH/3T3 fibroblast cells are cultured on its surface. This short study is aim to carry out a standard culture procedure and the primary experimental results are discussed.

8.2 Materials and cell culture procedure

8.2.1 Material

Commercially pure titanium (cp Ti, grade 2) (Goodfellow Cambridge Limited, UK) specimens were cut into square shape of 2 cm ×2 cm ×0.2 cm, with a working surface area of 4 cm^2. The samples were polished with SiC emery papers until #1200 and followed by an ultrasonic cleaning in acetone and then in ethanol for each 5 min.

NiH/3T3 fibroblast cells (NiH/3T3, ATCC®CRL1658™) were obtained from American Type Culture Collection (ATCC). Culture medium of Dulbecco's Modified Eagle's Medium (DMEM), antibiotics (penicillin-streptomycin, PS), fetal bovine serum (FBS) and trypsin were purchased from Life Technologies (Carlsbad, USA); plastic wares and pipettes from TPP (Trasadingen, Switzerland).

8.2.2 Cell culture

To investigate the behavior of cell proliferation on cp Ti surface, the modified fibroblast cells NiH/3T3 with green fluorescence protein (GFP) were seeded at a density of 5 ×10^4 cells/cm^2 on either tissue culture polystyrene (TCPS) as control or cp Ti surfaces and cultured in DMEM with 10% FBS and 1% PS. They were maintained in a total humidified 5% CO_2 incubator at 37^{o}C. The enzymatic digestion with trypsin was used to harvest the cells. The cells were counted using Hemacytometer under an optical microscope (Zeiss). In this study, three samples are tested meanwhile for each analysis at the culture time of 1 day, 2 days, 3 days and 7 days.

Figure 8-1 Tissue culture test plate with surface area of 8.96 cm^2 for each well used in this study.

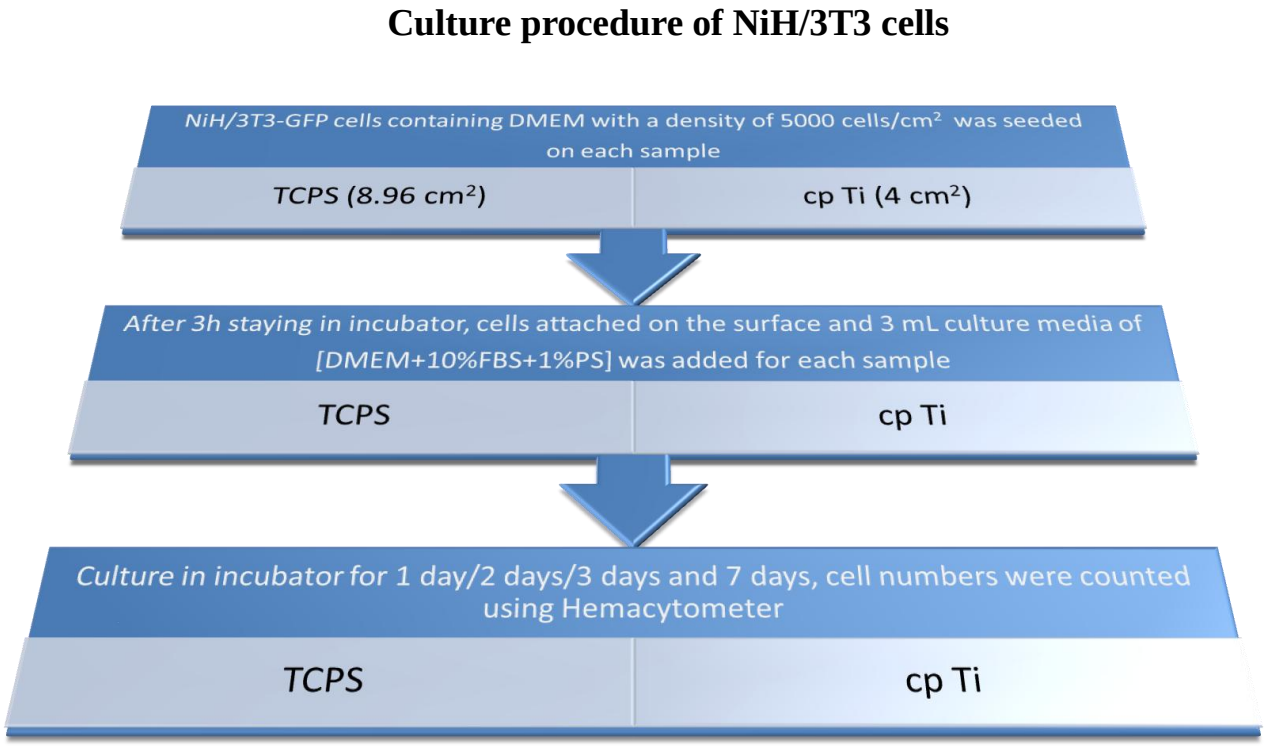

Details of cell count are illustrated as following:

(A) For cp Ti:

1. 0.5 mL typsin is used to activate the cell and then ejected quickly;

2. another 0.5 mL typsin is then added and put the sample inside an incubator for about 7 min to harvest all the cells;

3. 1.5 mL medium of [DMEM+10%FBS] is added into previous 0.5 mL typsin, and then mix these 2 mL solution to make the cells diffused uniformly;

4. centrigufation of cells inside these 2 mL is done at a speed of 2000 rpm in 3 min;

5. pouring the solution out and get the centrifuged cell aggregate;

6. adding 0.5 mL DMEM to make cell suspended uniformly and counting cell numbers;

7. taking 0.2 ml out from the 0.5 mL solution and then adding 0.1 mL trypan blue as an indicator of dead cells (volume ratio of trypan blue and cell containing DMEM is always 1:2);

8. counting the cell numbers in total and cell mortality

9. from the obtained cell numbers, ***M***, on Hemacytometer plate (volume of 1 μL as standard), the cell numbers in total, ***N***, for each sample after culture can be calculated as:

$$N = 3/2\ M\ 500 = 750\ M$$

(B) For TCPS, cell culture area and the total cells in one plate is bigger than cp Ti. So the volume of each product should be increased and the procedure of counts is changed slightly as followings:

1. 1 mL typsin is used to activate the cell and then ejected quickly;

2. another 1 mL typsin is then added and put the sample inside an incubator for about 7 min to harvest all the cells;

3. 1 mL medium of [DMEM+10%FBS] is added into previous 1 mL typsin, and then mix these 2 mL solution to make the cells diffused uniformly (centrifugation is not needed);

4. taking 0.2 ml out from the 2 mL solution and then adding 0.1 mL trypan blue as an indicator of dead cells (volume ratio of trypan blue and cell containing DMEM is always 1:2);

5. counting the cell numbers in total and cell mortality

6. from the obtained cell numbers, ***M***, on Hemacytometer plate (volume of 1 μL as standard), the cell numbers in total, ***N'***, for each sample after culture can be calculated as:

$$N' = 3/2\ M\ 2000 = 3000\ M$$

8.3 Preliminary results

Table 8-1 Cell numbers of NiH/3T3-GFP in 7 days.

Sample	Seeding area (cm^2)	Cell numbers at t = 0 day ($cells/cm^2$)	Cell numbers at t = 1 day ($cells/cm^2$)	Cell numbers at t = 2 days ($cells/cm^2$)	Cell numbers at t = 3 days ($cells/cm^2$)	Cell numbers at t = 7 days ($cells/cm^2$)
TCPS	~ 8.96	5000	6560 ± 760	11620 ± 2450	20100 ± 1910	341350 ± 17520
cp Ti	~ 4	5000	3040 ± 160	8450 ± 550	18800 ± 1570	396750 ± 11670

Table 8-2 Cell viability of NiH/3T3-GFP in 7 days.

Sample	Seeding area (cm^2)	Cell viability at t = 0 day (%)	Cell viability at t = 1 day (%)	Cell viability at t = 2 days (%)	Cell viability at t = 3 days (%)	Cell viability at t = 7 days (%)
TCPS	~ 8.96	96.7	95.3 ± 1.5	93.1 ± 0.6	97.2 ± 0.8	95.9 ± 1.3
cp Ti	~ 4	96.7	96.9 ± 1.0	94.9 ± 1.9	88.9 ± 4.0	96.4 ± 0.4

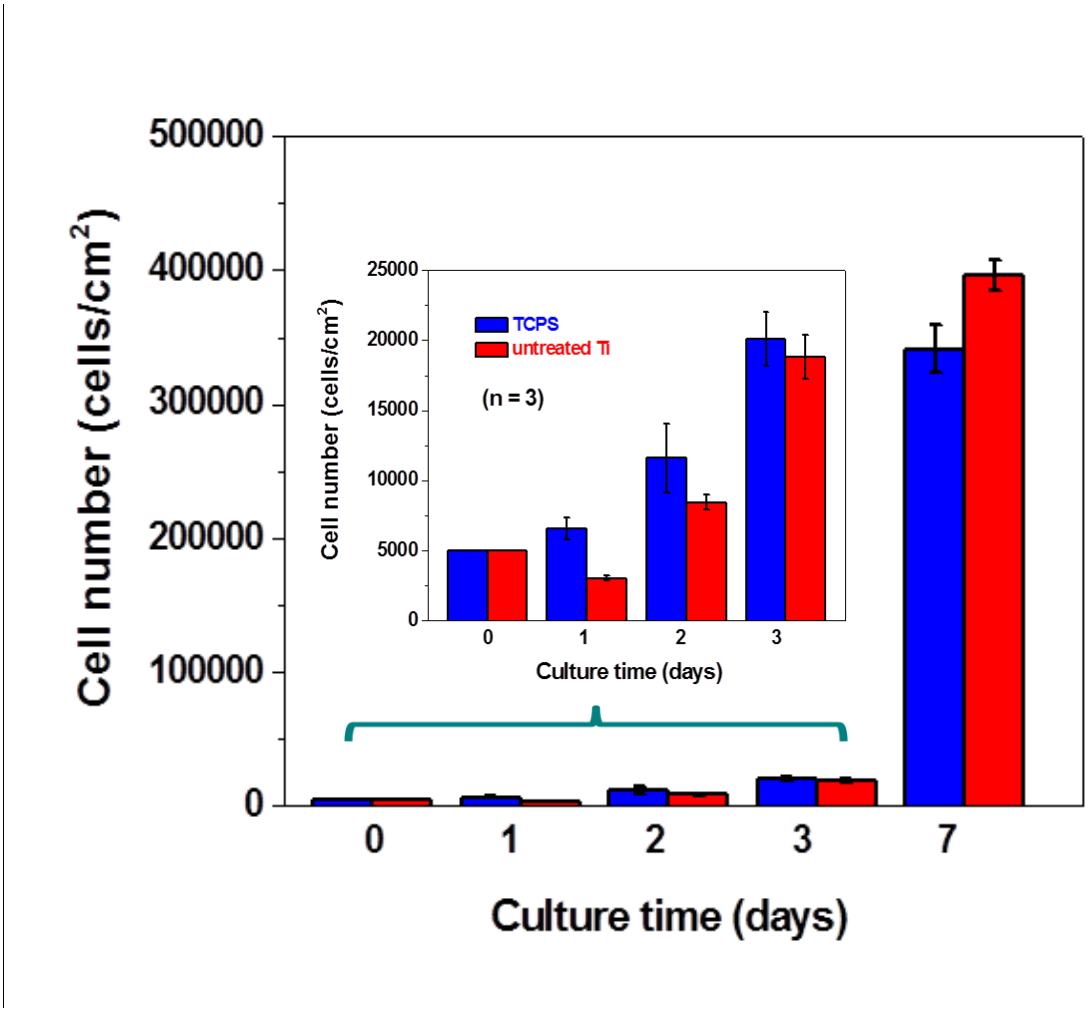

Figure 8-2 Cell counts at different culture time on TCPS (blue) and untreated cp Ti (red).

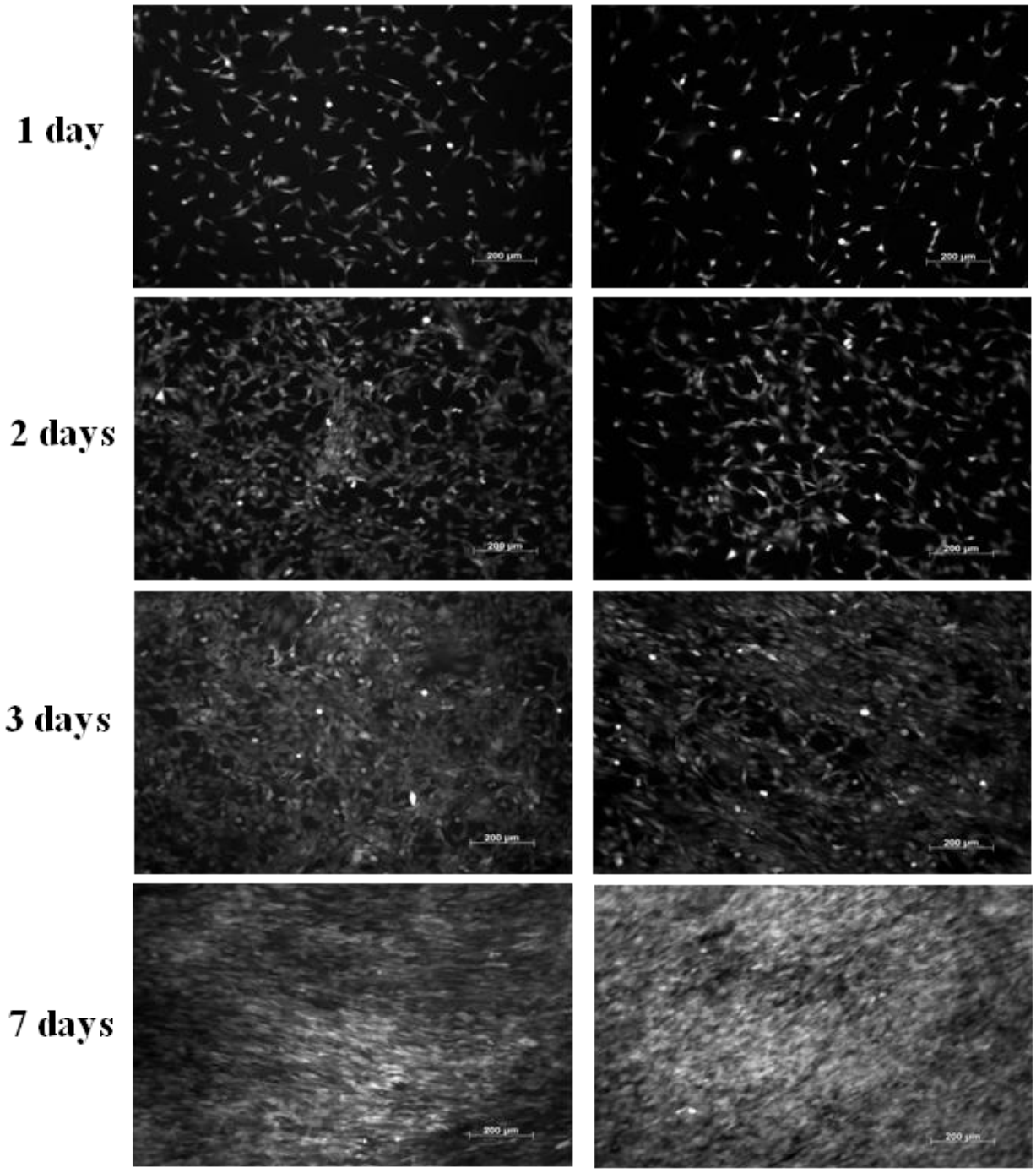

Figure 8-3 Fluorescence micrographs of NiH/3T3-GFP cells on TCPS (left) and cp Ti (right) at different culture time.

From the preliminary results on cp Ti without any surface modification, it can be concluded that this cell culture procedure is feasible and can provide an available method to investigate the biocompatibility of different materials like cp Ti with surface modification or other metals and their alloys in the application of biomedical implants.

Chapter 9: General conclusions and Perspectives

This chapter is devoted to the main conclusions obtained in this work and subsequent suggestions for further research.

9.1 General conclusions

The use of titanium and its alloys in orthopedic and dental-implant applications has increased tremendously in recent years. Once the titanium implants are sited in the hard bone tissues, an intimate contact occurs in the aggressive body fluid. Tribocorrosion, as the interplay between chemical, electrochemical and mechanical processes, leads to a further degradation of titanium implants under mechanical loaded condition rather than corrosion under static condition. This study has made some progress towards the understanding of fundamental tribocorrosion processes and material degradation mechanisms of cp Ti in tribocorrosion systems and thereafter, the modifications on cp Ti to improve its corrosion and tribocorrosion behavior. Some important findings are summarized in the followings.

For cp Ti without any modification, its corrosion behavior was investigated under static condition by electrochemical measurements like OCP, EIS and potentiodynamic polarization. The OCP evolution and EIS results obtained at different immersion time in the PBS solution indicate the corrosion resistance of cp Ti is excellent in the absence of mechanical loading and showing an enhancement of passivation with immersion time.

Under the guidance of the tribocorrosion protocol, continuous unidirectional sliding and intermittent unidirectional sliding tests were imposed to study the tribocorrosion behavior of cp Ti. The significant drop-down of potential and huge decrease of the specific polarization resistance indicate the degradation of passive film under continuous mechanical loaded condition. The periodic potential raise in the noble direction confirms the repassivation of cp Ti in the wear track under intermittent mechanical loaded condition.

The quantitative analysis results show that the contribution of mechanical material loss is dominant in the total material loss of cp Ti. Under continuous mechanical loaded condition, the materials loss increases with the increase of F_n in the range from 1 N to 10 N. Under intermittent mechanical loaded condition at F_n of 5 N, the extension of t_{lat} increases the material loss and the formation of passive film accelerates the mechanical removal of cp Ti. The sensitivity of the passive film to mechanical material loss is higher than that of the active bare material.

From the first experimental part, it is clearly known that cp Ti is a poor wear resistant material. To improve its wear-corrosion property, some surface modification methods are imposed.

For TO Ti, thermal oxidation at 650 ℃ for 48 h leads to the formation of an oxide film throughout the surface without any spallation. The oxide film consists of rutile and oxygen diffused

titanium as the predominant phases, which has no effect on the average roughness but significantly increases the microhardness of cp Ti.

Corrosion resistance of cp Ti is tremendously enhanced by thermal oxidation. Comparing with untreated Ti, TO Ti exhibits a more noble potential value, E_{oc}, a high polarization resistance, r_p and a low current density in the passive domain, i_{pass} under static condition. Even the corrosion resistance of untreated Ti enhances with immersion time increase but the corrosion resistance of TO Ti decreases with immersion time increase, it is still the TO Ti owing the higher r_p value in this study.

Under continuous mechanical loaded condition at F_n of 5 N, the impedance values r_p of both TO Ti and untreated Ti decrease due to the removal of passive film for untreated Ti and the destruction of thermal oxidized film for TO Ti. Unlike the repassivation ability of cp Ti, the destruction of the thermal oxidized film on TO Ti is an irrecoverable process. The friction coefficient value of TO Ti is much lower than that of untreated Ti during the whole mechanical sliding period. Considering the improved corrosion resistance and the better anti-wear performance, thermal oxidation is sure to be regarded as an excellent method to ameliorate the corrosion and tribocorrosion behavior of cp Ti, especially under high mechanical loaded condition.

For CaP bioactive film coated Ti, an electrochemical deposition method was imposed to get a uniform CaP bioactive film in the form of brushite ($CaHPO_4 \cdot 2H_2O$) on cp Ti. An optimized deposition condition was selected as -1.8 V vs. Ag/AgCl for 30 min in this study. The surface roughness and microhardness of CaP bioactive film are very different from the values of cp Ti substrate.

Corrosion resistance of cp Ti is significantly improved with the modification of CaP bioactive film under static condition. Like untreated Ti, the potential value, E_{oc} and the polarization resistance value, r_p of CaP bioactive film coated Ti increase with immersion time, revealing that the existence of CaP bioactive film doesn't change the continuous formation of passive film on cp Ti substrate. It should be noticed that this CaP bioactive film can be dissolved during immersion in the test electrolyte, but still with higher corrosion resistance than untreated Ti in this study.

Under continuous mechanical loaded condition at Fn of 500 mN, the specific polarization resistance value, r_p of CaP bioactive film coated Ti decreases significantly due to the dissolution and removal of CaP bioactive film/passive film. Meanwhile, the potential value, E_{oc} during sliding decreases quite a lot. However, considering the higher r_p value than untreated Ti before, during and after sliding test, and the relative lower friction coefficient in the rotation number range from 2500 cycles to 5000 cycles, CaP bioactive film coated Ti is still an attractive material in biomedical application as orthopedic and dental implants.

For CaP/TiO_2 bioceramic film coated Ti, a further thermal sintering step at 650 ℃ for 6 h was

imposed on CaP bioactive film coated Ti to get a CaP/TiO_2 bioceramic film mainly in the forms of $Ca_3(PO_4)_2$, TiO_2 and $CaTi_{21}O_{38}$. Surface morphology/chemical composition of CaP/TiO_2 bioceramic film coated Ti remains like the CaP bioactive film coated Ti with the same flower-like structure and the similar atomic ratio value of Ca/P.

Corrosion resistance of CaP/TiO_2 bioceramic film coated Ti is considered to be the best one by comparing the specific polarization resistance, r_p with all other samples, like cp Ti, CaP bioactive film coated Ti and TO Ti_6h prepared also at 650 ℃ for 6 h without any CaP bioactive film. The lower current densities of i_{bp} and i_{pass} indicate the better corrosion resistance of CaP/TiO_2 bioceramic film coated Ti in this study.

Unlike CaP bioactive film coated Ti, OCP evolution curves before, during and after sliding for CaP/TiO_2 bioceramic film coated Ti and TO Ti_6h have relative slight change in the noble direction in the whole test period, revealing that no destruction occurs on cp Ti substrate under the protection of CaP/TiO_2 bioceramic film and TiO_2 film. The excellent corrosion resistance can be further confirmed by the high specific polarization resistance, r_p value (above 10^7 Ω·cm^2) measured during sliding test at F_n of 500 mN.

Under mechanical loaded condition, the lower friction coefficients for CaP/TiO_2 bioceramic film coated Ti and TO Ti_6h in this study indicate the improved wear resistance of cp Ti with surface modification of CaP/TiO_2 bioceramic film and TiO_2 film. The remaining film inside and outside the track area of CaP/TiO_2 bioceramic film coated Ti after sliding test also proofs its excellent wear resistant property. Combining with its long-term bioactivity, CaP/TiO_2 bioceramic film coated Ti is considered to be the best choice for biomedical implant application in the mild loading applied parts.

A feasible cell culture procedure was assessed, using the NiH/3T3 fibroblast cells on cp Ti without any surface modification. The cell proliferation on cp Ti is well accepted in the preliminary study.

9.2 Perspectives

Corrosion and tribocorrosion behavior of cp Ti is a complicated and interesting process, especially for those materials with surface modifications. Although the findings from this work are exiting and useful to the understanding and the development of cp Ti and even its alloys as biomedical implant materials, several new questions have been proposed. And some directions are recommended to continue this study in future work, as listed below:

For cp Ti without any modification, the current study is based on a tribocorrosion protocol for passivated material. However, this protocol is not available to investigate the surface modified passivated substrate, due to the destruction and passivation/repassivation behavior under the

modification layers is different from that of untreated materials. The protocol might be further ameliorated with respect to more complicated surface state.

An important concern of the use of metallic implants is the influence of released wear debris and metal ions to patients. In this study, it is clearly to observe the wear debris after sliding test on untreated Ti, its exact effect on corrosion and tribocorrosion behavior of cp Ti should be investigated. The investigation of Ca^{2+} and HPO_4^{2-}/PO_4^{3-} ions dissolution from CaP bioactive film coated Ti or CaP/TiO_2 bioceramic film coated Ti and the corresponding influence on corrosion and tribocorrosion behavior of cp Ti substrate is also necessary.

The electrochemical deposition process used in current study should be developed. Some appropriate parameters might exist to directly obtain HA film from calcium phosphate containing precursor. Other deposition methods can also be used to get a bioactive film on cp Ti to improve its corrosion and tribocorrosion behavior. And further investigation of the effect of different surface modification methods on corrosion and tribocorrosion behavior of cp Ti under different mechanical solicitation conditions is also important to guide the use of biomedical implants.

Considering the application of cp Ti in biomaterial field, the biocompatibility and bioactivity of untreated and surface modified Ti are essential. The culture of fibroblast and osteoblast cells on the surface of biomedical implant materials can give a supplementary instruction in materials selection. A cell culture method is proposed at the end of this work and some preliminary results of NiH/3T3 cell culture on cp Ti without any modification are presented, as seen in Annex. Future work can be concerned with the amelioration of this cell culture method and then investigate the effect of surface modification on the proliferation and viability of cells.

References

[1] Bio-implants market-Global trends and forecasts till 2017, http://www.marketsandmarkets.com/Market-Reports/bio-implants-market-728.html.

[2] Annual report 2013, Nobel Biocare Corporate.

[3] L. Scheideler, F. Rupp, W. Lindemann, D. Axmann, G. Gomez-Roman, J. Geis-Gerstorfer, H. Weber, Biocompatibility of microstructured titanium implant surfaces., J Dent Res, 82 (2003) B241-B241.

[4] J. Pan, D. Thierry, C. Leygraf, Electrochemical impedance spectroscopy study of the passive oxide film on titanium for implant application, Electrochimica Acta, 41 (1996) 1143-1153.

[5] M. Long, H.J. Rack, Titanium alloys in total joint replacement—a materials science perspective, Biomaterials, 19 (1998) 1621-1639.

[6] P.-I. Brånemark, U. Breine, R. Adell, B.O. Hansson, J. Lindström, Å. Ohlsson, Intra-Osseous Anchorage of Dental Prostheses:I. Experimental Studies, Scandinavian Journal of Plastic and Reconstructive Surgery and Hand Surgery, 3 (1969) 81-100.

[7] R. Adell, U. Lekholm, B. Rockler, P.I. Brånemark, A 15-year study of osseointegrated implants in the treatment of the edentulous jaw, International Journal of Oral Surgery, 10 (1981) 387-416.

[8] C. Vasilescu, P. Drob, E. Vasilescu, I. Demetrescu, D. Ionita, M. Prodana, S.I. Drob, Characterisation and corrosion resistance of the electrodeposited hydroxyapatite and bovine serum albumin/hydroxyapatite films on Ti–6Al–4V–1Zr alloy surface, Corrosion Science, 53 (2011) 992-999.

[9] D.W. Hoeppner, V. Chandrasekaran, Fretting in orthopaedic implants: A review, Wear, 173 (1994) 189-197.

[10] J. Geringer, B. Forest, P. Combrade, Fretting-corrosion of materials used as orthopaedic implants, Wear, 259 (2005) 943-951.

[11] The orthopaedic industry annual report 2013, Orthoworld.

[12] J. Black, Biological Performance of Materials: Fundamentals of Biocompatibility Marcel Dekker, New York, 1992.

[13] P. Parida, A. Behera, S. Mishra, Classification of Biomaterials used in Medicine, International Journal of Advances in Applied Science, 1 (2012) 31-35.

[14] G. Manivasagam, D. Dhinasekaran, A. Rajamanickam, Biomedical Implants: Corrosion and its Prevention - A Review, Recent Patents on Corrosion Science, 2 (2010) 40-54.

[15] A. Sáenz, E. Rivera-Muñoz, W. Brostow, V.M. Castaño, Ceramic biomaterials: An introductory overview, Journal of Materials Education, 21 (1999) 297-306.

[16] M. Geetha, A.K. Singh, R. Asokamani, A.K. Gogia, Ti based biomaterials, the ultimate choice for orthopaedic implants – A review, Progress in Materials Science, 54 (2009) 397-425.

[17] K.S. Katti, Biomaterials in total joint replacement, Colloids and Surfaces B: Biointerfaces, 39 (2004) 133-142.

[18] K. de Groot, Bioceramics consisting of calcium phosphate salts, Biomaterials, 1 (1980) 47-50.

[19] D. Rokusek, C. Davitt, A. Bandyopadhyay, S. Bose, H.L. Hosick, Interaction of human osteoblasts with bioinert and bioactive ceramic substrates, J Biomed Mater Res A, 75A (2005) 588-594.

[20] Y. Iwashita, T. Yamamuro, R. Kasai, T. Kitsugi, T. Nakamura, H. Okumura, T. Kokubo, Osteoconduction of bioceramics in normal and osteopenic rats: Comparison between bioactive and bioinert ceramics, Journal of Applied Biomaterials, 3 (1992) 259-268.

[21] S. Kanchana, S. Hussain, Zirconia a Bio-inert Implant Material, IOSR Journal of Dental and Medical Science, 12 (2013) 66-67.

[22] J.C. Helmer, T.D. Driskell, Research on Bioceramics. Symposium on Use of Ceramics as Surgical Implants. South Carolina.Clemson University; 1969., South Carolina. Clemson University, (1969).

[23] P. Christel, A. Meunier, J.M. Dorlot, J.M. Crolet, J. Witvoet, L. Sedel, P. Boutin, Biomechanical Compatibility and Design of Ceramic Implants for Orthopedic Surgery, Annals of the New York Academy of Sciences, 523 (1988) 234-256.

[24] D. Kluess, W. Mittelmeier, R. Bader, Ceramics for Joint Replacements, in: P.A. Revell (Ed.) Joint Replacement Technology, Woodhead Publishing, Cambridge, UK, 2008.

[25] S. Affatato, L. Grillini, Topography in bio-tribocorrosion, in: Y. Yan (Ed.) Bio-tribocorrosion in biomaterials and medical implants, Woodhead Publishing, Cambridge, UK, 2013.

[26] L.S. Nair, C.T. Laurencin, Polymers as Biomaterials for Tissue Engineering and Controlled Drug Delivery, in: K. Lee, D. Kaplan (Eds.) Tissue Engineering I, Springer Berlin Heidelberg, 2006, pp. 47-90.

[27] L.S. Nair, C.T. Laurencin, Biodegradable polymers as biomaterials, Progress in Polymer Science, 32 (2007) 762-798.

[28] A.G. Pathiraja, R. Adhikari, Biodegradable synthetic polymers for tissue engineering, European Cells and Materials, 5 (2003) 1-16.

[29] L. Tan, X. Yu, P. Wan, K. Yang, Biodegradable Materials for Bone Repairs: A Review, Journal of Materials Science & Technology, 29 (2013) 503-513.

[30] H. Hermawan, D. Ramdan, J.R.P. Djuansjah, Metals for Biomedical Applications, in: R. Fazel-Rezai (Ed.) Biomedical Engineering - From Theory to Applications, InTech, 2011.

[31] W.A. Lane, Some remarks on the treatment of fractures, The British Medical Journal, 1 (1895) 861-863.

[32] A. Lambotte, Technique et indication des prothèses dans le traitement des fractures, Presse Med Belge, 17 (1909) 321-323.

[33] T. Ma, P. Wan, Y. Cui, G. Zhang, J. Li, J. Liu, Y. Ren, K. Yang, L. Lu, Cytocompatibility of High Nitrogen Nickel-Free Stainless Steel for Orthopedic Implants, Journal of Materials Science & Technology, 28 (2012) 647-653.

[34] S. Mischler, A.I. Munoz, Wear of CoCrMo alloys used in metal-on-metal hip joints: A tribocorrosion appraisal, Wear, 297 (2013) 1081-1094.

[35] S.S. Bhasin, V. Singh, T. Ahmed, B.P. Singh, Studies on titanium-based dental implant material, Ceram Eng Sci Proc, 24 (2003) 245-254.

[36] I. García, D. Drees, J.P. Celis, Corrosion-wear of passivating materials in sliding contacts based on a concept of active wear track area, Wear, 249 (2001) 452-460.

[37] M.T. Mathew, M.J. Runa, M. Laurent, J.J. Jacobs, L.A. Rocha, M.A. Wimmer, Tribocorrosion behavior of CoCrMo alloy for hip prosthesis as a function of loads: A comparison between two testing systems, Wear, 271 (2011) 1210-1219.

[38] Y. Yan, A. Neville, D. Dowson, S. Williams, Tribocorrosion in implants - assessing high carbon and low carbon Co-Cr-Mo alloys by *in situ* electrochemical measurements, Tribol Int, 39 (2006) 1509-1517.

[39] H. Hermawan, Biodegradable Metals: From Concept to Applications, Introduction to Metallic Biomaterials, Springer 2012.

[40] J.L. Gilbert, C.A. Buckley, J.J. Jacobs, *In vivo* corrosion of modular hip prosthesis components in mixed and similar metal combinations. The effect of crevice, stress, motion, and alloy coupling, Journal of Biomedical Materials Research, 27 (1993) 1533-1544.

[41] H.H. Uhlig, The Corrosion Handbook, Join Wiley&Sons, New York, 1948.

[42] N. Sato, Basics of Corrosion Chemistry, Jonh Wiley & Sons, New York, 2012.

[43] N. Sato, G. Okamoto, Electrochemical Passivation of Metals, in: J.O.M. Bockris, B. Conway, E. Yeager, R. White (Eds.) Electrochemical Materials Science, Springer US, 1981, pp. 193-245.

[44] M. Pourbaix, Atlas of electrochemical equilibria in aqueous solutions National Association of Corrosion Engineers, Houston, USA, 1974.

[45] D. Upadhyay, M.A. Panchal, R.S. Dubey, V.K. Srivastava, Corrosion of alloys used in dentistry: A review, Materials Science and Engineering: A, 432 (2006) 1-11.

[46] S. Virtanen, I. Milošev, E. Gomez-Barrena, R. Trebše, J. Salo, Y.T. Konttinen, Special modes of corrosion under physiological and simulated physiological conditions, Acta Biomaterialia, 4 (2008) 468-476.

[47] K. Fushimi, M. Seo, Initiation of a Local Breakdown of Passive Film on Iron due to Chloride Ions Generated by a Liquid-Phase Ion Gun, Journal of The Electrochemical Society, 148 (2001) B450-B456.

[48] Z. Szklarska-Smialowska, J. Mankowski, Crevice corrosion of stainless steels in sodium chloride solution, Corrosion Science, 18 (1978) 953-960.

[49] J.W. Oldfield, W.H. Sutton, Crevice Corrosion of Stainless Steels: II. Experimental studies, British Corrosion Journal, 13 (1978) 104-111.

[50] B. Grosgogeat, L. Reclaru, M. Lissac, F. Dalard, Measurement and evaluation of galvanic corrosion between titanium/Ti6Al4V implants and dental alloys by electrochemical techniques and auger spectrometry, Biomaterials, 20 (1999) 933-941.

[51] G. Song, B. Johannesson, S. Hapugoda, D. StJohn, Galvanic corrosion of magnesium alloy AZ91D in contact with an aluminium alloy, steel and zinc, Corrosion Science, 46 (2004) 955-977.

[52] R.B. Waterhouse, Fretting wear, Wear, 100 (1984) 107-118.

[53] K. Merritt, S.A. Brown, Effect of proteins and pH on fretting corrosion and metal ion release, Journal of Biomedical Materials Research, 22 (1988) 111-120.

[54] V.I. Pokhmurs'kyi, V.M. Dovhunyk, Tribocorrosion of Stainless Steels (Review), Mater Sci+, 46 (2010) 87-96.

[55] M. Azzi, J.A. Szpunar, Tribo-electrochemical technique for studying tribocorrosion behavior of biomaterials, Biomol Eng, 24 (2007) 443-446.

[56] J.P. Celis, P. Ponthiaux, F. Wenger, Tribo-corrosion of materials: Interplay between chemical, electrochemical, and mechanical reactivity of surfaces, Wear, 261 (2006) 939-946.

[57] P. McKay, D.B. Mitton, An Electrochemical Investigation of Localized Corrosion on Titanium in Chloride Environments, Corrosion, 41 (1985) 52-62.

[58] S. Barril, S. Mischler, D. Landolt, Electrochemical effects on the fretting corrosion behaviour of Ti6Al4V in 0.9% sodium chloride solution, Wear, 259 (2005) 282-291.

[59] M. Windler, J.E. MacDougall, R. Schenk, Investigation into wear-induced corrosion of orthopedic implant materials, in: G.L. Winters, M.J. Nutt (Eds.) Stainless steels for medical and surgical applications, ASTM International, West Conschohocken, 2003, pp. 211-221.

[60] I.M. Hutchings, Mechanisms of wear in powder technology: A review, Powder Technology, 76 (1993) 3-13.

[61] A.P. Harsha, U.S. Tewari, Two-body and three-body abrasive wear behaviour of polyaryletherketone composites, Polymer Testing, 22 (2003) 403-418.

[62] H. Unal, U. Sen, A. Mimaroglu, Abrasive wear behaviour of polymeric materials, Materials & Design, 26 (2005) 705-710.

[63] E. Rabinowicz, The least wear, Wear, 100 (1984) 533-541.

[64] A. Buford, T. Goswami, Review of wear mechanisms in hip implants: Paper I – General, Materials & Design, 25 (2004) 385-393.

[65] P. Blanchard, C. Colombie, V. Pellerin, S. Fayeulle, L. Vincent, Material effects in fretting wear: application to iron, titanium, and aluminum alloys, MTA, 22 (1991) 1535-1544.

[66] L. Rozeanu, Fatigue wear as a rate process, Wear, 6 (1963) 337-340.

[67] E. Rabinowicz, L.A. Dunn, P.G. Russell, A study of abrasive wear under three-body conditions, Wear, 4 (1961) 345-355.

[68] S.M. Kurtz, O.K. Muratoglu, M. Evans, A.A. Edidin, Advances in the processing, sterilization, and crosslinking of ultra-high molecular weight polyethylene for total joint arthroplasty, Biomaterials, 20 (1999) 1659-1688.

[69] M. Chandrasekaran, L.Y. Wei, K.K. Venkateshwaran, A.W. Batchelor, N.L. Loh, Tribology of UHMWPE tested against a stainless steel counterface in unidirectional sliding in presence of model synovial fluids: part 1, Wear, 223 (1998) 13-21.

[70] N. Diomidis, S. Mischler, N.S. More, M. Roy, S.N. Paul, Fretting-corrosion behavior of β titanium alloys in simulated synovial fluid, Wear, 271 (2011) 1093-1102.

[71] K.L. Dahm, Fatigue-like failure of thermally oxidised titanium in reciprocating pin-on-plate wear tests, Wear, 267 (2009) 409-416.

[72] C. Leinenbach, D. Eifler, Influence of oxidation treatment on fatigue and fatigue-induced damage of commercially pure titanium, Acta Biomaterialia, 5 (2009) 2810-2819.

[73] J.P. Celis, P. Ponthiaux, Testing tribocorrosion of passivating materials supporting research and industrial innovation-Handbook, 2012.

[74] A. Fischer, S. Mischler, Tribocorrosion: fundamentals, materials and applications, J Phys D Appl Phys, 39 (2006).

[75] Y.N. Kok, R. Akid, P.E. Hovsepian, Tribocorrosion testing of stainless steel (SS) and PVD coated SS using a modified scanning reference electrode technique, Wear, 259 (2005) 1472-1481.

[76] A. Bazzoni, S. Mischler, N. Espallargas, Tribocorrosion of Pulsed Plasma-Nitrided CoCrMo Implant Alloy, Tribol Lett, 49 (2013) 157-167.

[77] T.M. Manhabosco, I.L. Muller, Tribocorrosion of Diamond-Like Carbon Deposited on Ti6Al4V, Tribol Lett, 33 (2009) 193-197.

[78] P. Henry, J. Takadoum, P. Berçot, Tribocorrosion of 316L stainless steel and TA6V4 alloy in H_2SO_4 media, Corrosion Science, 51 (2009) 1308-1314.

[79] M.T. Mathew, E. Ariza, L.A. Rocha, F. Vaz, A.C. Fernandes, M.M. Stack, Tribocorrosion behaviour of TiC_xO_y thin films in bio-fluids, Electrochimica Acta, 56 (2010) 929-937.

[80] A.C. Fernandes, F. Vaz, E. Ariza, L.A. Rocha, A.R.L. Ribeiro, A.C. Vieira, J.P. Riviere, L. Pichon, Tribocorrosion behaviour of plasma nitrided and plasma nitrided plus oxidised Ti6A14V alloy, Surf Coat Tech, 200 (2006) 6218-6224.

[81] A.C. Alves, F. Oliveira, F. Wenger, P. Ponthiaux, J.P. Celis, L.A. Rocha, Tribocorrosion behaviour of anodic treated titanium surfaces intended for dental implants, Journal of Physics D: Applied Physics, 46 (2013) 404001.

[82] J. Liu, X. Wang, B.J. Wu, T.F. Zhang, Y.X. Leng, N. Huang, Tribocorrosion behavior of DLC-coated CoCrMo alloy in simulated biological environment, Vacuum, 92 (2013) 39-43.

[83] N.S. More, N. Diomidis, S.N. Paul, M. Roy, S. Mischler, Tribocorrosion behavior of beta titanium alloys in physiological solutions containing synovial components, Mat Sci Eng C-Mater, 31 (2011) 400-408.

[84] M.T. Mathew, P. Srinivasa Pai, R. Pourzal, A. Fischer, M.A. Wimmer, Significance of Tribocorrosion in Biomedical Applications: Overview and Current Status, Advances in Tribology, 2009 (2009) 1-12.

[85] J. Jiang, M.M. Stack, Modelling sliding wear: From dry to wet environments, Wear, 261 (2006) 954-965.

[86] M. Stemp, S. Mischler, D. Landolt, The effect of mechanical and electrochemical parameters on the tribocorrosion rate of stainless steel in sulphuric acid, Wear, 255 (2003) 466-475.

[87] Y. Sun, E. Haruman, Effect of electrochemical potential on tribocorrosion behavior of low temperature plasma carburized 316L stainless steel in 1 M H_2SO_4 solution, Surf Coat Tech, 205 (2011) 4280-4290.

[88] D. Landolt, S. Mischler, M. Stemp, Electrochemical methods in tribocorrosion: a critical appraisal, Electrochimica Acta, 46 (2001) 3913-3929.

[89] P. Ponthiaux, F. Wenger, D. Drees, J.P. Celis, Electrochemical techniques for studying tribocorrosion processes, Wear, 256 (2004) 459-468.

[90] P. Jemmely, S. Mischler, D. Landolt, Electrochemical modeling of passivation phenomena in tribocorrosion, Wear, 237 (2000) 63-76.

[91] D. Landolt, S. Mischler, M. Stemp, S. Barril, Third body effects and material fluxes in tribocorrosion systems involving a sliding contact, Wear, 256 (2004) 517-524.

[92] N. Diomidis, J.P. Celis, P. Ponthiaux, F. Wenger, A methodology for the assessment of the tribocorrosion of passivating metallic materials, Lubrication Science, 21 (2009) 53-67.

[93] R. Vannoort, Titanium - the Implant Material of Today, J Mater Sci, 22 (1987) 3801-3811.

[94] Y. Oshida, Bioscience and Bioengineering of Titanium Materials, Elsevier, Oxford, UK, 2007.

[95] P. Bania, Beta titanium alloys and their role in the titanium industry, JOM, 46 (1994) 16-19.

[96] R.W. Schutz, Environmental behavior of beta titanium alloys, JOM, 46 (1994) 24-29.

[97] Z.H. Guo, L. Zhou, M.D. Rong, A.D. Zhu, H.O. Geng, Bone Response to a Pure Titanium Implant Surface Modified by Laser Etching and Microarc Oxidation, Int J Oral Max Impl, 25 (2010) 130-136.

[98] R. Burgers, T. Gerlach, S. Hahnel, F. Schwarz, G. Handel, M. Gosau, *In vivo* and *in vitro* biofilm formation on two different titanium implant surfaces, Clin Oral Implan Res, 21 (2010) 156-164.

[99] J. Muyco, T. Ratto, C. Orme, J. McKittrick, J. Frangos, Interaction between titanium implant surfaces and hydrogen peroxide in biologically relevant environments, Mater Res Soc Symp P, 823 (2004) 219-224.

[100] H. Schiefer, M. Bram, H.P. Buchkremer, D. Stover, Porous Titanium for Dental Implant Applications, Porous Metals and Metallic Foams: Metfoam 2007, (2008) 259-262.

[101] H.Z. Ye, X.Y. Liu, H.P. Hong, Cladding of titanium/hydroxyapatite composites onto Ti6Al4V for load-bearing implant applications, Mat Sci Eng C-Mater, 29 (2009) 2036-2044.

[102] K. Gu, J. Wang, Y. Zhou, Effect of cryogenic treatment on wear resistance of Ti–6Al–4V alloy for biomedical applications, Journal of the Mechanical Behavior of Biomedical Materials, 30 (2014) 131-139.

[103] H. Güleryüz, H. Çimenoğlu, Effect of thermal oxidation on corrosion and corrosion–wear behaviour of a Ti–6Al–4V alloy, Biomaterials, 25 (2004) 3325-3333.

[104] C. Sittig, M. Textor, N.D. Spencer, M. Wieland, P.H. Vallotton, Surface characterization of implant materials c.p. Ti, Ti-6Al-7Nb and Ti-6Al-4V with different pretreatments, J Mater Sci: Mater Med, 10 (1999) 35-46.

[105] S. Rao, T. Ushida, T. Tateishi, Y. Okazaki, S. Asao, Effect of Ti, Al, and V ions on the relative growth rate of fibroblasts (L929) and osteoblasts (MC3T3-E1) cells, Bio-Medical Materials and Engineering, 6 (1996) 79-86.

[106] S. Nag, R. Banerjee, H.L. Fraser, Microstructural evolution and strengthening mechanisms in Ti–Nb–Zr–Ta, Ti–Mo–Zr–Fe and Ti–15Mo biocompatible alloys, Materials Science and Engineering: C, 25 (2005) 357-362.

[107] B. Kasemo, Biocompatibility of titanium implants: Surface science aspects, The Journal of Prosthetic Dentistry, 49 (1983) 832-837.

[108] J.W. Schultze, M.M. Lohrengel, Stability, reactivity and breakdown of passive films. Problems of recent and future research, Electrochimica Acta, 45 (2000) 2499-2513.

[109] C. Coddet, A.M. Craze, G. Beranger, Measurements of the adhesion of thermal oxide films: application to the oxidation of titanium, J Mater Sci, 22 (1987) 2969-2974.

[110] D. Reyes-Coronado, G. Rodríguez-Gattorno, M.E. Espinosa-Pesqueira, C. Cab, R.d. Coss, G. Oskam, Phase-pure TiO_2 nanoparticles: anatase, brookite and rutile, Nanotechnology, 19 (2008) 145605.

[111] M. Pourbaix, Electrochemical corrosion of metallic biomaterials, Biomaterials, 5 (1984) 122-134.

[112] E. Kelly, Electrochemical Behavior of Titanium, in: J.O.M. Bockris, B.E. Conway, R. White (Eds.) Modern Aspects of Electrochemistry, Springer US, 1982, pp. 319-424.

[113] J.E. Sundgren, P. Bodö, I. Lundström, Auger electron spectroscopic studies of the interface between human tissue and implants of titanium and stainless steel, Journal of Colloid and Interface Science, 110 (1986) 9-20.

[114] J.M. Anderson, The bone-biomaterial interface. J. E. Davies, (ed.), University of Toronto Press, Toronto, Canada, 1991, Journal of Biomedical Materials Research, 26 (1992) 1395-1396.

[115] T. Hanawa, *In vivo* metallic biomaterials and surface modification, Materials Science and Engineering: A, 267 (1999) 260-266.

[116] J.C.M. Souza, S.L. Barbosa, E. Ariza, J.P. Celis, L.A. Rocha, Simultaneous degradation by corrosion and wear of titanium in artificial saliva containing fluorides, Wear, 292–293 (2012) 82-88.

[117] G. Mabilleau, S. Bourdon, M.L. Joly-Guillou, R. Filmon, M.F. Baslé, D. Chappard, Influence of fluoride, hydrogen peroxide and lactic acid on the corrosion resistance of commercially pure titanium, Acta Biomaterialia, 2 (2006) 121-129.

[118] N. Schiff, B. Grosgogeat, M. Lissac, F. Dalard, Influence of fluoride content and pH on the corrosion resistance of titanium and its alloys, Biomaterials, 23 (2002) 1995-2002.

[119] M. Koike, H. Fujii, The corrosion resistance of pure titanium in organic acids, Biomaterials, 22 (2001) 2931-2936.

[120] M.P. Licausi, A.I. Munoz, V.A. Borras, Influence of the fabrication process and fluoride content

on the tribocorrosion behaviour of Ti6Al4V biomedical alloy in artificial saliva, Journal of the Mechanical Behavior of Biomedical Materials, 20 (2013) 137-148.

[121] H.-H. Huang, Effect of fluoride and albumin concentration on the corrosion behavior of Ti–6Al–4V alloy, Biomaterials, 24 (2003) 275-282.

[122] P.D. Miller, J.W. Holladay, Friction and wear properties of titanium, Wear, 2 (1958) 133-140.

[123] M.K. Dimah, F. Devesa Albeza, V. Amigó Borrás, A. Igual Muñoz, Study of the biotribocorrosion behaviour of titanium biomedical alloys in simulated body fluids by electrochemical techniques, Wear, 294–295 (2012) 409-418.

[124] R. Priya, C. Mallika, U.K. Mudali, Wear and tribocorrosion behaviour of 304L SS, Zr-702, Zircaloy-4 and Ti-grade2, Wear, 310 (2014) 90-100.

[125] A.C. Vieira, A.R. Ribeiro, L.A. Rocha, J.P. Celis, Influence of pH and corrosion inhibitors on the tribocorrosion of titanium in artificial saliva, Wear, 261 (2006) 994-1001.

[126] B. Rauschenbach, Formation of compounds by high-flux nitrogen ion implantation in titanium, J Mater Sci, 21 (1986) 395-404.

[127] F. Galliano, E. Galvanetto, S. Mischler, D. Landolt, Tribocorrosion behavior of plasma nitrided Ti-6Al-4V alloy in neutral NaCl solution, Surf Coat Tech, 145 (2001) 121-131.

[128] T. Hanawa, Y. Kamiura, S. Yamamoto, T. Kohgo, A. Amemiya, H. Ukai, K. Murakami, K. Asaoka, Early bone formation around calcium-ion-implanted titanium inserted into rat tibia, Journal of Biomedical Materials Research, 36 (1997) 131-136.

[129] S. Tugulu, K. Löwe, D. Scharnweber, F. Schlottig, Preparation of superhydrophilic microrough titanium implant surfaces by alkali treatment, J Mater Sci: Mater Med, 21 (2010) 2751-2763.

[130] S. Tamilselvi, H.B. Raghavendran, P. Srinivasan, N. Rajendran, *In vitro* and *in vivo* studies of alkali- and heat-treated Ti-6Al-7Nb and Ti-5Al-2Nb-1Ta alloys for orthopedic implants, J Biomed Mater Res A, 90A (2009) 380-386.

[131] J. Pan, H. Liao, C. Leygraf, D. Thierry, J. Li, Variation of oxide films on titanium induced by osteoblast-like cell culture and the influence of an H_2O_2 pretreatment, Journal of Biomedical Materials Research, 40 (1998) 244-256.

[132] J.-H. Park, Y.-K. Lee, K.-M. Kim, K.-N. Kim, Bioactive calcium phosphate coating prepared on H_2O_2-treated titanium substrate by electrodeposition, Surface and Coatings Technology, 195 (2005) 252-257.

[133] Y. Sasikumar, N. Rajendran, Influence of surface modification on the apatite formation and corrosion behavior of Ti and Ti-15Mo alloy for biomedical applications, Mater Chem Phys, 138 (2013) 114-123.

[134] R. Padma, K. Ramkumar, M. Satyam, Growth of titanium oxide overlayers by thermal oxidation of titanium, J Mater Sci, 23 (1988) 1591-1597.

[135] C. Panagopoulos, H. Badekas, The influence of anodic TiO_2 films on the thermal oxidation of titanium, Materials Letters, 5 (1987) 307-310.

[136] H. Lee, S. Dregia, S. Akbar, M. Alhoshan, Growth of 1-D TiO_2 nanowires on Ti and Ti alloys by oxidation, J. Nanomaterials, 2010 (2010) 1-7.

[137] B. Dinan, D. Gallego-Perez, H. Lee, D. Hansford, S.A. Akbar, Thermally grown TiO_2 nanowires to improve cell growth and proliferation on titanium based materials, Ceramics International, 39 (2013) 5949-5954.

[138] E. Arslan, Y. Totik, E. Demirci, A. Alsaran, Influence of Surface Roughness on Corrosion and Tribological Behavior of CP-Ti After Thermal Oxidation Treatment, J Mater Eng Perform, 19 (2010) 428-433.

[139] S. Kumar, T.S.N.S. Narayanan, S.G.S. Raman, S.K. Seshadri, Thermal oxidation of CP Ti — An electrochemical and structural characterization, Materials Characterization, 61 (2010) 589-597.

[140] A. Ashrafizadeh, F. Ashrafizadeh, Structural features and corrosion analysis of thermally oxidized titanium, Journal of Alloys and Compounds, 480 (2009) 849-852.

[141] S. Kumar, T.S.N.S. Narayanan, S.G.S. Raman, S.K. Seshadri, Thermal oxidation of CP-Ti: Evaluation of characteristics and corrosion resistance as a function of treatment time, Materials Science and Engineering: C, 29 (2009) 1942-1949.

[142] M. Jamesh, T.S.N. Sankara Narayanan, P.K. Chu, Thermal oxidation of titanium: Evaluation of corrosion resistance as a function of cooling rate, Mater Chem Phys, 138 (2013) 565-572.

[143] S. Wang, Z. Liao, Y. Liu, W. Liu, Influence of thermal oxidation temperature on the microstructural and tribological behavior of Ti6Al4V alloy, Surface and Coatings Technology, 240 (2014) 470-477.

[144] D. Siva Rama Krishna, Y.L. Brama, Y. Sun, Thick rutile layer on titanium for tribological applications, Tribol Int, 40 (2007) 329-334.

[145] F. Borgioli, E. Galvanetto, F. Iozzelli, G. Pradelli, Improvement of wear resistance of Ti–6Al–4V alloy by means of thermal oxidation, Materials Letters, 59 (2005) 2159-2162.

[146] P.A. Dearnley, K.L. Dahm, H. Çimenoğlu, The corrosion–wear behaviour of thermally oxidised CP-Ti and Ti–6Al–4V, Wear, 256 (2004) 469-479.

[147] S. Kumar, T.S.N. Sankara Narayanan, S. Ganesh Sundara Raman, S.K. Seshadri, Fretting corrosion behaviour of thermally oxidized CP-Ti in Ringer's solution, Corrosion Science, 52 (2010) 711-721.

[148] W. Castro, Elemental analysis of biological matrices by laser ablation high resolution inductively coupled plasma mass spectrometry (LA-HR-ICP-MS) and high resolution inductively coupled plasma mass spectrometry (HR-ICP-MS) [PhD Thesis], Florida International University, Miami, 2008.

[149] R. Le Geros, J. Legeros, Phosphate Minerals in Human Tissues, in: J. Nriagu, P. Moore (Eds.) Phosphate Minerals, Springer Berlin Heidelberg, 1984, pp. 351-385.

[150] R.A. Surmenev, M.A. Surmeneva, A.A. Ivanova, Significance of calcium phosphate coatings for the enhancement of new bone osteogenesis – A review, Acta Biomaterialia, 10 (2014) 557-579.

[151] M. Kumar, H. Dasarathy, C. Riley, Electrodeposition of brushite coatings and their transformation to hydroxyapatite in aqueous solutions, Journal of Biomedical Materials Research, 45 (1999) 302-310.

[152] M. Kumar, J. Xie, K. Chittur, C. Riley, Transformation of modified brushite to hydroxyapatite in aqueous solution: effects of potassium substitution, Biomaterials, 20 (1999) 1389-1399.

[153] X. Lu, Z. Zhao, Y. Leng, Calcium phosphate crystal growth under controlled atmosphere in electrochemical deposition, Journal of Crystal Growth, 284 (2005) 506-516.

[154] N. Dumeliė, H. Benhayoune, C. Rousse-Bertrand, S. Bouthors, A. Perchet, L. Wortham, J. Douglade, D. Laurent-Maquin, G. Balossier, Characterization of electrodeposited calcium phosphate coatings by complementary scanning electron microscopy and scanning-transmission electron microscopy associated to X-ray microanalysis, Thin Solid Films, 492 (2005) 131-139.

[155] M.F. Mohd Yusoff, M.R. Abdul Kadir, N. Iqbal, M.A. Hassan, R. Hussain, Dip coating of poly (ε-caprolactone)/hydroxyapatite composite coating on Ti6Al4V for enhanced corrosion protection, Surface and Coatings Technology, 245 (2014) 102-107.

[156] T. Li, J. Lee, T. Kobayashi, H. Aoki, Hydroxyapatite coating by dipping method, and bone bonding strength, J Mater Sci: Mater Med, 7 (1996) 355-357.

[157] B. Mavis, A.C. Taş, Dip Coating of Calcium Hydroxyapatite on Ti-6Al-4V Substrates, Journal of the American Ceramic Society, 83 (2000) 989-991.

[158] A. Montenero, G. Gnappi, F. Ferrari, M. Cesari, E. Salvioli, L. Mattogno, S. Kaciulis, M. Fini, Sol-gel derived hydroxyapatite coatings on titanium substrate, J Mater Sci, 35 (2000) 2791-2797.

[159] P.C. Rath, L. Besra, B.P. Singh, S. Bhattacharjee, Titania/hydroxyapatite bi-layer coating on Ti metal by electrophoretic deposition: Characterization and corrosion studies, Ceramics International, 38 (2012) 3209-3216.

[160] X.L. Zhu, K.H. Kim, Y.S. Jeong, Anodic oxide films containing Ca and P of titanium biomaterial, Biomaterials, 22 (2001) 2199-2206.

[161] L. Benea, E. Mardare-Danaila, M. Mardare, J.-P. Celis, Preparation of titanium oxide and

hydroxyapatite on Ti–6Al–4V alloy surface and electrochemical behaviour in bio-simulated fluid solution, Corrosion Science, 80 (2014) 331-338.

[162] Z.Q. Yao, Y. Ivanisenko, T. Diemant, A. Caron, A. Chuvilin, J.Z. Jiang, R.Z. Valiev, M. Qi, H.J. Fecht, Synthesis and properties of hydroxyapatite-containing porous titania coating on ultrafine-grained titanium by micro-arc oxidation, Acta Biomaterialia, 6 (2010) 2816-2825.

[163] Y.K. Pan, C.Z. Chen, D.G. Wang, Z.Q. Lin, Preparation and bioactivity of micro-arc oxidized calcium phosphate coatings, Mater Chem Phys, 141 (2013) 842-849.

[164] Y. Li, I.-S. Lee, F.-Z. Cui, S.-H. Choi, The biocompatibility of nanostructured calcium phosphate coated on micro-arc oxidized titanium, Biomaterials, 29 (2008) 2025-2032.

[165] S.R. Radin, P. Ducheyne, Plasma spraying induced changes of calcium phosphate ceramic characteristics and the effect on *in vitro* stability, J Mater Sci: Mater Med, 3 (1992) 33-42.

[166] R. McPherson, N. Gane, T.J. Bastow, Structural characterization of plasma-sprayed hydroxylapatite coatings, J Mater Sci: Mater Med, 6 (1995) 327-334.

[167] R. Palanivelu, S. Kalainathan, A. Ruban Kumar, Characterization studies on plasma sprayed (AT/HA) bi-layered nano ceramics coating on biomedical commercially pure titanium dental implant, Ceramics International, 40 (2014) 7745-7751.

[168] A. Kar, K.S. Raja, M. Misra, Electrodeposition of hydroxyapatite onto nanotubular TiO_2 for implant applications, Surf Coat Tech, 201 (2006) 3723-3731.

[169] Y. Huang, S. Han, X. Pang, Q. Ding, Y. Yan, Electrodeposition of porous hydroxyapatite/calcium silicate composite coating on titanium for biomedical applications, Applied Surface Science, 271 (2013) 299-302.

[170] C.-K. Lee, Fabrication, characterization and wear corrosion testing of bioactive hydroxyapatite/nano-TiO_2 composite coatings on anodic Ti–6Al–4V substrate for biomedical applications, Materials Science and Engineering: B, 177 (2012) 810-818.

[171] M. Eriksson, M. Andersson, E. Adolfsson, E. Carlstrom, Titanium-hydroxyapatite composite biomaterial for dental implants, Powder Metall, 49 (2006) 70-77.

[172] J.H. Xie, B.L. Luan, J.F. Wang, X.Y. Liu, C. Rorabeck, R. Bourne, Novel hydroxyapatite coating on new porous titanium and titanium-HDPE composite for hip implant, Surf Coat Tech, 202 (2008) 2960-2968.

[173] D. Gopi, E. Shinyjoy, M. Sekar, M. Surendiran, L. Kavitha, T.S. Sampath Kumar, Development of carbon nanotubes reinforced hydroxyapatite composite coatings on titanium by electrodeposition method, Corrosion Science, 73 (2013) 321-330.

[174] K. Venkateswarlu, N. Rameshbabu, A. Chandra Bose, V. Muthupandi, S. Subramanian, D. MubarakAli, N. Thajuddin, Fabrication of corrosion resistant, bioactive and antibacterial silver

substituted hydroxyapatite/titania composite coating on Cp Ti, Ceramics International, 38 (2012) 731-740.

[175] G. Singh, H. Singh, B.S. Sidhu, Characterization and corrosion resistance of plasma sprayed HA and HA–SiO_2 coatings on Ti–6Al–4V, Surface and Coatings Technology, 228 (2013) 242-247.

[176] M. Goudarzi, F. Batmanghelich, A. Afshar, A. Dolati, G. Mortazavi, Development of electrophoretically deposited hydroxyapatite coatings on anodized nanotubular TiO2 structures: Corrosion and sintering temperature, Applied Surface Science, 301 (2014) 250-257.

[177] J. Ciganovic, J. Stasic, B. Gakovic, M. Momcilovic, D. Milovanovic, M. Bokorov, M. Trtica, Surface modification of the titanium implant using TEA CO_2 laser pulses in controllable gas atmospheres - Comparative study, Applied Surface Science, 258 (2012) 2741-2748.

[178] S. Mischler, A. Spiegel, M. Stemp, D. Landolt, Influence of passivity on the tribocorrosion of carbon steel in aqueous solutions, Wear, 251 (2001) 1295-1307.

[179] A.I. Munoz, L.C. Julian, Influence of electrochemical potential on the tribocorrosion behaviour of high carbon CoCrMo biomedical alloy in simulated body fluids by electrochemical impedance spectroscopy, Electrochimica Acta, 55 (2010) 5428-5439.

[180] Standard guide for determining synergism between wear and corrosion ASTM, West Conshohocken, PA, 1998, pp. 529-534.

[181] S. Ningshen, U. Kamachi Mudali, G. Amarendra, P. Gopalan, R.K. Dayal, H.S. Khatak, Hydrogen effects on the passive film formation and pitting susceptibility of nitrogen containing type 316L stainless steels, Corrosion Science, 48 (2006) 1106-1121.

[182] L. Benea, P. Ponthiaux, F. Wenger, J. Galland, D. Hertz, J.Y. Malo, Tribocorrosion of stellite 6 in sulphuric acid medium: electrochemical behaviour and wear, Wear, 256 (2004) 948-953.

[183] N. Diomidis, J.P. Celis, P. Ponthiaux, F. Wenger, Tribocorrosion of stainless steel in sulfuric acid: Identification of corrosion–wear components and effect of contact area, Wear, 269 (2010) 93-103.

[184] N. Diomidis, N. Gödkan, P. Ponthiaux, F. Wenger, J.P. Celis, Assessment of the surface state behaviour of Al71Cu10Fe9Cr10 and Al3Mg2 complex metallic alloys in sliding contacts, Intermetallics, 17 (2009) 930-937.

[185] A. Lasia, Electrochemical Impedance Spectroscopy and its Applications, in: B.E. Conway, J.O.M. Bockris, R. White (Eds.) Modern Aspects of Electrochemistry, Springer US, 2002, pp. 143-248.

[186] N. Dalili, A. Edrisy, K. Farokhzadeh, J. Li, J. Lo, A.R. Riahi, Improving the wear resistance of Ti–6Al–4V/TiC composites through thermal oxidation (TO), Wear, 269 (2010) 590-601.

[187] H. Dong, T. Bell, Enhanced wear resistance of titanium surfaces by a new thermal oxidation treatment, Wear, 238 (2000) 131-137.

[188] M.C. García-Alonso, L. Saldaña, G. Vallés, J.L. González-Carrasco, J. González-Cabrero, M.E. Martínez, E. Gil-Garay, L. Munuera, *In vitro* corrosion behaviour and osteoblast response of thermally oxidised Ti6Al4V alloy, Biomaterials, 24 (2003) 19-26.

[189] B.B. Zhang, B.L. Wang, L. Li, Y.F. Zheng, Corrosion behavior of Ti–5Ag alloy with and without thermal oxidation in artificial saliva solution, Dental Materials, 27 (2011) 214-220.

[190] J. Katić, M. Metikoš-Huković, S.D. Škapin, M. Petravić, M. Varašanec, The potential-assisted deposition as valuable tool for producing functional apatite coatings on metallic materials, Electrochimica Acta, 127 (2014) 173-179.

[191] H. Wang, N. Eliaz, L.W. Hobbs, The nanostructure of an electrochemically deposited hydroxyapatite coating, Materials Letters, 65 (2011) 2455-2457.

[192] D. Velten, V. Biehl, F. Aubertin, B. Valeske, W. Possart, J. Breme, Preparation of TiO_2 layers on cp-Ti and Ti6Al4V by thermal and anodic oxidation and by sol-gel coating techniques and their characterization, Journal of Biomedical Materials Research, 59 (2002) 18-28.

[193] D. Wei, Y. Zhou, D. Jia, Y. Wang, Structure of calcium titanate/titania bioceramic composite coatings on titanium alloy and apatite deposition on their surfaces in a simulated body fluid, Surface and Coatings Technology, 201 (2007) 8715-8722.

[194] A.A. Egorov, V.V. Smirnov, L.I. Shvorneva, S.V. Kutsev, S.M. Barinov, High-temperature hydroxyapatite-titanium interaction, Inorg Mater, 46 (2010) 168-171.

List of Figures

List of Tables

Resume

Fonctionnalisations d'une surface de Titane commercialement pur en vue d'applications biomédicales : Une triple approche combinant corrosion, tribocorrosion et biologie

La tribocorrosion peut être définie comme l'étude de l'influence des facteurs environnementaux (chimiques et/ou électrochimiques) et mécanique (frottement) sur le comportement tribologique de surfaces en mouvement relatifs.

En raison de leurs caractéristiques particulières: performances mécaniques, associées à une faible densité, bonne tenue à la corrosion, biocompatibilité, le titane et ses alliages sont souvent utilisés dans le domaine médical comme implants dentaires et orthopédiques. Cependant, leur faible résistance vis-à-vis du frottement en milieu agressif et plus spécifiquement biologique reste un frein à leur usage courant dans le domaine prothétique.

Pour améliorer la résistance à la corrosion et à l'usure du titane et de ses alliages, différentes méthodes de modification de la surface ont été proposées durant ces dernières décennies.

Dans ce cadre, le but de ce travail est de comparer les comportements en corrosion et tribocorrosion du titane commercialement pur (cp Ti), avec ce même matériau ayant subi au préalable les traitements suivants :

- soit une étape d'oxydation thermique à 650 °C à l'air durant 48 h (formation d'un film d'oxyde de titane (TiO_2) en surface),
- soit un dépôt électrochimique de calcium phosphate (CaP) en surface,
- soit un dépôt électrochimique de calcium phosphate (CaP) suivi d'une étape d'oxydation thermique à 650 °C à l'air durant 6 h (formation d'un dépôt de type CaP/TiO_2 en surface).

Les phases cristallines des films modifiés ont été identifiées par diffraction des rayons X (XRD). La microscopie électronique à balayage (MEB) en combinaison avec la spectroscopie à dispersion d'énergie (EDS) a été utilisée pour caractériser la morphologie et la composition de ces films.

Le comportement en corrosion pure des échantillons cp Ti avec ou sans modifications de surface à été étudié in situ à partir des mesures électrochimiques de suivi du potentiel en circuit ouvert (OCP), de la spectroscopie d'impédance électrochimique (EIS) et du tracé de courbes de polarisation potentio-dynamiques.

Le comportement en tribocorrosion à été étudié quant à lui à l'aide d'un tribomètre de type pion-disque apte à travailler en milieu aqueux et permettant outre l'enregistrement des paramètres tribologiques classiques, la mise en œuvre in situ des techniques électrochimiques utilisées lors de l'étude en corrosion pure.

Caractérisation et analyses de la surface(composition, morphologie, rugosité…) sont effectuées avant et après chaque étude de comportement (corrosion et tribocorrosion).

Un protocole pour la culture des cellules sur la surface de titane a été validé, en se basant sur les résultats expérimentaux préliminaires.

Mots clés: corrosion, tribocorrosion, biological, cp Ti, thermal oxidation, CaP bioactive film.

Surface treated cp-titanium for biomedical applications: a combined corrosion, tribocorrosion and biological approach

Tribocorrosion is defined as the study of the interplay between chemical, electrochemical and mechanical processes that leads to a degradation of passivating materials in a corrosive environment. Due to the low density, excellent mechanical properties, high corrosion resistance and good biocompatibility, titanium and its alloys are widely used as dental and orthopedic implants. However, the poor wear resistant and bio-inert properties limit their further development as more efficient and economic biomedical implants.

To improve the corrosion-wear resistance and even bioactivity of metallic implants, different surface modification methods are imposed in the past decades.

The aim of this work is to provide a deep insight in the area of corrosion and tribocorrosion behavior of commercially pure titanium (cp Ti) under the guidance of a tribocorrosion protocol for passivating materials. And then three different surface modification treatments, as:

- one-step thermal oxidation at 650 ℃ for 48 h in air atmosphere to form a titania (TiO_2) film on the surface of cp Ti.
- one-step electrochemical deposition of calcium phosphate (CaP) bioactive film on the surface of cp Ti.
- electrochemical deposition of CaP bioactive film followed by thermal oxidation at 650 ℃ for 6 h in air atmosphere to form a CaP/TiO_2 bioceramic film on cp Ti surface.

The crystalline phases of the modified films were identified by X-ray diffraction (XRD). Scanning electron microscopy (SEM) combined with energy dispersive spectroscopy (EDS) was used to characterize the morphology and composition of these films on cp Ti surface.

In situ electrochemical measurements, like open circuit potential (OCP), electrochemical impedance spectroscopy (EIS) and potentiodynamic polarization are used to characterize the corrosion behavior of cp Ti samples without or with surface modification.

The tribocorrosion behavior was investigated in an aqueous environment by combining a pin-on-disc tribometer with the in situ electrochemical equipment. The classical tribological parameters could be also recorded under mechanical loaded condition.

Surface characterization and analysis (like chemical composition, morphology, roughness...) are carried out before and after each corrosion and tribocorrosion test.

A protocol for the culture of cells on the surface of titanium was validated, basing on the preliminary experimental results.

Keywords: corrosion, tribocorrosion, cp Ti, thermal oxidation, CaP bioactive film